Строительная механика инженерных конструкций и сооружений

2025 Том 21 № 5

DOI: 10.22363/1815-5235-2025-21-5

http://journals.rudn.ru/structural-mechanics

Издается с 2005 г.

Свидетельство о регистрации СМИ ПИ № ФС 77-19706 от 13 апреля 2005 г.
выдано Федеральной службой по надзору в сфере связи, информационных технологий и массовых коммуникаций (Роскомнадзор)
Учредитель: Федеральное государственное автономное образовательное учреждение высшего образования
«Российский университет дружбы народов имени Патриса Лумумбы»

ISSN 1815-5235 (Print), 2587-8700 (Online)
Периодичность: 6 выпусков в год.
Языки: русский, английский.
Журнал индексируют: РИНЦ, RSCI, Cyberleninka, DOAJ, Google Scholar, Ulrich's Periodicals Directory, WorldCat, Dimensions.
Включен в Перечень ведущих научных журналов и изданий ВАК при Минобрнауки России по группе научных специальностей 2.1.1. Строительные конструкции, здания и сооружения (технические науки), 2.1.2. Основания и фундаменты, подземные сооружения (технические науки), 2.1.9. Строительная механика (технические науки).

Международный научно-технический журнал *«Строительная механика инженерных конструкций и сооружений»* знакомит читателей с достижениями отечественных и зарубежных ученых в области геометрии пространственных конструкций, сопротивления материалов, строительной механики, теории упругости и расчета строительных и машиностроительных конструкций, освещает вопросы научно-технического прогресса в строительстве и машиностроении, публикует аналитические обзоры по теме журнала.

Сайт журнала содержит полную информацию о журнале, его редакционной политике и этических принципах, требования к подготовке и условия публикации статей, а также полные выпуски журнала с 2008 г. (в рамках политики свободного доступа).

СОДЕРЖАНИЕ

РАСЧЕТ ТОНКИХ УПРУГИХ ОБОЛОЧЕК

АНАЛИТИЧЕСКИЕ И ЧИСЛЕННЫЕ МЕТОДЫ РАСЧЕТА КОНСТРУКЦИЙ

Редактор И.Л. Панкратова
Редактор англоязычных текстов С.Л. Шамбина
Дизайн обложки Ю.Н. Ефремовой
Компьютерная верстка Н.В. Маркеловой

Адрес редакции:
Российский университет дружбы народов имени Патриса Лумумбы
Российская Федерация, 117198, Москва, ул. Миклухо-Маклая, д. 6; тел./факс: +7 (495) 955-08-28; e-mail: stmj@rudn.ru, i_mamieva@mail.ru

Подписано в печать 24.10.2025. Выход в свет 30.10.2025. Формат 60×84/8.
Бумага офсетная. Печать офсетная. Гарнитура «Times New Roman». Усл. печ. л. 13,95. Тираж 250 экз. Заказ № 1685. Цена свободная.

Федеральное государственное автономное образовательное учреждение высшего образования «Российский университет дружбы народов имени Патриса Лумумбы»
Российская Федерация, 117198, Москва, ул. Миклухо-Маклая, д. 6

Отпечатано в типографии ИПК РУДН
Российская Федерация, 115419, Москва, ул. Орджоникидзе, д. 3

STRUCTURAL MECHANICS OF ENGINEERING CONSTRUCTIONS AND BUILDINGS

2025 VOLUME 21 NO. 5

DOI: 10.22363/1815-5235-2025-21-5

http://journals.rudn.ru/structural-mechanics

Founded in 2005
by Peoples' Friendship University of Russia named after Patrice Lumumba

ISSN 1815-5235 (Print), 2587-8700 (Online)
Published 6 times a year.
Languages: Russian, English.
Indexed by RSCI, Russian Index of Science Citation, Cyberleninka, DOAJ, Google Scholar, Ulrich's Periodicals Directory, WorldCat, Dimensions.
The journal has been included in the list of the leading review journals and editions of the Highest Certification Committee of Ministry of Education and Science of Russian Federation in which the basic results of PhD and Doctoral Theses are to be published.

International scientific-and-technical peer-reviewed journal *"Structural Mechanics of Engineering Constructions and Buildings"* shows the readers round the achievements of Russian and foreign scientists in the area of geometry of spatial structures, strength of materials, structural mechanics, theory of elasticity and analysis of building and machine-building structures, illumines the problems of scientific-and-technic progress in building and machine-building, publishes analytic reviews on the aims and scope of the journal.

The journal website contains full information about the journal, editorial policy and ethics, requirements for the preparation and publication of the articles, etc., as well as full-text issues of the journal since 2008 (Open Access).

CONTENTS

Copy Editor I.L. Pankratova
English Texts' Editor S.L. Shambina
Graphic Designer Iu.N. Efremova
Layout Designer N.V. Markelova

Address of the Editorial Board:
Peoples' Friendship University of Russia named after Patrice Lumumba
6 Miklukho-Maklaya St, Moscow, 117198, Russian Federation; tel./fax: +7 (495) 955-08-28; e-mail: stmj@rudn.ru, i_mamieva@mail.ru

Printing run 250 copies. Open price

Peoples' Friendship University of Russia named after Patrice Lumumba
6 Miklukho-Maklaya St, Moscow, 117198, Russian Federation

Printed at Publishing House of RUDN University
3 Ordzhonikidze St, Moscow, 115419, Russian Federation

Строительная механика инженерных конструкций и сооружений
Structural Mechanics of Engineering Constructions and Buildings

2025. 21(5). 377–388

ISSN 1815-5235 (Print), 2587-8700 (Online)

HTTP://JOURNALS.RUDN.RU/STRUCTURAL-MECHANICS

РАСЧЕТ ТОНКИХ УПРУГИХ ОБОЛОЧЕК
ANALYSIS OF THIN ELASTIC SHELLS

DOI: 10.22363/1815-5235-2025-21-5-377-388
EDN: DQGYSO

Research article / Научная статья

Construction of Developable Surfaces with Two Director Curves

Sergey N. Krivoshapko

RUDN University, *Moscow, Russian Federation*
✉ sn_krivoshapko@mail.ru

Received: March 25, 2025
Revised: June 15, 2025
Accepted: August 7, 2025

Abstract. An analysis of a number of published materials regarding four types of developable surfaces with two director (supporting) algebraic curves of the second order lying in parallel or in intersecting planes has been conducted. Three types of developable surfaces are shortly described with references to sources, and visualizations of each type of developable surface are presented. For the developable surfaces with two supporting curves with intersecting axes in intersecting planes, the construction technique and the method of obtaining parametric equations are given. This method is illustrated with three examples. It is established that to date, there are no studies on the strength of thin shells in the form of the presented developable surfaces defined in curvilinear conjugate non-orthogonal coordinates that coincide with the external contour of the shells. It is shown that there are suggestions of application of the studied surfaces in architecture, shipbuilding, and agricultural machine engineering.

Keywords: parallel vectors, vector coplanarity, second-order algebraic curves, developable surface with two director curves, surface modelling, computer graphics

Conflicts of interest. The author declares that there is no conflict of interest.
For citation: Krivoshapko S.N. Construction of developable surfaces with two director curves. *Structural Mechanics of Engineering Constructions and Buildings.* 2025;21(5):377–388. http://doi.org/10.22363/1815-5235-2025-21-5-377-388 EDN: DQGYSO

Построение торсовых поверхностей на двух направляющих кривых

С.Н. Кривошапко

Российский университет дружбы народов, *Москва, Российская Федерация*
✉ sn_krivoshapko@mail.ru

Поступила в редакцию: 25 марта 2025 г.
Доработана: 15 июня 2025 г.
Принята к публикации: 7 августа 2025 г.

Аннотация. Проведен анализ ряда опубликованных материалов по четырем типам торсовых поверхностей с двумя направляющими (опорными) алгебраическими кривыми второго порядка, лежащими в параллельных или пересекающихся плоскостях. Три типа торсов описаны кратко со ссылками на источники и приведены графические иллюстрации для

Sergey N. Krivoshapko, Doctor of Technical Sciences, Consulting Professor of the Department of Construction Technology and Structural Materials, Academy of Engineering, RUDN University, 6 Miklukho-Maklaya St, Moscow, 117198, Russian Federation; eLIBRARY SPIN-code: 2021-6966, ORCID: 0000-0002-9385-3699; e-mail: sn_krivoshapko@mail.ru

каждого типа торсов, а для торсовых поверхностей с двумя опорными кривыми с пересекающимися осями в пересекающихся плоскостях представлен порядок построения этой поверхности и методика получения параметрических уравнений. Методика проиллюстрирована на трех примерах. Установлено, что до настоящего времени нет ни одного исследования напряженно-деформированного состояния предложенных тонких торсовых оболочек, заданных в криволинейных неортогональных сопряженных координатах, которые совпадают с внешним контуром торсовых оболочек. Показано, что есть предложения по применению предложенных поверхностей в архитектуре, судостроении и сельскохозяйственном машиностроении.

Ключевые слова: параллельность векторов, компланарность векторов, алгебраические кривые второго порядка, торс с двумя направляющими кривыми, моделирование поверхностей, компьютерная графика

Заявление о конфликте интересов: Автор заявляет об отсутствии конфликта интересов.

Для цитирования: *Кривошапко С.Н.* Построение торсовых поверхностей на двух направляющих кривых // Строительная механика инженерных конструкций и сооружений. 2025. Т. 21. № 5. С. 377–388. http://doi.org/10.22363/1815-5235-2025-21-5-377-388 EDN: DQGYSO

1. Introduction

Over the last five years, the author has published articles on the construction of developable surfaces containing two prespecified plane algebraic curves on opposite sides of rectangular [1], trapezoidal [2], and arbitrary quadrilateral [3] bases. Moreover, the generator lines of the resulting developable surfaces coincide with the opposite sides of the rectangular and trapezoidal bases. In the case of an arbitrary quadrilateral base, the generator lines do not coincide with the sides, but are only projected onto them.

The construction of the considered developable surfaces is based on the works of G. Monge, G.E. Pavlenko [4], J.N. Gorbatovich [5], B. Bhattacharya [6], V.G. Rekach and N.N. Ryzhov [7], V.N. Ivanov [8], M.E. Ershov, E.M. Tupikova [9], Fr. Perez-Arribas and L. Fernandez-Jambrina [10].

Despite the fact that many geometers and engineers have been creating and improving methods for constructing developable surfaces with two prespecified plane curves, there are very few illustrations of specific developable surfaces, literally only a handful.

The *purpose of the study* is to draw the attention of experts to the possibility of obtaining parametric equations of developable surfaces constructed with two prespecified supporting plane curves lying in parallel or intersecting planes. Until now, graphical methods have been mainly used to construct these surfaces [11; 12]. Implicit or parametric equations have been obtained only for 5–6 developable surfaces [13]. Engineers and designers in the mechanical and textile industries are interested in expanding the list of developable surfaces defined by analytical formulas, which is also the goal of the proposed study [14; 15].

2. Algebraic Curves as Director Curves for Construction of Developable Surfaces

In all publications [1; 2; 3], second- and fourth-order algebraic curves were used as director curves. These curves can be defined as follows:

- ***parabola:***

$$x = x(u) = au, y = y(u) = h\left(1 - u^2\right), \tag{1}$$

- ***ellipse fragment:***

$$x = x\left(u\right) = au,\ y = y\left(u\right) = h_1\left(\sqrt{1 - u^2a^2 / a_1^2} - \sqrt{1 - a^2 / a_1^2}\right), \tag{2}$$

where a_1 and h_1 are the lengths of the semiaxes of a complete ellipse, $a_1 \geq a$. By assuming the value of a_1, the length of the other semiaxis of the complete ellipse h_1 can be determined,

- ***circle fragment:***

$$x_1 = x(u) = au,\ y_1 = y(u) = \sqrt{R^2 - a^2u^2} - \sqrt{R^2 - a^2}, \tag{3}$$

- ***hyperbola:***

$$x = x(u) = au,\ y = c + h - \sqrt{c^2 + hu^2(2c + h)}, \tag{4}$$

constant parameter c is chosen arbitrarily, but $c \neq 0$,

- ***biquadratic parabola:***

$$x = x(u) = au,\ y = y(u) = h\left(1 - u^4\right), \tag{5}$$

- ***superellipse:***

$$x = x(u) = au,\ y = y(u) = h\sqrt[r]{1 - |u|^t}\ . \tag{6}$$

The tangent to the curve at angle φ is determined by the formula:

$$\text{tg}\,\varphi = \frac{dy}{dx}, \tag{7}$$

$$-1 \le u \le 1.$$

The remaining geometric parameters are shown in Figure 1. More detailed information on curves (1)–(6) can be found in any reference book on analytical geometry or in publications [1–3].

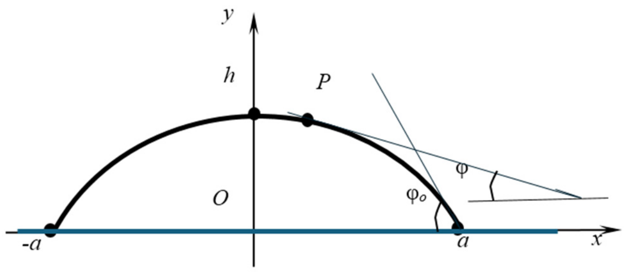

Figure 1. Constant geometrical parameters of curves
S o u r c e: compiled by S.N. Krivoshapko.

2.1. Examples of Developable Surfaces with Rectangular, Trapezoida and Quadrilateral Bases with Two Director Curves at Opposite Ends

2.1.1.Cylindrical surfaces with rectangular base (Figure 2)

All algebraic second-order cylindrical surfaces are considered in [16]. A cylindrical surface is an improper developable surface, in which the edge of regression is moved off to infinity. It is very easy to define a cylindrical surface with a rectangular base in parametric form. For example, if the identical director parabolas are specified as: $y = ax^2$, where $a = h/c^2$, then the parametric equations of the cylindrical surface will be: $x = x$, $y = ax^2$, $z = z$.

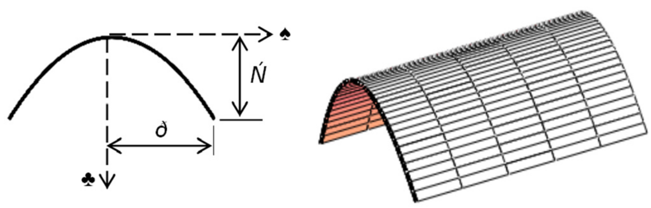

Figure 2. Cylindrical surface with parabolas at the ends
S o u r c e: compiled by V.N. Ivanov et al. [16].

2.1.2. Developable surfaces with two prespecified plane curves in parallel planes

For the construction of a developable surface, which contains plane curves in parallel xOy planes, i.e. at $z = 0$, and at $z = l$, and in which the opposite straight generator lines lie in the horizontal xOz plane parallel to the coordinate plane yOz, it is necessary to assume that angles φ_0 of both director curves are equal (Figure 1).

Given a pair of any director curves defined by equations (1)–(6), their vector equations can be represented as:

$$\boldsymbol{r}_1 = \boldsymbol{r}_1(u) \text{ and } \boldsymbol{r}_2 = \boldsymbol{r}_2(v) \tag{8}$$

with respect to origin O, where u, v are the corresponding parameters, then the equation of the developable surface can be represented in the form [6]:

$$\boldsymbol{r}(u,\lambda) = \boldsymbol{r}_1(u) + \lambda[\boldsymbol{r}_2(v) - \boldsymbol{r}_1(u)], \tag{9}$$

where λ is a dimensionless parameter, $0 \le \lambda \le 1$.

By defining the developable surface in the form of (9), coordinate lines λ = 0 and λ = 1 coincide with the director curves. The following relation must hold true between parameters u and v [4]:

$$\frac{y_1'(u)}{x_1'(u)} = \frac{y_2'(v)}{x_2'(v)}. \tag{10}$$

The geometric meaning of equation (10) is that the straight generator of the developable surface passes through two corresponding points of the plane curves, for which the angular coefficients of the tangents φ_0 are equal, i.e., the tangents drawn through the corresponding points of the two curves must be parallel.

Vector equation (9) may be represented in parametric form:

$$\begin{aligned} x &= x(u,\ \lambda) = x_1(u)(1-\lambda) + \lambda x_2[v(u)], \\ y &= y(u,\ \lambda) = y_1(u)(1-\lambda) + \lambda y_2[v(u)], \\ z &= z(\lambda) = \lambda l. \end{aligned} \tag{11}$$

The method described above for determining parametric equations (11) of the developable surfaces in [1] has been tested on five examples of pairs of plane curves as director curves: ellipse (2) + parabola (1), circle fragment (3) + parabola (1), hyperbola (4) + parabola (1) (Figure 3), parabola (1) + biquadratic parabola (5) (Figure 4), superellipse (6) with $r = t = 2$ + superellipse (6) with $r = t = 3$.

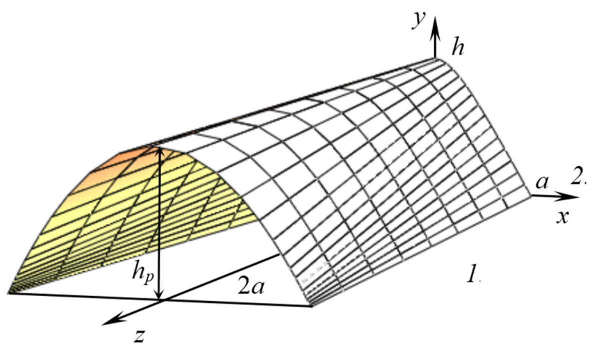

Figure 3. Developable surface with a parabola and a hyperbola at the ends
S o u r c e: compiled by S.N. Krivoshapko.

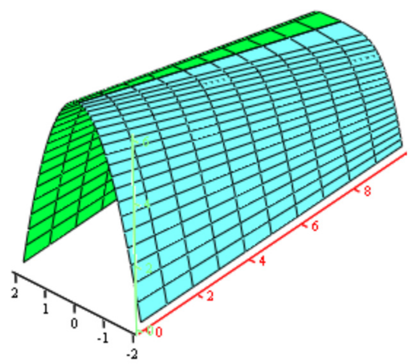

Figure 4. Developable surface with a second- and a fourth-order parabola at the ends
S o u r c e: compiled by S.N. Krivoshapko.

The developable surface with a circle and a parabola in parallel planes also attracted the attention of J.N. Gorbatovich [5]. The surface with an ellipse and a parabola in parallel planes was studied in article [17]. A developable surface with parabolas was used to illustrate the method of constructing its projection onto a plane [9]. There is an example of approximating a developable surface with parabolas of the 2nd and 4th orders in parallel planes with a folded structure [18]. These developments can be applied to the considered surfaces with rectangular base, but in the articles [5; 9; 18], the contour generator lines do not lie in the horizontal plane.

Article [2] considers developable surfaces with two prespecified plane curves (1)–(6) in parallel planes, but with a trapezoidal base. In this case, for the first curve (Figure 1) $-1 \le u \le 1$, i.e. $-a \le x \le a$, and for the second curve $-1 \le v \le 1$, i.e. $-b \le v \le b$. If the plane director curves (8) lie in parallel planes, relation (10) must hold between parameters u and v.

When constructing a developable surface, which has plane director curves of same rise h along axis Oz and two straight generator lines, which coincide with the sides of the trapezoidal base in the xOz plane, the following additional condition must be satisfied (Figure 1):

tgφ_o of one curve at $x = \pm a$ must be equal to tgφ_o of the other curve at $x = \pm b$.

After satisfying the above condition and condition (10), parametric equations (11) of the considered developable surface can be written. In article [2], the construction method is tested on examples of six pairs of plane curves as directors: ellipse (2) + parabola (1) (Figure 5), circle fragment (3) + parabola (1) (Figure 6), hyperbola (4) + parabola (1), parabola (1) + biquadratic parabola (5), superellipse (6) with $r = t = 2$ + + superellipse (6) with $r = t = 3$, hyperbola (4) + biquadratic parabola (5).

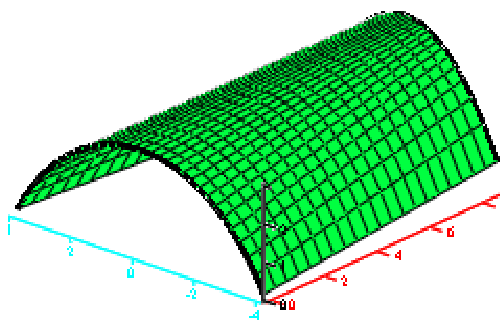

General view

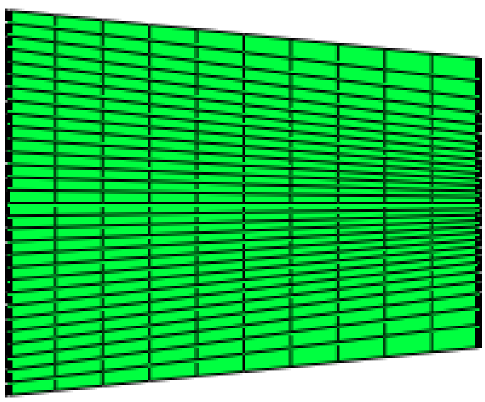

View in yOz plane

Figure 5. Developable surface with an ellipse fragment and a parabola at parallel ends
S o u r c e: compiled by S.N. Krivoshapko.

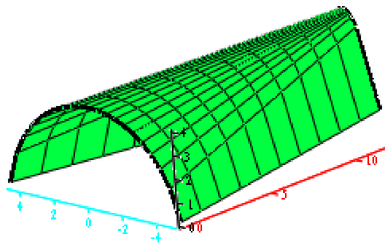

General view

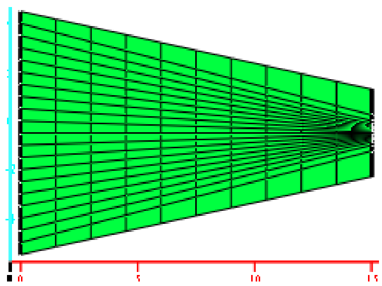

View in xOz plane

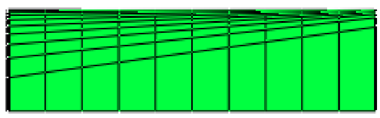

View in yOz plane

Figure 6. Developable surface with a circle fragment and a parabola at parallel ends
S o u r c e: compiled by S.N. Krivoshapko.

Developable surfaces with trapezoidal base with two prespecified plane curves at the two parallel edges and with straight generators resting on the lateral sides were considered only in article [7] from an architectural point of view.

2.1.3. Developable Surfaces with Two Prespecified Plane Curves in Intersecting Planes

Under these conditions, there are two possible cases that are acceptable for practical application: when the axes of the director curves are parallel (case 1) and when the axes of the director curves intersect (case 2). The first case is discussed in detail in article [3]. Curves (1)–(6) are taken in pairs as director curves, and six developable surfaces are constructed. Two of them are shown in Figures 7 and 8.

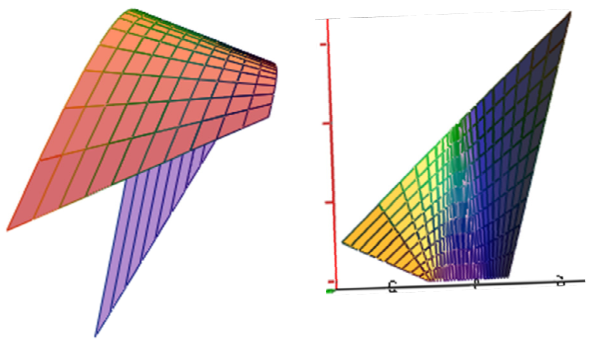

a *b*

Figure 7. Developable surface with a second- and fourth-order parabola in intersecting planes: *a* — general view; *b* — view in xOz plane
S o u r c e: compiled by S.N. Krivoshapko.

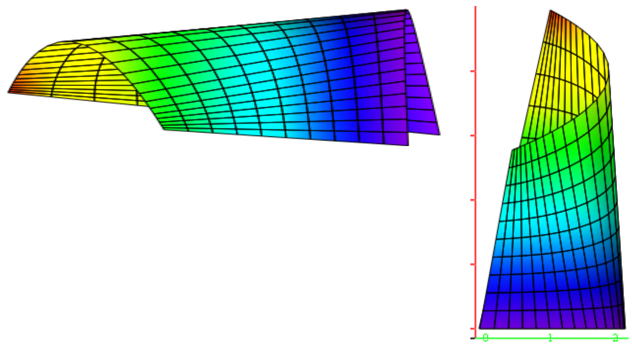

a *b*

Figure 8. Developable surface with a parabola and a hyperbola in intersecting planes: *a* — general view; *b* — view in yOz plane
S o u r c e: compiled by S.N. Krivoshapko.

The second case is considered in more detail below. Assuming that the two curves lie in intersecting planes and their axes intersect (Figure 9), then their parametric equations can be represented as:

Curve 1: $x_1 = x_1(u), y_1 = u, z_1 = 0;$

Curve 2: $x_2 = x_2(v), y_2 = v, z_2 = x_2 \mathrm{tg}\varphi.$ (12)

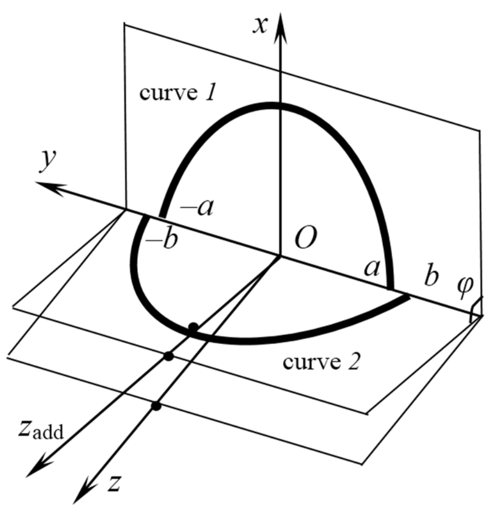

Figure 9. Two director curves with intersecting axes in intersecting planes
S o u r c e: compiled by S.N. Krivoshapko.

The coplanarity condition of the three vectors is written as:

$$\left(\boldsymbol{r}_2 - \boldsymbol{r}_1, \boldsymbol{r}_1^{/}, \boldsymbol{r}_2^{/}\right) = 0,$$

or

$$\begin{vmatrix} x_2 - x_1 & v - u & x_2 \mathrm{tg}\varphi \\ x_1^{/} & 1 & 0 \\ x_2^{/} & 1 & x_2 \mathrm{tg}\varphi \end{vmatrix} = 0,$$

or in expanded form:

$$x_2^{/} x_1^{/} \left(v - u\right) + x_1 x_2^{/} - x_2 x_1^{/} = 0, \quad (13)$$

by taking

$$y_1^{/}(u) = 1, y_2^{/}(v) = 1, z_2^{/} = x_2^{/} \mathrm{tg}\varphi, x_2 = z_{add}(v)\cos\varphi,$$

φ is the angle between the intersecting planes.

Vector equation (9) for the considered case of director curves (12) can be converted into parametric form of definition of the desired developable surface:

$$x = x(u,\lambda) = x_1(u)(1-\lambda) + \lambda x_2\left[v(u)\right];$$

$$y = y(u,\lambda) = y_1(u)(1-\lambda) + \lambda y_2\left[v(u)\right] = u(1-\lambda) + \lambda v;$$

$$z = z(u,\lambda) = \lambda x_2\left[v(u)\right]\operatorname{tg}\varphi. \tag{14}$$

Example 1. Two square parabolas, which lie in planes intersecting at angle φ, are specified (Figure 9):

$$x_1 = x_1(u) = h\left[1 - u^2/a^2\right], y_1 = y_1(u) = u, \ z_1 = 0;$$

$$x_2 = x_2(v) = H\left[1 - v^2/b^2\right]\cos\varphi, \ y_2 = y_2(v) = v, \quad z_2 = z_2(v) = H\left[1 - v^2/b^2\right]\sin\varphi. \tag{15}$$

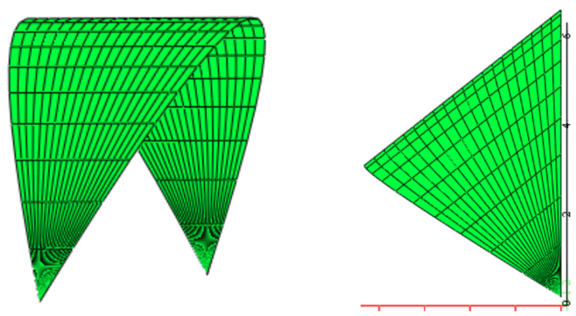

a *b*

Figure 10. Developable surface defined by equations (17):
a — general view; *b* — view in *xOz* plane
S o u r c e: compiled by S.N. Krivoshapko.

The relation between parameters *u* and *v* is determined by formula (13):

$$v_{1,2} = \frac{1}{2}\left(u + \frac{a^2}{u}\right) \pm \frac{1}{2}\sqrt{\left(u + \frac{a^2}{u}\right)^2 - 4b^2}. \tag{16}$$

By taking $a = b$, one obtains $v_1 = u$ and $v_2 = a^2/u$.

By further taking $v = v_1 = u$ and $a = b$, parametric equations (14) of the desired developable surface will be

$$x = x(u,\lambda) = \left(1 - \frac{u^2}{a^2}\right)\left[h(1-\lambda) + \lambda H\cos\varphi\right];$$

$$y = y(u) = u;$$

$$z = z(u,\lambda) = \lambda H\left(1 - \frac{u^2}{a^2}\right)\sin\varphi. \tag{17}$$

Figure 10 shows the surface defined by parametric equations (17), where

$h = 6$ m, $H = 5$ m, $a = 2$ m, $\varphi = 60^\circ$, $-a \le u \le a$, $0 \le \lambda \le 1$.

Example 2. By assuming that parabolas (15) lie in mutually perpendicular planes, then φ = 90°, and parametric equations (17) will take the following form:

$$x = x(u,\lambda) = \left(1 - \frac{u^2}{a^2}\right)\left[h(1-\lambda)\right];$$

$$y = y(u) = u;$$

$$z = z(u,\lambda) = \lambda H\left(1 - \frac{u^2}{a^2}\right). \quad (18)$$

Parametric equations (18) can be transformed into implicit form:

$$\frac{z}{H} + \frac{y^2}{a^2} + \frac{x}{h} - 1 = 0.$$

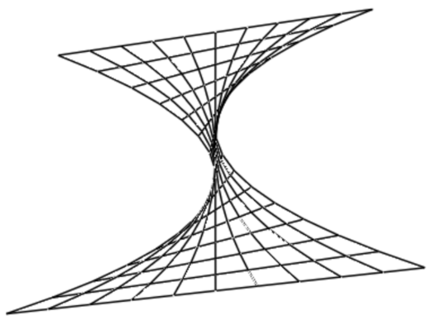

Figure 11. Parabolic developable surface
Source: compiled by S.N. Krivoshapko.

It is evident that this implicit equation describes a parabolic cylinder.

Encyclopedia [13] describes two developable surfaces: one with parabolas, the axes of which intersect, but the parametric equations of which differ from equations (15), and another developable surface containing two ellipses in mutually perpendicular planes.

V.S. Obukhova and R.I. Vorobkevich [19] proposed using two parabolas in mutually perpendicular coordinate planes as director curves, with their vertices touching one of the coordinate axes and the axes of the parabolas perpendicular to this axis (Figure 11).

Example 3. A semiellipse (curve *1*) and a parabola (curve *2*) are taken as director curves:

$$x_1 = x_1(u) = h\sqrt{1 - \frac{u^2}{a^2}}, \quad y_1 = u, \quad z_1 = 0;$$

$$x_2 = x_2(v) = H\left(1 - \frac{v^2}{b^2}\right)\cos\varphi, \quad y_2 = v, \quad z_2(v) = H\left(1 - \frac{v^2}{b^2}\right)\sin\varphi.$$

The relation between parameters u and v is determined by formula (13):

$$u = \frac{2va^2}{b^2 + v^2}. \quad (19)$$

Parametric equations (14) of the desired developable surface will be written as

$$x = x(v,\lambda) = h(1-\lambda)\sqrt{1 - \frac{4v^2a^2}{\left(b^2 + v^2\right)^2}} + \lambda H\left(1 - \frac{v^2}{b^2}\right)\cos\varphi;$$

$$y = y(v,\lambda) = (1-\lambda)\frac{2va^2}{\left(b^2 + v^2\right)} + \lambda v;$$

$$z = z(v,\lambda) = \lambda H\left(1 - \frac{v^2}{b^2}\right)\sin\varphi. \quad (20)$$

Figure 12 shows the surface defined by parametric equations (20), where

$h = 4$ m, $H = 5$ m, $a = 1.2$ m, $b = 1.8$ m;

$\varphi = 60^{\circ}$, $-b \leq v \leq b$, $0 \leq \lambda \leq 1$.

In further introduction of developable surfaces defined by parametric equations (14) for practical application, the resulting surface can be rotated around the *y*-axis, so that the extreme straight generator lines rest on the specified base. In this case, the intersecting planes with director curves will be inclined to the base at corresponding angles (Figure 10, *a*).

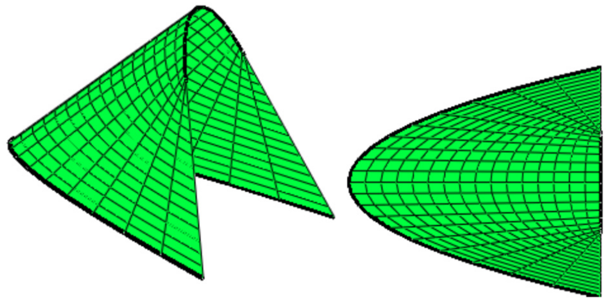

a *b*

Figure 12. Developable surface defined by equations (20): *a* — general view; *b* — view in *yOz* plane
S o u r c e: compiled by S.N. Krivoshapko.

3. Review of Studies on Strength Analysis of Four Types of Developable Shells with Proposed Middle Surfaces

G. Monge laid the foundation for geometric research on proper developable surfaces in 1805. Since then, hundreds of scientific papers have been published on the geometry and application of these surfaces. Less than two dozen papers are devoted to the study of the stress-strain state of proper developable thin shells, with the exception of developable helicoids [20] and shells of equal slope [21]. All known developable shells have their middle surfaces defined in a non-orthogonal conjugate system of curvilinear coordinates, which significantly complicates the analytical calculation of these shells.

The system of 20 equations for determining 19 two-dimensional parameters, presented by A.L. Goldenveiser, provided that the mid-surface is specified in the arbitrary system of curvilinear coordinates, contains internal “pseudo-forces” and “pseudo-moments” as opposed to internal forces and moments adopted in the system of 20 equations containing 19 unknowns obtained by the author [22]. These two systems of equations were used in a simplified version only for the momentless analysis of two types of developable shells. G.Ch. Bajoria [23] applied A.L. Goldenveiser’s equilibrium equations for the momentless analysis of a developable shell defined in the form:

$$\boldsymbol{r} = \boldsymbol{r}(u,v) = \boldsymbol{\rho}(v) + u\boldsymbol{l}(v), \tag{21}$$

where $\boldsymbol{\rho}(v)$ is the current position vector of the edge of regression; $\boldsymbol{l}(v)$ is the unit tangent vector to the edge of regression. B. Bhattacharya [24] also applied A.L. Goldenveiser’s equilibrium equations, but on the premise of defining the middle surface of the developable shell in the form of (9).

A developable shell with an arbitrary quadrangular base with two plane parabolas lying in intersecting planes with parallel axes is calculated according to the momentless theory [25]. The results of calculating a developable shell with a circle and an ellipse in parallel planes, subjected to a linear load on the circular edge, are presented in [26]. The same shell, but loaded with self-weight, is considered in [27].

4. Results

1. When constructing a developable surface with two *n*-order algebraic director curves in parallel planes (Figures 3, 4) passing through opposite sides of a rectangular base $2a \times l$, any algebraic curves can be taken as director curves, with the rise *h* (Figure 1) of one of the two curves being arbitrary, and the rise of the second curve being calculated based on the geometric parameters of the two specified curves from the condition of equality of angles φ_0. Distance *l* between the planes with the curves does not affect the rise values of the curves.

2. The rise of two superellipses (6) in parallel planes can be any value.

3. To construct developable surfaces with two n-order algebraic director curves in parallel planes (Figures 3, 4) passing through opposite sides of a rectangular base $2a \times l$, and developable surfaces with two specified plane curves (1)–(6) in parallel planes, but with trapezoidal base with the parallel sides equal to $2a$ and $2b$, the same parametric equations (11) can be used.

4. The rise values h and H of the two director curves lying in intersecting planes, and the magnitude of angle φ between these planes, do not affect the relationship between parameters u and v (see, for example, formulas (16) and (19)).

5. It is shown that to date, 6 developable surfaces with director curves in parallel planes and with specified boundary conditions on the contours of rectangular bases [1], 8 developable surfaces with director curves in parallel planes and with specified boundary conditions on the contours of trapezoidal bases [2], 5 developable surfaces with director curves with parallel axes in intersecting planes [3], and only 3 developable surfaces with director curves with intersecting axes in intersecting planes have been studied. In this article, 3 more developable surfaces with director curves with intersecting axes in intersecting planes are introduced.

6. The literature review has shown that there are currently no studies on the strength analysis of thin shells with the considered developable middle surfaces, specified in curvilinear non-orthogonal conjugate coordinates u, λ in the form (11) or (14) using the moment theory of shells. Researchers from the Academy of Engineering of RUDN University, Moscow have published a large number of studies on geometry, application, approximation of developable surfaces by folds, unfolding developable surfaces onto a plane and their parabolic bending, and determination of the strength parameters of some special cases of developable shells. In addition to their studies, some of which are listed in the "References" section, most of the scientific articles published over the last 25 years are devoted to the implementation of methods for unfolding developable surfaces with two specified director curves onto a plane with maximum use of computers [14; 28; 29] and the practical application of developable surfaces [30] in avant-garde architecture, agricultural machine engineering, shipbuilding [10], the fashion industry [15], as well as the solution of mathematical problems related to developable surfaces [31].

7. It is established that the only study on finding the optimal cylindrical shell with two variable supporting curves at the ends is the article by V.N. Ivanov, O.O. Aleshina, E.A. Larionov [16]. Cylindrical surfaces are improper developable surfaces in which the edge of regression is moved off to infinity.

5. Conclusion

Scientific and technical literature proposes 10 methods for constructing developable surfaces. The most well-known of them are constructing developable surfaces based on two specified director curves, based on the specified edge of regression, and the kinematic method of winding a plane with a straight line onto a cylinder and cone. The first method listed above is recommended mainly for designing large-area roofs in construction, the second is widely used to create screw and helical products in mechanical engineering, and the third method is used when studying the trajectory of a straight line in space and when studying the carved ruled Monge surface.

Despite the fact that there are sketches of architectural objects in the form of developable surfaces with specified supporting plane curves, they are most commonly used in the design of river and sea vessel hulls. Virtually all publications on the manufacture of ship hulls use graphic representations of the ideas for design of these developable surfaces.

The article offers analytical solutions to the problems posed. For convenience of studying developable surfaces with two specified curves, they are divided into four types, for each of which the procedure for obtaining explicit or parametric equations is shown, according to which the corresponding developable surfaces with specified geometric parameters are constructed using computer graphics.

The presented material may encourage architects and practicing engineers to make wider use of the proposed developable surfaces in the forms of real products, structures, and buildings.

References

1. Krivoshapko S.N. Torse surfaces on a rectangular plan with two plane curves on the opposite ends. *Building and Reconstruction*. 2025;1(117):3–15. (In Russ.) https://doi.org/10.33979/2073-7416-2025-117-1-3-15 EDN: ACOCGO
2. Krivoshapko S.N. Torse surfaces on trapezoidal plan with given in advance curves on the ends and straight generatrixes coinciding with its other sides. *Structural Mechanics and Analysis of Constructions.* 2025;(4):62–72. (In Russ.) https://doi.org/10.37538/0039-2383.2025.4.62.72 EDN: BOGAHV
3. Krivoshapko S.N. Torses with two curves in intersecting planes and with parallel axes. *Structural Mechanics of Engineering Constructions and Buildings*. 2025;21(2):155–166. https://doi.org/10.22363/1815-5235-2025-21-2-155-166 EDN: NRNOQA
4. Pavlenko G.E. *Simplified Shapes of Ships*. Moscow: MRF SSSR, 1948. (In Russ.)
5. Gorbatovich J.N. Design of torse surfaces with two plane cross sections. *Proceedings of BSTU. Ser. 5. Physical and Mathematical Sciences.* 1995;(2):33–36. (In Russ.) Available from: https://elib.belstu.by/handle/123456789/65082 (accessed: 12.03.2025).
6. Bhattacharya B. Theory of a new class of shells. *Symposium on Industrialized Spatial and Shell Structures*. Poland, 1973. p. 115–124.
7. Rekach V.G., Ryzhov N.N. Some opportunities of broadening number of problems on design and analysis of shells. *Structural Mechanics.* Moscow: UDN Publ.; 1970;48(6):3–8. (In Russ.)
8. Ivanov V.N. Ruled surfaces on the given supporting curves. *Structural Mechanics of Engineering Constructions and Buildings*. 2015;(3):9–17. (In Russ.) EDN: TNEVUR
9. Ershov M.E., Tupikova E.M. Construction of development of a torse surface with the parabolas on the opposite edges. *Engineering Research: Scientific-and-Practical Conference.* RUDN University. 2020:31–41. (In Russ.) EDN: JDIESQ
10. Francisco Perez-Arribas, Leonardo Fernandez-Jambrina. Computer-aided design of developable surfaces: designing with developable surfaces. *Journal of Computers*. October 2018;13(10):1171–1176. http://doi.org/10.17706/jcp.13.10.1171-1176
11. Chih-Hsing Chu, Charlie C.L. Wang, Chi-Rung Tsai. Computer aided geometric design of strip using developable Bezier patches. *Computers in Industry.* 2008;59:601–611. http://doi.org/10.1016/j.compind.2008.03.001
12. Vaskov A.A., Dorokhov A.S., Trushina L.N. Graphical construction of surfaces of plows. *Bulletin of the Federal State Educational Institution of Higher Professional Education “Goryachkin Moscow State Agroengineering University.”* 2012;(2):51–53. (In Russ.) EDN: RBFFND
13. Krivoshapko S.N., Ivanov V.N. *Encyclopedia of Analytical Surfaces*. Springer International Publishing Switzerland, 2015. http://doi.org/10.1007/978-3-319-11773-7
14. Yang J.X., Liu J.Q., Wang C.Y., Liu J. Design and development of developable surface based on engineering requirement. *3rd International Congress on Image and Signal Processing*, Yantai, China, 2010:1231–1234. http://doi.org/10.1109/CISP.2010.5647252
15. Miori I., Haruki I. A method of predicting sewn shapes and a possibility of sewing by the theory of developable surfaces. *Journal of the Japan Research Association for Textile End-Uses*. 2007;48(1):42–51.
16. Ivanov V.N., Aleshina O.O., Larionov E.A. Determination of optimal cylindrical shells in the form of second order surfaces. *Structural Mechanics of Engineering Constructions and Buildings*. 2025;21(1):37–47. (In Russ.) http://doi.org/10.22363/1815-5235-2025-21-1-37-47 EDN: IQCXLS
17. Belyaeva Z.V., Berestova S.A., Mityushov E.A. Tangent developable surfaces elements in thin-walled structures. *VIII International Conference on Textile Composites and Inflatable Structures Structural Membranes 2017.* 2018. p. 415–426. EDN: XYCRPV
18. Olodo E.T., Adjovi E.C., Krivoshapko S.N. Geometrical modeling of a composite folded membrane by a developable membrane with parabolic guidelines of any order. *International Journal of Scientific & Engineering Research*. 2013;4(4): 338–343. ISSN 2229-5518
19. Obukhova V.S., Vorobkevich R.I. Analytical description of parabolical torses of the fourth order. *Applied Geometry and Engineering Graphics.* 1982;33:16–19. (In Russ.)
20. Rynkovskaya M. Support draft calculation for a ramp in the form of developable helicoid. *2018 IOP Conf. Ser.: Mater. Sci. Eng*. 2018;371:012041. http://doi.org/10.1088/1757-899X/371/1/012041 EDN: VBTPRE
21. Ivanov V.N., Alyoshina O.O. Comparative analysis of the results of determining the parameters of the stress-strain state of equal slope shell with a directrix ellipse at the base. *Structural Mechanics of Engineering Constructions and Buildings*. 2019;15(5):374–383. (In Russ.) http://doi.org/10.22363/1815-5235-2019-15-5-374-383 EDN: LZSVVI
22. Krivoshapko S.N., Razin A.D. Comparison of two systems of governing equations for the thin shell analysis. Conference: *Proceedings of the International Conference on Engineering Research 2021* (ICER 2021), Moscow, 2021; 2559(1):020009. August 2022. http://doi.org/10.1063/5.0099905
23. Bajoria G.Ch. Application of a system of equations of A.L. Goldenveiser for analysis of torse shells on momentless theory. *Issledovaniya po Raschotu Elementov Prostranstvennyh Sistem*. Moscow: UDN Publ.; 1987. p. 65–72.

24. Bhattacharya B. Membrane theory of new class of developable shells. *Journal of Structural Engineering*. 1983; 10(3):81–88.

25. Rekach V.G., Krivoshapko S.N. Analysis of non-degenerated torse shells in curvilinear non-orthogonal coordinates. *Structural Mechanics and Analysis of Constructions*. 1982;(6):23–29. (In Russ.)

26. Krivoshapko S.N. Application of tangential developable surfaces in shipbuilding. *Shipbuilding.* 1983;7:5–7 (In Russ.)

27. Krivoshapko S.N. Design, analysis, and opportunity of application of torse shells in thin-walled structures. *Analysis of Shells of Building Structures.* Pross. Moscow: UDN, 1982:54–66. (In Russ.)

28. Bhanage A. An overview of flat pattern development (FPD) methodologies used in blank development of sheet metal components of aircraft. *International Journal of Mechanical Engineering and Robotics Research*. April 2014;3(2): 33–43. Available from: https://www.ijmerr.com/currentissue.php (accessed: 12.03.2025).

29. Nelson T.G., Zimmerman T.K., Magleby S.P., Lang R.J., Howell L.L. Developable mechanisms on developable surfaces. *Science Robotics.* 20 Feb 2019;4(27). http://doi.org/10.1126/scirobotics.aau5171

30. Lawrence S. Developable surfaces: Their history and application. *Nexus Network Journal.* October 2011;13(3): 701–714. http://doi.org/10.1007/s00004-011-0087-z EDN: HJZITK

31. Ishikawa G. Singularities of parallels to tangent developable surfaces. *arXiv: Differential Geometry.* 16 May 2021. Available from: https://scispace.com/papers/singularities-of-parallels-to-tangent-developable-surfaces-2cdy3p4ifc (accessed: 12.03.2025).

СТРОИТЕЛЬНАЯ МЕХАНИКА ИНЖЕНЕРНЫХ КОНСТРУКЦИЙ И СООРУЖЕНИЙ
STRUCTURAL MECHANICS OF ENGINEERING CONSTRUCTIONS AND BUILDINGS

2025. 21(5). 389–398

ISSN 1815-5235 (Print), 2587-8700 (Online)
HTTP://JOURNALS.RUDN.RU/STRUCTURAL-MECHANICS

DOI: 10.22363/1815-5235-2025-21-5-389-398
EDN: DQUGGN

Research article / Научная статья

Mathematical Model of Deformation of an Orthotropic Shell Under Blast Loading

Alexey A. Semenov

Saint Petersburg State University of Architecture and Civil Engineering, *Saint Petersburg, Russian Federation*
✉ sw.semenov@gmail.com

Received: August 6, 2025
Revised: September 22, 2025
Accepted: October 4, 2025

Abstract. This paper proposes a mathematical model of the deformation of a thin-walled shell structure under dynamic loading, specifically, blast loading. To account for the damping of the resulting vibrations, the author's previously proposed model was modified by adding a Rayleigh dissipation function to the Euler — Lagrange equations. The mathematical model also accounts for geometric nonlinearity, transverse shear, and material orthotropy. The software implementation performed in Maple. To demonstrate the applicability of the developed model, examples of calculations of shallow doubly curved shells under blast loading of varying intensities and with different damping coefficients in the Rayleigh dissipation function are provided.

Keywords: shells, blast loading, geometric nonlinearity, damping, Rayleigh dissipation function

Conflicts of interest. The author declares that there is no conflict of interest.

Funding. The article is published based on the results of the implementation of the SPbGASU grant in 2025.

For citation: Semenov A.A. Mathematical model of deformation of an orthotropic shell under blast loading. *Structural Mechanics of Engineering Constructions and Buildings.* 2025;21(5):389–398. http://doi.org/10.22363/1815-5235-2025-21-5-389-398 EDN: DQUGGN

Математическая модель деформирования ортотропной оболочки при действии взрывной нагрузки

А.А. Семенов

Санкт-Петербургский государственный архитектурно-строительный университет, *Санкт-Петербург, Российская Федерация*
✉ sw.semenov@gmail.com

Поступила в редакцию: 6 августа 2025 г.
Доработана: 22 сентября 2025 г.
Принята к публикации: 5 октября 2025 г.

Аннотация. Предложена математическая модель деформирования тонкостенной оболочечной конструкции при динамическом воздействии, в частности — взрывной нагрузки. Для учета затухания возникающих колебаний была модифицирована предложенная автором ранее модель путем добавления в уравнения Эйлера — Лагранжа функции диссипации Рэлея. Также математическая модель учитывает геометрическую нелинейность, поперечные сдвиги и ортотропию материала. Программная реализация выполнена в ПО Maple. Для демонстрации применимости разработанной модели приведены примеры расчетов пологих оболочек двоякой кривизны при действии взрывной нагрузки разной интенсивности и при выборе разного коэффициента демпфирования в функции диссипации Рэлея.

Alexey A. Semenov, Doctor of Technical Sciences, Professor of the Department of Information Systems and Technologies, Saint Petersburg State University of Architecture and Civil Engineering, 4, 2-nd Krasnoarmeiskaja St, St. Petersburg, 190005, Russian Federation; eLIBRARY SPIN-code: 9057-9882, ORCID: 0000-0001-9490-7364; e-mail: sw.semenov@gmail.com

Ключевые слова: оболочки, взрывная нагрузка, геометрическая нелинейность, демпфирование, функция диссипации Рэлея

Заявление о конфликте интересов. Автор заявляет об отсутствии конфликта интересов.

Финансирование. Статья публикуется по результатам исполнения гранта СПбГАСУ (Санкт-Петербургский государственный архитектурно-строительный университет, Россия) 2025 года.

Для цитирования: *Семенов А.А.* Математическая модель деформирования ортотропной оболочки при действии взрывной нагрузки // Строительная механика инженерных конструкций и сооружений. 2025. Т. 21. № 5. С. 389–398. http://doi.org/10.22363/1815-5235-2025-21-5-389-398 EDN: DQUGGN

1. Introduction

Thin-walled shells deform in a significantly nonlinear manner, and special methods and algorithms must be developed to calculate them [1–5]. One important task in the study of thin-walled structures is the analysis of their deformation under dynamic loads.

Dynamic impacts on shells cause vibrations, and one of the important factors in performing calculations is taking damping into account [6; 7]. It is especially important to consider damping when the load is applied for a short time, as in the case of explosive impacts, and further behavior of the structure can only be accurately described by taking into account the attenuation of vibrations. In relation to the calculation of shell structures, explosive loads were considered in [8–13]. For example, Godoy and Ameijeiras [12] investigate the deformation of vertical steel oil storage tanks with flat roofs during an explosion close to the structure. The energy values are analyzed at changing peak pressure and buckling shape. In [9], calculations of spherical shells made of FGM are performed, and the calculation algorithm and results are presented in the form of dynamic responses, phase portraits, and natural frequency values.

Mechanics uses the variational principles of Lagrange and Hamilton, which solve time-dependent problems based on the law of conservation of energy and are therefore not applicable to dissipative systems [14]. A number of attempts to overcome this problem can be found in literature. One of the first papers devoted to accounting for dissipation in the Lagrangian formulation was published by Leech [14] in 1958. The Lagrangian function was extended by the Rayleigh dissipation function (1877). This formulation was called the modified Hamilton principle [15] (or extended [16]). Effectively, this approach allows the “classical” Lagrange equations to be extended to non-conservative (i.e., dissipative) systems [14; 17; 18].

The approach based on adding Rayleigh dissipation function to the Euler — Lagrange equations [14; 19–23] was also used in [25–27].

Thus, [24] investigates forced nonlinear vibration of double-curved shells in accordance with Koiter's theory. Various types of bifurcations are analyzed.

M. Amabili [26] investigates high-amplitude (geometrically nonlinear) vibration of circular cylindrical shells. The equations of motion are obtained using the energy approach that takes into account damping via the Rayleigh dissipative function. The results for four different nonlinear theories of thin shells are compared.

The study of E.P. Detina [6] is also worth noting, in which the Rayleigh dissipative function is modified, called the Kelvin — Voigt dissipative function. The proposed function is proportional to the square of the material strain rate, in contrast to the Rayleigh dissipative function, which is proportional to the square of the displacement velocity.

There is also an approach that takes into account energy dissipation by adding to the functional the ratio of damping energy, dissipated per vibration cycle, to the maximum deformation energy [27–31]. However, implementing this approach is computationally more complex.

The aim of this study is to extend the mathematical model and the algorithm previously developed by the author [32; 33] to the problems of calculating shell structures under blast load taking into account damping.

2. Theory and Methods

To obtain the principal relations of the mathematical model, the total energy functional is used (dissipation is not taken into account at this stage):

$$I=\int_{t_0}^{t_1}\left(E_k-E_s\right)dt, \tag{1}$$

where E_k is the kinetic energy; t is time; $E_s=E_p-\mathrm{A}$ is the difference between the potential energy of deformation of the system and the work of external forces

$$E_s=\frac{1}{2}\int_{a_1}^{a}\int_{0}^{b}\Bigg(N_x\varepsilon_x+N_y\varepsilon_y+\frac{1}{2}\left(N_{xy}+N_{yx}\right)\gamma_{xy}+M_x\chi_1+M_y\chi_2+\left(M_{xy}+M_{yx}\right)\chi_{12}+$$

$$+Q_x\left(\Psi_x-\theta_1\right)+Q_y\left(\Psi_y-\theta_2\right)-2\left(P_xU+P_yV+qW\right)\Bigg)ABdxdy. \tag{2}$$

Geometric relations taking into account nonlinearity will take the following form:

$$\varepsilon_x=\frac{1}{A}\frac{\partial U}{\partial x}+\frac{1}{AB}V\frac{\partial A}{\partial y}-k_xW+\frac{1}{2}\theta_1^{\,2};$$

$$\varepsilon_y=\frac{1}{B}\frac{\partial V}{\partial y}+\frac{1}{AB}U\frac{\partial B}{\partial x}-k_yW+\frac{1}{2}\theta_2^{\,2};$$

$$\gamma_{xy}=\frac{1}{A}\frac{\partial V}{\partial x}+\frac{1}{B}\frac{\partial U}{\partial y}-\frac{1}{AB}U\frac{\partial A}{\partial y}-\frac{1}{AB}V\frac{\partial B}{\partial x}+\theta_1\theta_2; \tag{3}$$

$$\theta_1=-\left(\frac{1}{A}\frac{\partial W}{\partial x}+k_xU\right),\quad \theta_2=-\left(\frac{1}{B}\frac{\partial W}{\partial y}+k_yV\right),\quad k_x=\frac{1}{R_1},\quad k_y=\frac{1}{R_2}.$$

Curvatures χ_1, χ_2 and twist χ_{12} functions for this model become the following:

$$\chi_1=\frac{1}{A}\frac{\partial \Psi_x}{\partial x}+\frac{1}{AB}\frac{\partial A}{\partial y}\Psi_y,\quad \chi_2=\frac{1}{B}\frac{\partial \Psi_y}{\partial y}+\frac{1}{AB}\frac{\partial B}{\partial x}\Psi_x;$$

$$\chi_{12}=\frac{1}{2}\left(\frac{1}{A}\frac{\partial \Psi_y}{\partial x}+\frac{1}{B}\frac{\partial \Psi_x}{\partial y}-\frac{1}{AB}\left(\frac{\partial A}{\partial y}\Psi_x+\frac{\partial B}{\partial x}\Psi_y\right)\right). \tag{4}$$

The geometry of the shell structure is defined by the Lamé parameters and the values of the principal radii of curvature.

Also, expressions for the forces and moments reduced to the mid-surface of the shell and per unit length of the cross-section are required for the use in functional (2):

$$N_x=\frac{E_1h}{1-\mu_{12}\mu_{21}}\left(\varepsilon_x+\mu_{21}\varepsilon_y\right);$$

$$N_y=\frac{E_2h}{1-\mu_{12}\mu_{21}}\left(\varepsilon_y+\mu_{12}\varepsilon_x\right);$$

$$N_{xy}=N_{yx}=G_{12}h\gamma_{xy};$$

$$M_x=\frac{E_1}{1-\mu_{12}\mu_{21}}\left(\frac{h^3}{12}\right)\left(\chi_1+\mu_{21}\chi_2\right); \tag{5}$$

$$M_y = \frac{E_2}{1-\mu_{12}\mu_{21}}\left(\frac{h^3}{12}\right)(\chi_2 + \mu_{12}\chi_1);$$

$$M_{xy} = M_{yx} = 2G_{12}\left(\frac{h^3}{12}\right)\chi_{12};$$

$$Q_x = G_{13}kh\left(\Psi_x - \theta_1\right);$$

$$Q_y = G_{23}kh\left(\Psi_y - \theta_2\right),$$

where N_x, N_y, N_{xy}, N_{yx} are the normal forces along axes x, y and membrane shear forces in the xOy plane; M_x, M_y, M_{xy}, M_{yx} are the bending and twisting moments; Q_x, Q_y are the shear forces in the xOz and yOz planes; E_1, E_2 are the elasticity moduli; G_{12}, G_{13}, G_{23} are the shear moduli; μ_{12}, μ_{21} are the Poisson's ratios.

The proposed mathematical model is based on the hypotheses of the Timoshenko model (Reissner–Mindlin, FSDT) and allows for the consideration of rotational inertia and transverse shear. Then the kinetic energy [32; 33]

$$E_k = \frac{\rho}{2}\int_{a_1}^{a}\int_{0}^{b}\int_{-h/2}^{h/2}\left(\left(\frac{\partial U^z}{\partial t}\right)^2 + \left(\frac{\partial V^z}{\partial t}\right)^2 + \left(\frac{\partial W^z}{\partial t}\right)^2\right)ABdxdydz, \tag{6}$$

$$U^z = U + z\Psi_x, \quad V^z = V + z\Psi_y, \quad W^z = W .$$

By evaluating the integral with respect to variable z in (6), one obtains

$$E_k = \frac{\rho}{2}\int_{a_1}^{a}\int_{0}^{b}\left(h\left(\left(\frac{\partial U}{\partial t}\right)^2 + \left(\frac{\partial V}{\partial t}\right)^2 + \left(\frac{\partial W}{\partial t}\right)^2\right) + \frac{h^3}{12}\left(\left(\frac{\partial \Psi_x}{\partial t}\right)^2 + \left(\frac{\partial \Psi_y}{\partial t}\right)^2\right)\right)ABdxdy. \tag{7}$$

The approximating functions (in accordance with the L.V. Kantorovich's method) are substituted into functional (1). After evaluating the integrals with respect to variables x and y in terms of known functions, functional I represents a one-dimensional functional in terms of functions $U_{ij}(t) - \Psi_{yij}(t)$. Next, the well-known Euler — Lagrange equation [32; 33] is used:

$$\frac{d}{dt}\frac{\partial E_k}{\partial \dot{X}_j(t)} + \frac{\partial E_s}{\partial X_j(t)} = 0, \quad j = 1, 2, ..., 5N, \tag{8}$$

where $X(t) = \left(U_{ij}(t), V_{ij}(t), W_{ij}(t), \Psi_{xij}(t), \Psi_{yij}(t)\right)^T$, $i, j = 1,.., \sqrt{N}$, and the dot represents the derivative with respect to time.

Next, the Kantorovich method and the Rosenbrock method (for numerical solution of rigid ODE systems) are used to perform the calculations. The Kantorovich method is used to reduce a multidimensional functional to a one-dimensional one. For this, the unknown displacement functions and deflection angles are represented as follows [33]:

$$U(x,y,t) = \sum_{k=1}^{\sqrt{N}}\sum_{l=1}^{\sqrt{N}} U_{kl}(t) X_1^k Y_1^l, \quad V(x,y,t) = \sum_{k=1}^{\sqrt{N}}\sum_{l=1}^{\sqrt{N}} V_{kl}(t) X_2^k Y_2^l,$$

$$W(x,y,t)=\sum_{k=1}^{\sqrt{N}}\sum_{l=1}^{\sqrt{N}}W_{kl}(t)X_3^kY_3^l, \tag{9}$$

$$\Psi_x(x,y,t)=\sum_{k=1}^{\sqrt{N}}\sum_{l=1}^{\sqrt{N}}\Psi_{xkl}(t)X_4^kY_4^l,\quad \Psi_y(x,y,t)=\sum_{k=1}^{\sqrt{N}}\sum_{l=1}^{\sqrt{N}}\Psi_{ykl}(t)X_5^kY_5^l,$$

where $U_{kl}-\Psi_{ykl}$ are the unknown functions of *t*; $X_1^k,...,X_5^k$, $Y_1^l,...,Y_5^l$ are the known approximation functions.

The Euler — Lagrange equations (8) are supplemented with a term that takes into account damping based on the Rayleigh dissipation function. In well-known studies, the Rayleigh dissipation function written for the model of structural deformation does not take into account transverse shear (Kirchhoff — Love, Koiter, CSDT models) and the membrane thickness

$$F=\frac{c}{2}\int_{a_1}^{a}\int_{0}^{b}\left(\left(\frac{\partial U}{\partial t}\right)^2+\left(\frac{\partial V}{\partial t}\right)^2+\left(\frac{\partial W}{\partial t}\right)^2\right)ABdxdy. \tag{10}$$

At the same time, how exactly coefficient *c* is defined, as well as its dimension and order, depends on accounting for the membrane thickness.

In this study, similar to the expression for kinetic energy, the Rayleigh dissipation function for the Timoshenko — Reissner model is written:

$$F=\frac{c}{2}\int_{a_1}^{a}\int_{0}^{b}\int_{-h/2}^{h/2}\left(\left(\frac{\partial U^z}{\partial t}\right)^2+\left(\frac{\partial V^z}{\partial t}\right)^2+\left(\frac{\partial W^z}{\partial t}\right)^2\right)ABdxdydz. \tag{11}$$

After integrating (11) with respect to variable *z*, one obtains

$$F=\frac{c}{2}\int_{a_1}^{a}\int_{0}^{b}\left(h\left(\left(\frac{\partial U}{\partial t}\right)^2+\left(\frac{\partial V}{\partial t}\right)^2+\left(\frac{\partial W}{\partial t}\right)^2\right)+\frac{h^3}{12}\left(\left(\frac{\partial \Psi_x}{\partial t}\right)^2+\left(\frac{\partial \Psi_y}{\partial t}\right)^2\right)\right)ABdxdy. \tag{12}$$

Now, a term containing the Rayleigh dissipation function (taking into account the proposed refinements) is added to the Euler — Lagrange equation, as it is done, for example, in [19; 24; 26]

$$\frac{d}{dt}\frac{\partial E_k}{\partial \dot{X}_j(t)}+\frac{\partial E_s}{\partial X_j(t)}-\frac{\partial F}{\partial \dot{X}_j(t)}=0,\quad j=1,2,...,5N. \tag{13}$$

System of equations (13) is complemented with initial conditions at $t = 0$

$$U_{ij}=V_{ij}=W_{ij}=\Psi_{xij}=\Psi_{yij}=0,\ \dot{U}_{ij}=\dot{V}_{ij}=\dot{W}_{ij}=\dot{\Psi}_{xij}=\dot{\Psi}_{yij}=0,\quad i,j=1,2,..,\sqrt{N}, \tag{14}$$

or

$$X_j=0,\quad \dot{X}_j=0,\quad j=1,2,..,5N.$$

The system of differential equations (13), (14) is further solved using one of the numerical methods; in this study, the Rosenbrock method is applied to the problem.

3. Analysis

To demonstrate the applicability of the above approach, a thin-walled shallow shell of double curvature with thickness $h = 0.09$ m, linear dimensions $a = b = 10.8$ m and principal curvature radii $R_1 = R_2 = 40.05$ m is analyzed. The material parameters correspond to fiberglass T10/UPE22-27 (elasticity moduli $E_1 = 0.294\times10^5$ MPa, $E_2 = 0.178\cdot10^5$ MPa, shear moduli $G_{12} = G_{13} = G_{23} = 0.0301\times10^5$ MPa, Poisson's ratio $\mu = 0.123$, density $\rho = 1800$ kg/m^3), the edges of the structure are simply supported. The load is explosive, directed perpendicular to the surface, and depends on time as follows: $q = q_0 \exp\left(-\frac{t}{t_0}\right) + q_{sv}$, $q_0 = 1$ MPa, $t_0 = 0.01$ s.

Self-weight is also taken into account. The analysis is performed with $N = 4$ in the Kantorovich method. Using a program developed by the author in Maple software, the dynamic response of the system at different coefficients $c = 100$ N·s/m^3 = 0.0001 MPa·s/m, $c = 0.001$ MPa·s/m, $c = 0.002$ MPa·s/m is shown. For comparison, the results without considering damping, when $c = 0$ N·s/m^3, are presented (Figure 1). Hereinafter in the figures it is shown that the curve with a larger amplitude corresponds to the central part of the structure ($x = a / 2$, $y = b / 2$), while the one with a smaller amplitude corresponds to the quarter ($x = a / 4$, $y = b / 4$). Figure 2 shows the same data for $q_0 = 10$ MPa.

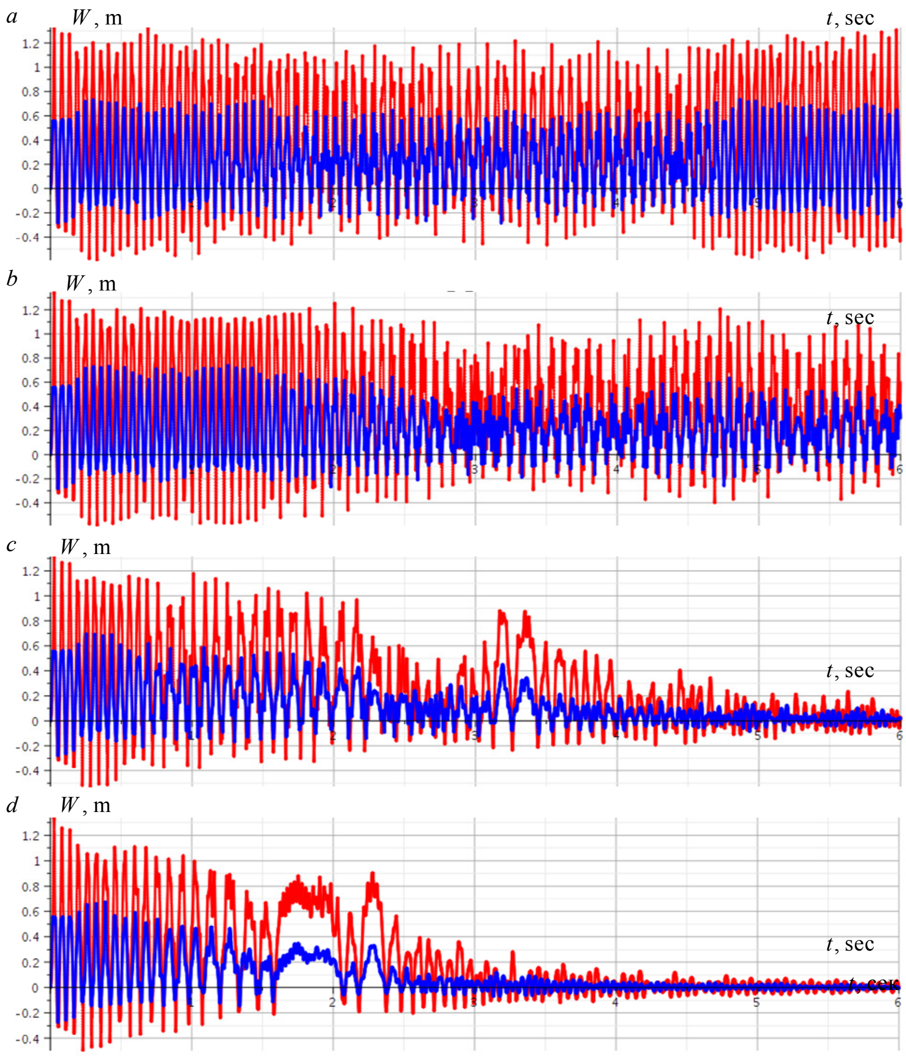

Figure 1. Dynamic response under blast loading ($q_0 = 1$ MPa):
a — $c = 0$ MPa·s / m; *b* — $c = 0.0001$ MPa·s / m; *c* — $c = 0.001$ MPa·s / m; *d* — $c = 0.002$ MPa·s / m
S o u r c e: made by A.A. Semenov.

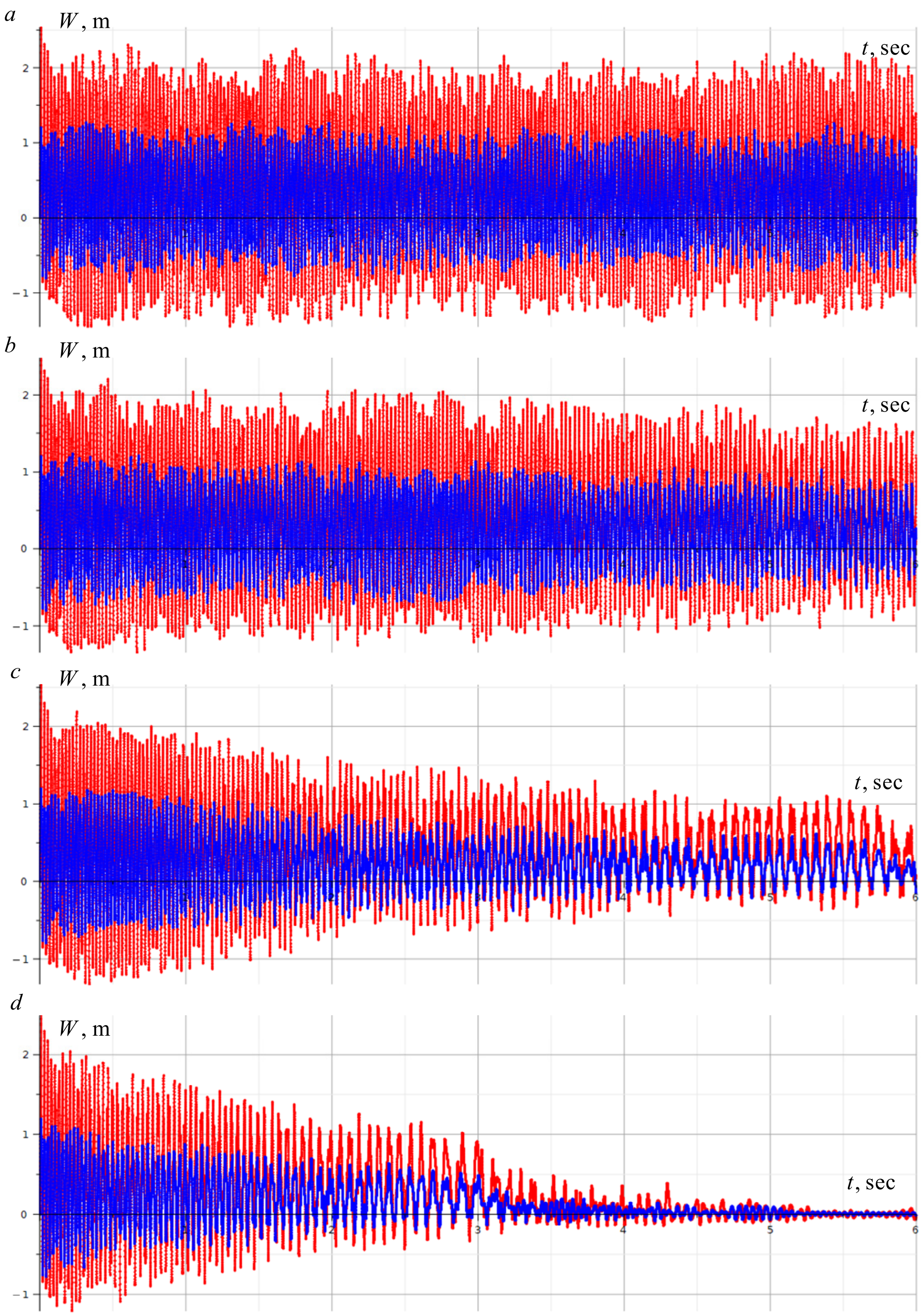

Figure 2. Dynamic response under blast loading (q_0 = 10 MPa):
a — *c* = 0 MPa·s / m; *b* — *c* = 0.0001 MPa·s / m; *c* — *c* = 0.001 MPa·s / m; *d* — *c* = 0.002 MPa·s / m
S o u r c e: made by A.A. Semenov.

It is evident that with a higher value of coefficient *c*, the damping of vibration occurs more rapidly. The search and analysis of its possible values close to the real data for the materials under consideration will be the subject of further research.

To assess how destructive the impact of an explosive load is, the graphs of normal stresses are also constructed for $q_0 = 1$ MPa and $c = 0.001$ MPa·s/m (Figure 3), and further — for $q_0 = 10$ MPa and $c = 0.001$ MPa·s/m (Figure 4). It can be seen from the graphs that at $q_0 = 10$ MPa the values of stress exceed the ultimate stress values for this material by several times, and at $q_0 = 1$ MPa they are close to the ultimate stress values, and at certain moments they surpass them.

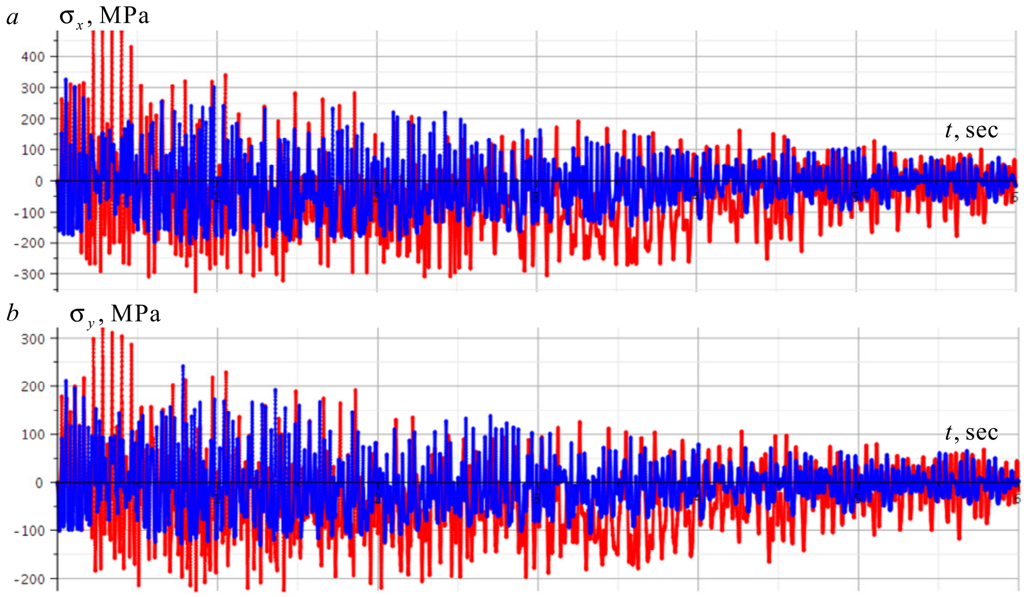

Figure 3. Normal stress values under blast loading ($q_0 = 1$ MPa), $c = 0.001$ MPa·s / m

S o u r c e: made by A.A. Semenov.

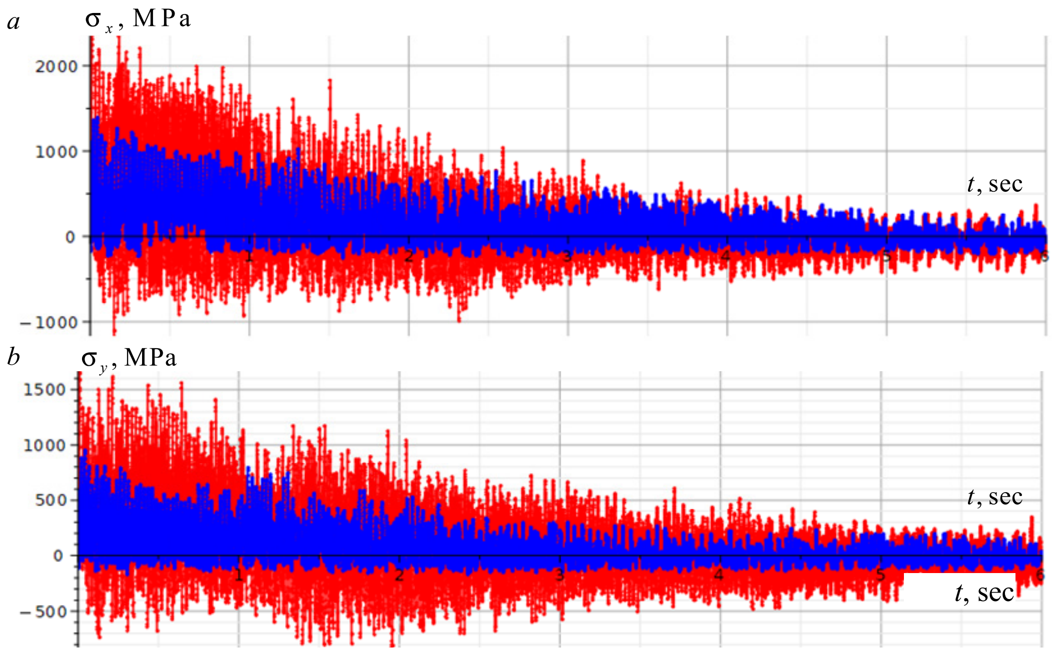

Figure 4. Normal stress values under blast loading ($q_0 = 10$ MPa), $c = 0.001$ MPa·s / m

S o u r c e: made by A.A. Semenov.

4. Conclusion

Computer modeling technologies allow to study thin-walled structures taking into account nonlinear effects. The proposed mathematical model using the Rayleigh dissipation function allows to extend the applicability of the models and calculation algorithms previously developed by the author to a wider class of problems. This includes simulating the dynamic response of a structure to an explosive load when the load application time is short and the vibration process involves damping. The data obtained on the stress values during vibrations are also of interest, as they may exceed the ultimate values.

Thus, a new mathematical model of the deformation of an orthotropic shell under the action of an explosive load has been obtained.

References

1. Karpov V.V., Kobelev E.A., Maslennikov A.M., Panin A.N. Ritz Method in the Discrete Approximation of Displacements for Slab Calculation. *Architecture and Engineering*. 2023;8(4):57–67. http://doi.org/10.23968/2500-0055-2023-8-4-57-67 EDN: FTPEME

2. Korovaytseva E.A. Parameter Differentiation Method in Solution of Axisymmetric Soft Shells Stationary Dynamics Nonlinear Problems. *Journal of Samara State Technical University, Ser. Physical and Mathematical Sciences*. 2021;25(3):556–570. (In Russ.) http://doi.org/10.14498/vsgtu1855 EDN: UKLUQJ

3. Raghib R., Naciri I., Khalfi H., Elmaimouni L., Yu J., Bybi A., Sahal M. Free Vibration Modeling in a Functionally Graded Hollow Cylinder Using the Legendre Polynomial Approach. *Architecture and Engineering*. 2023;8(4):82–98. http://doi.org/10.23968/2500-0055-2023-8-4-82-98 EDN: AJNBMP

4. Razov I.O. Parametric Vibrations and Dynamic Stability Of Homogeneous And Inhomogeneous Toroidal Shells in Elastic Medium. *Bulletin of Civil Engineers*. 2025;(3):74–83. (In Russ.) http://doi.org/10.23968/1999-5571-2025-22-3-74-83 EDN: EZXRPQ

5. Eshmatov B., Abdikarimov R., Amabili M., Vatin N. Nonlinear vibrations and dynamic stability of viscoelastic anisotropic fiber reinforced plates. *Magazine of Civil Engineering*. 2023;118(1):11811. http://doi.org/10.34910/MCE.118.11 EDN: POZQZX

6. Detina E.P. Numerical model of vibration damping of beam elements of structures made of structurally complex materials based on the principles of non-local mechanics : diss. Cand. Tech. Sci., Moscow: MGSU, 2024. (In Russ.)

7. Sidorov V., Shitikova M., Badina E., Detina E. Review of Nonlocal-in-Time Damping Models in the Dynamics of Structures. *Axioms*. 2023;12(7):676. http://doi.org/10.3390/axioms12070676 EDN: DNTVCF

8. Nguyen T.P., Tran M.T. Response of Vertical Wall Structures under Blast Loading by Dynamic Analysis. *Procedia Engineering.* 2011;14:3308–3316. http://doi.org/10.1016/j.proeng.2011.07.418

9. Do N.-T., Le P.B., Tran T.T., Pham Q.H. Nonlinear transient analysis of functionally graded sandwich spherical shells subjected to blast loading in the thermal environment. *Case Studies in Thermal Engineering*. 2023;52:103765. http://doi.org/10.1016/j.csite.2023.103765 EDN: RNSRMC

10. Tu P.H., Van Ke T., Trai V.K., Hoai L. An isogeometric analysis approach for dynamic response of doubly-curved magneto electro elastic composite shallow shell subjected to blast loading. *Defence Technology*. 2024;41:159–180. http://doi.org/10.1016/j.dt.2024.06.005 EDN: EFGQML

11. Zhao Z., Hou H., Li D., Wu X., Li Y., Chen Z., Wu L. Investigation on dynamic response of liquid-filled cylindrical shell structures under the action of combined blast and fragments loading. *Defence Technology*. 2025;49:334–354. http://doi.org/10.1016/j.dt.2025.03.007

12. Godoy L.A., Ameijeiras M.P. Plastic buckling of oil storage tanks under blast loads. *Structures.* 2023;53:361–372. http://doi.org/10.1016/j.istruc.2023.04.057 EDN: YXCDOO

13. Volodin G.T., Novikov A.S. In Geonetrically Nonlinear Problem of the Breaking of the Shell Designs Explosion. *Izvestiya Tula State University*. 2014;(3):94–103. (In Russ.) EDN: SIKKUX

14. Hackl K., Svoboda J., Fischer F.D. On the coupling of Hamilton's principle and thermodynamic extremal principles. *Journal of the Mechanics and Physics of Solids*. 2024;187:105633. http://doi.org/10.1016/j.jmps.2024.105633 EDN: QRZDUS

15. Leech J.W. *Classical Mechanics. 2nd*. Dordrecht: Springer Netherlands, 1965. http://doi.org/10.1007/978-94-010-9169-5

16. Kim J., Dargush G.F., Ju Y.-K. Extended framework of Hamilton's principle for continuum dynamics. *International Journal of Solids and Structures*. 2013;50(20–21):3418–3429. http://doi.org/10.1016/j.ijsolstr.2013.06.015

17. Yang Q., Stainier L., Ortiz M. A variational formulation of the coupled thermo-mechanical boundary-value problem for general dissipative solids. *Journal of the Mechanics and Physics of Solids*. 2006;54(2):401–424. http://doi.org/10.1016/j.jmps.2005.08.010 EDN: JFRWPW

18. Vujanović B.D., Jones S.E. *Variational methods in nonconservative phenomena: Mathematics in science and engineering.* Elsevier Publ.; 1989. http://doi.org/10.1016/S0076-5392(08)X6103-X

19. Bui T.T., Vu M.D., Pham N.N., Cao V.D., Vu H.N. Nonlinear thermo-mechanical dynamic buckling and vibration of FG-GPLRC circular plates and shallow spherical shells resting on the nonlinear viscoelastic foundation. *Archive of Applied Mechanics.* 2024;94:3715–3729. http://doi.org/10.1007/s00419-024-02691-6 EDN: QSZFWZ

20. Roy S., Bhadra S. Study of nonlinear dissipative pulse propagation under the combined effect of two-photon absorption and gain dispersion: A variational approach involving Rayleigh's dissipation. *Physica D: Nonlinear Phenomena*. 2007;232(2):103–107. http://doi.org/10.1016/j.physd.2007.06.002

21. Scaife B.K.P. On the Rayleigh dissipation function for dielectric media. *Journal of Molecular Liquids.* 1989;43:101–107. http://doi.org/10.1016/0167-7322(89)80010-8

22. Lemoȍ N.A. Remark on Rayleigh's dissipation function. *American Journal of Physics*. 1991;59(7):660–661. http://doi.org/10.1119/1.16791

23. Podio-Guidugli P., Virga E.G. Analytical Thermodynamics. *Journal of Elasticity*. 2023;153(4–5):787–812. http://doi.org/10.1007/s10659-023-09997-6 EDN: UYQNIT

24. Pinho F.A.X.C., Amabili M., Del Prado Z.J.G.N., Da Silva F.M.A. Nonlinear forced vibration analysis of doubly curved shells via the parameterization method for invariant manifold. *Nonlinear Dynamics.* 2024;112(23):20677–20701. http://doi.org/10.1007/s11071-024-10135-7 EDN: TQEXRH

25. Touzé C., Amabili M., Thomas *O.* Reduced-order models for large-amplitude vibrations of shells including in-plane inertia. *Computer Methods in Applied Mechanics and Engineering.* 2008;197(21–24):2030–2045. http://doi.org/10.1016/j.cma.2008.01.002 EDN: WOFWQZ

26. Amabili M. A comparison of shell theories for large-amplitude vibrations of circular cylindrical shells: Lagrangian approach. *Journal of Sound and Vibration*. 2003;264(5):1091–1125. http://doi.org/10.1016/S0022-460X(02)01385-8 EDN: XQDOKX

27. Li H., Zeyu Zou, Wu H., Zhao J., Sun H., Sun W., Wang Q., Wang X. Theoretical and experimental investigations of vibration and damping behaviors of carbon fiber-reinforced composite thin shells with partial bolt looseness constraints. *European Journal of Mechanics — A/Solids.* 2023;97:104839. http://doi.org/10.1016/j.euromechsol.2022.104839 EDN: AQGPXM

28. Li H., Wu H., Zhang T., Wen B., Guan Z. A nonlinear dynamic model of fiber-reinforced composite thin plate with temperature dependence in thermal environment. *Composites Part B: Engineering*. 2019;162:206–218. http://doi.org/10.1016/j.compositesb.2018.10.070

29. Maheri M.R., Adams R.D. Modal Vibration Damping of Anisotropic FRP Laminates Using the Rayleigh — Ritz Energy Minimization Scheme. *Journal of Sound and Vibration*. 2003;259(1):17–29. http://doi.org/10.1006/jsvi.2002.5151 EDN: BCVKJB

30. Zinoviev P.A., Ermakov J.N. *Energy dissipation in composite materials.* Lancaster: Technomic Publ.; 1994.

31. Zinov'ev P.A., Smerdov A.A., Kulish G.G. Experimental investigation of elastodissipative characteristics of carbon-fiber-reinforced plastics. *Mechanics of Composite Materials*. 2003;39(5):393–398. http://doi.org/10.1023/B:MOCM.0000003289.12297.84 EDN: LIEDXP

32. Semenov A.A. Dynamic response of doubly-curved shallow shells to periodic external action. *Structural Mechanics of Engineering Constructions and Buildings.* 2024;20(5):433–440. (In Russ.) http://doi.org/10.22363/1815-5235-2024-20-5-433-440 EDN: CQAEAZ

33. Semenov A.A. Simulation of Deformation of Thin-Walled Shell Structures under Dynamic Loads of Various Types. *Bulletin of Civil Engineers.* 2024;(5):41–48. (In Russ.) http://doi.org/10.23968/1999-5571-2024-21-5-41-48 EDN: STVEJW

СТРОИТЕЛЬНАЯ МЕХАНИКА ИНЖЕНЕРНЫХ КОНСТРУКЦИЙ И СООРУЖЕНИЙ
STRUCTURAL MECHANICS OF ENGINEERING CONSTRUCTIONS AND BUILDINGS

2025. 21(5). 399–413

ISSN 1815-5235 (Print), 2587-8700 (Online)

HTTP://JOURNALS.RUDN.RU/STRUCTURAL-MECHANICS

DOI: 10.22363/1815-5235-2025-21-5-399-413
EDN: DRENKL

Research article / Научная статья

Analysis of Geometry and Strength of Shells with Middle Surfaces Defined by Two Superellipses and a Circle

Valery V. Karnevich✉, **Iraida A. Mamieva**

RUDN University, *Moscow, Russian Federation*
✉ valera.karnevich@gmail.com

Received: August 11, 2025
Revised: October 2, 2025
Accepted: October 12, 2025

Abstract. In this study, thin shells in the form of algebraic surfaces defined by a geometric frame of three plane superellipses lying respectively in three coordinate planes are considered. As the main focus of the study, the case when the horizontal superellipse is a circle is examined. It is shown that depending on the type of the other two superellipses, it is possible to obtain a conical surface, or a surface of negative Gaussian curvature, including conoids, or surfaces of positive Gaussian curvature. The construction of 12 particular cases of such surfaces with a circular base is illustrated. Six of them are investigated in detail using the methods of differential geometry, i.e. expressions of the fundamental quadratic forms are obtained, for the first time. Out of the 12 presented shell shapes, two ruled shells of zero and negative Gaussian curvature (conical and cylindroidal respectively) with the same geometric frame were selected for comparative static analysis. The two shells were analyzed for uniform distributed load using displacement-based FEM implemented in the SCAD software. It is shown that despite the two shells having identical geometric frames, the conical shell demonstrated better performance over the most strength parameters.

Keywords: circular base, algebraic surface, cylindroid, cone, static analysis, FEM

Conflicts of interest. The authors declare that there is no conflict of interest.

Authors' contribution: *Karnevich V.* — investigation, formal analysis, software, visualization, writing — original draft; *Mamieva I.A.* — methodology, validation, writing — review & editing. Both of the authors read and approved the final version of the article.

Acknowledgements: The authors sincerely thank Prof. Sergey N. Krivoshapko for his swift, undemanding and engaged assistance and comprehensive commentary at any stage of preparing this paper, and for his suggestions of future research. His help and advice always extended beyond the original inquiry and was not bounded by subject or time. It was his broad and deep knowledge of the topic, easily understandable explanation and enthusiastic delivery that originally sparked and further fueled the interest in the study of thin-walled structures and fundamentally encouraged pursuing science.

For citation: Karnevich V.V., Mamieva I.A. Analysis of geometry and strength of shells with middle surfaces defined by two superellipses and a circle. *Structural Mechanics of Engineering Constructions and Buildings.* 2025;21(5):399–413. http://doi.org/10.22363/1815-5235-2025-21-5-399-413 EDN: DRENKL

Valery V. Karnevich, Post-graduate student of the Department of Construction Technologies and Structural Materials, Academy of Engineering, RUDN University, 6 Miklukho-Maklaya St, Moscow, 117198, Russian Federation; eLIBRARY SPIN-code: 4233-3099, ORCID: 0000-0002-6232-2676; e-mail: valera.karnevich@gmail.com

Iraida A. Mamieva, Assistant of the Department of Construction Technology and Structural Materials, Academy of Engineering, RUDN University, 6 Miklukho-Maklaya St, Moscow, 117198, Russian Federation; eLIBRARY SPIN-code: 3632-0177; ORCID: 0000-0002-7798-7187; e-mail: i_mamieva@mail.ru

Исследование геометрии и напряженно-деформированного состояния оболочек со срединными поверхностями, заданными двумя суперэллипсами и окружностью

В.В. Карневич✉, **И.А. Мамиева**

Российский университет дружбы народов, *Москва, Российская Федерация*
✉ valera.karnevich@gmail.com

Получено: 11 августа 2025 г.
Доработана: 2 октября 2025 г.
Принята к публикации: 12 октября 2025 г.

Аннотация. Рассмотрены тонкие оболочки в форме алгебраических поверхностей с геометрическим каркасом из трех суперэллипсов, лежащих в трех координатных плоскостях, в случае, когда горизонтальный суперэллипс представляет собой круглое основание. Показано, что в зависимости от формы остальных двух суперэллипсов можно получить коническую поверхность, поверхность отрицательной гауссовой кривизны, включая коноиды, или поверхность положительной гауссовой кривизны. Проиллюстрировано построение 12 примеров таких поверхностей на круглом основании. Из них 6 поверхностей впервые исследованы подробно методами дифференциальной геометрии, получены их коэффициенты квадратичных форм. Из 12 представленных форм оболочек для сравнительного статического расчета выбраны две линейчатые оболочки нулевой и отрицательной гауссовой кривизны (коническая поверхность и цилидроид) с одинаковым геометрическим каркасом. Расчет оболочек с равномерно распределенной нагрузкой производился с использованием метода конечных элементов (МКЭ) в перемещениях, реализованном в программном комплексе SCAD. Показано, что, несмотря на одинаковый геометрический каркас этих двух оболочек, по большинству параметров НДС лучшие показатели у конической оболочки.

Ключевые слова: круглое основание, алгебраическая поверхность, цилиндроид, коническая поверхность, статический расчет, МКЭ

Заявление о конфликте интересов. Авторы заявляют об отсутствии конфликта интересов.

Вклад авторов: *Карневич В.В.* — исследование, анализ, программное обеспечение, визуализация, написание оригинального проекта; *Мамиева И.А.* — методология, валидация, написание, рецензирование и редактирование текста. Оба автора ознакомлены с окончательной версией статьи и одобрили ее.

Благодарности: Авторы всегда будут помнить профессора Сергея Николаевича Кривошапко за его отзывчивость, готовность прийти на помощь и глубокий интерес к работе над статьей. Особую признательность хочется выразить за его детальные комментарии и ценные рекомендации на всех этапах подготовки текста, а также за конструктивные идеи касательно дальнейших научных изысканий. Сергей Николаевич, оказавший значительное влияние на развитие науки в области тонкостенных конструкций, благодаря своему богатому опыту, широте взглядов и способности доступно преподносить сложный материал, сыграл ключевую роль в пробуждении интереса к исследованию поверхностей и оболочек.

Для цитирования: *Karnevich V.V., Mamieva I.A.* Analysis of geometry and strength of shells with middle surfaces defined by two superellipses and a circle // Строительная механика инженерных конструкций и сооружений. 2025. Т. 21. № 5. С. 399–413. http://doi.org/10.22363/1815-5235-2025-21-5-399-413 EDN: DRENKL

1. Introduction

In descriptive geometry, the frame of a surface is a set of lines, which define the surface. Surfaces constructed from a geometric frame of three curves lying respectively in three coordinate planes are widely used in shipbuilding for the design of hulls of above- and under-water vessels. In [1], the author discusses issues of modelling hull surfaces with discrete points and the computational advantages and geometric intuitivity of using parametric representation in the surface modeling. In [2], thirteen analytical surfaces for preliminary stages of hull shape selection and different methods of their construction are presented. There were suggestions of using superellipses as the plane curves of the geometric frame [3–6], which allow to significantly expand the number of shapes for ship hulls by varying the parameters of the superellipses.

Карневич Валерий Вячеславович, аспирант кафедры технологий строительства и конструкционных материалов, инженерная академия, Российский университет дружбы народов, Российская Федерация, 117198, г. Москва, ул. Миклухо-Маклая, д. 6; eLIBRARY SPIN-код: 4233-3099; ORCID: 0000-0002-6232-2676; e-mail: valera.karnevich@gmail.com

Мамиева Ираида Ахсарбеговна, ассистент кафедры технологий строительства и конструкционных материалов, инженерная академия, Российский университет дружбы народов, Российская Федерация, 117198, г. Москва, ул. Миклухо-Маклая, д. 6; eLIBRARY SPIN-код: 3632-0177; ORCID: 0000-0002-7798-7187; e-mail: i_mamieva@mail.ru

Paper [7] presents parametric equations and a technique for generating complex submarine hull shapes, which are composed of fragments of surfaces defined by a frame of superellipses. In [8], thin shells with middle surfaces containing three plane superellipses as the geometric frame were originally suggested to be used in construction and architecture.

In [5; 9], the curves defining the considered surfaces are expressed in the following form:

- the first curve of the geometric frame in the xOy plane ($z = 0$):

$$|y|^r = W^r\left(1-\frac{|x|^t}{L^t}\right), \tag{1}$$

- the second curve of the geometric frame in the yOz plane ($x = 0$):

$$|z|^n = T^n\left(1-\frac{|y|^m}{W^m}\right), \tag{2}$$

- the third curve of the geometric frame in the xOz plane ($y = 0$):

$$|z|^s = T^s\left(1-\frac{|x|^k}{L^k}\right), \tag{3}$$

where for convex curves r, t, n, m, s, $k > 1$; for concave curves r, t, n, m, s, $k < 1$. Curves (1)–(3) represent superellipses if the exponents within each equation are equal, or arbitrary plane curves otherwise. The exponents in equations (1)–(3) can take on any positive value. In this study, only superellipses are considered to constitute the geometric frame, so $r = t$, $n = m$, $s = k$. If $r = t = 1$, $n = m = 1$, $s = k = 1$, then curves (1)–(3) degenerate into straight lines, and superellipses degenerate into rhombs.

Using the method described in [6; 9], it is possible to derive the explicit equations of three algebraic surfaces with the same geometric frame of curves (1)–(3):

- generated by a family of sections in x = const planes:

$$|z| = T\left(1-|x|^k / L^k\right)^{1/s}\left[1-|y/W|^m / \left(1-|x/L|^t\right)^{m/r}\right]^{1/n}, \tag{4}$$

- generated by a family of sections in y = const planes:

$$|z| = T\left(1-|y|^m / W^m\right)^{1/n}\left[1-|x/L|^k / \left(1-|y/W|^r\right)^{k/t}\right]^{1/s}, \tag{5}$$

- generated by a family of sections in z = const planes:

$$|y| = WW\left(1-|z|^n / T^n\right)^{1/m}\left[1-|x/L|^t / \left(1-|z/T|^s\right)^{t/k}\right]^{1/r}, \tag{6}$$

where $-L \le x \le L,\ -W \le y \le W,\quad 0 \le z \le T.$

The explicit equations of surfaces (4)–(6) can be transformed into parametric equations:

$$x = x(u) = \pm uL,\ y = y(u,v) = vW\left[1-u^t\right]^{1/r},\quad z = z(u,v) = T\left[1-u^k\right]^{1/r}\left[1-|v|^m\right]^{1/n}; \tag{7}$$

$$x = x(u,v) = vL\left[1-u^r\right]^{1/t},\ y = y(u) = \pm uW,\quad z = z(u) = T\left[1-u^m\right]^{1/n}\left[1-|v|^k\right]^{1/s}; \tag{8}$$

$$x = x(u,v) = vL\left[1-u^s\right]^{1/k},\ y = y(u,v) = \pm W\left[1-u^n\right]^{1/m}\left[1-|v|^t\right]^{1/r},\quad z = z(u) = uT, \tag{9}$$

where $0 \le u \le 1,\ -1 \le v \le 1;\quad u,\ v$ are non-dimensional parameters.

The considered surfaces can be referred to as "kinematic surfaces", since they are formed by the motion of a generatrix of variable or constant curvature along a directrix. By taking each of the three super-ellipses of the geometric frame as the generatrix one-at-a-time, three analytical surfaces are obtained, which are defined by explicit equations (4)–(6) or parametric equations (7)–(9).

Equations (4)–(9) were used in paper [10] for constructing five groups of new ruled surfaces. Some of these ruled surfaces were taken as middle surfaces of thin shells, which were analyzed for dead load in [11].

In scientific literature and in practice, thin shells with a circular base are the most popular. Virtually all shells with a circular base known to date are shells of rotation, for which about three dozens of optimality criteria have been proposed [12]. Less known is the method of defining the geometry of shells where middle surfaces contain three plane curves as the frame, and one of these curves is a circle.

The objective of this paper is to investigate shells with middle surfaces defined by a geometric frame of superellipses in the particular case when the horizontal curve (base outline) is a circle. Some specific groups of such surfaces are analysed in detail using the methods of differential geometry for the first time to demonstrate the geometrical equivalence or distinction of surfaces with the same frame, but different method of generation. In addition, static analysis is applied to shells with middle surfaces from a particular group to identify the differences in the structural behavior.

2. Methods

2.1. Construction of Surfaces Defined by Two Superellipses and a Circle

Assuming that a surface with the frame of superellipses has a circular base in the *xOy* coordinate plane, then the following values of parameters in equations (1)–(9) can be adopted:

$$r = t = 2,\ L = W = R,\quad 0 \le z \le 0,\ -R \le x \le R,\ -R \le y \le R,$$

and *z*-axis is directed upwards. In this case, expressions (7)–(9) can be rewritten as

$$x = x(u) == \pm vR,\quad y = y(u,v) = \pm vR\left[1-u^2\right]^{1/2},\quad z = z(u,v) = T\left[1-u^k\right]^{1/s}\left[1-v^m\right]^{1/n}; \tag{10}$$

$$x = x(u,v) = \pm vR\left[1-u^2\right]^{1/2},\quad y = y(u) = \pm uR,\quad z = z(u) = T\left[1-u^m\right]^{1/n}\left[1-v^k\right]^{1/s}; \tag{11}$$

$$x = x(u,v) = \pm vR\left[1-u^s\right]^{1/k},\quad y = y(u,v) = \pm R\left[1-u^n\right]^{1/m}\left[1-v^2\right]^{1/2},\quad z = z(u) = uT, \tag{12}$$

where $0 \le u \le 1,\quad 0 \le v \le 1;\quad u,v$ are non-dimensional parameters.

Parametric equations (10)–(12) allow to construct an unlimited number of groups of three surfaces. And in each group, the three surfaces will have the same geometric frame of two half-superellipses in vertical coordinate planes and the same circular base in the horizontal plane.

Several specific groups of three surfaces with the same frame are constructed and illustrated below. Using parametric equations (10)–(12), the first group of three surfaces is constructed for the case of $n = m = s = k = 1$ (Figure 1), the second group of three is constructed with $n = m = 1$, $s = k = 2$ (Figure 2), the third group of three has $s = k = 1$, $n = m = ¾$ (Figure 3), and the fourth group of three is constructed with $n = m = 2$, $s = k = ¾$ (Figure 4). The surfaces are visualized using Matplotlib v3.4.2 plotting library for Python programming language [13].

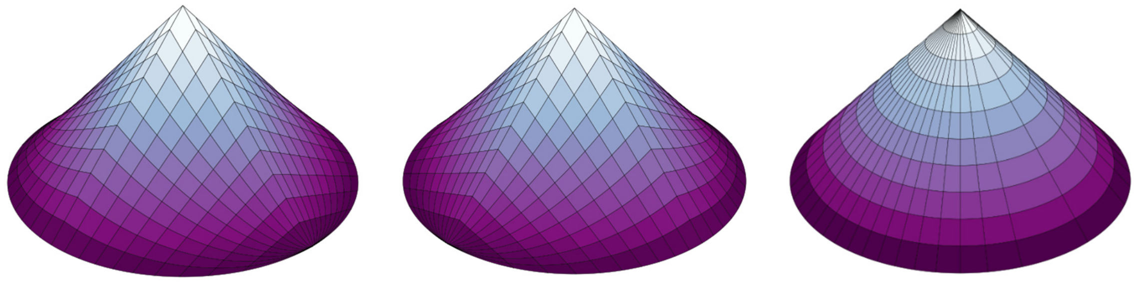

a *b* *c*

Figure 1. Analytical surfaces with a circular base (the 1st group of three where $n = m = s = k = 1$):
a — generated using equations (10); *b* — generated using equations (11); *c* — generated using equations (12)
S o u r c e: compiled by Valery Karnevich.

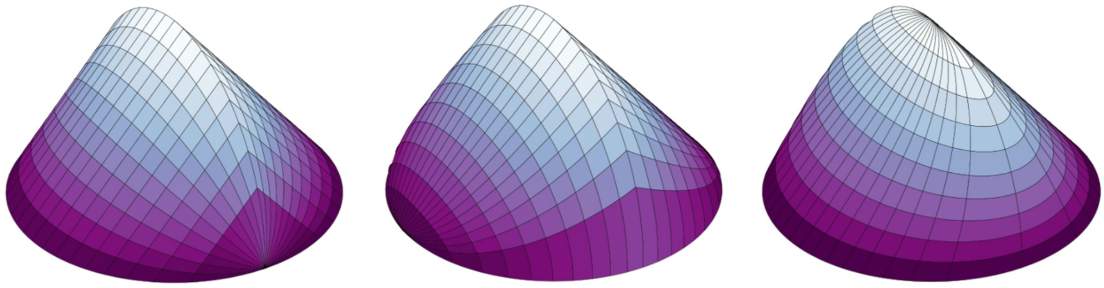

a *b* *c*

Figure 2. Analytical surfaces with a circular base (the 2nd group of three where $n = m = 1$, $s = k = 2$):
a — generated using equations (10); *b* — generated using equations (11); *c* — generated using equations (12)
S o u r c e: compiled by Valery Karnevich.

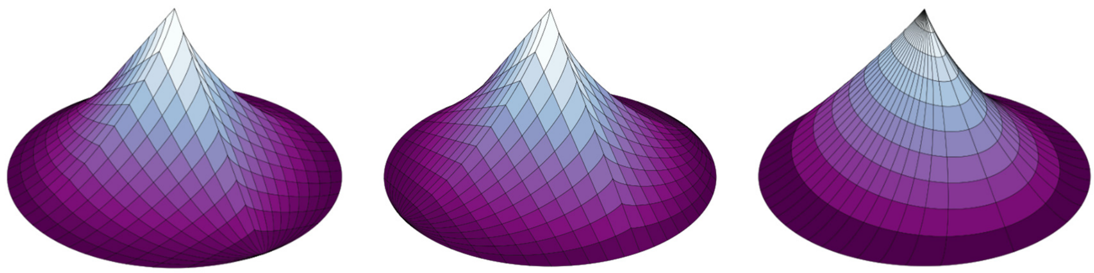

a *b* *c*

Figure 3. Analytical surfaces with a circular base (the 3rd group of three where $s = k = 1$, $n = m = 3/4$):
a — generated using equations (10); *b* — generated using equations (11); *c* — generated using equations (12)
S o u r c e: compiled by Valery Karnevich.

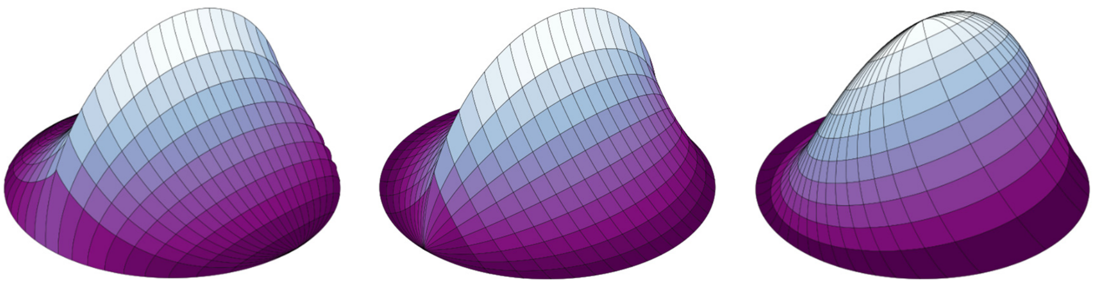

a *b* *c*

Figure 4. Analytical surfaces with a circular base (the 4th group of three where $n = m = 2$, $s = k = 3/4$):
a — generated using equations (10); *b* — generated using equations (11); *c* — generated using equations (12)
S o u r c e: compiled by Valery Karnevich.

By changing the values of exponents n, m, s, k in equations (10)–(12), it is possible to continue the construction of various surfaces with a circular base. The surfaces demonstrated in Figures 1–4 can be implemented as architectural structures in the form of rigid shells or in the forms of tent coverings. The potential for application of thin shells with middle surfaces shown in Figures 1–4 was originally considered in [14].

2.2. Geometric Analysis

Geometric properties of the first two groups of the presented surfaces (Figures 1 and 2) are examined using the methods of differential geometry.

A two-dimensional manifold (surface) naturally involves the use of two independent parameters. Any analytical surface defined by parametric equations can be expressed in vector form:

$$\boldsymbol{r} = \boldsymbol{r}(u,v) = x(u,v)\boldsymbol{i} + y(u,v)\boldsymbol{j} + z(u,v)\boldsymbol{k},$$

where u and v are independent parameters. The terminal points of all vectors $\boldsymbol{r} = \boldsymbol{r}(u,v)$ form a surface in space.

Internal and external geometry of a surface is described numerically by the coefficients of the fundamental forms. Coefficients E, G, F of the first quadratic form characterize the internal geometry of a surface, coefficients L, M, N of the second quadratic form characterize the curvature of the surface in space and coefficient K defines the Gaussian curvature [15]:

$$E = A^2 = \boldsymbol{r}_u^2, \quad G = B^2 = \boldsymbol{r}_v^2, \quad F = \boldsymbol{r}_u \boldsymbol{r}_v;$$

$$L = \frac{(\boldsymbol{r}_{uu}\boldsymbol{r}_u\boldsymbol{r}_v)}{\sqrt{A^2B^2 - F^2}}, \quad M = \frac{(\boldsymbol{r}_{uv}\boldsymbol{r}_u\boldsymbol{r}_v)}{\sqrt{A^2B^2 - F^2}}, \quad N = \frac{(\boldsymbol{r}_{vv}\boldsymbol{r}_u\boldsymbol{r}_v)}{\sqrt{A^2B^2 - F^2}};$$

$$K = \frac{LN - M^2}{A^2B^2 - F^2}.$$

2.3. Static Analysis

Thin shells with the middle surfaces shown in Figure 1 is are selected for a comparative static analysis under uniformly distributed vertical load. The choice of the analysis method is discussed below.

Four stages of creation and development of the theory of plates and shells, which gave rise to mechanism of analysis of spatial roof systems of large-span buildings and structures on a contemporary level, are presented in [16]. The author supposes that the fourth stage of development of the shell theory, design and construction of large-span structures has begun in the 21st century.

Now, a large variety of analytical, semi-analytical, and numerical methods of analysis of shells and shell structures exist. In the previous section, it was shown that the considered middle surfaces of shells can be defined in Cartesian coordinates using algebraic equations (4)–(6) or using parametric equations (10)–(12). Curved coordinate lines u, v of these surfaces can be non-orthogonal ($F \neq 0$) or orthogonal ($F = 0$), non-conjugate ($M \neq 0$) or conjugate ($M = 0$).

Taking this into account, one may use Goldenveiser's system of 20 governing equations [17] of the thin shell theory for arbitrary curvilinear coordinates containing internal "pseudo-forces" and "pseudo-moments", or the system of governing equations suggested by S.N. Krivoshapko [18] containing internal forces and moments generally used in engineering calculations, or the governing equations of Ya.M. Grigorenko, A.M. Timonin [19] expressed in tensor form. The linear theory of thin elastic shells is an approximate two-dimensional case of three-dimensional linear theory of elasticity [20]. The linear theory of thin elastic shells belongs to classical special two-dimensional models within linear elasticity [21]. The governing equations suggested by these researchers contain coefficients of the fundamental quadratic forms, which have not been previously presented for the specific surfaces examined in this paper.

Relevant literature analysis has shown that these three groups of governing equations of the linear theory of thin shells have been used only in the case of the simplified momentless theory of shells or for the analysis of ruled shells with a number of simplifications in geometry or governing equations. Hence, accurate application of analytical methods for the shells in question cannot be realized at present time.

Several numerical methods were considered for the analysis of the shells in this study. Such included: method of numerical integration of the system of governing differential equations, asymptotic semi-analytical method with a small parameter, finite difference energy method, finite element method in terms of displacements, and others [22]. It was decided to use displacement-based FEM [23]. In the 21st century, such FEM software as LIRA, SCAD, STARK, MicroFE, STADIO, ABAQUS, ADINA, ANSYS, LS-DYNA, COSMOS, MSC/NASTRAN, SOFISTIC, and other were successfully used for similar tasks. It was decided to select SCAD [24], which allows to conveniently define shell geometry using parametric equations and set the mesh discretization step along the curved coordinate lines. By changing the overall dimensions of shells, selecting appropriate exponents of algebraic curves (1)–(3) of the main frame of the shells, and by assuming a particular parameter of optimization, one can select an optimal structure among a large number of shells in automatic mode.

3. Results

3.1. Geometric Analysis

3.1.1. First Group of Three Surfaces

The coefficients of the fundamental forms of the surface in Figure 1, *a* can be expressed in the following form:

$$E = A^2 = \boldsymbol{r}_u^2 = R^2 + R^2u^2v^2 / \left(1-u^2\right) + T^2\left(1-v\right)^2; \tag{13}$$

$$G = B^2 = \boldsymbol{r}_v^2 = T^2\left(1-u\right)^2 + R^2\left(1-u^2\right) = B^2\left(u\right); \tag{14}$$

$$F = \boldsymbol{r}_u\boldsymbol{r}_v = -R^2uv + T^2\left(1-u\right)\left(1-v\right); \tag{15}$$

$$L = -\frac{R^2Tv\left(1-u\right)}{\sqrt{A^2B^2-F^2}\left(1-u^2\right)^{\frac{3}{2}}}; \tag{16}$$

$$M = \frac{R^2T\left(1-u\right)}{\sqrt{A^2B^2-F^2}\left(1-u^2\right)^{\frac{1}{2}}}; \tag{17}$$

$$N = 0; \tag{18}$$

$$K = -M^2 / \left(A^2B^2-F^2\right) < 0. \tag{19}$$

In expressions (13)–(19), the coefficient of the first fundamental form $F \neq 0$ shows that coordinate lines u, v are non-orthogonal. The coefficient of the second fundamental form $N = 0$ shows that coordinate lines v coincide with the straight generators of the surface. The coefficient of the second fundamental form $M \neq 0$ shows that the coordinate grid u, v is non-conjugate. The ruled surface presented in Figure 1, *a* is a surface of negative Gaussian curvature, since $K < 0$.

The coefficients of the fundamental quadratic forms of the surface shown in Figure 1, *b* are also determined by expressions (13)–(19). Since the ruled surfaces presented in Figure 1, *a* and 1, *b* have the same coefficients of the fundamental forms, they are identical surfaces. They are both cylindroids [25].

The coefficients of the fundamental quadratic forms of the surface in Figure 1, *c* are expressed as follows:

$$E = A^2 = \boldsymbol{r}_u^2 = T^2 + R^2; \tag{20}$$

$$F = \boldsymbol{r}_u \boldsymbol{r}_v = 0; \tag{21}$$

$$G = B^2 = \boldsymbol{r}_v^2 = R^2 (1-u)^2 / \left(1-v^2\right); \tag{22}$$

$$L = 0; \tag{23}$$

$$M = 0; \tag{24}$$

$$N = \frac{(\boldsymbol{r}_{vv} \boldsymbol{r}_u \boldsymbol{r}_v)}{\sqrt{A^2 B^2 - F^2}} = \frac{-TR(1-u)}{\left(T^2 + R^2\right)^{\frac{1}{2}} \left(1-v^2\right)}; \tag{25}$$

$$K = \frac{LN - M^2}{A^2 B^2 - F^2} = 0. \tag{26}$$

In expressions (20)–(26), the coefficient of the second fundamental form $L = 0$ shows that the curved coordinate lines *u* coincide with the straight generators of the surface. The coefficient of the first fundamental form $F = 0$ shows that coordinate lines *u, v* are orthogonal and the coefficient of the second fundamental form $M = 0$ shows that the coordinate grid *u, v* is conjugate. Therefore, the introduced curvilinear system of coordinates *u, v* is defined in lines of principal curvatures. The ruled surface shown in Figure 1, *c* is a surface of zero Gaussian curvature, since $K = 0$.

This ruled surface is a right circular cone. Differentials of the corresponding arclengths of coordinate lines *u* and *v* can be determined using the expressions

$$ds_u = A du, \quad ds_v = B dv.$$

3.1.2. Second Group of Three Surfaces

The coefficients of the fundamental quadratic forms of the surface shown in Figure 2, *a* have the following form:

$$E = A^2 = r_u^2 = u^2 v^2 R^2 / \left(1-u^2\right) + u^2 T^2 (1-v)^2 / \left(1-u^2\right) + R^2; \tag{27}$$

$$G = B^2 = \boldsymbol{r}_v^2 = \left(T^2 + R^2\right)\left(1-u^2\right) = B^2(u); \tag{28}$$

$$F = \boldsymbol{r}_u \boldsymbol{r}_v = -vR^2 u + T^2 u (1-v); \tag{29}$$

$$L = -\frac{R^2 T}{\sqrt{A^2 B^2 - F^2} \left(1-u^2\right)}; \tag{30}$$

$$M = 0; \tag{31}$$

$$N = 0; \tag{32}$$

$$K = 0. \tag{33}$$

Expressions (27)–(33) indicate that the system of curvilinear coordinates *u, v* is non-orthogonal ($F \neq 0$), but conjugate ($M = 0$). Coordinate lines *v* coincide with the straight generators ($N = 0$) of the cylindrical surface ($K = 0$) shown in Figure 2, *a*.

The coefficients of the fundamental quadratic forms of the surface shown in Figure 2, *b* have the following form:

$$E = A^2 = \boldsymbol{r}_u^2 = R^2 + R^2v^2u^2 / \left(1-u^2\right) + T^2\left(1-v^2\right); \tag{34}$$

$$G = B^2 = \boldsymbol{r}_v^2 = R^2\left(1-u^2\right) + T^2v^2\left(1-u\right)^2 / \left(1-v^2\right); \tag{35}$$

$$F = \boldsymbol{r}_u\boldsymbol{r}_v = -R^2uv + vT^2\left(1-u\right); \tag{36}$$

$$L = \frac{R^2T\left(1-u\right)v^2}{\sqrt{A^2B^2-F^2}\left(1-u^2\right)^{\frac{3}{2}}\left(1-v^2\right)^{\frac{1}{2}}}; \tag{37}$$

$$M = -\frac{R^2T\left(1-u\right)v}{\sqrt{A^2B^2-F^2}\left(1-u^2\right)^{\frac{1}{2}}\left(1-v^2\right)^{\frac{1}{2}}}; \tag{38}$$

$$N = \frac{R^2T\left(1-u\right)\left(1-u^2\right)^{\frac{1}{2}}}{\sqrt{A^2B^2-F^2}\left(1-v^2\right)^{3/2}}; \tag{39}$$

$$K = \frac{R^4T^2\left(1-u\right)^2v^4}{\left(A^2B^2-F^2\right)^2\left(1-u^2\right)\left(1-v^2\right)^2} > 0. \tag{40}$$

The corresponding coefficients of the fundamental quadratic forms of the surface shown in Figure 2, *c* have the following form:

$$E = A^2 = \boldsymbol{r}_u^2 = T^2 + R^2v^2u^2 / \left(1-u^2\right) + R^2\left(1-v^2\right); \tag{41}$$

$$G = B^2 = \boldsymbol{r}_v^2 = R^2\left(1-u^2\right) + R^2v^2\left(1-u\right)^2 / \left(1-v^2\right); \tag{42}$$

$$F = \boldsymbol{r}_u\boldsymbol{r}_v = vR^2\left(1-2u\right); \tag{43}$$

$$K = -\frac{R^2T\left(1-u\right)v^2}{\sqrt{A^2B^2-F^2}\left(1-u^2\right)^{\frac{3}{2}}\left(1-v^2\right)^{\frac{1}{2}}}; \tag{44}$$

$$M = \frac{R^2T\left(1-u\right)v}{\sqrt{A^2B^2-F^2}\left(1-u^2\right)^{\frac{1}{2}}\left(1-v^2\right)^{\frac{1}{2}}}; \tag{45}$$

$$N = -\frac{R^2T\left(1-u\right)\left(1-u^2\right)^{\frac{1}{2}}}{\sqrt{A^2B^2-F^2}\left(1-v^2\right)^{\frac{3}{2}}}; \tag{46}$$

$$K = \frac{R^4 T^2 (1-u)^2 v^4}{\left(A^2 B^2 - F^2\right)^2 \left(1-u^2\right)\left(1-v^2\right)^2} > 0. \tag{47}$$

By comparing equations (34)–(40) and (41)–(47), it can be observed that the surfaces presented in Figures 2, *b* and 2, *c* have the same values of the coefficients of the second fundamental form (L, M, N), only with the opposite signs, and the same positive Gaussian curvature ($K > 0$).

The geometry of the remaining two groups of three surfaces (Figures 3 and 4) can be investigated in a similar manner.

3.2. Static Analysis

The shells with the middle surfaces shown in Figure 1 are subjected to a uniformly distributed load $q = 1$ kN/m^2. The load acts in the opposite direction to the fixed axis Oz.

It is assumed that $T = R = 5$ m, constant shell thickness $h = 7$ cm, elastic modulus of the shell material $E_b = 32500$ MPa and Poisson's ratio $\nu = 0.17$. The shell is fixed at the base along the contour $z = 0$.

It was previously established that the surfaces in Figure 1, *a* and 1b are identical, despite being constructed differently by the process of moving the straight generators within the geometric frame. Thus, the static analysis is performed for two cases of the middle surface: cylindroid (Figure 1, *a*) and cone (Figure 1, *c*). The finite element models are developed in SCAD v21 software for the two cases of shells and are depicted in Figure 5, including the directions of curvilinear coordinates *u* and *v*. The geometry of the models is defined by parametric equations (10) and (12) respectively. The meshes of FE-models consist of plane shell elements.

Figure 6 shows the exaggerated deformed shapes of the analyzed shells under the applied vertical load.

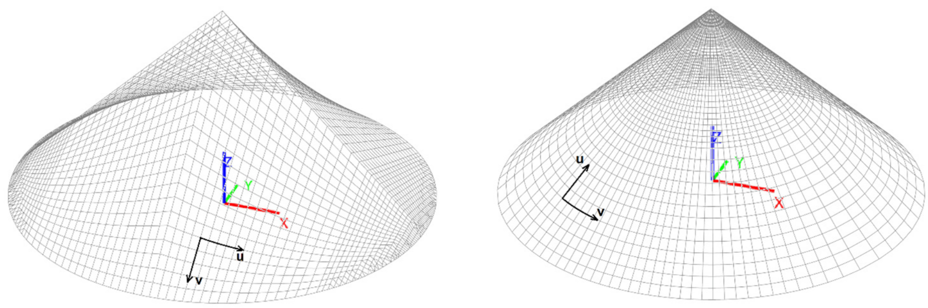

a *b*

Figure 5. Finite element model:
a — shell with cylindroidal middle surface; *b* — shell with conical middle surface
Source: compiled by Valery Karnevich.

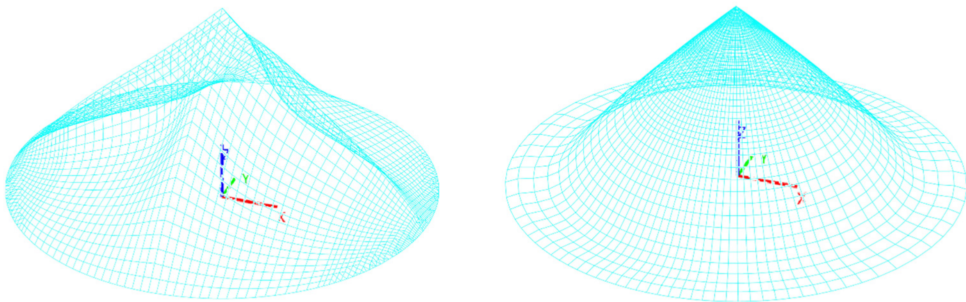

a *b*

Figure 6. Deformed shape:
a — shell with cylindroidal middle surface; *b* — shell with conical middle surface
Source: compiled by Valery Karnevich.

The left-hand sides (a) of Figures 7–12 demonstrate the computed strength parameters of the shell with the middle surface shown in Figure 1, *a*. Correspondingly, the right-hand sides (b) of Figures 7–12 show the computed stress-strain state parameters of the shell with the middle surface shown in Figure 1, *c*. Vertical displacements (Figure 7) are positive in the upwards direction. Normal stresses N_u and N_v (Figures 8–9) are directed along coordinate lines *u* and *v* respectively; positive values of normal stress indicate tension. M_u and M_v (Figures 10–11) represent bending moments, which act in the sections orthogonal to coordinate lines *u* and *v* respectively and are calculated as moment per unit length of these lines. Equivalent compressive stress (Figure 12) is computed as von Mises stress.

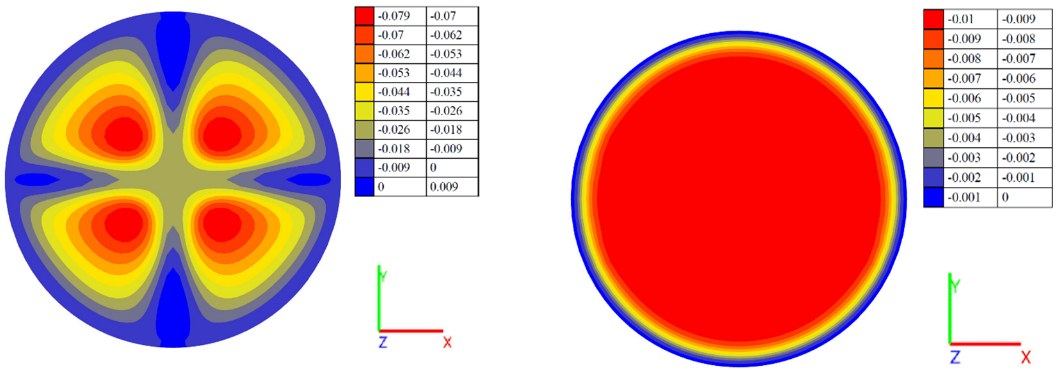

a *b*

Figure 7. Distribution of displacements along *z*-axis (mm):
a — shell with cylindroidal middle surface; *b* — shell with conical middle surface
S o u r c e: compiled by Valery Karnevich.

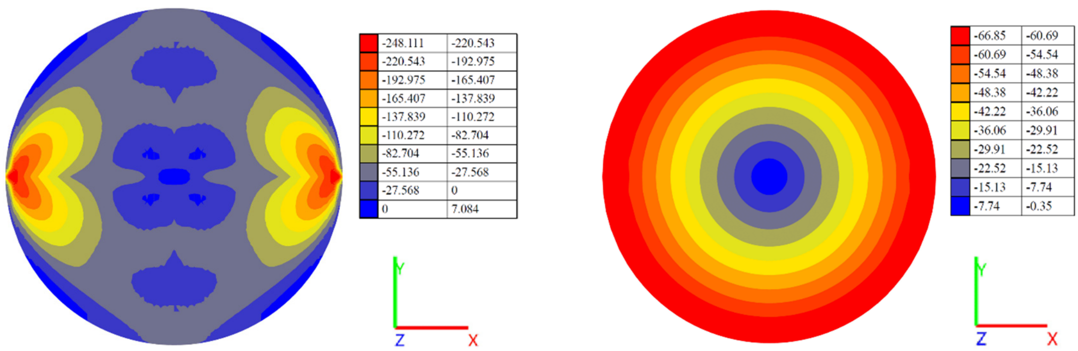

a *b*

Figure 8. Distribution of normal stresses N_u (kN/m^2):
a — shell with cylindroidal middle surface; *b* — shell with conical middle surface
S o u r c e: compiled by Valery Karnevich.

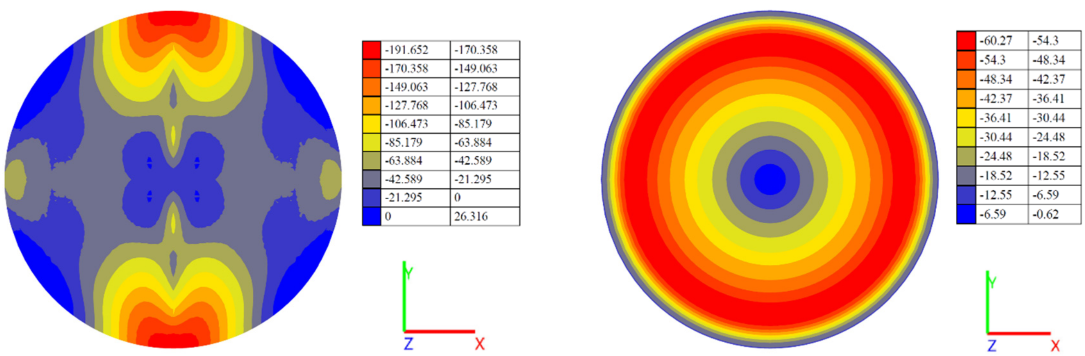

a *b*

Figure 9. Distribution of normal stresses N_v (kN/m^2):
a — shell with cylindroidal middle surface; *b* — shell with conical middle surface
S o u r c e: compiled by Valery Karnevich.

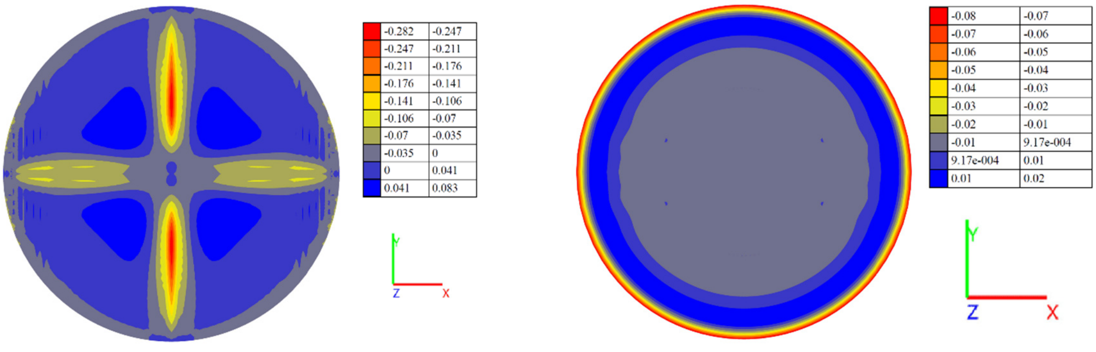

a *b*

Figure 10. Distribution of bending moments M_u (kN·m/m):
a — shell with cylindroidal middle surface; *b* — shell with conical middle surface
S o u r c e: compiled by Valery Karnevich.

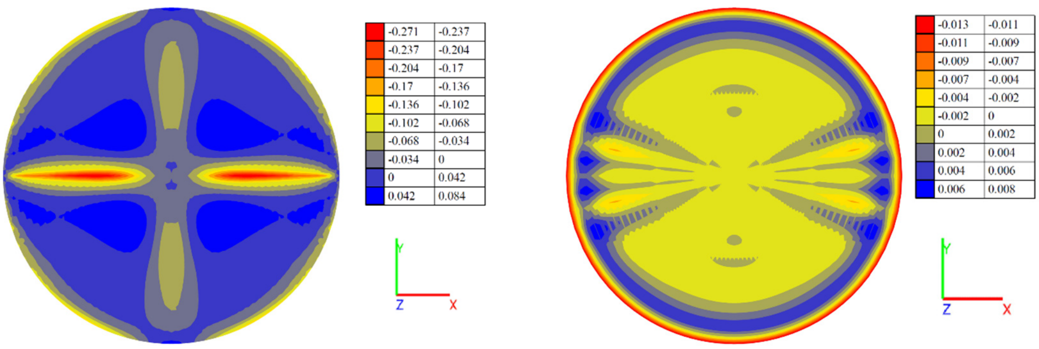

a *b*

Figure 11. Distribution of bending moments M_v (kN·m/m):
a — shell with cylindroidal middle surface; *b* — shell with conical middle surface
S o u r c e: compiled by Valery Karnevich.

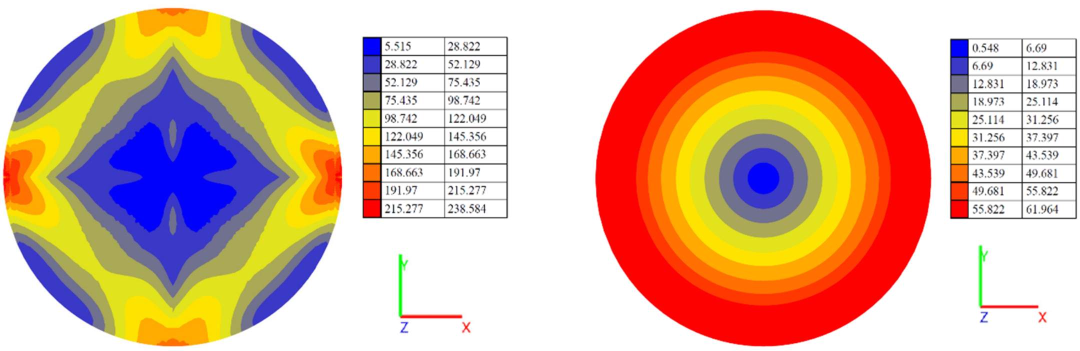

a *b*

Figure 12. Distribution of equivalent von Mises compressive stress at the middle surface (kN/m^2):
a — shell with cylindroidal middle surface; *b* — shell with conical middle surface
S o u r c e: compiled by Valery Karnevich.

4. Discussion

This paper shows the construction of 4 groups of three surfaces, based on the previously obtained analytical and parametric equations of surfaces with the geometric frame of three superellipses. All 12 surfaces contain a circle as one of the plane curves of the frame. The presented surfaces are visualized graphically (see Figures 1–4) for better perception by architects and engineers. Using the methods of differential geometry, the detailed analysis of 6 algebraic middle surfaces of shells was performed for the first time. As a result of the geometric analysis, two surfaces in one group of three surfaces (see Figure 1) came out identical, and in the case of the other group (see Figure 2) all three surfaces are geometrically different. In the opinion of the authors, these surfaces can be taken as a basis for the shapes of civil and mechanical engineering structures. At least, these surfaces can be in the reserve of surfaces waiting for their implementation [26] within the framework of one of the modern architectural styles. The number of new forms of thin shells can be significantly expanded by taking fragments of different superellipses as the plane curves of the geometric frame [27].

The comparative static analysis of two thin shells (see Figure 5), the middle surfaces of which belong to one group of three surfaces with identical frames, was undertaken to provide insight into the structural differences. It is clear from the deformed shapes (Figure 6), displacement distributions (Figure 7), stress and moment distributions (Figures 8–12) that the behavior of the two shells with the same dimensions, material and applied static load differs drastically. All distributions of the strength factors in the circular cone are rotationally symmetric. In the cylindroid, these distributions are symmetric about the radial edges of the shell, which lie along the x and y axes. The maximum vertical displacement of the cylindroid is about 8 times higher than that of the cone (see Figure 7). The maximum stresses and moments (see Figures 8–12) are about 3–4 times greater in the cylindroid. The greatest normal stresses along curvilinear coordinates u, v in the cylindroid concentrate at the bottom of the radial edges (see Figure 8). The normal stresses in the circular cone are more linearly distributed and are larger near the circular base (see Figure 9). Moreover, the cylindroid shell has areas of tensile stress, whereas the cone exhibits pure compression. The maximum bending moments in the cylindroid concentrate along the radial edges (Figure 10). The bending moments in the circular cone are slightly greater near the base (see Figure 11), but are very small overall. It should be noted that the values of the strength factors along curvilinear coordinates u, v cannot be compared directly for the two shells, since their curvilinear coordinate grids are different (Figure 5). Hence, the distributions of von Mises compressive stress were obtained for the two shells (see Figure 12). These equivalent stress distributions roughly locate the dangerous areas of the shells.

5. Conclusion

Developments in mechanical and civil engineering require new more efficient solutions. One possible method of improving the load-bearing capacity of shell structures is modification of their geometry. This paper examines thin shells, the middle surfaces of which are defined by three plane curves of the geometric frame: a circle in the horizontal plane and two superellipses in the two vertical planes. It is shown that by varying the values of the exponents of the superellipses, it is possible to obtain a variety of outstanding shapes.

1. The method of defining the geometry of surfaces by using the curves of their frames allows to obtain a group of three surfaces — one for each curve of the frame. Further geometric analysis is required to determine the differences within the group. Some surfaces within a group may be identical, and in the other group some may share particular geometric characteristics, but be different overall, as confirmed by the findings in this paper.

2. It is shown that shells with geometrically different middle surfaces, but defined by the same frame, exhibit completely dissimilar behavior under static load. The presented static analysis of the two shells formed by the same main frame shows advantage of the circular cone over the cylindroid. However, a more detailed analysis is required for selecting the optimal shell, by testing for different dimensions, material properties and constraints. In some cases, material consumption, the simplest method of shell fabrication, or enclosed volume may be taken as the optimality criterion, which can be potentially satisfied by particular shell shapes demonstrated in this paper.

The analysis of available sources allowed to conclude that in the beginning of the 21st century the period of decline of interest for shell structures and thin-walled shells was over. This happened owing to the appearance of new structural materials, expansion of the inventory of analytical, point, spline and frame surfaces suitable for use as middle surfaces of shells, the development of more accurate calculation methods and computer software on their basis, and most importantly there was an increased demand for the creation of curvilinear large-span shell structures. These conclusions are confirmed by appearance of new architectural styles, directions, and style flows in the recent decades. Most architects and designers believe that curvilinear structures can become an alternative to traditional forms of buildings, while others, on the contrary, believe that the curvilinearity of buildings will quickly bore the inhabitants.

References / Список литературы

1. Ko K.H. A survey: Application of geometric modeling techniques to ship modeling and design. *International Journal of Naval Architecture and Ocean Engineering*. 2010;2(4):177–184. http://doi.org/10.2478/IJNAOE-2013-0034
2. Krivoshapko S.N. Tangential developable and hydrodynamic surfaces for early stage of ship shape design. *Ships and Offshore Structures*. 2023;18:660–668. http://doi.org/10.1080/17445302.2022.2062165 EDN: TQOCBY
3. Ma Y.Q., Wang C., Ang K.K., Xiang Y. Buckling of superellipsoidal shells under uniform pressure. *Thin-Walled Structures.* 2008;46:584–591. http://doi.org/10.1016/j.fws.2008.01.013
4. Moonesun M., Mahdion A., Korol Y., Dadkhah M., Javadi M. Concepts in submarine shape design. *Indian Journal of Geo-Marine Sciences*. 2016;45(1):100–104. EDN: XLIBAL
5. Krivoshapko S.N., Gebre T. Algebraic surfaces with three super ellipses for formation of submarine hull surfaces. *Journal of Ship Research*. 2024;68(1):16–22. http://doi.org/10.5957/JOSR.09220026 EDN: ENRCZU
6. Karnevich V.V. Hydrodynamic surfaces with midsection in the form of Lame curve. *RUDN Journal of Engineering Research.* 2021;22(4):323–328. http://doi.org/10.22363/2312-8143-2021-22-4-323-328 EDN: GYCACT
7. Karnevich V.V. Generating hydrodynamic surfaces by families of Lame curves for modelling submarine hulls. *RUDN Journal of Engineering Research.* 2022;23(1):30–37. https://doi.org/10.22363/2312-8143-2022-23-1-30-37 EDN: QVQEZM
8. Strashnov S.V. Computer simulation of new forms of shell structures. *Geometry & Graphics*. 2022;10(4):26–34. http://doi.org/10.12737/2308-4898-2022-10-4-26-34 EDN: PXTLAU
9. Krivoshapko S.N. Algebraic ship hull surfaces with a main frame from three plane curves in coordinate planes. *RUDN Journal of Engineering Research.* 2022;23(3):207–212. (In Russ.) http://doi.org/10.22363/2312-8143-2022-23-3-207-212 EDN: HEXIBR

   Кривошапко С.Н. Алгебраические судовые поверхности с каркасом из трех плоских кривых в координатных плоскостях // Вестник Российского университета дружбы народов. Серия: Инженерные исследования. 2022. Т. 23. № 3. С. 207–212. http://doi.org/10.22363/2312-8143-2022-23-3-207-212 EDN: HEXIBR
10. Mamieva I.A. Ruled algebraic surfaces with a main frame from three superellipses. *Structural Mechanics of Engineering Constructions and Buildings.* 2022;18(4):387–395. (In Russ.) http://doi.org/10.22363/1815-5235-2022-18-4-387-395 EDN: KAGFQC

    Мамиева И.А. Линейчатые алгебраические поверхности с главным каркасом из трех суперэллипсов // Строительная механика инженерных конструкций и сооружений. 2022. Т. 18. № 4. С. 387–395. http://doi.org/10.22363/1815-5235-2022-18-4-387-395 EDN: KAGFQC
11. Mamieva I.A., Karnevich V.V. Geometry and static analysis of thin shells with ruled middle surfaces of three superellipses as main frame. *Building and Reconstruction*. 2023;1(105):16–27. http://doi.org/10.33979/2073-7416-2023-105-1-16-27 EDN: LSIOLJ
12. Krivoshapko S.N. Optimal shells of revolution and main optimizations. *Structural Mechanics of Engineering Constructions and Buildings*. 2019;15(3):201–209. http://doi.org/10.22363/1815-5235-2019-15-3-201-209 EDN: XGRSDR
13. Hunter J.D. Matplotlib: A 2D Graphics Environment. *Computing in Science & Engineering*. 2017;9(3):90–95. http://doi.org/10.1109/MCSE.2007.55
14. Krivoshapko S.N. Surfaces with a main framework of three given curves which include one circle. *Structural Mechanics of Engineering Constructions and Buildings*. 2023;19(2):210–219. http://doi.org/10.22363/1815-5235-2023-19-2-210-219EDN: CWWLDM
15. Schlichtkrull H. *Curves and Surfaces: Lecture Notes for Geometry 1*. University of Copenhagen. 2011. Available from: https://noter.math.ku.dk/geom1.pdf (accessed: 27.05.2025)
16. Sysoeva E.V. Scientific approaches to calculation and design of large-span structures. *Proceedings of Moscow State University of Civil Engineering.* 2017;12(2):131–141. (In Russ.) http://doi.org/10.22227/1997-0935.2017.2.131-141 EDN: YGJDWF

    Сысоева Е.В. Научные подходы к расчету и проектированию большепролетных конструкций // Вестник МГСУ. 2017. Т. 12. № 2 (101). С. 131–141. http://doi.org/10.22227/1997-0935.2017.2.131-141 EDN: YGJDWF

17. Goldenveizer A.L. *Theory of Elastic Thin Shells.* Published by Pergamon Press, New York, 1961. Available from: https://archive.org/details/theoryofelastict0000algo (accessed: 12.05.2025)

18. Krivoshapko S.N., Razin A.D. Comparison of two systems of governing equations for the thin shell analysis. *Proceedings of the ICER 2021*, Moscow, 2022;2559:020009. http://doi.org/10.1063/5.0099905

19. Grigorenko Ya.M., Timonin A.M. On one approach to the numerical solution of boundary problems on theory of complex geometry shells in the non-orthogonal curvilinear coordinate systems. *Reports of AS of Ukraine USR*. 1991;(4):41–44. (In Russ.)

Григоренко Я.М., Тимонин А.М. Об одном подходе к численному решению краевых задач теории оболочек сложной геометрии в неортогональных криволинейных системах координат // Доклады Академии наук Украинской ССР. 1991. № 4. Вып. 9. С. 41–44.

20. Pietraszkiewicz W. *Thin Elastic Shells, Linear Theory, Encyclopedia of Continuum Mechanics.* Encyclopedia of Continuum Mechanics. Springer, Berlin, Heidelberg, 2018. https://doi.org/10.1007/978-3-662-53605-6_187-1

21. Karpov V.V., Bakusov P.A., Maslennikov A.M., Semenov A.A. Simulation models and research algorithms of thin shell structures deformation Part I. Shell deformation models. *Izvestiya of Saratov University. Mathematics. Mechanics. Informatics*. 2023;23(3):370–410. (In Russ.) https://doi.org/10.18500/1816-9791-2023-23-3-370-410 EDN: YSOXDU

Карпов В.В., Бакусов П.А., Масленников А.М., Семенов А.А. Математические модели деформирования оболочечных конструкций и алгоритмы их исследования. Часть I: Модели деформирования оболочечных конструкций // Известия Саратовского университета. Новая серия. Серия: Математика. Механика. Информатика. 2023. Т. 23. № 3. С. 370–410. https://doi.org/10.18500/1816-9791-2023-23-3-370-410 EDN: YSOXDU

22. Schnobrich W.C. Different methods of numerical analysis of shells. *Lecture Notes in Engineering.* 1987;26:1–17. https://doi.org/10.1007/978-3-642-83015-0_1

23. Noor A.K. Bibliography of books and monographs on finite element technology. *Applied Mechanics Reviews.* 1991;44:307–317. https://doi.org/10.1115/1.3119505

24. Karpilovskiy V.S., Kriksunov E.Z., Malyarenko A.A., Mikitarenko M.A., Perelmuter A.V., Perelmuter M.A. *Computer Complex SCAD*. Kyiv; 2025. Available from: https://scadsoft.com/download/Section1033.pdf (accessed: 12.06.2025).

25. Zhi W.Z., Jiang L.Y. Analysis of cylindroid shell subject to internal linearly increased pressure. *Advanced Materials Research.* 2011;239–242:2584–2589. http://doi.org/10.4028/www.scientific.net/amr.239-242.2584

26. Mathieu G. Reserve of analytical surfaces for architecture and construction. *Building and Reconstruction.* 2021;6(98):63–72. https://doi.org/10.33979/2073-7416-2021-98-6-63-72 EDN: BCWXIS

27. Rosin P.L., Geoff W. Curve Segmentation and Representation by Superellipses. *IEE Proceedings — Vision Image and Signal Processing.* 1995;142:280–288. https://doi.org/10.1049/ip-vis:19952140

СТРОИТЕЛЬНАЯ МЕХАНИКА ИНЖЕНЕРНЫХ КОНСТРУКЦИЙ И СООРУЖЕНИЙ
STRUCTURAL MECHANICS OF ENGINEERING CONSTRUCTIONS AND BUILDINGS

2025. 21(5). 414–431
ISSN 1815-5235 (Print), 2587-8700 (Online)
HTTP://JOURNALS.RUDN.RU/STRUCTURAL-MECHANICS

АНАЛИТИЧЕСКИЕ И ЧИСЛЕННЫЕ МЕТОДЫ РАСЧЕТА КОНСТРУКЦИЙ
ANALYTICAL AND NUMERICAL METHODS OF STRUCTURAL ANALYSIS

DOI: 10.22363/1815-5235-2025-21-5-414-431
EDN: ECUDSM

Научная статья / Research article

Реологические уравнения состояния бетона

Е.А. Ларионов[1], **В.П. Агапов**[1], **А.С. Маркович**[1,2]✉, **К.Р. Айдемиров**[3]

[1] Российский университет дружбы народов, *Москва, Российская Федерация*
[2] Национальный исследовательский Московский государственный строительный университет, *Москва, Российская Федерация*
[3] Дагестанский государственный технический университет, *Махачкала, Российская Федерация*
✉ markovich-as@rudn.ru

Поступила в редакцию: 8 июня 2025
Доработана: 4 сентября 2025 г.
Принята к публикации: 3 октября 2025 г.

Аннотация. Установлено квазилинейное представление нелинейного реологического уравнения состояния бетона, выведенного на основе концепции статистического распределения прочности отдельных фракций, в объединении образующих элемент конструкции. В нелинейной постановке для нестареющего бетона известный принцип Л. Больцмана суперпозиции деформаций ползучести реализуется по приращениям структурного напряжения способных к силовому сопротивлению фракций при неубывающем нагружении. Для стареющего бетона в отличие от предшествующих подходов реализовано наложение частичных приращений деформаций, порожденных приращениями уровня напряжений. Это приводит к корректному учету старения бетона, уточняющему вид известных реологических уравнений. Приведены удобные в приложениях квазилинейные формы реологических уравнений. Концепция прочностной структуры бетона и идентичность функций старения прочности, модуля упругости и ползучести позволяют сведение уравнения ползучести к линейному дифференциальному уравнению с постоянными коэффициентами. Это упрощает, в частности, решение задач релаксации напряжений, значимых в расчетах конструкций на долгосрочную безопасность.

Ключевые слова: наложение, прочность, старение, ползучесть бетона, релаксация напряжений, деформация

Заявление о конфликте интересов. Авторы заявляют об отсутствии конфликта интересов.

Вклад авторов: *Ларионов Е.А.* — общая концепция исследования, валидация; *Агапов В.П.* — выводы и рекомендации; *Маркович А.С., Айдемиров К.Р.* — анализ научной литературы, написание текста. Все авторы ознакомлены с окончательной версией статьи и одобрили ее.

Для цитирования: *Ларионов Е.А., Агапов В.П., Маркович А.С., Айдемиров К.Р.* Реологические уравнения состояния бетона // Строительная механика инженерных конструкций и сооружений. 2025. Т. 21. № 5. С. 414–431. http://doi.org/10.22363/1815-5235-2025-21-5-414-431 EDN: ECUDSM

Ларионов Евгений Алексеевич, доктор технических наук, профессор кафедры технологии строительства и конструкционных материалов, инженерная академия, Российский университет дружбы народов, Российская Федерация, 117198, г. Москва, ул. Миклухо-Маклая, д. 6; eLIBRARY AuthorID: 365207, ORCID: 0000-0002-4906-5919; e-mail: evgenylarionov39@yandex.ru

Агапов Владимир Павлович, доктор технических наук, профессор кафедры технологий строительства и конструкционных материалов, инженерная академия, Российский университет дружбы народов, Российская Федерация, 117198, г. Москва, ул. Миклухо-Маклая, д. 6; eLIBRARY SPIN-код: 2422-0104, ORCID: 0000-0002-1749-5797; e-mail: agapovpb@mail.ru

Маркович Алексей Семенович, доктор технических наук, доцент кафедры технологий строительства и конструкционных материалов, инженерная академия, Российский университет дружбы народов, Российская Федерация, 117198, г. Москва, ул. Миклухо-Маклая, д. 6; профессор кафедры металлических и деревянных конструкций, Национальный исследовательский Московский государственный строительный университет, Российская Федерация, 129337, г. Москва, Ярославское ш., д. 26; eLIBRARY SPIN-код: 9203-1434; ORCID: 0000-0003-3967-2114; e-mail: markovich-as@rudn.ru

Айдемиров Курбан Рабаданович, кандидат технических наук, доцент кафедры строительных конструкций и гидротехнических сооружений, Дагестанский государственный технический университет, Российская Федерация, 367026, г. Махачкала, пр. Имама Шамиля, д. 70; eLIBRARY SPIN-код: 8167-4343, ORCID: 0009-0005-1474-4275; e-mail: kyrayd@mail.ru

Rheological Equations of State of Concrete

Evgeny A. Larionov[1], Vladimir P. Agapov[1], Alexey S. Markovich[1,2]✉, Kurban R. Aidemirov[3]

[1]RUDN University, *Moscow, Russian Federation*
[2]Moscow State University of Civil Engineering (National Research University), *Moscow, Russian Federation*
[3]Daghestan State Technical University, *Makhachkala, Russian Federation*
✉ markovich-as@rudn.ru

Received: July 27, 2025
Revised: September 4, 2025
Accepted: October 3, 2025

Abstract. A quasilinear representation of a nonlinear rheological equation of concrete state has been established, derived on the basis of the concept of statistical strength distribution of individual fractions combined to form a structural element. In the nonlinear formulation for ageless concrete, L. Boltzmann's well-known principle of superposition of creep deformations is realized by increments of structural stress of fractions capable of force resistance under non-decreasing loading. For aging concrete, in contrast to previous approaches, the superposition of partial increments of deformations generated by increments in stress levels is implemented. This leads to the correct consideration of concrete aging, clarifying the type of known rheological equations. Quasilinear forms of rheological equations that are convenient in applications are given. The concept of the strength structure of concrete and the identity of the aging functions of strength, modulus of elasticity and creep make it possible to reduce the creep equation to a linear differential equation with constant coefficients. This simplifies, in particular, the solution of stress relaxation problems, which are important in the calculations of structures for long-term safety.

Keywords: superposition, strength, aging, concrete creep, stress relaxation, deformation

Conflicts of interest. The authors declare no conflict of interest.

Authors' contribution: *Larionov E.A.* — general concept of research, validation; *Agapov V.P.* — conclusions and recommendations; *Markovich A.S., Aidemirov K.R.* — analysis of scientific literature, writing. All authors read and approved the final version of the article.

For citation: *Larionov E.A., Agapov V.P., Markovich A.S., Aidemirov K.R.* Rheological equations of state of concrete. *Structural Mechanics of Engineering Constructions and Buildings.* 2025;21(5):414–431. (In Russ.) http://doi.org/10.22363/1815-5235-2025-21-5-414-431 EDN: ECUDSM

1. Введение

Уравнения механического состояния значимы в теории бетона, и им посвящено большое количество работ, отраженных частично в [1; 2]. Эти уравнения представляют теоретические обоснования экспериментально выявленных при эталонных нагружениях феноменологических зависимостей. В неравновесном процессе силового деформирования существенную роль играет явление прироста деформации при постоянном напряжении, называемое ползучестью. Учет ползучести бетона, естественно, приводит к реологическим уравнениям состояния. Традиционный вывод этих уравнений использует принцип наложения деформаций и заключается в суммировании в некоторый момент t частичных приращений $\Delta\varepsilon_{cr}(t,\tau_i)$ деформаций ползучести, порожденных частичными приращениями $\Delta\sigma(\tau_i)$ напряжения $\sigma(\tau)$ в последовательные предыдущие моменты времени τ_i. В линейной теории ползучести идеального (нестареющего) бетона принцип наложения известен как принцип суперпозиции Л. Больцмана [3] — деформация $\Delta\varepsilon_{cr}(t,\tau_i)$ определяется напряжением $\Delta\sigma(\tau_i)$ и его продолжительностью $(t-\tau_i)$ и не зависит от $\Delta\sigma(\tau_j)$ и $(t-\tau_j)$ при $i \neq j$. Взаимонезависимость деформа-

Evgeny A. Larionov, Doctor of Technical Sciences, Professor of the Department of Construction Technology and Structural Materials, Engineering Academy, RUDN University, 6 Miklukho-Maklaya St, Moscow, 117198, Russian Federation; eLIBRARY AuthorID: 365207, ORCID: 0000-0002-4906-5919; e-mail: evgenylarionov39@yandex.ru

Vladimir P. Agapov, Doctor of Technical Sciences, Professor of the Department of Construction Technology and Structural Materials, Academy of Engineering, RUDN University, 6 Miklukho-Maklaya St, Moscow, 117198, Russian Federation; eLIBRARY SPIN-code: 2422-0104, ORCID: 0000-0002-1749-5797; e-mail: agapovpb@mail.ru

Alexey S. Markovich, Doctor of Technical Sciences, Associate Professor of the Department of Construction Technology and Structural Materials, Academy of Engineering, RUDN University, 6 Miklukho-Maklaya St, Moscow, 117198, Russian Federation; Professor of the Department of Metal and Timber Structures, National Research Moscow State University of Civil Engineering, 26 Yaroslavl Highway, Moscow, 129337, Russian Federation; eLIBRARY SPIN-code: 9203-1434, ORCID: 0000-0003-3967-2114; e-mail: markovich-as@rudn.ru

Kurban R. Aidemirov, PhD, Associate Professor, Associate Professor of the Department of Building Structures and Hydraulic Structures, Dagestan State Technical University, 70, I. Shamily avenue, Makhachkala, 367026, Russian Federation; eLIBRARY SPIN-code: 8167-4343, ORCID: 0009-0005-1474-4275; e-mail: kyrayd@mail.ru

ций $\Delta\varepsilon_{cr}(t,\tau_i)$ позволяет нахождение отвечающего приращению напряжения $\Delta\sigma(t,t_0)=\sum_{i=0}^{n-1}\Delta\sigma(\tau_i)$ полного приращения $\Delta\varepsilon_{cr}(t,t_0)$ деформации ползучести суперпозицией (наложением) $\Delta\varepsilon_{cr}(t,\tau_i)$:

$$\Delta\varepsilon_{cr}(t,t_0)=\sum_{i=0}^{n-1}\Delta\varepsilon_{cr}(t,\tau_i)=\sum_{i=0}^{n-1}C_0(t,\tau_i)\Delta\sigma(\tau_i), \tag{1}$$

где $C_0(t,\tau_i)$ — мера ползучести идеального бетона в момент t при нагружении в момент τ_i.

При постоянном модуле упругости E приращению $\Delta\sigma(t,t_0)$ отвечает приращение мгновенной деформации:

$$\Delta\sigma_{el}(t,t_0)=\sum_{i=0}^{n-1}\frac{\Delta\sigma(\tau_i)}{E}. \tag{2}$$

Согласно (1) и (2) получим равенство

$$\Delta\varepsilon(t,t_0)=\sum_{i=0}^{n-1}\left[\frac{1}{E}+C_0(t,\tau_i)\right]\Delta\sigma(\tau_i), \tag{3}$$

выражающее принцип наложения деформаций в наследственной теории ползучести Больцмана – Вольтерра.

Предельный переход в (3) позволяет получить выражение

$$\Delta\varepsilon(t,t_0)=\frac{\Delta\sigma(t,t_0)}{E}+\int_{t_0}^{t}C_0(t,\tau)d\sigma(\tau). \tag{4}$$

Добавление к $\Delta\varepsilon(t,t_0)$ деформации $\left[\frac{1}{E}+C_0(t,\tau_i)\right]\sigma(t_0)$ приводит к уравнению

$$\varepsilon(t,t_0)=\frac{\sigma(t)}{E}+\int_{t_0}^{t}C_0(t,\tau)d\sigma(\tau)+C_0(t,t_0)\sigma(t_0),$$

преобразующемуся к виду

$$\varepsilon(t,t_0)=\frac{\sigma(t)}{E}-\int_{t_0}^{t}\sigma(\tau)\frac{\partial C_0(t,\tau)}{\partial\tau}d\tau. \tag{5}$$

Для стареющего бетона принимается мера ползучести

$$C^*(t,\tau)=\Theta(t)C_0(t,\tau),\quad C_0(t,\tau)=C_0(\infty,28)f(t,\tau), \tag{6}$$

где $\Theta(t)$ — функция старения; $C_0(\infty,28)$ — предельная мера ползучести $C_0(t,\tau)$ при $t_0=28$ суток; $f(t,\tau)$ — функция накопления деформаций ползучести, причем

$$f(t,\tau)=1-ke^{-\gamma(t-t_0)},$$

где $0<k\le 1$, γ — эмпирический коэффициент.

Зависимость функции $f(t,\tau)$ от аргумента $(t-\tau)$ определяется природой запаздывающих деформаций ползучести.

Решением дифференциального уравнения

$$\frac{dC^*(t,\tau)}{dt}=\gamma\left[C^*(\infty,\tau)-C(t,\tau)\right], \tag{7}$$

отражающего пропорциональность скорости затухания деформаций ползучести ее дефициту, является функция

$$f(t,\tau)=1-e^{-\gamma(t-t_0)}. \tag{8}$$

З а м е ч а н и е. Полагая $k<1$ в функции $f(t,\tau)$, при $\tau=t$ получим

$$C^*(t,t)=\Theta(t)C_0(\infty,28)(1-k)\neq 0.$$

Это соответствует наличию так называемой кратковременной ползучести, что противоречит инерционной природе запаздывающих деформаций ползучести. Вместе с тем соотношение $C^*(t,t)\neq 0$ коррелирует с экспериментально наблюдаемым начальным всплеском кривой ползучести, рассматриваемым как следствие быстро натекающей ползучести.

В [4; 5] для стареющего бетона по аналогии с уравнением Больцмана – Вольтерра предлагается линейное реологическое уравнение

$$\varepsilon(t,t_0)=\frac{\sigma(t)}{E(t)}-\int_{t_0}^{t}\sigma(\tau)\frac{\partial C^*(t,\tau)}{\partial\tau}d\tau. \tag{9}$$

А.А. Гвоздев, принимая линейную зависимость для мгновенной деформации $\varepsilon_{el}(t)=\dfrac{\sigma(t)}{E(t)}$, полагал, что ползучесть состоит из линейной части $\varepsilon_{cr}^{l}(t,t_0)=\int_{t_0}^{t}C^*(t,\tau)d\sigma(\tau)$ и нелинейной части $\varepsilon_{cr}^{nl}(t,t_0)=\int_{t_0}^{t}L(t,\tau,\sigma)d\sigma(\tau)$, порожденной структурными повреждениями [2].

В.М. Бондаренко, наряду с деформацией ползучести $\varepsilon_{cr}(t,t_0)$, полагал нелинейной зависимость и мгновенной деформации $\varepsilon_{el}(t)$ от $\sigma(t)$ и вывел нелинейное реологические уравнение [1]

$$\varepsilon(t,t_0)=\frac{S_{el}(t)}{E(t)}-\int_{t_0}^{t}S_{cr}(\tau)\frac{\partial C^*(t,\tau)}{\partial\tau}d\tau, \tag{10}$$

где $S_{el}(t)$ и $S_{cr}(\tau)$ — нелинейные функции напряжений, порождающие мгновенные и запаздывающие деформации соответственно.

В [6; 7] на основе концепции прочностной структуры бетона получена модификация принципа суперпозиции Л. Больцмана и выведено нелинейное реологическое уравнение с единой для мгновенных и запаздывающих деформаций функцией напряжений $S(t)$.

Согласно концепции прочностной структуры величина $S(\tau)$ представляет напряжение $\sigma_{str}(\tau)$, способных к силовому сопротивлению фракций бетонного элемента, названного в [6] структурным. При этом $\sigma_{str}(\tau)=S^0(\tau)\sigma(\tau)$, $S^0(\tau)$ является нелинейной функцией уровня напряжений $\eta=\dfrac{\sigma(\tau)}{R(\tau)}$ и выводится нелинейное реологическое уравнение [7–9]

$$\varepsilon(t,t_0)=\frac{S^0(t)\sigma(t)}{E(t)}-\int_{t_0}^{t}S^0(\tau)\sigma(\tau)\frac{\partial C^*(t,\tau)}{\partial\tau}d\tau. \tag{11}$$

При допущении равенств $S_{el}(t)=S_{el}^0(t)\sigma(t)$ и $S_{cr}(\tau)=S_{cr}^0(\tau)\sigma(\tau)$ уравнение (10) приводится к виду

$$\varepsilon(t,t_0)=\frac{S_{el}^0(t)\sigma(t)}{E(t)}-\int_{t_0}^{t}S_{cr}^0(\tau)\sigma(\tau)\frac{\partial C^*(t,\tau)}{\partial\tau}d\tau. \tag{12}$$

В приложениях удобна квазилинейная форма нелинейных уравнений, означающая представление деформации $\varepsilon(t,t_0)$ как произведение порожденной напряжением $\sigma(\tau)$ деформации $\varepsilon_{el}(t,t_0)$ на множитель квазилинейности $\hat{S}^0(t)$:

$$\varepsilon(t,t_0)=\hat{S}^0(t)\sigma(t)\left[\frac{1}{E(t)}-\int_{t_0}^{t}\frac{\sigma(\tau)}{\sigma(t)}\frac{\partial C^*(t,\tau)}{\partial\tau}d\tau\right]. \tag{13}$$

Из равенств (12) и (13) явствует, что $\hat{S}^0(t)$ есть решение уравнения

$$\hat{S}^0(t)\sigma(t)\left[\frac{1}{E(t)}-\int_{t_0}^{t}\frac{\sigma(\tau)}{\sigma(t)}\frac{\partial C^*(t,\tau)}{\partial\tau}d\tau\right]=\frac{S_{el}^0(t)\sigma(t)}{E(t)}-\int_{t_0}^{t}S_{cr}^0(\tau)\sigma(\tau)\frac{\partial C^*(t,\tau)}{\partial\tau}d\tau. \tag{14}$$

В [10; 11] полагают $S_{el}^o(t)=1+V_{el}\left[\eta(t)\right]^{m_{el}}$, $S_{cr}^o(t)=1+V_{cr}\left[\eta(t)\right]^{m_{cr}}$, $\hat{S}^0(t)=1+\hat{V}\left[\eta(t)\right]^{\hat{m}}$. Параметры $\hat{V}$ и $\hat{m}$ определяют согласно (14) при $\sigma(\tau)=R$ и $\sigma(\tau)=\gamma R$, $0{,}6\le\gamma\le 0{,}8$ и предъявляют равенство

$$\varepsilon(t,t_0)=\frac{\left\{1+\hat{V}\left[\eta(t)\right]^{\hat{m}}\right\}\sigma(t)}{E_l^{ep}(t,t_0)} \tag{15}$$

как квазилинейное представление нелинейного уравнения (12),

где $E_l^{ep}(t,t_0)=\left[\frac{1}{E(t)}-\int_{t_0}^{t}\frac{\sigma(\tau)}{\sigma(t)}\frac{\partial C^*(t,\tau)}{\partial\tau}d\tau\right]^{-1}$ — временный линейный модуль деформаций.

Функция $f\left[\eta(t)\right]=1+\hat{V}\left[\eta(t)\right]^{\hat{m}}$ является грубой аппроксимацией решения $\hat{S}^0(t)$ уравнения (14), и равенство (15) не выражает квазилинейное представление уравнения (12).

Таким образом, возникает задача корректного квазилинейного представления уравнений (11) и (12).

Уравнение (9) в [4; 5] выводится по приведенной выше схеме наложением деформаций $\Delta\varepsilon_{cr}(t,\tau_i)=C^*(t,\tau_i)\Delta\sigma(\tau_i)$. При этом не учитывается прочность бетона $R(\tau_i)$ в момент приложения напряжения $\Delta\sigma(\tau_i)$, что приводит к некорректному ядру ползучести в [12; 13].

Задача уточнения известных уравнений модификацией принципа суперпозиции Л. Больцмана реализуется в контексте.

З а м е ч а н и е. Нелинейные относительно $\sigma(\tau)$ уравнения состояния бетона являются линейными относительно $\sigma_{str}(\tau)$, и в релаксационных задачах нахождение $\sigma^0_{str}(t)$ осуществляется известными методами, а напряжение $\sigma^0(t)$ определяется решением уравнения $S^0\left[\dfrac{\sigma(t)}{R(t)}\right]\sigma(t)=\sigma^0_{str}(t)$ [14; 15].

Идентичность функций старения меры ползучести и модуля упругости позволяет сведение интегрального уравнения состояния к линейному дифференциальному уравнению с постоянными коэффициентами относительно деформации $\varepsilon_{el}(t)=\dfrac{\sigma_{str}(t)}{E(t)}$. Решение $\varepsilon^0_{el}(t)$ этого уравнения определяет $\sigma^0_{str}(t)=E(t)\varepsilon^0_{el}(t)$.

2. Линейные реологические уравнения состояния

Физико-механические процессы влекут изменение показателей прочности $R(\tau)$, упругости $E(\tau)$ и меры ползучести $C^*(t,\tau)$.

На основе экспериментальных данных [16] выявлена общность функций старения этих показателей и установлено равенство [17]

$$\Theta(\tau)=\frac{R(28)}{R(\tau)}. \tag{16}$$

При постоянном на интервале (t,τ) напряжении $\sigma(\tau)$

$$\varepsilon_{cr}(t,\tau)=\Theta(\tau)C_0(t,\tau)\sigma(\tau),$$

или

$$\varepsilon_{cr}(t,\tau)=C_0(t,\tau)\hat{\sigma}(\tau),\quad \hat{\sigma}(\tau)=\Theta(\tau)\sigma(\tau), \tag{17}$$

и согласно (11)

$$\varepsilon_{cr}(t,\tau)=C_0(t,\tau)R(28)\eta(\tau), \tag{18}$$

где $\eta(\tau)=\dfrac{\sigma(\tau)}{R(\tau)}$ — уровень напряжений, $\hat{\sigma}(\tau)$ — приведенное к моменту τ его приложения напряжение, $\hat{\sigma}(\tau)=R(28)\eta(\tau)$.

Приращение уровня напряжений $\Delta\eta(\tau_i)$ порождает приращение деформаций ползучести

$$\Delta\varepsilon_{cr}(t,\tau_i)=C_0(t,\tau_i)\Delta\hat{\sigma}(\tau_i)=C_0(t,\tau_i)R(28)\Delta\eta(\tau_i). \tag{19}$$

Полагая в линейной постановке зависимость приращения лишь от величины $\Delta\hat{\sigma}(\tau_i)$ и его длительности, получим аналогичное (19) равенство

$$\Delta\varepsilon_{cr}(t,t_0)=\sum_{i=1}^{n-1}C_0(t,\tau_i)\Delta\hat{\sigma}(\tau_i), \tag{20}$$

а переходя к пределу:

$$\Delta\varepsilon_{cr}(t,t_0)=\int_{t_0}^{t}C_0(t,\tau)\,d\hat{\sigma}(\tau)=\int_{t_0}^{t}C_0(t,\tau)R(28)\,d\eta(\tau). \tag{21}$$

Поскольку $d\hat{\sigma}(\tau)=\Theta(\tau)d\sigma(\tau)+\sigma(\tau)\dot{\Theta}(\tau)d\tau$, то

$$\Delta\varepsilon_{cr}(t,t_0)=\int_{t_0}^{t}C^*(t,\tau)\,d\sigma(\tau)+\int_{t_0}^{t}C_0(t,\tau)\sigma(\tau)\dot{\Theta}(\tau)\,d\tau. \tag{22}$$

Интегрируя первый интеграл по частям, получим

$$\Delta\varepsilon_{cr}(t,t_0)=-C^*(t,t_0)\sigma(t_0)-\int_{t_0}^{t}\sigma(\tau)\frac{\partial C^*(t,\tau)}{\partial\tau}d\tau+\int_{t_0}^{t}C_0(t,\tau)\sigma(\tau)\dot{\Theta}(\tau)\,d\tau. \tag{23}$$

Учитывая, что

$$\int_{t_0}^{t}\sigma(\tau)\frac{\partial C^*(t,\tau)}{\partial\tau}d\tau=\int_{t_0}^{t}\Theta(\tau)\sigma(\tau)\frac{\partial C_0(t,\tau)}{\partial\tau}d\tau+\int_{t_0}^{t}C_0(t,\tau)\sigma(\tau)\dot{\Theta}(\tau)\,d\tau$$

и уравнение (22), имеем

$$\Delta\varepsilon_{cr}(t,t_0)=-C^*(t,t_0)\sigma(t_0)-\int_{t_0}^{t}\Theta(\tau)\sigma(\tau)\frac{\partial C_0(t,\tau)}{\partial\tau}d\tau,$$

а, добавляя начальную деформацию, получим

$$\varepsilon_{cr}(t,t_0)=-\int_{t_0}^{t}\Theta(\tau)\sigma(\tau)\frac{\partial C_0(t,\tau)}{\partial\tau}d\tau. \tag{24}$$

Сумма $\varepsilon(t,t_0)=\varepsilon_{el}(t)+\varepsilon_{cr}(t,t_0)$ представляет собой линейное реологическое уравнение состояния бетона наследственной теории старения. Таким образом,

$$\varepsilon(t,t_0)=\frac{\sigma(t)}{E(t)}-\int_{t_0}^{t}\Theta(\tau)\sigma(\tau)\frac{\partial C_0(t,\tau)}{\partial\tau}d\tau. \tag{25}$$

З а м е ч а н и е. Для меры ползучести $C^*(t,\tau)=\Theta(\tau)C_0(t,\tau)$ уравнение (9) представлено в виде

$$\varepsilon(t,t_0)=\frac{\sigma(t)}{E(t)}-\int_{t_0}^{t}\Theta(\tau)\sigma(\tau)\frac{\partial C_0(t,\tau)}{\partial\tau}d\tau-\int_{t_0}^{t}C_0(t,\tau)\sigma(\tau)\dot{\Theta}(\tau)\,d\tau. \tag{26}$$

Различие уравнений (9) и (25) возникает из-за учета при выводе уравнения (25) не только величины приращения напряжения $\Delta\sigma(\tau_i)$, но и прочности $R(\tau_i)$ в момент его приложения. Этот учет реализуется при наложении частичных приращений деформации ползучести $\Delta\varepsilon_{cr}(t,\tau_i)$ согласно равенству (19), выражающему модификацию принципа суперпозиции Л. Больцмана [3].

З а м е ч а н и е. Для старого бетона величина $\dot{\Theta}(\tau)\approx 0$ и допустимо пренебречь последним слагаемым в уравнении (26).

Наряду с применением принципа наложения частичных приращений деформаций ползучести величину $\Delta\varepsilon_{cr}(t,t_0)$ можно определить путем интегрирования полного дифференциала [14]

$$d\left[C^*(t,\tau)\sigma(\tau)\right]=C^*(t,\tau)d\sigma(\tau)+\sigma(\tau)\left[\frac{\partial C^*(t,\tau)}{\partial\tau}d\tau+\frac{\partial C^*(t,\tau)}{\partial t}dt\right] \tag{27}$$

функции $\varepsilon_{cr}(t,\tau)=C^*(t,\tau)\sigma(\tau)$.

Поскольку $\int\limits_{t_0}^{t}C^*(t,\tau)d\sigma(\tau)=-C^*(t,t_0)\sigma(t_0)-\int\limits_{t_0}^{t}\sigma(\tau)\frac{\partial C^*(t,\tau)}{\partial\tau}d\tau$, с учетом (8) в результате получим

$$\Delta\varepsilon_{cr}(t,t_0)=-C^*(t,t_0)\sigma(t_0)-\int\limits_{t_0}^{t}\Theta(\tau)\sigma(\tau)\frac{\partial C_0(t,\tau)}{\partial\tau}d\tau$$

и добавлением деформаций $C^*(t,t_0)\sigma(t_0)$ и $\frac{\sigma(t)}{E(t)}$, приходим к уравнению (25).

З а м е ч а н и е. Предлагаемый способ представляет другой подход для вывода уравнения состояния (25) и формально реализует принцип наложения частичных деформаций $\frac{\Delta\sigma(\tau_i)}{E(t)}$ и $C_0(t,\tau_i)R(28)\Delta\eta(\tau_i)$ с учетом эволюции модуля упругости $E(t)$ и прочности $R(t)$.

З а м е ч а н и е. Представлением деформаций $\varepsilon(t,\tau)=\left[\frac{1}{E(t)}+C^*(t,\tau)\right]\sigma(\tau)$ в виде $\varepsilon(t,\tau)=\left[\frac{1}{E(\tau)}+C(t,\tau)\right]\sigma(\tau)$ вводится мера ползучести $C(t,\tau)$, не учитывающая эволюцию модуля упругости $E(\tau)$. Это обстоятельство влечет следующее соотношение между мерами ползучести $C^*(t,\tau)$ и $C(t,\tau)$:

$$C^*(t,\tau)=C(t,\tau)+\frac{1}{E(\tau)}-\frac{1}{E(t)}. \tag{28}$$

Согласно (28) уравнение (9) приобретает вид

$$\varepsilon(t,t_0)=\frac{\sigma(t)}{E(t)}-\int\limits_{t_0}^{t}\sigma(\tau)\frac{\partial C(t,\tau)}{\partial\tau}d\tau-\int\limits_{t_0}^{t}\sigma(\tau)\frac{\partial}{\partial\tau}\left[\frac{1}{E(\tau)}\right]d\tau. \tag{29}$$

Неизбежно возникающее при подстановке соотношения (28) в уравнение (9) слагаемое $J_0=-\int\limits_{t_0}^{t}\sigma(\tau)\frac{\partial}{\partial\tau}\left[\frac{1}{E(\tau)}\right]d\tau$ в работе [12] ошибочно объявлено лишним, что послужило поводом для заявления «Принцип наложения как основополагающая ошибка в теории ползучести…» [13].

3. Нелинейные реологические уравнения состояния

Согласно двухкомпонентной ползучести по А.А. Гвоздеву [2] при одноосном напряженном состоянии

$$\varepsilon(t,t_0)=\frac{\sigma(t)}{E(t)}-\int_{t_0}^{t}\sigma(\tau)\frac{\partial}{\partial\tau}\left[\frac{1}{E(\tau)}\right]d\tau-\int_{t_0}^{t}\sigma(\tau)\frac{\partial C(t,\tau)}{\partial\tau}d\tau-\int_{0}^{\sigma_{\max}} f(\sigma)F\left[T(\sigma,t)\right]d\sigma, \tag{30}$$

где $f(\sigma)$ — нелинейная функция напряжений, $F\left[T(\sigma,t)\right]$ — функция от суммарной длительности $T(\sigma,t)$ напряжений к моменту t.

В [4] для нелинейной теории предлагается уравнение

$$\varepsilon(t,t_0)=\frac{\sigma(t)}{E(t)}-\int_{t_0}^{t}\sigma(\tau)\frac{\partial}{\partial\tau}\left[\frac{1}{E(\tau)}\right]d\tau-\int_{t_0}^{t} f\left[\sigma(\tau)\right]\frac{\partial C(t,\tau)}{\partial\tau}d\tau. \tag{31}$$

Нелинейное реологическое уравнение состояния бетона впервые вывел В.М. Бондаренко [1]. Представленные в (10) функции $S_{el}\left[\eta(t)\right]$ и $S_{cr}\left[\eta(\tau)\right]$ в виде $S_{el}(\eta)=S_{el}^{0}(\eta)\sigma(t)$ и $S_{cr}(\eta)=S_{cr}^{0}(\eta)\sigma(\tau)$ преобразуют уравнение (10) в форму

$$\varepsilon(t,t_0)=\frac{S_{el}^{0}(\eta)\sigma(t)}{E(t)}-\int_{t_0}^{t} S_{cr}^{0}(\eta)\sigma(\tau)\frac{\partial C^{*}(t,\tau)}{\partial\tau}d\tau. \tag{32}$$

В отличие от традиционного подхода бетон рассматривается как объединение твердых фракций (зерен), соединенных упругими связями — цементными волокнами со статистически распределенными прочностями. Концепция прочностной структуры позволяет обосновать принцип наложения деформаций в нелинейной постановке [6; 7].

Структурные повреждения при неубывающем нагружении $N(\tau)$ порождают перераспределение напряжений с разрушенных связей на способные к силовому сопротивлению целые связи, увеличивая их расчетное напряжение

$$\sigma(\tau)=\frac{N(\tau)}{A} \tag{33}$$

до так называемого структурного напряжения

$$\sigma_{str}(\tau)=\frac{N(\tau)}{A(\tau)}, \tag{34}$$

где $A(\tau)$ — площадь нормального сечения целых (рабочих) в момент времени τ связей и фракций.

Согласно (33) и (34)

$$\sigma_{str}(\tau)=\frac{A}{A(\tau)}\sigma(\tau)=S^{0}(\tau)\sigma(\tau). \tag{35}$$

Функция $S^{0}(\tau)=\dfrac{A}{A(\tau)}$ определяет меру увеличения расчетного напряжения $\sigma(\tau)$ до структурного $\sigma_{str}(\tau)$ в процессе постепенного разрушения части связей. Поскольку разрушение каждой связи в момент τ зависит от ее прочности в этот момент, следовательно, мера $S^{0}(\tau)$ является функцией от уровня напряжений $\eta(\tau)=\dfrac{\sigma(\tau)}{R(\tau)}$.

Например, по П.И. Васильеву [18]:

$$S^0(\tau) = 1 + V\left[\frac{\sigma(\tau)}{R(\tau)}\right]^m, \tag{36}$$

где V и m — эмпирические коэффициенты.

Перераспределение напряжений влечет нелинейную зависимость деформаций $\varepsilon(\tau)$ от напряжений $\sigma(\tau)$ и взаимозависимость частичных приращений деформации ползучести $\Delta\varepsilon_{cr}(t,\tau_i)$ [6], ибо эффект каждого догружения $\Delta\sigma(\tau_i)$ определяется площадью рабочих фракций $A(\tau_i)$, зависящей от всех предшествующих догружений $\Delta\sigma(\tau_j)$, $j \le i$.

Реологическое уравнение описывает напряженно-деформированное состояние целых на промежутке (t_0, t) связей и фракций, объединение которых образует рабочую часть V_t бетонного элемента V.

Приращение $\Delta\sigma_{str}(\tau_i)$ не разрушает связи и фракции V_t, и именно это влечет независимость приращений деформаций ползучести в момент τ_i:

$$\Delta\varepsilon_{cr}(t,\tau_i) = C_0(t,\tau_i)\Delta\sigma_{str}(\tau_i) \tag{37}$$

от остальных приращений в момент τ_j $(i \ne j)$, а потому

$$\Delta\varepsilon_{cr}(t,t_0) = \sum_{i=1}^{n-1} C_0(t,\tau_i)\Delta\sigma_{str}(\tau_i). \tag{38}$$

Соотношение (38) является аналогом принципа наложения Л. Больцмана в нелинейной постановке и приводит к уравнениям состояния для нестареющего бетона

$$\varepsilon(t,t_0) = \frac{\sigma_{str}(t)}{E} - \int_{t_0}^{t} \sigma_{str}(\tau)\frac{\partial C_0(t,\tau)}{\partial\tau}d\tau \tag{39}$$

или

$$\varepsilon(t,t_0) = \frac{S^0(t)\sigma(t)}{E} - \int_{t_0}^{t} S^0(\tau)\sigma(\tau)\frac{\partial C_0(t,\tau)}{\partial\tau}d\tau. \tag{40}$$

По аналогии с линейной постановкой получим нелинейное уравнение состояния для стареющего бетона:

$$\varepsilon(t,t_0) = \frac{\sigma_{str}(t)}{E(t)} - \int_{t_0}^{t} \Theta(\tau)\sigma_{str}(\tau)\frac{\partial C_0(t,\tau)}{\partial\tau}d\tau. \tag{41}$$

Расчетная модель структуры бетона в статистической теории прочности представляется набором зерен, соединенных неравновесными связями, прочность которых является случайной величиной. Эта модель восходит к Вейбулу [19] и развита в [20; 21].

Гипотеза, что в процессе нагружения $N(\tau)$ связи деформируются линейно с одинаковым модулем упругости, приводит к линейной диаграмме $\sigma - \varepsilon$. Экспериментальные диаграммы, для построения которых используются напряжения $\sigma(\tau)$, не зависящие от площади рабочих связей $A(\tau)$, получаются нелинейными. По концепции прочностной структуры бетона зависимость $\sigma_{str}(t)$ и $\varepsilon(t)$ является линейной и отношение $\varepsilon(t)=\dfrac{\sigma_{str}(t)}{E(t)}$ на диаграмме изображается прямой, названной в [22; 23] фиктивной диаграммой.

Замечание. С позиции прочностной структуры бетона эта прямая представляет графическую интерпретацию деформирования целых на отрезке $[0,t]$ связей при неубывающем нагружении.

Замечание. При разгружении работают лишь целые связи и экспериментально построенный параллельный фиктивной (согласно [22; 23]) диаграмме отрезок подтверждает линейную зависимость $\sigma_{str}(t)$ от $\varepsilon(t)$.

4. Квазилинейные представления уравнений состояния

Согласно равенствам $\Theta(\tau)\sigma(\tau)\dfrac{\partial C_0(t,\tau)}{\partial\tau}=-\sigma(\tau)\dfrac{\partial C^*(t,\tau)}{\partial t}$ и $\sigma_{str}(\tau)=S^0(\tau)\sigma(\tau)$ уравнения (25) и (41) представлены в виде

$$\varepsilon(t,t_0)=\sigma(t)\left[\frac{1}{E(t)}+\int_{t_0}^{t}\frac{\sigma(\tau)}{\sigma(t)}\frac{\partial C^*(t,\tau)}{\partial t}d\tau\right], \tag{42}$$

$$\varepsilon(t,t_0)=S^0(t)\sigma(t)\left[\frac{1}{E(t)}+\int_{t_0}^{t}\frac{S^0(\tau)\sigma(\tau)}{S^0(t)\sigma(t)}\frac{\partial C^*(t,\tau)}{\partial t}d\tau\right]. \tag{43}$$

Введем величины $\tilde{\delta}_l(t,t_0)$ и $\tilde{\delta}_{nl}(t,t_0)$, представляющие собой линейные и нелинейные податливости соответственно. Тогда на основании уравнений (42) и (43) получим временные упругопластические модули в линейной и нелинейной поставках:

$$\tilde{E}_l^{ep}(t,t_0)=\frac{1}{\tilde{\delta}_l(t,t_0)}=\left[\frac{1}{E(t)}+\int_{t_0}^{t}\frac{\sigma(\tau)}{\sigma(t)}\frac{\partial C^*(t,\tau)}{\partial t}d\tau\right]^{-1}, \tag{44}$$

$$\tilde{E}_{nl}^{ep}(t,t_0)=\frac{1}{\tilde{\delta}_{nl}(t,t_0)}=\left[\frac{1}{E(t)}+\int_{t_0}^{t}\frac{S^0(\tau)\sigma(\tau)}{S^0(t)\sigma(t)}\frac{\partial C^*(t,\tau)}{\partial t}d\tau\right]^{-1}. \tag{45}$$

Уравнению (25), представленному в виде

$$\varepsilon(t,t_0)=\sigma(t)\left[\frac{1}{E(t)}-\int_{t_0}^{t}\Theta(\tau)\frac{\sigma(\tau)}{\sigma(t)}\frac{\partial C_0(t,\tau)}{\partial t}d\tau\right]=\sigma(t)\delta_l(t,t_0), \tag{46}$$

соответствует временный линейный модуль

$$E_l^{ep}(t,t_0)=\frac{1}{\delta_l(t,t_0)}=\left[\frac{1}{E(t)}-\int_{t_0}^{t}\Theta(\tau)\frac{\sigma(\tau)}{\sigma(t)}\frac{\partial C_0(t,\tau)}{\partial\tau}d\tau\right]^{-1}, \tag{47}$$

а в нелинейной постановке — временный модуль

$$E_{nl}^{ep}(t,t_0)=\frac{1}{\delta_{nl}(t,t_0)}=\left[\frac{1}{E(t)}-\int_{t_0}^{t}\Theta(\tau)\frac{S^0(\tau)\sigma(\tau)}{S^0(t)\sigma(t)}\frac{\partial C_0(t,\tau)}{\partial\tau}d\tau\right]^{-1}. \quad (48)$$

Согласно (43) и (45) при суперпозиции по приращениям уровня напряжений

$$\varepsilon(t,t_0)=\frac{S^0(t)\sigma(t)}{\tilde{E}_{nl}^{ep}(t,t_0)}, \quad (49)$$

а при суперпозиции по приращениям напряжений

$$\varepsilon(t,t_0)=\frac{S^0(t)\sigma(t)}{E_{nl}^{ep}(t,t_0)}. \quad (50)$$

Представления деформации $\varepsilon(t,t_0)$ в нелинейной постановке

$$\varepsilon(t,t_0)=\frac{\tilde{S}^0(t)\sigma(t)}{\tilde{E}_{l}^{ep}(t,t_0)}, \quad (51)$$

$$\varepsilon(t,t_0)=\frac{\hat{S}^0(t)\sigma(t)}{E_{l}^{ep}(t,t_0)} \quad (52)$$

с соответствующими функциями квазилинейности $\tilde{S}^0(t)$ и $\hat{S}^0(t)$ называются квазилинейными.

При постоянном на отрезке $[t_0,t]$ напряжении $\sigma(\tau)$

$$\tilde{S}^0(t)=S^0(t), \quad \hat{S}^0(t)=S^0(t), \quad (53)$$

а при неубывающем $\sigma(\tau)$ эти функции определяются из равенств

$$\tilde{S}^0(t)\tilde{\delta}_l(t,t_0)=S^0(t)\tilde{\delta}_{nl}(t,t_0), \quad \hat{S}^0(t)\delta_l(t,t_0)=S^0(t)\delta_{nl}(t,t_0). \quad (54)$$

Согласно (54) и равенствам (42)–(45)

$$\tilde{S}^0(t)=S^0(t)\frac{\tilde{E}_{l}^{ep}(t,t_0)}{\tilde{E}_{nl}^{ep}(t,t_0)}, \quad \hat{S}^0(t)=S^0(t)\frac{E_{l}^{ep}(t,t_0)}{E_{nl}^{ep}(t,t_0)}. \quad (55)$$

При неубывающем напряжении $\sigma(\tau)$ имеем $S^0(\tau)<S^0(t)$, а потому $\tilde{\delta}_{nl}(t,t_0)<\tilde{\delta}_l(t,t_0)$ и $\tilde{E}_{nl}^{ep}(t,t_0)>\tilde{E}_{l}^{ep}(t,t_0)$. Аналогично получим $E_{nl}^{ep}(t,t_0)>E_{l}^{ep}(t,t_0)$ и с учетом (55)

$$\tilde{S}^0(t)<S^0(t), \quad \hat{S}^0(t)<S^0(t). \quad (56)$$

Согласно $\hat{S}^0(t)<S^0(t)$ представление $\varepsilon(t,t_0)$ в виде

$$\varepsilon(t,t_0)=\frac{S^0(t)\sigma(t)}{E_{l}^{ep}(t,t_0)}, \quad (57)$$

предъявляемое как квазилинейное, получается из квазилинейного

$$\varepsilon(t,t_0)=\frac{\hat{S}^0(t)\sigma(t)}{E_l^{ep}(t,t_0)} \tag{58}$$

заменой $\hat{S}^0(t)$ на $S^0(t)$, что в силу (55) эквивалентно замене $E_{nl}^{ep}(t,t_0)$ на $E_l^{ep}(t,t_0)$.

Равенством (57) согласно (55) дается оценка величины $\varepsilon(t,t_0)$ сверху.

Замечание. При $S^0(\tau)=S^0\left[\eta(\tau)\right]=1+V\left[\frac{\sigma(\tau)}{R(\tau)}\right]^m$ равенство (57) при напряжениях $\sigma(\tau)$, близких к $R(\tau)$, является аппроксимацией квазилинейного представления.

Идея квазилинейного представления деформации $\varepsilon(t,t_0)$ для согласования уравнений с экспериментальными данными принадлежит Ю.Н. Работнову [24], предложившему для нестареющего бетона $\left(E(\tau)=E,\ \Theta(\tau)=1\right)$ уравнение

$$S\left[\varepsilon(t,t_0)\right]=\frac{\sigma(t)}{E}-\int_{t_0}^{t}\sigma(\tau)\frac{\partial C_0(t,\tau)}{\partial\tau}d\tau. \tag{59}$$

Замечание. В [24] принимается одинаковость функций нелинейности напряжений $S_{el}^o(\tau)$ и $S_{cr}^o(\tau)$. Это коррелирует с прочностной структурой бетона, согласно которой функции напряжений $S_{el}(\tau)$ и $S_{cr}(\tau)$ представляют структурное напряжение $\sigma_{str}(\tau)=S^0(\tau)\sigma(\tau)$. Из $S_{el}(\tau)=\sigma_{str}(\tau)$ и $S_{cr}(\tau)=\sigma_{str}(\tau)$ следует $S_{el}(\tau)=S_{cr}(\tau)=S^0(\tau)\sigma(\tau)$, а потому $S_{el}(\tau)=S_{cr}(\tau)=S^0(\tau)$.

В [1] функции $S_{el}(\tau)$ и $S_{cr}(\tau)$ принимаются в форме [18]:

$$S_{el}^o\left[\eta(\tau)\right]=1+V_e\left[\eta(\tau)\right]^{m_e}, \tag{60}$$

$$S_{cr}^o\left[\eta(\tau)\right]=1+V_c\left[\eta(\tau)\right]^{m_c}, \tag{61}$$

где V_e, V_c, m_e, m_c — эмпирические коэффициенты.

Принятие в равенстве $S_{cr}(\tau)=S^0(\tau)\sigma(\tau)$ функции $S^0(\tau)$ в аналогичной форме (по П.И. Васильеву [18]) естественно, ибо $S^0(\tau)=\frac{A}{A(\tau)}$ и соответствующая при напряжениях $\sigma(\tau)$ целым фракциям площадь $A(\tau)$ определяется условием $R_i(\tau)\geq\sigma(\tau)$, что эквивалентно $\frac{R_i(\tau)}{R(\tau)}\geq\frac{\sigma(\tau)}{R(\tau)}$.

При постоянном на отрезке времени $[t_0,t]$ напряжении $\sigma(\tau)$, согласно [1]

$$\varepsilon(t,t_0)=\frac{S_{el}^0(\eta)\sigma(t)}{E(t)}+C^*(t,t_0)S_{cr}^0(\eta)\sigma(t). \tag{62}$$

Полагая, что постоянное на (t_0,t) напряжение $\sigma_{str}(\tau)=S^0(\eta)\sigma(\tau)$ порождает такую же деформацию, получим

$$\varepsilon(t,t_0)=\frac{S^0(\eta)\sigma(t)}{E(t)}+C^*(t,t_0)S^0(\eta)\sigma(t). \tag{63}$$

Согласно уравнениям (62) и (63)

$$S^0(\eta)\left[\frac{1}{E(t)}+C^*(t,t_0)\right]=\frac{S_{el}^0(\eta)}{E(t)}+C^*(t,t_0)S_{cr}^0(\eta)$$

и

$$S^0(\eta)=\frac{S_{el}^0(\eta)+S_{cr}^0(\eta)E(t)C^*(t,t_0)}{1+E(t)C^*(t,t_0)}. \tag{64}$$

Из равенств (60), (61), (36) и (64) при $\eta=1$ получим

$$S^0(1)=1+V=\frac{1+V_e+(1+V_c)E(t)C^*(t,t_0)}{1+E(t)C^*(t,t_0)}, \tag{65}$$

$$V=S^0(1)-1. \tag{66}$$

При некотором $0<\eta_0<1$ имеем $V\eta_0^m=S^0(\eta_0)-1$, $\eta_0^m=\dfrac{S^0(\eta_0)-1}{V}$, $m\ln\eta_0=\ln\dfrac{S^0(\eta_0)-1}{S^0(1)-1}$ и

$$m=\frac{1}{\ln\eta_0}\ln\frac{S^0(\eta_0)-1}{S^0(1)-1}. \tag{67}$$

З а м е ч а н и е. Определенная по заданным функциям $S_{el}^o(\eta)$ и $S_{cr}^o(\eta)$ функция $S^0(\eta)$ не обеспечивает квазилинейное представление $\varepsilon(t,t_0)$ при $\sigma(\tau)\neq\text{const}$. Кроме того, не исключено, что наблюдаемое различие V_e и V_c, m_e и m_c в уравнениях (60) и (61) принадлежит диапазону погрешностей измерений.

Согласно (59) имеет место равенство

$$S\left[\varepsilon(t,t_0)\right]=\varepsilon_l(t,t_0). \tag{68}$$

При $S\left[\varepsilon(t,t_0)\right]=\dfrac{\varepsilon_l(t,t_0)}{S_{el}^0(t)}$, где $S_{el}^0(t)$ (с учетом $E(t)=E$ и $\Theta(\tau)=1$) определяется вторым из равенств (55), получим квазилинейное представление

$$\varepsilon(t,t_0)=\frac{\hat{S}^0(t)\sigma(t)}{E_l^{ep}(t,t_0)}. \tag{69}$$

Для реологического уравнения состояния бетона [1]

$$e^{-\varepsilon(t,t_0)/\varepsilon_R(t)}\varepsilon(t,t_0)=\sigma(t)\left[\frac{1}{E(t)}-\int_{t_0}^{t}\frac{\sigma(\tau)}{\sigma(t)}\frac{\partial C^*(t,\tau)}{\partial\tau}d\tau\right]. \tag{70}$$

$\varepsilon(t,t_0)=e^{\varepsilon(t,t_0)/\varepsilon_R(t)}\varepsilon_l(t,t_0)$ и квазилинейное представление

$$\varepsilon\left(t,t_0\right)=\frac{e^{\varepsilon\left(t,t_0\right)/\varepsilon_R\left(t\right)}\sigma\left(t\right)}{E_l^{ep}\left(t,t_0\right)} \tag{71}$$

при кратковременном нагружении, полагая $\varepsilon\left(t,t_0\right)=\varepsilon$, $\sigma\left(t\right)=\sigma$, $R\left(t\right)=R$, $E_l^{ep}\left(t,t_0\right)=E$, согласно (71) получим функцию

$$\sigma=E\varepsilon e^{-\varepsilon/\varepsilon_R}\ , \tag{72}$$

описывающую диаграмму $\sigma-\varepsilon$ (включая ниспадающую ветвь) в форме В.М. Бондаренко [1].

При $\sigma=R$ имеем $R=E\varepsilon_R e^{-1}$ и $E=eR/\varepsilon_R$, а потому

$$\sigma=\frac{eR}{\varepsilon_R}\varepsilon e^{-\varepsilon/\varepsilon_R}\ ,\quad \frac{\sigma}{R}=\frac{\varepsilon}{\varepsilon_R}e^{1-\varepsilon/\varepsilon_R}\ . \tag{73}$$

Величины η и ξ являются уровнями напряжений и деформаций, а равенство

$$\eta=\xi e^{1-\xi} \tag{74}$$

представляет уравнение состояния бетона, описываемое в параметрах η и ξ.

При $\hat{S}^0\left(t\right)=e^{m^{-1}\left[\varepsilon\left(t,t_0\right)/\varepsilon_R\left(t\right)\right]^m}$ диаграмма $\sigma-\varepsilon$ получается в виде $\sigma=E\dfrac{\varepsilon}{\varepsilon_R}e^{m^{-1}\left(\varepsilon/\varepsilon_R\right)^m}$ [25], а параметрическое уравнение

$$\eta=\xi e^{m^{-1}-\xi}. \tag{75}$$

Если диаграмма $\sigma-\varepsilon$ задается согласно $\sigma=R\sum\limits_{i=1}^{n}a_i\left(\varepsilon/\varepsilon_R\right)^i$ [26], то соответствующее параметрическое уравнение имеет вид

$$\eta=\sum_{i=1}^{n}a_i\xi^i\ . \tag{76}$$

Зависимость $\sigma-\varepsilon$ на плоскости в координатах $\left(\varepsilon,\sigma\right)$ изображается графиком функции $\sigma=f\left(\varepsilon\right)$. Длительное нагружение описывается функцией $\sigma=\varphi\left[t,\varepsilon\left(t\right)\right]$, которой отвечает поверхность в координатах $\left(t,\varepsilon,\sigma\right)$. Ее пересечением с плоскостью $\tau=t$ (параллельной плоскости $\varepsilon-\sigma$) является кривая Γ_t, по которой, с учетом того, что $\xi=\varepsilon\left(t,t_0\right)/\varepsilon_R\left(t\right)$ и $\eta=\sigma\left(t\right)/R\left(t\right)$, строится кривая $\tilde{\Gamma}_t$ на плоскости $\varepsilon-\sigma$. Эта кривая описывает диаграмму $\sigma-\varepsilon$, а соответствующая функция $\eta=F\left(\xi\right)$ представляет собой параметрическое уравнение состояния.

Таким образом, параметры η и ξ для неравновесного процесса деформирования являются аналогами параметров σ и ε для равновесных механических систем.

З а м е ч а н и е. Структура параметрического уравнения, определяемая функцией $\hat{S}^0\left(t\right)$, не зависит от режима нагружения. Это позволяет по найденным при кратковременном нагружении значениям η и ξ определить параметры $\sigma\left(t\right)=\eta R\left(t\right)$ и $\varepsilon\left(t,t_0\right)=\xi\varepsilon_R\left(t\right)$ длительного нагружения.

Параметрическое уравнение (74) при условии идентичности $S_{el}^0\left(t\right)$ и $S_{cr}^0\left(t\right)$ вывел В.Г. Назаренко, рассматривая состояние бетона как состояние неравновесной термодинамической системы

[27]. Параметры η и ξ, характеризующие прочностные и деформационные свойства бетона, связываются с помощью его удельной энергии целостности $W(t)$ [28]. Величина $W(t)$ является максимальным энергетическим ресурсом сопротивления деформированию единицы объема бетона и представляется площадью, ограниченной полной диаграммой $\sigma - \varepsilon$ фигуры.

Адаптация теории ползучести к методу конечных элементов при формулировке уравнений ползучести в приращениях выполнена в монографии [29].

5. Заключение

В результате проведенного исследования авторами сделан ряд выводов.

1. Наложением частичных приращений деформаций, порожденных последовательными приращениями уровня напряжений, выведены уравнения механического состояния бетона. Учет прочности бетона в моменты приложения нагружения уточняет его известные уравнения состояния в линейной и нелинейной постановке.

2. Общий для мгновенных и запаздывающих деформаций множитель нелинейности напряжений превышает множитель квазилинейности, умножением на который линейной части деформации получается ее квазилинейное представление. Делением нелинейной деформации на эти множители выделяются соответственно обратимая и линейная ее части.

3. Обратимые деформации реализуются целыми до момента начала разгружения связями за счет накопленного ими приращения потенциальной энергии при нагружении. Отсутствие в процессе разгружения перераспределения напряжений между этими связями влечет линейную зависимость напряжений от деформаций. Это обосновывает наблюдаемый в экспериментах факт, известный как признак Ясинского — Энгессера.

4. Отмеченная выше некорректность уравнений механического состояния бетона порождена не принципом наложения деформаций, а его реализацией по приращениям напряжений как для идеального бетона. Наложение деформаций по приращениям уровня напряжений приводит к корректным уравнениям состояния, что означает необоснованность заявлений об ошибочности принципа наложения.

5. Правомерность принципа наложения в теории ползучести бетона создает возможность применения этой теории в расчетах бетонных и железобетонных конструкций методом конечных элементов.

Список литературы

1. *Бондаренко В.М., Бондаренко С.В.* Инженерные методы нелинейной теории железобетона. Москва : Стройиздат, 1982. 287 с.

2. *Галустов К.З.* Нелинейная теория ползучести бетона и расчет железобетонных конструкций. Москва : Физматлит, 2006. 248 с. ISBN 5-94052-116-9 EDN: QNMEHH

3. *Boltzmann L.* Zur theorie der elastischen nachwirkung // Sitzungsberichte Kaiserliche Akademie wissenhaft Wien Mathematische-Naturwissenhaft. 1874. Vol. 70. No. 2. P. 275–305. https://doi.org/10.1002/andp.18782411107

4. *Арутюнян Н.Х.* Ползучесть стареющих материалов. Ползучесть бетона // Механика в СССР за 50 лет. 1972. Т. 3. С. 155–202.

5. *Арутюнян Н.Х., Колмановский В.Б.* Теория ползучести неоднородных тел. Москва : Наука, 1983. 336 с.

6. *Ларионов Е.А., Бондаренко В.М.* Принцип наложения деформаций при структурных повреждениях элементов конструкций // Строительная механика инженерных конструкций и сооружений. 2011. № 2. С. 16–22. EDN: NUCYYV

7. *Ларионов Е.А., Ларионов А.Е.* К теории нелинейной ползучести // Строительная механика и расчет сооружений. 2015. № 2 (259). С. 58–65. EDN: TQATUF

8. *Ларионов Е.А., Рынковская М.И., Гринько Е.А.* Реологические уравнения состояния бетона и релаксация напряжений // Строительная механика инженерных конструкций и сооружений. 2022 Т. 18 № 1. С. 22–34. http://doi.org/10.22363/1815-5235-2022-18-1-22-34 EDN: WXGEUF

9. *Ларионов Е.А., Маркович А.С., Алешина О.О.* Принцип наложения деформаций в теории железобетона // Строительная механика и расчет сооружений. 2024. № 3 (314). С. 2–12. http://doi.org/10.37538/0039-2383.2024.3.2.12 EDN: KITWID

10. *Бондаренко В.М.* Элементы диссипативной теории силового сопротивления железобетона // Строительная механика инженерных конструкций и сооружений. 2014. № 2. С. 47–57. EDN: RZRQOF

11. *Бондаренко В.М., Римшин В.И.* Квазилинейные уравнения силового сопротивления и диаграмма σ — ε бетона // Строительная механика инженерных конструкций и сооружений. 2014. № 6. С. 40–44. EDN: SYZJHL

12. *Санжаровский Р.С., Манченко М.М.* Ошибки в теории ползучести железобетона и современные нормы // Строительная механика инженерных конструкций и сооружений. 2016. № 3. С. 25–32. EDN: VUCZKL

13. *Санжаровский Р.С., Тер-Эммануильян Т.Н., Манченко М.М.* Принцип наложения как основополагающая ошибка теории ползучести и стандартов по железобетону // Строительная механика инженерных конструкций и сооружений. 2018. Т. 14. № 2. С. 92–104. http://doi.org/10.22363/1815-5235-2018-14-2-92-104 EDN: XQIAXR

14. *Larionov E.A., Nazarenko V.G., Rynkovskaya M.I., Grinko E.A.* Relaxation of stress in elements of reinforced concrete structures // Structural Mechanics of Engineering Constructions and Buildings. 2022. Vol. 18. No. 6. P. 534–543. http://doi.org/10.22363/1815-5235-2022-18-6-534-543

15. *Ларионов Е.А., Маркович А.С., Гринько Е.А.* Релаксация напряжений в железобетонных элементах конструкций // Строительная механика и расчет сооружений. 2024. № 1. С. 32–38. http://doi.org/10.37538/0039-2383.2024.1.32.38 EDN: KDMPWU

16. *Александровский С.В., Соломонов С.В.* Зависимость деформаций ползучести бетона от начального уровня напряжений // Межотраслевые вопросы строительства. 1972. № 6. С. 6–12.

17. *Назаренко В.Г., Звездов А.И., Ларионов Е.А., Квасников А.А.* Некоторые аспекты теории ползучести бетона // Бетон и железобетон. 2021. № 603 (1). С. 40–43. EDN: RNJWLR

18. *Васильев П.И.* К вопросу о выборе феноменологической теории ползучести бетона // Ползучесть строительных материалов и конструкций: Москва : Стройиздат. 1964. С. 106–114.

19. *Weibull W.A.* Statistical representation of fatigue failures in solids // Transactions of the Royal Institute of Technology. Göteborg: Elanders boktr., 1949. 49 p.

20. *Болотин В.В.* Некоторые вопросы теории хрупкого разрушения. Расчеты на прочность. Москва : Машиностроение. 1962. Вып. 8. С. 36–52.

21. *Харлаб В.Д.* Обобщение вейбуловской статистической теории хрупкого разрушения // Механика стержневых систем и сплошных сред. 1987. № 11. С. 150–152.

22. *Санжаровский Р.С., Манченко М.М.* Ползучесть бетона и его мгновенная нелинейность деформирования в расчетах конструкций // Строительная механика инженерных конструкций и сооружений. 2015. № 2. С. 33–40. EDN: TNEVQL

23. *Беглов А.Д., Санжаровский Р.С., Тер-Эммануильян Т.Н.* Современная теория ползучести железобетона // Строительная механика инженерных конструкций и сооружений. 2024. Т. 20. № 1. С. 3–13. http://doi.org/10.22363/1815-5235-2024-20-1-3-13 EDN: WVKFJM

24. *Работнов Ю.Н.* Ползучесть элементов конструкций. Москва : Наука, 1966. 752 с.

25. *Маилян Д.Р.* Влияние армирования и эксцентриситета сжимающего усилия на деформативность бетона и характер диаграммы сжатия // Вопросы прочности, деформативности и трещиностойкости железобетона. Ростов-на-Дону, 1979. С.70–82.

26. *Бамбура А.Н.* Диаграмма напряжение — деформация для бетона при центральном сжатии // Вопросы прочности, деформативности и трещиностойкости железобетона : сб. науч. тр. Ростов-на-Дону : РИСИ, 1980. С. 19–22.

27. *Назаренко В.Г., Боровских А.В.* Диаграмма деформирования бетонов с учетом ниспадающей ветви // Бетон и железобетон. 1999. № 2. С. 18–22. URL: https://science.totalarch.com/magazine/concrete/concrete_1999_02.pdf (дата обращения: 12.07.2025).

28. *Ларионов Е.А.* К вопросу о длительной прочности бетона // Известия высших учебных заведений. Строительство. 2005. № 8 (560). С. 28–33. EDN: PFAILF

29. *Агапов В.П., Маркович А.С.* Нелинейные модели бетонных и железобетонных конструкций. Теория и реализация в ВК ПРИНС. Москва : РУДН, 2023. 263 с. ISBN 978-5-209-11784-1

References

1. Bondarenko V.M., Bondarenko S.V. *Engineering methods of nonlinear theory of reinforced concrete*. Moscow: Strojizdat Publ.; 1982. (In Russ.)

2. Galustov K.Z. *Nonlinear theory of concrete creep and calculation of reinforced concrete structures*. Moscow: Fizmatlit Publ.; 2006. (In Russ.) ISBN 5-94052-116-9 EDN QNMEHH

3. Boltzmann L. On the theory of elastic aftereffects. *Proceedings of the Imperial Academy of Sciences Vienna, mathematical and natural sciences*. 1874;70(2):275–305. (In German)

4. Arutyunyan N.Kh. Creep of aging materials. Creep of concrete. *Mechanics in the USSR for 50 years*. 1972;3:155–202. (In Russ.)

5. Arutyunyan N.Kh., Kolmanovsky V.B. *Theory of creep of inhomogeneous bodies*. Moscow: Nauka Publ.; 1983. (In Russ.)

6. Larionov E.A., Bondarenko V.M. Strains superposition principle when construction elements have structural damages. *Structural Mechanics of Engineering Constructions and Buildings*. 2011;(2):16–22. (In Russ.) EDN NUCYYV

7. Larionov E.A., Larionov A.E. On the theory of nonlinear creep. *Structural Mechanics and Analysis of Constructions*. 2015;(2):58–65. (In Russ.) EDN TQATUF

8. Larionov E.A., Rynkovskaya M.I., Grinko E.A. Rheological equations of concrete state and relaxation of stress. *Structural Mechanics of Engineering Constructions and Buildings*. 2022;18(1):22–34. (In Russ.) http://doi.org/10.22363/1815-5235-2022-18-1-22-34

9. Larionov E.A., Markovich A.S., Aleshina O.O. The principle of superposition of deformations in the theory of reinforced concrete. *Structural Mechanics and Analysis of Constructions*. 2024;3(314):2–12. (In Russ.) http://doi.org/10.37538/0039-2383.2024.3.2.12 EDN KITWID

10. Bondarenko V.M. Elements of the dissipative theory of force resistance of reinforced concrete. *Structural Mechanics of Engineering Constructions and Buildings*. 2014;(2):47–57. (In Russ.) EDN RZRQOF

11. Bondarenko V.M., Rimshin V.I. Quasilinear equations of force resistance and the σ — ε diagram of concrete. *Structural Mechanics of Engineering Constructions and Buildings*. 2014;(6):40–44. (In Russ.) EDN SYZJHL

12. Sanzarovsky R.S., Manchenko M.M. Errors in the concrete theory and creepmodern regulations. *Structural Mechanics of Engineering Constructions and Buildings*. 2016;(3):25–32. (In Russ.) EDN VUCZKL

13. Sanzharovsky R.S., Ter-Emmanuilyan T.N., Manchenko M.M. Superposition principle as the fundamental error of the creep theory and standards of the reinforced concrete. *Structural Mechanics of Engineering Constructions and Buildings*. 2018;14(2):92–104. (In Russ.) http://doi.org/10.22363/1815-5235-2018-14-2-92-104

14. Larionov E.A., Nazarenko V.G., Rynkovskaya M.I., Grinko E.A. Relaxation of stress in elements of reinforced concrete structures. *Structural Mechanics of Engineering Constructions and Buildings.* 2022;18(6):534–543. http://doi.org/10.22363/1815-5235-2022-18-6-534-543

15. Larionov E.A., Markovich A.S., Grinko E.A. Relaxation of stress in elements of reinforced concrete structures. *Structural Mechanics and Analysis of Constructions*. 2024;(1):32–38. (In Russ.) http://doi.org/10.37538/0039-2383.2024.1.32.38 EDN KDMPWU

16. Aleksandrovsky S.V., Solomonov S.V. Dependence of concrete creep deformations on the initial stress level. *In the collection of inter-industry issues in construction*. 1972;(6):6–12. (In Russ.)

17. Nazarenko V.G., Zvezdov A.I., Larionov E.A., Kvasnikov A.A. Some aspects of the concrete creep theory. *Concrete and Reinforced Concrete*. 2021;603(1):40–43. (In Russ.)

18. Vasiliev P.I. *On the issue of choosing a phenomenological theory of concrete creep*. In the book Creep of building materials and structures. Moscow: Stroyizdat Publ.; 1964. p. 106–114.

19. Weibull W.A. *Statistical representation of fatigue failures in solids.* Transactions of the Royal Institute of Technology. Gothenburg: Elanders Bookstore; 1949.

20. Bolotin V.V. *Some questions of the theory of brittle fracture*. Strength calculations, Moscow: Mashinostroenie Publ.; 1962. Vol. 8. p. 36–52. (In Russ.)

21. Kharlab V.D. Generalization of Weibull statistical theory of brittle fracture. *Mechanics of Rod Systems and Continuous Media*. 1987;(11):150–152.

22. Sanzarovsky R.S., Manchenko M.M. The creep of concrete and its instantaneous nonlinearity of deformation in the structural calculations. *Structural Mechanics of Engineering Constructions and Buildings*. 2015;(2):33–40.

23. Beglov A.D., Sanjarovskiy R.S., Ter-Emmanuilyan T.N. Modern theory of creep of reinforced concrete. *Structural Mechanics of Engineering Constructions and Buildings*. 2024;20(1):3–13. (In Russ.) http://doi.org/10.22363/1815-5235-2024-20-1-3-13

24. Rabotnov Yu.N. *Creep of structural elements*. Moscow: Nauka Publ.; 1966. (In Russ.)

25. Mailyan D.R. *Effect of reinforcement and eccentricity of compressive force on the deformability of concrete and the nature of the compression diagram*. In the book. Issues of strength, deformability and crack resistance of reinforced concrete, Rostov-on-Don, 1979:70–82. (In Russ.)

26. Bambura A.N. Stress-strain diagram for concrete under central compression. *Issues of strength, deformability and crack resistance of reinforced concrete: Collection of scientific papers.* Rostov-on-Don: RISI Publ.; 1980. P. 19–22. (In Russ.)

27. Nazarenko V.G., Borovskikh A.V. Concrete deformation diagram taking into account the falling branch. *Concrete and Reinforced Concrete*. 1999;(2):18–22. (In Russ.) Available from: https://science.totalarch.com/magazine/concrete/concrete_1999_02.pdf (accessed: 12.07.2025).

28. Larionov E.A. On the issue of long-term strength of concrete. *News of Higher Educational Institutions. Construction.* 2005;8(560):28–33. (In Russ.) EDN PFAILF

29. Agapov V.P., Markovich A.S. *Nonlinear models of concrete and reinforced concrete structures. Theory and implementation in PRINS software:* monograph. Moscow: RUDN, 2023. (In Russ.) ISBN 978-5-209-11784-1

СТРОИТЕЛЬНАЯ МЕХАНИКА ИНЖЕНЕРНЫХ КОНСТРУКЦИЙ И СООРУЖЕНИЙ
STRUCTURAL MECHANICS OF ENGINEERING CONSTRUCTIONS AND BUILDINGS

2025. 21(5). 432–440

ISSN 1815-5235 (Print), 2587-8700 (Online)
HTTP://JOURNALS.RUDN.RU/STRUCTURAL-MECHANICS

DOI: 10.22363/1815-5235-2025-21-5-432-440
EDN: EDACPF

Research article / Научная статья

Fracture Mechanics of a Three-Layer Wall Panel Based on Two-Stage Concrete

Alexey O. Syromyasov[1]✉, Yuri A. Makarov[1], Tatiana F. Elchishcheva[2], Vladimir T. Erofeev[3], Dmitry A. Kozhanov[4]

[1] National Research Mordovian State University named after N.P. Ogarev, *Saransk, Russian Federation*
[2] Tambov State Technical University, *Tambov, Russian Federation*
[3] National Research Moscow State University of Civil Engineering, *Moscow, Russian Federation*
[4] Nizhny Novgorod State University of Architecture and Civil Engineering, *Nizhny Novgorod, Russian Federation*
✉ syal1@yandex.ru

Received: July 17, 2025
Revised: September 10, 2025
Accepted: September 19, 2025

Abstract. Stress distribution in a three-layer wall panel based on two-stage concrete with rigid contact between the layers is modelled. The calculation is performed in ANSYS Workbench finite-element software. Values of failure criteria (principal stress and equivalent stress) are calculated near stress concentrators, i.e. edges separating the loaded and fixed faces of the panel. It is obtained that fracture begins at the boundary between the loaded and non-loaded layers of the structure. It is shown that the thermal insulation layer made of porous concrete in the center of the panel can carry part of the load acting on the bearing layer. So, structures made using the two-stage technology may withstand loads that are higher compared to that of panels with flexible ties. Moreover, it is shown that thermal resistance of the three-layer two-stage concrete panel is twice as high as for a single-layer panel of the same width. Therefore, the use of two-stage concrete panels is an effective measure for heat conservation in buildings.

Keywords: computer modeling, multilayer enclosing structures, strength, porous concrete, thermal insulation properties, finite-element analysis

Conflicts of interest. The authors declare that there is no conflict of interest.

Authors' contribution: *Syromyasov A.O.* — mathematical model, numerical calculations, text and illustrations; *Makarov Yu.A.* — mathematical model, text and illustrations; *Elchishcheva T.F.*, *Kozhanov D.A.* — data collection, verification of numerical results; *Erofeev V.T.* — supervision, problem statement, literature review. All authors read and approved the final version of the article.

For citation: Syromyasov A.O., Makarov Yu.A., Elchishcheva T.F., Erofeev V.T., Kozhanov D.A. Fracture mechanics of a three-layer wall panel based on two-stage concrete. *Structural Mechanics of Engineering Constructions and Buildings.* 2025;21(5): 432–440. http://doi.org/10.22363/1815-5235-2025-21-5-432-440 EDN: EDACPF

Alexey O. Syromyasov, Candidate of Physical and Mathematical Sciences, Associate Professor at the Department of Applied Mathematics, National Research Mordovia State University, 68/1 Bolshevistskaya St, Saransk, 430005, Russian Federation; eLIBRARY SPIN-code: 7617-8578, ORCID: 0000-0001-6520-0204; e-mail: syal1@yandex.ru

Yuri A. Makarov, Candidate of Technical Sciences, Associate Professor at the Department of Applied Mathematics, National Research Mordovia State University, 68/1, Bolshevistskaya St, Saransk, 430005, Russian Federation; eLIBRARY SPIN-code: 4679-9363, ORCID: 0000-0002-6242-4138; e-mail: makarov.yira75@mail.ru

Tatiana F. Elchishcheva, Candidate of Technical Sciences, Head of the Department of Architecture and Urban Planning, Tambov State Technical University, 106/5 Sovetskaya St, Tambov, 392000, Russian Federation; eLIBRARY SPIN-code: 9764-3898, ORCID: 0000-0002-0241-3808; e-mail: elschevat@mail.ru

Vladimir T. Erofeev, Doctor of Technical Sciences, Professor at the Department of Construction Materials Science, National Research Moscow State University of Civil Engineering, 26 Yaroslavskoye shosse, Moscow, 129337, Russian Federation; eLIBRARY SPIN-code: 4425-5045, ORCID: 0000-0001-8407-8144; e-mail: erofeevvt@bk.ru

Dmitry A. Kozhanov, Candidate of Physical and Mathematical Sciences, Associate Professor at the Department of Structural Theory and Technical Mechanics, Nizhny Novgorod State University of Architecture and Civil Engineering, 65 Ilyinskaya St, Nizhny Novgorod, 603000, Russian Federation; eLIBRARY SPIN-code: 8722-2173, ORCID: 0000-0002-8443-1291; e-mail: pbk996@mail.ru

Механика разрушения трехслойной стеновой панели на основе каркасного бетона

А.О. Сыромясов[1]✉, Ю.А. Макаров[1], Т.Ф. Ельчищева[2], В.Т. Ерофеев[3], Д.А. Кожанов[4]

[1] Национальный исследовательский Мордовский государственный университет им. Н.П. Огарева, *Саранск, Российская Федерация*
[2] Тамбовский государственный технический университет, *Тамбов, Российская Федерация*
[3] Национальный исследовательский Московский государственный строительный университет, *Москва, Российская Федерация*
[4] Нижегородский государственный архитектурно-строительный университет, *Нижний Новгород, Российская Федерация*
✉ syal1@yandex.ru

Поступила в редакцию: 17 июля 2025 г.
Доработана: 10 сентября 2025 г.
Принята к публикации: 19 сентября 2025 г.

Аннотация. Моделируется распределение напряжений в трехслойной каркасной стеновой панели с жестким контактом между слоями. Для расчета использован конечно-элементный пакет ANSYS Workbench. Значения критериев разрушения (главного и эквивалентного напряжений) вычислены вблизи концентраторов напряжений, т.е. ребер, разделяющих нагруженные и закрепленные грани панели. Получено, что разрушение начинается на границе нагруженного и ненагруженного слоев изделия. Показано, что теплоизоляционный слой из крупнопористого бетона, расположенный в центре панели, способен участвовать в восприятии части нагрузки, приходящейся на несущий слой. В связи с этим несущая способность конструкций, изготовленных по каркасной технологии, существенно повышается за счет частичного нагружения теплоизолирующего слоя. Поэтому каркасная панель может выдерживать большие нагрузки по сравнению с панелями, имеющими гибкие связи. Кроме того, показано, что термическое сопротивление трехслойной каркасной панели вдвое выше, чем у однослойной панели такой же толщины. Тем самым использование каркасных панелей является эффективным средством сохранения тепла в зданиях.

Ключевые слова: компьютерное моделирование, многослойные ограждающие конструкции, прочность, крупнопористый бетон, теплоизоляционные свойства, конечно-элементный анализ

Заявление о конфликте интересов. Авторы заявляют об отсутствии конфликта интересов.

Вклад авторов: *Сыромясов А.О.* — математическая модель, проведение расчетов, создание иллюстраций, написание текста; *Макаров Ю.А.* — математическая модель, создание иллюстраций, написание текста; *Ельчищева Т.Ф.*, *Кожанов Д.А.* — сбор материала, проверка результатов расчета; *Ерофеев В.Т.* — научное руководство, постановка задачи, литературный обзор. Все авторы ознакомлены с окончательной версией статьи и одобрили ее.

Для цитирования: *Сыромясов А.О., Макаров Ю.А., Ельчищева Т.Ф., Ерофеев В.Т., Кожанов Д.А.* Механика разрушения трехслойной стеновой панели на основе каркасного бетона // Строительная механика инженерных конструкций и сооружений. 2025. Т. 21. № 5. С. 432–440. http://doi.org/10.22363/1815-5235-2025-21-5-432-440 EDN: EDACPF

1. Introduction

The walls of a building are one of the main structural elements that carry loads and provide spatial rigidity and stability for the entire structure [1]. In addition to their load-bearing function, exterior walls also serve as enclosures, creating a favorable microclimate for the people inside the building. Therefore, effective materials and technologies are increasingly being used in their manufacture to ensure the strength and resistance of the products to aggressive environments and external loads [2], as well as sufficient thermal and sound insulation properties [3].

The required values for the load-bearing capacity and thermal resistance of building structures are determined based on various criteria, including economic ones [4]. It is known that walls made of prefabricated single-layer and multi-layer reinforced concrete panels are the most economical in terms of material consumption and construction technology.

Single-layer panels are sufficiently strong and technologically advanced, but their thermal insulation properties are insufficient for residential buildings in regions with cold climatic conditions. Therefore, such walls are currently used in regions with warm climate or in the construction of industrial and agricultural buildings.

Compared to single-layer panels, multi-layer panels are significantly more effective in terms of thermal performance. Such a panel consists of an insert (insulation) made of a material with low thermal conductivity, density, and strength [5], for example, mineral wool or glass wool, confined between the outer and inner layers. The outer layer, made of structural concrete, protects the insulation from external influences. The inner load-bearing layer is designed to carry the load transferred from the floor slabs; the insulation layer and the outer textured layer are attached to it by means of flexible ties, reinforced concrete ribs, or dowels.

However, along with their advantages, layered panels have significant disadvantages [6; 7]:

- short service life of the insulation and ties, which require anti-corrosion protection;
- lack of reliable connection of the insert to the concrete layers due to discrete arrangement of the ties;
- formation of cold bridges between the outer and inner layers due to high thermal conductivity of metal ties;
- uneven heat distribution in the wall and condensation in the interlayer space due to differences in thermal characteristics of the layers.

The consequences of these shortcomings are the exclusion of joint action of concrete layers in resistance to external loads, a tendency to develop significant shear strains due to deformation of the middle layer, and the short service life of such panels.

An alternative to such layered panels are three-layer wall panels based on two-stage concrete with a continuous connection between the layers, manufactured using a special technology [8]. Such products consist of two layers of dense expanded clay concrete, between which there is a middle layer of porous expanded clay concrete. The use of the latter type of concrete as insulation allows for the creation of materials with increased strength and stiffness and reduced thermal conductivity, as well as eliminating the structural disadvantages inherent in the three-layer panels with inserts. For example, the layer of porous concrete can effectively remove condensed moisture [9]. In operating conditions with biologically active environments, panels based on two-stage concrete are less susceptible to biodegradation [10; 11]. In turn, biostability contributes to the preservation of physical and mechanical properties of the construction products [12].

Porous concrete has reliable adhesion to the external concrete layers and is capable of resisting shear. Rigid contact between the layers allows the panel to be considered as one-piece, while panels with inserts are composite structures. The joint action of different types of concrete forming a single continuous section has been studied, for example, in [13; 14].

There are known calculation methods and additional hypotheses that take into account the aspects of deformation of three-layer structures [15]; in Russia, they are also regulated by state standards. Nevertheless, the behavior of these structures under different deformation modes is still insufficiently studied, which hinders their introduction into construction.

Computer modeling using CAE systems offers broad opportunities for studying this type of structure. In this article, such modeling is applied to the behavior of a loaded three-layer wall panel made on the basis of a two-stage composite using the technology described in [8] and implemented at OAO "ZhBK-1" in Saransk, Russian Federation.

The aim of the study is to test the hypothesis that the middle porous concrete layer not only acts as an effective insulator, but is also capable of carrying part of the load acting on the load-bearing layer.

2. Methods

2.1. Panel Geometry and its Physical and Mechanical Characteristics

The panel is modelled as a rectangular prism of length $l = 6$ m, height $h = 1.2$ m and total thickness of all layers $b = 0.4$ m.

The layers perform the following tasks:

- inner layer 1 is the load-bearing layer designed to carry load from the supported floor slabs; the thickness of this layer is $\delta_1 = 80$ mm;

- middle layer 2 is heat-insulating, designed to provide effective thermal protection for the building; its thickness is calculated based on the thermal properties of the materials used and the thermal insulation requirements for buildings of various types; in this study it is assumed to be δ_2 = 240 mm;
- outer layer 3 is protective and decorative; it protects the insulation from external climatic effects and creates architectural expressiveness of the structure; the thickness of this layer δ_3 is also equal to 80 mm.

The physical and mechanical characteristics of the layers are different and are shown in Table 1. The cross-sectional diagram of the panel is shown in Figure 1.

Poisson's ratio for all structural layers is the same and is ν = 0.18. Thermal conductivity is specified for type A service conditions of enclosing structures in accordance with the regulatory documents in force in Russia — design code[1].

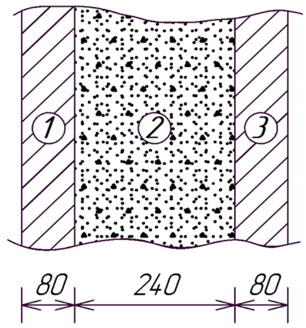

Figure 1. Sectional view of the three-layer wall panel
Source: made by Yu.A. Makarov.

The use of technologies such as fiber reinforcement and the like allows to obtain concrete, shear strength R_S of which is close to prismatic strength R_b. Therefore, it is assumed that $R_S = R_b$ for the layers of the studied panel.

Table 1

Physical and mechanical characteristics of the wall panel layers

ID and name of the structural layer	Layer material	Density ρ, kg/m³	Prismatic strength R_b, MPa	Initial modulus of elasticity E, MPa	Thermal conductivity λ, W/(m·°C)
1 — inner (load-bearing) layer	Dense concrete	1800	40	10000	0.483
2 — middle (thermal insulation) layer	Porous concrete	700	10	3500	0.206
3 — outer (decorative) layer	Dense concrete	1800	40	10000	0.483

Source: data on mechanical properties by V.T. Erofeev.

2.2. Verification of Panel Insulation Performance

First, the hypothesis that the studied three-layer panel is an effective heat insulator was tested. To do this, its thermal resistance was compared with the equivalent characteristic of a homogeneous panel of standard single-layer structure and of the same thickness.

The heat transfer resistance of a multilayer enclosing structure is determined by the following formula:

$$R_0 = 1/\alpha_B + \sum(\delta_i/\lambda_i) + 1/\alpha_H, \tag{1}$$

where α_B = 8.7 W/(m^2×°C) and α_H = 23 W/(m^2×°C) are the heat transfer coefficients of the internal and external surfaces of the enclosing structure, respectively; δ_i and λ_i are the thickness and thermal conductivity of the i-th layer of the wall.

In this analysis, the parameters of the panel layers were taken from Table 1; the thickness and thermal conductivity of a single-layer panel were assumed to be δ = 400 mm and λ = 0.58 W/(m×°C), respectively.

2.3. Modelling Panel Loading

Several options for loading the two-stage concrete panel were considered in the study, and the one that provides the maximum linear load that the panel can withstand without failure was selected.

[1] SP 50.13330.2024. Thermal performance of buildings. Intr. 2024–06–16. Moscow: Russian Standardization Institute, 2024. 70 p.

In the model it was assumed that the bottom and both side faces of the panel were fixed, and the width of the restrained strip $b_0 \geq \delta_1$; in other words, the load-bearing layer and (partially) insulation layer are fixed. A downwards normal force (pressure) P is applied to the section of the panel selected in this way; moreover, self-weight G is also applied to the structure (Figure 2).

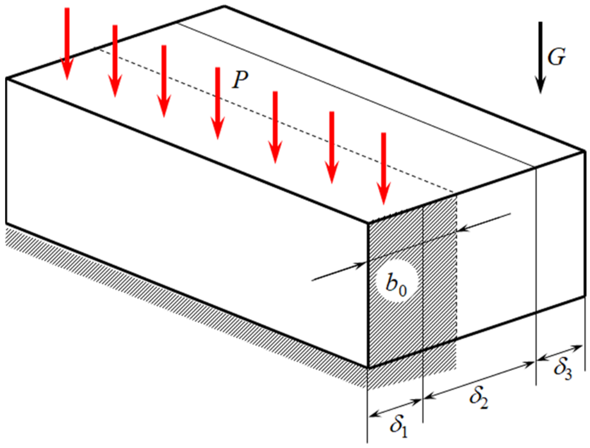

Figure 2. Panel loading diagram
S o u r c e: made by A.O. Syromyasov.

The described methods of restraint and loading simulate the interaction of the panel with its neighbors below and to the side (through a layer of cement mortar), as well as supporting the floor slab.

The method of computer modeling of three-layer two-stage concrete panels under such loads is described in detail in [16]; since in this study not only the load-bearing layer but also the thermal insulation layer is loaded, minor adjustments had to be made to it. The method takes into account the fact that, due to only a part of the panel cross-sectional area being loaded, its material is in a combined stress state, and the critical strength parameters cannot be described by a uniaxial stress state model. Therefore, when evaluating the load-bearing capacity of the panel, several strength criteria are used, the values of which are examined at several different points.

The ANSYS Workbench finite element software, installed under license on the Mordovia State University computing cluster, was used for the calculations. Figure 3 shows one of the calculation results — an overall distribution pattern of equivalent stress (von Mises) on the external surface of the panel loaded by $P = 4.55$ MPa and with loaded layer thickness $b_0 = 200$ mm.

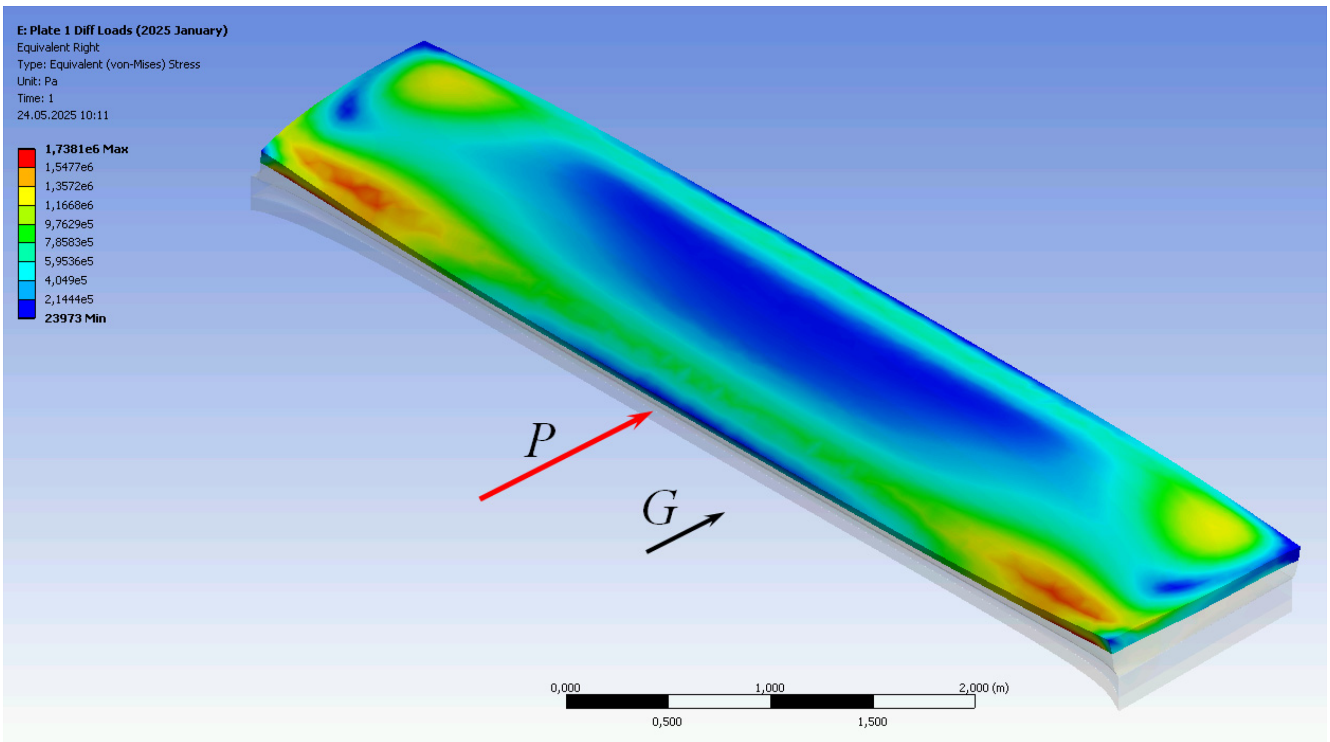

Figure 3. Distribution of equivalent stress on the panel surface
S o u r c e: made by A.O. Syromyasov in ANSYS Workbench software.

The panel is most likely to fracture in the area of stress concentration, i.e., near two symmetrical edges **e** and **e**', where the fixed side faces are adjacent to the loaded upper face. Therefore, internal stresses in the panel should be calculated along the control line segment L, which is located at a distance of 1 cm from the side and 1 cm from the upper face parallel to edge **e**. Particularly, the principal normal stress σ_1 and equivalent stress σ_{eq} according to the Huber — Henky — von Mises theory was calculated.

3. Results and Discussion

When calculating the thermal insulation properties of the panel in (1), it was found that the thermal resistance of the single-layer structure $R_0 = 0.848$ m^2·°C/W, and for the proposed three-layer structure $R_0 = 1.655$ m^2·°C/W. Thus, the use of multi-layer enclosing structures based on two-stage concrete instead of standard single-layer panels of the same thickness significantly reduces heat loss in buildings.

The graphs of σ_1 and σ_{eq} along segment L provide a general idea of the stress distribution inside the panel. Thus, Figure 4 presents the graph of σ_{eq} at $b_0 = 200$ mm and $P = 4.55$ MPa. The value at $x = 0$ corresponds to the interior boundary of the load-bearing layer, and the value at $x = 400$ mm – to the exterior face of the panel. At other values of b_0 and P, the graphs of σ_1 and σ_{eq} look similar.

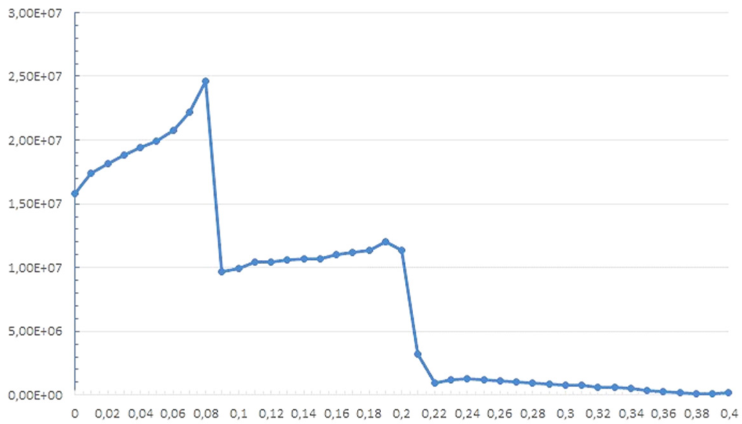

Figure 4. Distribution of equivalent stress (von Mises) along the control line
S o u r c e: made by A.O. Syromyasov.

Two peak values of the failure criterion are reached at $x = \delta_1$ and $x = b_0$, i.e. at the boundary between the load-bearing and insulation layers, and at the boundary between the loaded and non-loaded layers.

Based on the calculation results, the stress arising in the outer layer is many times smaller than that in the inner layer. This implies that the loads in the outer layer can be disregarded. Indeed, the mechanical characteristics of the two layers are identical, which means that failure will occur sooner in the more intensely loaded inner layer.

Based on the above, the failure criterion for the studied panel is considered to be the fulfillment of at least one of the following conditions:

- at the boundary between the load-bearing and insulation layers (on the *load-bearing* layer side), principal normal stress σ_1 exceeds the prismatic strength R_b of the load-bearing layer *or* equivalent stress σ_{eq} exceeds the value of $1.15R_b$;
- at the boundary between the load-bearing and insulation layers (now on the *insulation* layer side) stress σ_1 exceeds R_b of the insulation layer *or* equivalent stress σ_{eq} exceeds the value of $1.15R_b$ of the same layer;
- at the boundary between the loaded and non-loaded regions (inside the insulation layer) $\sigma_1 > R_b$ *or* $\sigma_{eq} > 1.15R_b$, in which case the prismatic strength of the insulation layer is considered.

In doing so, the values of σ_1 and σ_{eq} are examined at three points P_1, P_1' и P_1^*, located at the intersection of line L and the boundaries of the aforementioned layers.

To investigate the influence of the thermal insulation layer on the magnitude of fracture stress and the load-bearing capacity of the structure, the panel was loaded with an increase in the total width of the loaded strip b_0 from 80 to 200 mm with a step of 40 mm. The results of the analysis are presented in Table 2.

Table 2

Relationship between of the fracture stress and the width of the loaded layer

Type of criterion	Critical value, MPa	Value, MPa (b_0 = 80 mm)	Value, MPa (b_0 = 120 mm)	Value, MPa (b_0 = 160 mm)	Value, MPa (b_0 = 200 mm)
		***P* = 9.04 МПа / MPa**	***P* = 5.78 МПа / MPa**	***P* = 5.15 МПа / MPa**	***P* = 4.55 MPa**
$\sigma_1(P_1)$	30	***30.77***	22.99	22.47	21.22
$\sigma_{eq}(P_1)$	34.5	34.17	27.50	26.37	24.62
$\sigma_1(P_1')$	10	9.92	8.23	8.01	7.62
$\sigma_{eq}(P_1')$	11.5	12.10	10.16	9.53	8.80
$\sigma_1(P_1^*)$	10	–	9.55	9.85	***10.01***
$\sigma_{eq}(P_1^*)$	11.5	–	***11.49***	***11.47***	11.36
$\tau_{xz}(P_1)$	–	7.03	8.86	8.69	8.14
$\tau_{xz}(P_1^*)$	–	–	2.65	2.72	2.57

S o u r c e: obtained by A.O. Syromyasov using ANSYS Workbench software.

P indicates the pressure at which the panel fails. For every b_0, criteria values close to or exceeding the maximum allowable values are highlighted in bold. For reference, shear stress values τ_{xz} at the layer boundaries are also given; as can be seen, their values are quite far from the critical value R_b.

The data in Table 2 shows that failure always occurs at the boundary between the loaded and non-loaded layers – at point P_1^* (when b_0 = 80 mm it coincides with P_1).

By increasing width b_0 the value of failure pressure P drops. However, it is not the value of P itself that plays a key role, but rather the maximum allowable load per unit length $f = Pb_0$ that can be resisted by the panel. The value of f depending on the width of the loaded layer is presented in Table 3.

Table 3

Relationship between the linear load and the width of the loaded layer

b_0, mm	P, MPa	$f = Pb_0$, kN/m
80	9.04	723.2
120	5.78	693.6
160	5.15	824.0
200	4.55	910.0

S o u r c e: obtained by A.O. Syromyasov using ANSYS Workbench software.

Thus, supporting floor slabs by a 200 mm wide strip instead of standard 80 mm allows to increase the maximum allowable load by more than 25% — from 723.2 kN/m to 910.0 kN/m.

Multilayer panels with inserts lack such properties, since their insulation layers are made of materials that cannot carry loads. All loads in such panels are resisted exclusively by a thin inner load-bearing layer.

Further improvement of the load-bearing capacity of products based on two-stage concrete can be achieved, for example, by modifying the cement binder with polymer compounds [17; 18], finely dispersed fillers [19; 20], and nanoparticles [21; 22].

4. Conclusion

Thus, the article examined the behavior of a loaded three-layer panel manufactured using the two-stage technology. The interaction of the panel with adjacent panels was modeled by fixing three of its side faces, with pressure applied to the upper face reflecting the load carried by the panel. The study tested the assumption that the middle (thermal insulation) layer of the two-stage concrete panel is capable of partially resisting the external forces. It was necessary to determine at what loads the panel would begin to fracture and where exactly this fracture would begin.

The ANSYS Workbench software, which implements the finite element method, was used for calculations. Special attention was paid to calculating the failure criteria near the edges, along which the loaded face “joins” with the fixed ones. The principal and equivalent (according to von Mises) stresses were selected as such criteria; it was assumed that fracture would begin if at least one of them exceeded the “dangerous” value. The magnitude of the applied pressure and the width of the loaded part varied in the calculations.

The obtained results allow to draw the following conclusions:

1. The panel fractures at the boundary between the loaded and non-loaded layers near the edge, which is the stress concentrator.

2. When the width of the loaded part increases, the failure pressure may decrease due to the fact that the load is applied to the less strong insulation layer. However, the linear load at failure increases due to the increase in the area of the section that carries this load.

3. It follows from the previous conclusion that by partially loading the thermal insulation layer, the load-bearing capacity of the panels manufactured using the two-stage technology can be significantly increased compared to panels containing mineral wool or other thermal insulation inserts, since such inserts cannot be loaded.

In addition, the article shows that three-layer panels based on two-stage concrete have twice the thermal resistance of standard single-layer panels of the same thickness, making the use of two-stage products an effective method of heat conservation.

References

1. Sheina S.G., Umnyakova N.P., Fedaeva P.V., Minenko E.N. The best European experience in implementing energy-saving technologies in the housing stock of the Russian Federation. *Housing Construction.* 2020;(6):29–34. (In Russ.) https://doi.org/10.31659/0044-4472-2020-6-29-34 EDN: GQLQGC

2. Mayhoub O.A., Nasr E.S.A.R., Ali Y.A., Kohail M. The influence of ingredients on the properties of reactive powder concrete: A review. *Ain Shams Engineering Journal.* 2021;12(1):145–158. https://doi.org/10.1016/j.asej.2020.07.016 EDN: QFSFAB

3. Kornilov T.A., Everstova V.N. Assessment of thermal protection properties of external walls made of polystyrene concrete blocks of a frame-monolithic building. *Academia. Architecture and Construction.* 2024;3:137–144. (In Russ.) https://doi.org/10.22337/2077-9038-2024-3-137-144 EDN: AISSKC

4. Malyavina E.G., Frolova A.A. Selection of economically feasible thermal insulation of buildings in the north of the Russian Federation. *Housing Construction.* 2022;12:72–78. (In Russ.) https://doi.org/10.31659/0044-4472-2022-12-72-78 EDN: NMLVMK

5. Sizov V.D., Pavlovskaya A.V. Efficient multilayer wall panel. *Science and Technology.* 2022;21(5):410–418. (In Russ.) EDN: PXHEGF

6. Fedosov S.V., Ibragimov A.M., Gnedina L.Yu. Problems of three-layer enclosing structures. *Housing construction.* 2012;7:9–12. (In Russ.) EDN: NRMGFG

7. House M.W., Weiss W.J. Review of microbially induced corrosion and comments on needs related to testing procedures. *Proceedings of the 4th International Conference on the Durability of Concrete Structures*. ICDCS, 24–26 July 2014:94–103. https://doi.org/10.5703/1288284315388

8. Erofeev V.T. Fundamentals of the theory of technology for obtaining, calculating physical and mechanical properties and indicators of chemical and biological resistance of frame building composites. *Structural Mechanics of Engineering Structures and Structures.* 2022;18(4):283–296. (In Russ.) EDN: EOPEXD

9. Chromkova I., Cechmanek R., Kotlanova M.K. Effect of silages on concrete and process of its corrosion in the course of time. *Journal of Physics: Conference Series 2792(1).* Czechia, 2024:1–14. https://doi.org/10.1088/1742-6596/2792/1/012013 EDN: VGGAHI

10. Marquez-Peñaranda J.F., Sanchez-Silva M., Husserl J., Bastidas-Arteaga E. Effects of biodeterioration on the mechanical properties of concrete. *Materials and Structures*. 2016;49:4085–4099. https://doi.org/10.1617/s11527-015-0774-4 EDN: UKSSWN

11. Erofeev V., Stepina I., Badamshin R., Afonin V., Smirnov V., Samchenko S., Kozlova I. Effect of wooden fillers on strength and biodegradation of caustic magnesite. *BioResourses.* 2025;20(3):5790–5800. https://doi.org/10.15376/biores.20.3.5790-5800

12. Erofeev V., Rodin A.I., Karpushin S.N., Klyuev S.V., Sabitov L.S. Biological and climatic resistance of cement composites based on biocidal binders. *Lecture Notes in Civil Engineering.* 2023;307:168–179. https://doi.org/10.1007/978-3-031-20459-3_22

13. Ustarkhanov O.M., Muselemov Kh.M., Ustarkhanov T.O., Gapparov Kh.M. Effect of convergence of layers of a three-layer structure on its stress-strain state. *Bulletin of Mechanical Engineering.* 2020;12:34–37. (In Russ.) EDN: STEQPQ

14. Zotov A.A., Volkov A.N., Boykov A.A. Design and manufacturing of a three-layer spherical shell with discrete filler using 3d printing technology. *Bulletin of Mechanical Engineering.* 2020;8:41–44. (In Russ.) EDN: IBBBEF

15. Zhu P., Lei Z.X., Liew K.M. Static and free vibration analyses of carbon nanotube-reinforced composite plates using finite element method with first order shear deformation plate theory. *Composite Structures.* 2012;94(4):1450–1460. https://doi.org/10.1016/ j.compstruct.2011.11.010

16. Syromyasov A.O., Makarov Yu.A., Erofeev V.T. Modeling the failure of an eccentrically loaded wall panel manufactured using frame technology. *Journal of the Middle Volga Mathematical Society.* 2024;26(3):313–325. (In Russ.) https://doi.org/10.15507/2079-6900.26.202403.313-325 EDN: OVZIIR

17. Kujawa W., Olewnik-Kruszkowska E., Nowaczyk J. Concrete strengthening by introducing polymer-based additives into the cement matrix — A mini review. *Materials.* 2021;14(20):6071. https://doi.org/10.3390/ma14206071 EDN: RSGPHH

18. Salazar B., Aghdasi P. Williams I.D. et al. Polymer lattice-reinforcement for enhancing ductility of concrete. *Materials and Design.* 2020;196:109184. https:/doi.org/10.1016/j.matdes.2020.109184 EDN: DOYCNX

19. Vishwakarma V., Sudha U., Ramachandran D. et al. Enhancing antimicrobial properties of fly ash mortars specimens through nanophase modification. *Materials Today Proceedings.* 2016;3(6):1389–1397. https://doi.org/10.1016/j.matpr.2016.04.020

20. Senhadji Y., Escadeillas G., Mouli M. et al. Influence of natural pozzolan, silica fume and limestone fine on strength, acid resistance and microstructure of mortar. *Powder Technology.* 2014;254:314–323. https://doi.org/10.1016/j.powtec.2014.01.046

21. Fan Y., Zhang S., Wang Q., Shah P.S. The effects of nano-calcined kaolinite clay on cement mortar exposed to acid deposits. *Construction and Building Materials.* 2016;102:486–495. https://doi.org/ 10.1016/j.conbuildmat.2015.11.016

22. Hendi A., Rahmani H., Mostofinejad D. et al. Simultaneous effects of microsilica and nanosilica on self consolidating concrete in a sulfuric acid medium. *Construction and Building Materials.* 2017;152:192–205. https://doi.org/10.1016/j.conbuildmat.2017.06.165

СТРОИТЕЛЬНАЯ МЕХАНИКА ИНЖЕНЕРНЫХ КОНСТРУКЦИЙ И СООРУЖЕНИЙ
STRUCTURAL MECHANICS OF ENGINEERING CONSTRUCTIONS AND BUILDINGS

2025. 21(5). 441–461

ISSN 1815-5235 (Print), 2587-8700 (Online)
HTTP://JOURNALS.RUDN.RU/STRUCTURAL-MECHANICS

DOI: 10.22363/1815-5235-2025-21-5-441-461
EDN: DEEXQA

Research article / Научная статья

Triangular Layered Finite Element Method for Reinforced Concrete Slabs

Dara A. Mawlood✉, **Alexandr A. Koyankin**

Siberian Federal University, *Krasnoyarsk, Russian Federation*
✉ dara.mawloud@univsul.edu.iq

Received: August 3, 2025
Revised: October 4, 2025
Accepted: October 14, 2025

Abstract. This study presents an advanced layered triangular finite element method for modeling reinforced concrete (RC) slabs, incorporating material nonlinearity based on a refined global-local plate theory. The RC slab's cross-section is discretized into concrete and steel layers, each modeled as an individual plate element with distinct material properties. The proposed formulation independently considers displacement field variables and out-of-plane stress components, enabling precise nodal stress determination through constitutive relationships. A three-node triangular element maintaining C1-continuity is employed for spatial discretization, with governing equations derived using a triangular layered plate theory. Benchmark verification studies confirm the method's computational accuracy and efficiency, with ultimate deflection predictions exhibiting errors ranging from 2.59% (minimum) to 11.2% (maximum). Comprehensive numerical tests demonstrate that the proposed triangular layered finite element approach delivers high-precision solutions while significantly reducing computational expense.

Keywords: kinematic layer, strain field, stress field, layered FE discretization, numerical results

Conflicts of interest. The authors declare that there is no conflict of interest.

Authors' contribution: *Mawlood D.A.* — data collection and processing, analysis and interpretation of results, scientific writing; *Koyankin A.A.* — concept development, approval of the final version of the manuscript. Both of the authors read and approved the final version of the article.

For citation: Mawlood D.A., Koyankin A.A. Triangular-layered finite element method for reinforced concrete slabs. *Structural Mechanics of Engineering Constructions and Buildings.* 2025;21(5):441–461. http://doi.org/10.22363/1815-5235-2025-21-5-441-461 EDN: DEEXQA

Метод многослойных треугольных конечных элементов для железобетонных плит перекрытия

Д.А. Мавлуд✉, **А.А. Коянкин**

Сибирский федеральный университет, *Красноярск, Российская Федерация*
✉ dara.mawloud@univsul.edu.iq

Поступила в редакцию: 3 августа 2025 г.
Доработана: 4 октября 2025 г.
Принята к публикации: 14 октября 2025 г.

Аннотация. Представлен усовершенствованный многослойный треугольный метод конечных элементов для моделирования железобетонных плит, учитывающий нелинейность материала на основе усовершенствованной глобально-локальной теории пластин. Поперечное сечение железобетонной плиты разбито на бетонные и стальные слои, представ-

Dara A. Mawlood, Master student, Department of Building Structures and Controlled Systems, Institute of Civil Engineering, Siberian Federal University, 79 Svobodny av., 660041, Krasnoyarsk, Russian Federation; ORCID: 0009-0003-2819-3107; e-mail: dara.mawloud@univsul.edu.iq

Alexandr A. Koyankin, Candidate of Technical Sciences, Associate Professor of the Department of Building Structures and Controlled Systems, Institute of Civil Engineering, Siberian Federal University, 79 Svobodny av., 660041, Krasnoyarsk, Russian Federation; eLIBRARY SPIN-code: 2779-8314, ORCID: 0000-0001-5271-9904; e-mail: KoyankinAA@mail.ru

ляющие собой отдельные элементы с различными свойствами материала. Предлагаемая формулировка независимо учитывает переменные поля смещений и компоненты напряжений вне плоскости, что позволяет точно устанавливать узловое напряжение с помощью определяющих соотношений. Для пространственной дискретизации используется треугольный элемент с тремя узлами, поддерживающий непрерывность порядка С1, а основные уравнения получены с использованием теории многослойных треугольных пластин. Сравнительные проверочные исследования подтвердили точность вычислений и эффективность метода, при этом погрешность результатов расчета прогиба составляет от 2,59 % (минимум) до 11,2 % (максимум). Всесторонние численные эксперименты демонстрируют, что предложенный метод многослойных треугольных конечных элементов обеспечивает высокую точность решений при значительном снижении вычислительных затрат.

Ключевые слова: кинематический слой, поле деформаций, поле напряжений, разбиение на многослойные КЭ, численные результаты

Заявление о конфликте интересов. Авторы заявляют об отсутствии конфликта интересов.

Вклад авторов: *Мавлуд Д.А.* — сбор и обработка материалов, анализ и интерпретация данных, подготовка и редактирование текста; *Коянкин А.А.* — разработка концепции, утверждение окончательного варианта статьи. Оба автора ознакомлены с окончательной версией статьи и одобрили ее.

Для цитирования: *Mawlood D.A., Koyankin A.A.* Triangular layered finite element method for reinforced concrete slabs // Строительная механика инженерных конструкций и сооружений. 2025. Т. 21. № 5. С. 441–461. http://doi.org/10.22363/1815-5235-2025-21-5-441-461 EDN: DEEXQA

1. Introduction

From the 2010–2025 construction period, reinforced concrete (RC) slabs are essential structural components, serving as flooring systems while carrying vertical loads. Accurate performance analysis is critical to ensure both safety and cost-effectiveness in RC building designs [1; 2]. However, predicting the nonlinear response of RC slabs remains a significant challenge due to the complex behavior of reinforced concrete structures, making it an active research area [3; 4]. This complexity arises from material nonlinearity in concrete and steel, cracking, imperfect bond-slip behavior, and time-dependent effects such as creep and shrinkage [5].

Several material models have been developed to capture the layered nonlinear behavior of RC slabs. For reinforcing steel, a uniaxial elastic-plastic stress-strain relationship is typically employed, exhibiting symmetrical response under both tension and compression. Similarly, concrete behavior can be effectively represented using a bilinear stress-strain approximation that incorporates tensile capacity [5; 6].

To address the limitations of conventional 3D finite element models, researchers have developed innovative layered methods [7; 8]. Unlike simplified effective stiffness approaches, these layered FE models enable precise prediction of ultimate bending and shear capacity in RC slabs [9; 10]. The methods employ triangular plate elements composed of perfectly bonded, superimposed equivalent layers representing both concrete and steel reinforcement. This layered triangular element facilitates detailed tracking of concrete failure mechanisms (including cracking and crushing) and progressive steel yielding throughout the slab depth [11; 12]. Although numerous layer-based FE models exist for RC slab analysis, current implementations remain predominantly limited by Kirchhoff-Thin Plate Theory (KTPT) assumptions [13; 14].

Current research indicates a strong preference for displacement-based formulations in finite element modeling of RC slabs and plate structures [15; 16]. While these layered triangular elements derive stress components indirectly through numerical differentiation of displacement fields, the resulting post-processed stresses particularly out-of-plane components, often demonstrate reduced accuracy compared to their displacement counterparts. In contrast, advanced layered FE formulations for composite structures treat stresses and displacements as independent variables, thereby achieving superior stress prediction accuracy [17; 18].

Although layered finite element formulations have been widely adopted for laminated composite analysis, their application to nonlinear RC slab modeling remains relatively limited. Recent advances by Liguori et al. [19; 20] introduced a mixed finite element formulation for nonlinear material analysis of RC shell structures. These layered triangular elements utilize conventional Mindlin-Reissner plate theory to describe displacement fields in

Мавлуд Дара, магистрант кафедры строительных конструкций и управляемых систем, Инженерно-строительный институт, Сибирский федеральный университет, Российская Федерация, 660041, г. Красноярск, пр. Свободный, д. 79; ORCID: 0009-0003-2819-3107; e-mail: dara.mawloud@univsul.edu.iq

Коянкин Александр Александрович, кандидат технических наук, доцент кафедры строительных конструкций и управляемых систем, Инженерно-строительный институт, Сибирский федеральный университет, Российская Федерация, 660041, г. Красноярск, пр. Свободный, д. 79; eLIBRARY SPIN-код: 2779-8314, ORCID: 0000-0001-5271-9904; e-mail: KoyankinAA@mail.ru

RC structural analysis. In contrast to their methods the present study implements an innovative global-local kinematic framework for displacement field representation in plate analysis. Notably, while Liguori et al. [20] treated both membrane/flexural stresses and displacement fields as primary unknowns in their formulation, the current approach adopts a distinct strategy for variable selection. Wang et al. proposed an efficient quasi-three-dimensional mixed finite element formulation based on a refined layered global-local plate theory for nonlinear analysis of RC slabs. In this approach, the cross-section is discretized into distinct concrete and steel layers, with each layer modeled as an independent plate element characterized by unique material properties [21].

This study introduces an innovative computational framework for nonlinear analysis of RC slabs, based on an advanced triangular-layered global-local plate theory formulation. The proposed triangular layered plate methods offer optimal computational advantages, combining superior geometric flexibility with adaptive finite element analysis capabilities for RC slab modeling. The framework employs a 3-node triangular composite plate element augmented with additional nodal degrees of freedom to explicitly represent out-of-plane stress components. While requiring additional field variables, this approach enables direct computation of through-thickness stress distributions during nonlinear solution procedures.

The formulation is derived through a parameterized mixed variational principle, providing rigorous mathematical foundations for the methods The RC slab is modeled as an assembly of perfectly bonded concrete and steel layers, with material nonlinearities addressed through: (1) a smeared crack formulation for concrete behavior, and (2) elasto-plastic theory for steel reinforcement response.

2. Methods

For reinforced concrete slab elements, the principles of membrane and plate bending theory **exist**, as will be demonstrated in the subsequent steps.

2.1. Membrane Element Analysis

For the membrane component, a standard 3-node triangular element is defined by its node numbering and their (*x, y*) coordinates. (Figures 1 and 2) [6; 13].

$$u = N_1u_1 + N_2u_2 + N_3u_3,$$
$$v = N_1v_1 + N_2v_2 + N_3v_3 \qquad (1)$$

where *(u_i, v_i)* represent the horizontal and vertical displacements at node *i*, and N_i denotes the corresponding shape function for that node.

The shape functions for the 3-noded triangular element are derived as follows:

$$u = \alpha_1 + \alpha_2 x + \alpha_3 y,$$
$$v = \beta_1 + \beta_2 x + \beta_3 y. \qquad (2)$$

The system was solved for coefficients, and substituting these solutions back into Equation (2) produces:

$$u = 1/\left(2A^{(e)}\right)\left[\left(a_1 + b_1x + c_1y\right)u_1 + \left(a_2 + b_2x + c_2y\right)u_2 + \left(a_3 + b_3x + c_3y\right)u_3\right],$$

where $A^{(e)}$ is the element area and,

$$i, j\ \ a_i = x_jy_k - x_ky_j,\ b_i = y_j - y_k,\ c_i = x_k - x_j \qquad i, j, k = 1, 2, 3.$$

The coefficients a_i, b_i, and c_i are determined through cyclic permutation of the indices (i, j, k). A comparison of Equation (2) with Equation (1) yields the explicit expressions for the shape functions:

$$N_i = 1/\left(2A^{(e)}\right)\left(a_i + b_ix + c_iy\right) \qquad i = 1, 2, 3. \qquad (3)$$

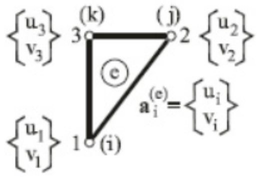

Figure 1. Discretization of a structure into 3-noded triangular elements

S o u r c e: made by H. Werkle [6].

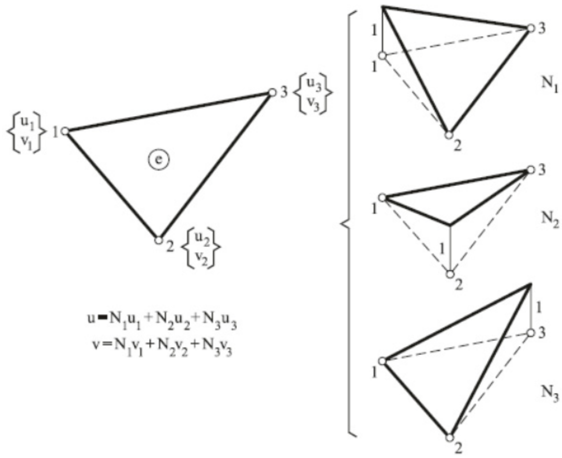

Figure 2. Shape functions for the 3-noded triangular element

S o u r c e: made by E. Oñate [13].

2.1.1. Membrane-Induced Strain

The strain components (ε_x, ε_y, γ_{xy}) are computed via differentiation of the displacement fields *u(x,y)* and *v(x,y)* represented by their respective shape functions:

$$\begin{pmatrix}\varepsilon_x\\ \varepsilon_y\\ \gamma_{xy}\end{pmatrix}=\begin{pmatrix}\dfrac{\partial u}{\partial x}\\ \dfrac{\partial v}{\partial y}\\ \dfrac{\partial u}{\partial y}+\dfrac{\partial v}{\partial x}\end{pmatrix}=\begin{bmatrix}\dfrac{\partial N1}{\partial x} & 0 & \dfrac{\partial N2}{\partial x} & 0 & \dfrac{\partial N3}{\partial x} & 0\\ 0 & \dfrac{\partial N1}{\partial y} & 0 & \dfrac{\partial N2}{\partial y} & 0 & \dfrac{\partial N3}{\partial y}\\ \dfrac{\partial N1}{\partial y} & \dfrac{\partial N1}{\partial x} & \dfrac{\partial N2}{\partial y} & \dfrac{\partial N2}{\partial x} & \dfrac{\partial N3}{\partial y} & \dfrac{\partial N3}{\partial x}\end{bmatrix}\begin{bmatrix}u_1\\ v_1\\ u_2\\ v_2\\ u_3\\ v_3\end{bmatrix}, \tag{4}$$

$$\varepsilon_m=\beta_m.u_e, \tag{5}$$

where

$$B_{mi}=\frac{1}{2A^e}\begin{bmatrix}b_i & 0\\ 0 & c_i\\ c_i & b_i\end{bmatrix}.$$

2.1.2. Membrane-Induced Stress

The stresses in the element are calculated from the strains by applying Hooke's law, as shown in [11; 12]:

$$\begin{bmatrix}\sigma_x\\ \sigma_y\\ \tau_{xy}\end{bmatrix}=\frac{E}{1-\mu^2}\begin{bmatrix}1 & \mu & 0\\ \mu & 1 & 0\\ 0 & 0 & \dfrac{1-\mu}{2}\end{bmatrix}\begin{bmatrix}\varepsilon_x\\ \varepsilon_y\\ \gamma_{xy}\end{bmatrix}\quad \text{or}\quad \sigma_m=D_m\,\varepsilon_m,$$

$$\sigma_m=D_mB_mu_e$$

and with the strains defined in (eq. 5), as:

$$s_m = D_m B_m u_e, \tag{6}$$

where

$$D_m = \begin{bmatrix} d_{11} & d_{12} & 0 \\ d_{21} & d_{22} & 0 \\ 0 & 0 & d_{33} \end{bmatrix} = \frac{E}{1-\mu^2}\begin{bmatrix} 1 & \mu & 0 \\ \mu & 1 & 0 \\ 0 & 0 & \dfrac{1-\mu}{2} \end{bmatrix}.$$

These stresses are also referred to as membrane stresses [13].

2.1.3. Membrane Stiffness Formulation

Based on the stresses obtained from Equation (6), which were derived from displacement shape functions, the equivalent nodal forces are calculated using the principle of virtual displacements. The element stiffness submatrix $K_{ij}^{(e)}$, representing the interaction between nodes i and j within the element, is typically calculated as:

$$K_e^m = \int t B_m^T D_m B_m dxdy \tag{7}$$

substituting Equation (5) and (6) into Equation (7), yields:

$$K_{ij(e)}^m = \iint\limits_{A^{(e)}} \frac{1}{2A^{(e)}}\begin{bmatrix} b_i & 0 & c_i \\ 0 & c_i & b_i \end{bmatrix}\begin{bmatrix} d_{11} & d_{12} & 0 \\ d_{21} & d_{22} & 0 \\ 0 & 0 & d_{33} \end{bmatrix}\frac{1}{2A^{(e)}}\begin{bmatrix} b_i & 0 \\ 0 & c_j \\ c_j & b_j \end{bmatrix} t\, dA.$$

For a homogeneous material, the integrand in Equation (8) remains constant, leading to:

$$K_{ij(e)}^{(m)} = \left(\frac{t}{4A}\right)^{(e)}\begin{bmatrix} b_i b_j d_{11} + c_i c_j d_{33} & b_i c_j d_{12} + b_j c_i d_{33} \\ c_i b_j d_{21} + b_i c_j d_{33} & b_i b_j d_{33} + c_i c_j d_{22} \end{bmatrix}. \tag{8}$$

2.2. Component for Bending

The Reissner — Mindlin plate theory is an advanced plate theory that incorporates shear deformation effects. This theory is commonly preferred for formulating finite plate elements. Plate deformations are described by the vertical displacement (w) and the rotational angles $(\varphi_x,\ \varphi_y)$ at each point on the plate. Consequently, every node in the plate element possesses three degrees of freedom: one translational displacement (w_i) and two rotational components $(\varphi_x,\ \varphi_y)$. The corresponding nodal forces consist of a transverse force (F_{zi}) and two bending moments (M_{xi}, M_{yi}). Figures 3, *a, b* show that, this 3-node element possesses nine degrees of freedom in total. The shape functions of a 3-node triangular element are constructed through bilinear interpolation of the nodal variables [6; 12].

$$w(x,y) = \alpha_1 + \alpha_2 x + \alpha_3 y + \alpha_4 x^2 + \alpha_5 xy + \alpha_6 y^2 + \alpha_7 x^3 + \alpha_8 x^2 y + \alpha_9 x y^2, \tag{9}$$

where

$$\varphi_x = \frac{\partial w}{\partial y}, \quad \text{and} \quad \varphi_y = \frac{\partial w}{\partial x}.$$

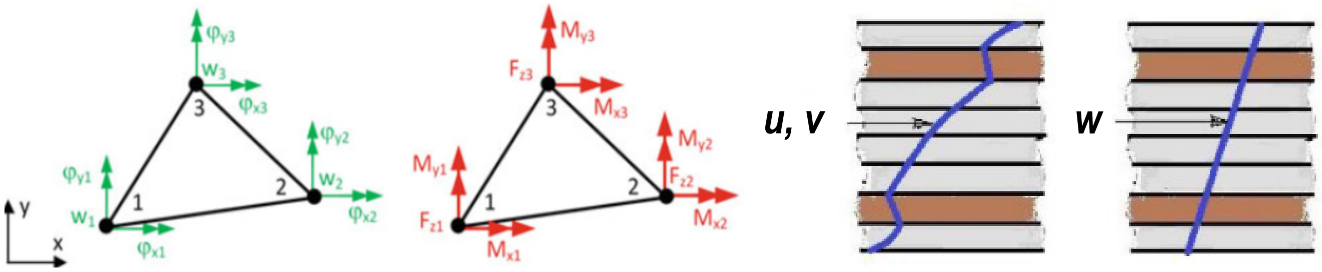

a *b* *1* *2*

S o u r c e: made by E. Oñate [13]. S o u r c e: made by R.Wang [21].

Figure 3. 3-node triangular element:
a — Triangular plate elements; *b* — Graphical illustration of the displacement field:
1 — in plane components, *2* — transverse component

$$\begin{bmatrix} w \\ \varphi_x \\ \varphi_y \end{bmatrix} = \begin{bmatrix} N_1 & 0 & 0 & N_2 & 0 & 0 & N_3 & 0 & 0 \\ 0 & N_1 & 0 & 0 & N_2 & 0 & 0 & N_3 & 0 \\ 0 & 0 & N_1 & 0 & 0 & N_2 & 0 & 0 & N_3 \end{bmatrix} \begin{bmatrix} w_1 \\ \varphi_{x1} \\ \varphi_{y1} \\ w_2 \\ \varphi_{x2} \\ \varphi_{y2} \\ w_3 \\ \varphi_{x3} \\ \varphi_{y3} \end{bmatrix}; \tag{10}$$

$u = N \cdot u_e$ N are denoted as *shape function.*

2.2.1. Bending Strain Components

The strain state of a plate element is determined by its curvature components and transverse shear deformations [5; 6]:

$$\begin{bmatrix} k_x \\ k_y \\ k_{xy} \end{bmatrix} = \begin{bmatrix} \dfrac{\partial \varphi_{xi}}{\partial x} \\ \dfrac{\partial \varphi_{yi}}{\partial y} \\ \dfrac{\partial \varphi_{xi}}{\partial y} + \dfrac{\partial \varphi_{yi}}{\partial x} \end{bmatrix} = \begin{bmatrix} 0 & \dfrac{\partial N_1}{\partial x} & 0 & 0 & \dfrac{\partial N_2}{\partial x} & 0 & 0 & \dfrac{\partial N_3}{\partial x} & 0 \\ 0 & 0 & \dfrac{\partial N_1}{\partial y} & 0 & 0 & \dfrac{\partial N_2}{\partial y} & 0 & 0 & \dfrac{\partial N_3}{\partial y} \\ 0 & \dfrac{\partial N_1}{\partial y} & \dfrac{\partial N_1}{\partial x} & 0 & \dfrac{\partial N_2}{\partial y} & \dfrac{\partial N_2}{\partial x} & 0 & \dfrac{\partial N_3}{\partial y} & \dfrac{\partial N_3}{\partial x} \end{bmatrix} \begin{bmatrix} w_1 \\ v_{x1} \\ \varphi_{y1} \\ w_2 \\ \varphi_{x2} \\ \varphi_{y2} \\ w_3 \\ \varphi_{x3} \\ \varphi_{y3} \end{bmatrix},$$

$$k_b = B_b u_e$$

and shear strain

$$\begin{bmatrix} \gamma_{xz} \\ \gamma_{yz} \end{bmatrix} = \begin{bmatrix} \text{j}_x + \dfrac{\partial w}{\partial x} \\ \varphi_y + \dfrac{\partial w}{\partial y} \end{bmatrix} \quad \text{or} \quad \begin{bmatrix} \gamma_{xz} \\ \gamma_{yz} \end{bmatrix} = \begin{bmatrix} \dfrac{\partial N_1}{\partial x} & N_1 & 0 & \dfrac{\partial N_2}{\partial x} & N_2 & 0 & \dfrac{\partial N_3}{\partial x} & N_3 & 0 \\ \dfrac{\partial N_1}{\partial y} & 0 & N_1 & \dfrac{\partial N_2}{\partial y} & 0 & N_2 & \dfrac{\partial N_3}{\partial y} & 0 & N_3 \end{bmatrix} \begin{bmatrix} w_1 \\ \varphi_{x1} \\ \varphi_{y1} \\ w_2 \\ \varphi_{x2} \\ \varphi_{y2} \\ w_3 \\ \varphi_{x3} \\ \varphi_{y3} \end{bmatrix};$$

$$\gamma = B_s u_e \tag{11}$$

2.2.2. Stiffness Matrix for Plate Bending

The stiffness matrix establishes the proportional relationship between applied nodal forces/moments and resulting nodal displacements/rotations. The virtual displacement field utilizes identical interpolation functions as the real displacement field, satisfying:

$$\underline{\bar{u}} = \underline{N}\,\underline{\bar{u}}_e \tag{12}$$

The virtual curvatures (k) and virtual shear strains (γ) derived from the virtual displacement field are:

$$\underline{\bar{k}} = \underline{B}_b\,\underline{\bar{u}}_e \quad \text{or} \quad \underline{\bar{k}}^T = \underline{\bar{u}}_e^T\,\underline{B}_b^T;$$

$$\underline{\bar{\gamma}} = \underline{B}_s\,\underline{\bar{u}}_e \quad \text{or} \quad \underline{\bar{\gamma}}^T = \underline{\bar{u}}^T\,\underline{B}_s^T.$$

The internal virtual work comprises two terms: the product of real bending moments and their corresponding virtual curvatures, plus the product of actual shear forces and associated virtual shear angles.

$$\begin{aligned} \bar{W}_i &= \int \underline{\bar{k}}^T \underline{m}\, dxdy + \int \underline{\bar{\gamma}}^T \underline{v} dxdy; \\ \bar{W}_i &= \int \underline{\bar{u}}_e^T \underline{B}_e^T \underline{D}_b \underline{B}_b \underline{u}_e dxdy + \int \underline{\bar{u}}_e^T \underline{B}_s^T \underline{D}_s \underline{B}_s \underline{u}_e dxdy; \\ \bar{W}_i &= \underline{\bar{u}}_e^T \left(\int \underline{B}_b^T \underline{D}_b\, \underline{B}_b dxdy + \int \underline{B}_s^T\, \underline{D}_s\, \underline{B}_s dxdy\right) \underline{u}_e. \end{aligned} \tag{13}$$

The virtual work done by external loads consists of force-displacement and moment-rotation products at all nodes:

$$\overline{W_a} = \overline{\underline{u}_e^T}\, \underline{F}_e. \tag{14}$$

The principle of virtual work is satisfied when the sum of internal virtual work equals external virtual work:

$$\begin{aligned} &\underline{\bar{u}}_e^T \left(\int \underline{B}_b^T\, \underline{D}_b\, \underline{B}_b dxdy + \int \underline{B}_s^T\, \underline{D}_s\, \underline{B}_s dxdy\right) \underline{u}_e = \underline{\bar{u}}_e^T\, \underline{F}_e; \\ &\left(\int \underline{B}_b^T \underline{D}_b\, \underline{B}_b dxdy + \int \underline{B}_s^T\, \underline{D}_s\, \underline{B}_s dxdy\right) \underline{u}_e = \underline{F}_e; \\ &\underline{K}_e^b \underline{u}_e = \underline{F}_e; \\ &\underline{K}_e^b = \int \underline{B}_b^T \underline{D}_b \underline{B}_b dxdy + \int \underline{B}_s^T\, \underline{D}_s\, \underline{B}_s dxdy. \end{aligned} \tag{15}$$

(Bending) (Shear)

The plate element's stiffness matrix [K] comprises two distinct sub-matrices: a bending stiffness component and a shear stiffness component. As a conforming element, it maintains C^0 continuity across both displacement and rotation fields.

2.3. Mathematical Principle

Among existing analytical approaches, the layered finite element method (LFEM) with triangular formulation demonstrates high efficacy in evaluating the flexural behavior of RC slabs. The methods employs a stratified representation of plate elements, discretizing the cross-section into distinct concrete and steel layers, as illustrated conceptually in Figure 4 [5; 22; 23]. This layered approach facilitates accurate modeling of stress distributions across the RC slab using an assembly of plane stress elements.

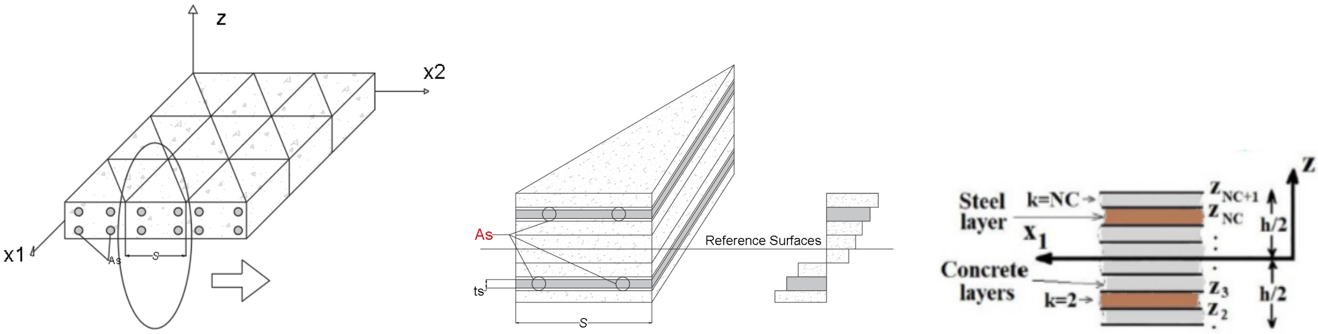

Figure 4. Typical triangular plate element for reinforced concrete plate structures
S o u r c e: made by D.A. Mawlood.

In this modeling approach, the RC slab is idealized as a composite system of perfectly bonded, uncracked concrete layers and equivalent steel layers. The reinforcement is represented using a smeared-layer approximation, with horizontal steel layers positioned at the centroidal levels of the actual reinforcement bars. The computational model employs the same number of smeared layers as physical reinforcement layers in the cross-section. Each equivalent steel layer is assigned uniaxial material properties corresponding to the orientation of the actual rebars. The equivalent thickness (t_s) of each steel layer is determined from the rebar cross-sectional area (A_s) and spacing (s) according to the relationship: $t_s = A_s / s$ [21].

Reddy's Third-Order Shear Deformation Theory (TSDT) overcomes the fundamental limitations of classical plate theories by eliminating both the normal hypothesis constraint and the requirement for planar cross-sections to remain plane after deformation [11]. The theory is founded on the following kinematic relations:

$$u(x,y,z) = z\psi_x(x,y) + z^2\theta_x(x,y) + z^3\lambda_x(x,y);$$
$$v(x,y,z) = z\psi_y(x,y) + z^2\theta_y(x,y) + z^3\lambda_y(x,y); \quad (16)$$
$$w(x,y) = w_0(x,y).$$

The kinematic functions ψ_x, ψ_y, θ_x, θ_y, λ_x, and λ_y represent undetermined parameters that characterize the cross-sectional warping deformation. Within the TSDT framework, these functions collectively introduce seven independent displacement variables. Specifically, the bending rotation components ψ_x and ψ_y describe the slope of the warped cross-section at the neutral plane $z = 0$, while the remaining variables account for higher-order deformation effects [11]. $\psi_x = \dfrac{\partial u}{\partial z}$, $\psi_y = \dfrac{\partial v}{\partial z}$, where $z = 0$.

The displacement field is mathematically represented by Equations (1) in the following form:

$$u(x,y,z)=z\psi_x(x,y)-\left(4z^3\right)/\left(3h^2\right)\left(\left(\psi_x(x,y)+\partial w_0(x,y)\right)/\partial x\right);$$

$$v\left(x,y,z\right)=z\,\psi_y\left(x,y\right)-\left(4z^3\right)/\left(3h^2\right)\left(\left(\psi_y(x,y)+\partial w_0(x,y)\right)/\partial y\right);$$

$$w(x,y)=w_0(x,y), \qquad (17)$$

where

$$\psi_x=-\frac{\partial w_0}{\partial x},\psi_y=-\frac{\partial w_0}{\partial y}.$$

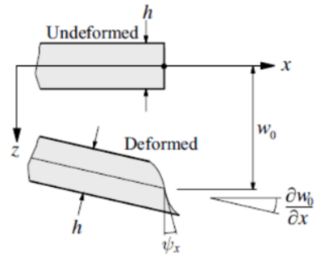

Figure 5. Unreformed and deformed plate segment
S o u r c e: made by C. Mittelstedt [11].

Consequently, Reddy's Third-Order Shear Deformation Theory incorporates just three degrees of freedom, as depicted in Figure 5.

2.4. Interconnections Between Layers

2.4.1. Strain Distribution Field

Based on the derived displacement-strain relationships, the strain components in the *i*-th layer of the RC slab can be determined [11], as illustrated in Figure 5.

$$\varepsilon_{xx}=\frac{\partial u}{\partial x}=z\frac{\partial\psi_x}{\partial x}-\frac{4z^3}{3h^2}\left(\frac{\partial\psi_x}{\partial x}+\frac{\partial^2 w_0}{\partial x^2}\right);$$

$$\varepsilon_{yy}=\frac{\partial u}{\partial y}=z\frac{\partial\psi_y}{\partial y}-\frac{4z^3}{3h^2}\left(\frac{\partial\psi_y}{\partial y}+\frac{\partial^2 w_0}{\partial y^2}\right);$$

$$\varepsilon_{zz}=\frac{\partial w}{\partial z}=0;$$

$$\gamma_{yz}=\frac{\partial v}{\partial z}+\frac{\partial w}{\partial y}=\psi_y-\frac{4z^2}{h^2}\left(\psi_y+\frac{\partial w_0}{\partial y}\right)+\frac{\partial w_0}{\partial y};$$

$$\gamma_{xz}=\frac{\partial u}{\partial z}+\frac{\partial w}{\partial x}=\psi_x-\frac{4z^2}{h^2}\left(\psi_x+\frac{\partial w_0}{\partial x}\right)+\frac{\partial w_0}{\partial x};$$

$$\gamma_{xy}=\frac{\partial u}{\partial y}+\frac{\partial v}{\partial x}=z\left(\frac{\partial\psi_x}{\partial y}+\frac{\partial\psi_y}{\partial x}\right)-\frac{4z^3}{3h^2}\left(\frac{\partial\psi x}{\partial y}+\frac{\partial\psi_y}{\partial x}+2\frac{\partial^2 w_0}{\partial x\partial y}\right).$$

These can be represented in vector form as:

$$\varepsilon^{(1)}=\begin{pmatrix}\varepsilon_{xx}^{(1)}\\ \varepsilon_{yy}^{(1)}\\ \gamma_{xy}^{(1)}\end{pmatrix}=\begin{pmatrix}\dfrac{\partial\psi_x}{\partial x}\\ \dfrac{\partial\psi_y}{\partial y}\\ \dfrac{\partial\psi_x}{\partial y}+\dfrac{\partial\psi_y}{\partial x}\end{pmatrix};\ \varepsilon^{(3)}=\begin{pmatrix}\varepsilon_{xx}^{(3)}\\ \varepsilon_{yy}^{(3)}\\ \gamma_{xy}^{(3)}\end{pmatrix}=\begin{pmatrix}-\dfrac{4}{3h^2}\left(\dfrac{\partial\psi_x}{\partial x}+\dfrac{\partial^2 w_0}{\partial x^2}\right)\\ -\dfrac{4}{3h^2}\left(\dfrac{\partial\psi_y}{\partial y}+\dfrac{\partial^2 w_0}{\partial y^2}\right)\\ -\dfrac{4}{3h^2}\left(\dfrac{\partial\psi x}{\partial y}+\dfrac{\partial\psi_y}{\partial x}+2\dfrac{\partial^2 w_0}{\partial x\partial y}\right)\end{pmatrix};$$

$$\gamma^{(0)} = \begin{pmatrix} \gamma_{yz}^{(0)} \\ \gamma_{xz}^{(0)} \end{pmatrix} = \begin{pmatrix} \psi_y + \dfrac{\partial w_0}{\partial y} \\ \psi_x + \dfrac{\partial w_0}{\partial x} \end{pmatrix}; \; \gamma^{(2)} = \begin{pmatrix} \gamma_{yz}^{(2)} \\ \gamma_{xz}^{(2)} \end{pmatrix} = \begin{pmatrix} -\dfrac{4}{h^2}\left(\psi_y + \dfrac{\partial w_0}{\partial y}\right) \\ -\dfrac{4}{h^2}\left(\psi_x + \dfrac{\partial w_0}{\partial x}\right) \end{pmatrix}.$$

The strain field can be expressed as follows:

$$\varepsilon = z\varepsilon^{(1)} + z^3\varepsilon^{(3)};$$
$$\gamma = \gamma^{(0)} + z^2\gamma^{(2)}. \tag{18}$$

2.4.2. Stress Fields in the Out-of-Plane Direction

The normal stress components are obtained from the strain field by applying Hooke's law, as given below: [6; 13]

$$\begin{bmatrix} \sigma_x \\ \sigma_y \\ \tau_{xy} \end{bmatrix} = \frac{E_i}{1-\mu^2} \begin{bmatrix} 1 & \mu & 0 \\ \mu & 1 & 0 \\ 0 & 0 & \dfrac{1-\mu}{2} \end{bmatrix} \begin{bmatrix} \varepsilon_x \\ \varepsilon_y \\ \gamma_{xy} \end{bmatrix};$$

$$\sigma^i = \underline{D}^i \underline{\varepsilon}^i.$$

Using the strain definitions from Equation (18), the strains can be expressed as:

$$\sigma^i = \underline{D}^i\left(z\varepsilon^{(1)} + z^{(3)}\varepsilon^{(3)}\right). \tag{19}$$

The transverse shear stress components $\left(\tau_{xi}, \tau_{yi}\right)$ for each layer in the reinforced concrete slab are determined using the following expressions:

$$\begin{bmatrix} \tau_{xz} \\ \tau_{yz} \end{bmatrix} = \frac{E_i}{2(1+\mu)} \begin{bmatrix} 1 & 0 \\ 0 & 1 \end{bmatrix} \begin{bmatrix} \gamma_{xz} \\ \gamma_{yz} \end{bmatrix};$$

$$\tau^i = \underline{D}_s^i \gamma^i;$$
$$\tau^i = \underline{D}_s^i\left(\gamma^{(0)} + z^{(2)}\gamma^{(2)}\right), \tag{20}$$

where E_i represents the elastic modulus of the *i-th* layer in the reinforced concrete slab system, and μ denotes the Poisson's ratio characteristic of the reinforced concrete layers.

The layer-wise constitutive formulation accounts for material heterogeneity through distinct elastic modulus E_i, and Poisson's ratios μ for each layer i. The governing equations employ standard stress resultants obtained via thickness integration of stress components [24]:

$$M^0 = \begin{pmatrix} M_{xx}^0 \\ M_{yy}^0 \\ M_{xy}^0 \end{pmatrix} = \int_{-\frac{h}{2}}^{+\frac{h}{2}} \begin{pmatrix} \sigma_{xx} \\ \sigma_{yy} \\ \tau_{xy} \end{pmatrix} zdz; \qquad Q = \begin{pmatrix} Q_y \\ Q_x \end{pmatrix} = \int_{-\frac{h}{2}}^{+\frac{h}{2}} \begin{pmatrix} \tau_{yz} \\ \tau_{xz} \end{pmatrix} dz. \tag{21}$$

Here's a rigorous academic formulation of the additional force/moment resultants in TSDT:

$$P = \begin{pmatrix} P_{xx} \\ P_{yy} \\ P_{xy} \end{pmatrix} = \int_{-\frac{h}{2}}^{+\frac{h}{2}} \begin{pmatrix} \sigma_{xx} \\ \sigma_{yy} \\ \tau_{xy} \end{pmatrix} z^3 d\ ; \qquad R = \begin{pmatrix} Ry \\ Rx \end{pmatrix} = \int_{-\frac{h}{2}}^{+\frac{h}{2}} \begin{pmatrix} \tau_{yz} \\ \tau_{xz} \end{pmatrix} z^2 dz\ . \tag{22}$$

2.4.3. Layer Interaction Mechanics in Reinforced Concrete Slabs

2.4.3.1. Layer of Steel Reinforcement

The reinforcing steel layers exhibit elastoplastic behavior, characterized by an idealized bilinear response. For the *i-th* reinforcement layer in the pre-yield regime, the constitutive [11] relationship is expressed as:

$$\sigma^i_{steel} = \underline{D}^i_{steel}\underline{\varepsilon}^i \quad ,$$

where (ε^i) is represented by Equation 19. The sectional properties D_{steel} for steel;

$$\underline{D}^i_{steel} = \begin{bmatrix} E_s & 0 & 0 \\ 0 & 0 & 0 \\ 0 & 0 & 0 \end{bmatrix}. \tag{23}$$

In Equation (23), E_s represents the elastic modulus of the *i-th* reinforcing steel layer. Upon yielding, the constitutive relationship transitions to a plastic regime, with the post-yield behavior described by the following incremental formulation:

$$\underline{D}^i_{steel} = \begin{bmatrix} E_{sp} & 0 & 0 \\ 0 & 0 & 0 \\ 0 & 0 & 0 \end{bmatrix}.$$

The term E_{ps} refers to the plastic modulus of the steel layer after it has yielded [21].

2.4.3.2. Concrete Layer Properties

In its uncracked state, the concrete material exhibits isotropic, homogeneous linear elastic behavior. The constitutive relationship governing the *i-th* concrete layer's pre-cracking response is expressed as:

$$\sigma^i_{concrete} = \underline{D}^i_{concrete}\ \underline{\varepsilon}^i, \tag{24}$$

where (ε^i) is defined by Equation (18), and $D^i_{concrete} = \dfrac{E_i}{1-\mu^2}\begin{bmatrix} 1 & \mu & 0 \\ \mu & 1 & 0 \\ 0 & 0 & \dfrac{1-\mu}{2} \end{bmatrix}$.

The transverse shear stress components τ_{xz} and τ_{yz} in each concrete layer can be evaluated through application of the appropriate constitutive relationship:

$$\tau^i_{concrete} = \underline{D}^i_s\ \underline{\gamma}^i, \quad D^i_s = \frac{E_i}{2(1+\mu)}\begin{bmatrix} 1 & 0 \\ 0 & 1 \end{bmatrix}, \tag{25}$$

where E_i denotes the elastic modulus of the *i-th* concrete layer, and (μ) represents the Poisson's ratio characterizing the concrete material's transverse strain response.

When the principal stress state exceeds the concrete's tensile capacity (f_t), the elastic constitutive relations (Eqs. 24–25) no longer apply. This investigation adopts a smeared crack formulation [24] to model post-cracking concrete behavior. The smeared crack approach necessitates a material symmetry transition from isotropic to orthotropic behavior in the local coordinate frame (ξ, η, ζ). Here, the ξ-axis normal to the crack plane defines the material softening direction, while the η- and ζ-axes plane (aligned with principal stresses) maintains elastic stiffness. In the post-cracking phase, the constitutive relationship for the *i-th* concrete layer transforms to an orthotropic formulation in the local crack-aligned coordinate system (ξ, η, ζ), expressed as:

$$\begin{bmatrix} \sigma_\xi \\ s_\eta \\ \tau_{\xi\eta} \end{bmatrix} = \frac{E_i}{1-\mu^2} \begin{bmatrix} 1 & \mu & 0 \\ \mu & 1 & 0 \\ 0 & 0 & \rho\left(\dfrac{1-\mu}{2}\right) \end{bmatrix} \cdot \begin{bmatrix} \varepsilon_\xi \\ \varepsilon_\eta \\ \gamma_{\xi\eta} \end{bmatrix}; \tag{26}$$

$$\begin{bmatrix} \tau_{\xi\zeta} \\ \tau_{\eta\zeta} \end{bmatrix} = \frac{E_i}{2(1+\mu)} \begin{bmatrix} 1 & 0 \\ 0 & \rho \end{bmatrix} \begin{bmatrix} \gamma_{\xi\zeta} \\ \gamma_{\eta\zeta} \end{bmatrix}. \tag{27}$$

Note that $(\rho \in (0.1])$ represents the shear retention factor, which is utilized to model the effects of aggregate interlock.

2.5. Mixed Element Stiffness Formulation

The element stiffness matrix components can be decomposed into membrane and bending contributions as follows:

$$K_{ei} = \sum_{i=1}^{L} K_{e,i}^m + K_{e,i}^b; \tag{28}$$

$$\underline{K}_{e,i}^m = \iint \underline{t}\, \underline{B}_m^T\, \underline{D}_{m,i}\, \underline{B}_{m,i} dxdy;$$

$$\underline{K}_{e,i}^b = \iint \underline{B}_{b,i}^T\, \underline{D}_{b,i}\, \underline{B}_{b,i} dxdy + \iint \underline{B}_{s,i}^T\, \underline{D}_{s,i}\, \underline{B}_{s,i} dxdy.$$

The stiffness contribution exhibits material-specific behavior: the steel reinforcement provides only membrane (in-plane) stiffness, while the concrete contributes to both membrane and bending (flexural) resistance.

$$K_{e,i}^m = K_{concrete}^m + K_{steel}^m = [K_{6,6}^m];$$

$$K_{e,i} = K_{e,i}^m + K_{e,i}^b = \begin{bmatrix} K_{6,6}^m & 0 \\ 0 & K_{9,9}^b \end{bmatrix}. \tag{29}$$

where $K_{6,6}^m$ and $K_{9,9}^b$ represent the membrane and bending stiffness matrices for the element, respectively.

2.6. Discretization of Finite Elements

The reinforced concrete slab is modeled using a three-node, triangular layered plate element that accounts for thickness effects. The development of this composite finite element requires discrete approximations of three key field quantities: (1) geometric configuration, (2) displacement fields, and (3) stress distributions. The proposed layered plate formulation incorporates 15 degrees of freedom (DOFs) per element, with the complete nodal configuration detailed in Figure 6.

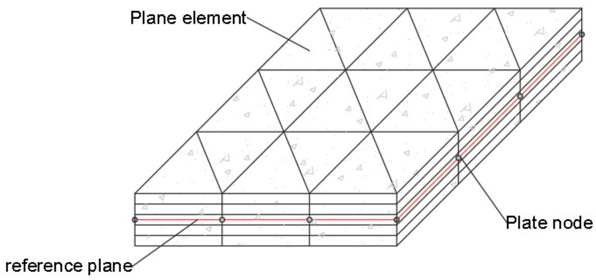

Figure 6. Meshing process of the RC slab using layered plate elements
S o u r c e: made by D.A. Mawlood.

2.7. Load Distribution Elements

The element loads are converted into equivalent nodal loads that yield identical external virtual work under virtual displacements as the original loads. This relationship is defined by Equations (10) and (15):

$$\underline{K}_e\, \underline{u}_e = \underline{F}_e \quad \text{or} \quad [K][d]=[P].$$

The reinforced concrete slab, subjected to element loads combining membrane and bending effects, can be expressed as:

$$\begin{bmatrix} K^m_{6,6} & 0 \\ 0 & K^b_{9,9} \end{bmatrix} \begin{bmatrix} d^m \\ d^b \end{bmatrix} = \begin{bmatrix} P^m \\ P^b \end{bmatrix},$$

where: d^m, d^b...membrane (u_1, u_2, u_3, v_1, v_2, v_3) and bending $(w_1, \varphi_{x1}, \varphi_{y1}, w_2, \varphi_{x2}, \varphi_{y2}, w_3, \varphi_{x3}, \varphi_{y3})$ element displacement; P^m, P^b ……membrane and bending element loads.

The nonlinear algebraic system is solved using a mixed-step iterative method that combines incremental loading with Newton — Raphson equilibrium iterations. Figures 7 and 8 illustrate how this approach applies loads incrementally while performing iterative corrections at each step to satisfy equilibrium conditions. Although the Newton-Raphson method improves solution accuracy, it requires additional computational effort.

The computational algorithm for the non-incremental Newton — Raphson method (Figure 8) executes the following sequence:

1. In the initialization phase, the structure is loaded with $\vartriangle P_1$, followed by computation of the first displacement approximation according to:

$$\overline{d}_0 = [\overline{K}_0(E_0)]^{-1} \vartriangle P_1, \tag{30}$$

where the global stiffness matrix is computed using the initial elastic modulus E_0.

2. From the computed displacements, element stresses σ (or strain ε) and updated moduli $E_i^{(N)}$ are determined. Equilibrium verification with the updated stiffness matrix yields residual forces:

$$\overline{r}_0 = \overline{K}_1(E_1)\overline{d}_0 - \vartriangle \overline{P}_1. \tag{31}$$

3. The residual forces induce corresponding corrective displacements:

$$\vartriangle \overline{d}_1 = [\overline{K}_1(E_1)]^{-1}\overline{r}_0. \tag{32}$$

4. The iterative correction process computes successive deflections $\overline{d}_1 = \overline{d}_0 + \vartriangle \overline{d}$, where each step generates residual forces $\overline{r}_2$ and displacement increments $\vartriangle \overline{d}_1$, until equilibrium is attained. The algorithm's general form is given by:

$$\begin{aligned} &\overline{r}_j = \overline{K}_{j+1}(E_{j+1})\overline{d}_j - \overline{P}; \\ &\vartriangle\overline{d}_{j+1} = [\overline{K}_{j+1}(E_{j+1})]^{-1}\overline{r}_j, \end{aligned} \quad \text{for} \quad j = 1, 2, 3... \tag{33}$$

The iterative process terminates when the residual forces diminish to a negligible magnitude. The total plate deflection is subsequently obtained through superposition of all incremental displacement components [5].

$$\overline{d} = \overline{d}_0 + \sum_{j=0}^{m} \vartriangle\overline{d}_{j+1} \,. \tag{34}$$

The described numerical procedure is successively applied to all load increments $\vartriangle P_1$ ($i = 1, 2, ..., n$).

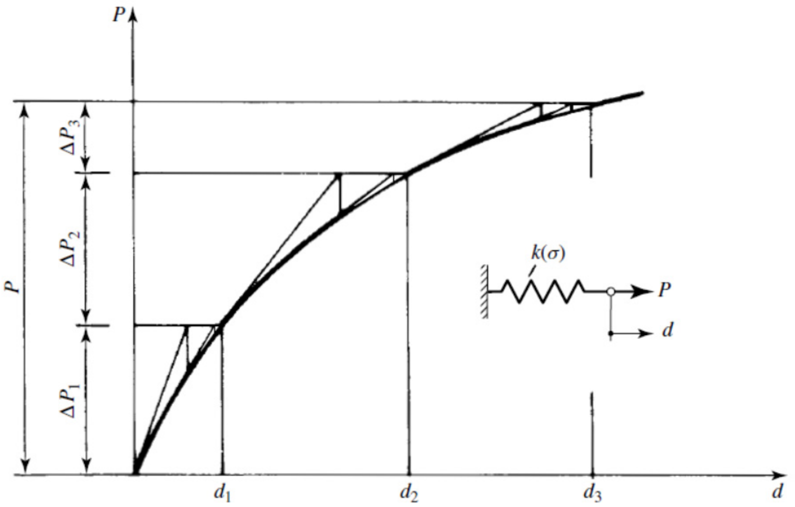

Figure 7. Step iteration or mixed procedure
S o u r c e: made by D.A. Mawlood.

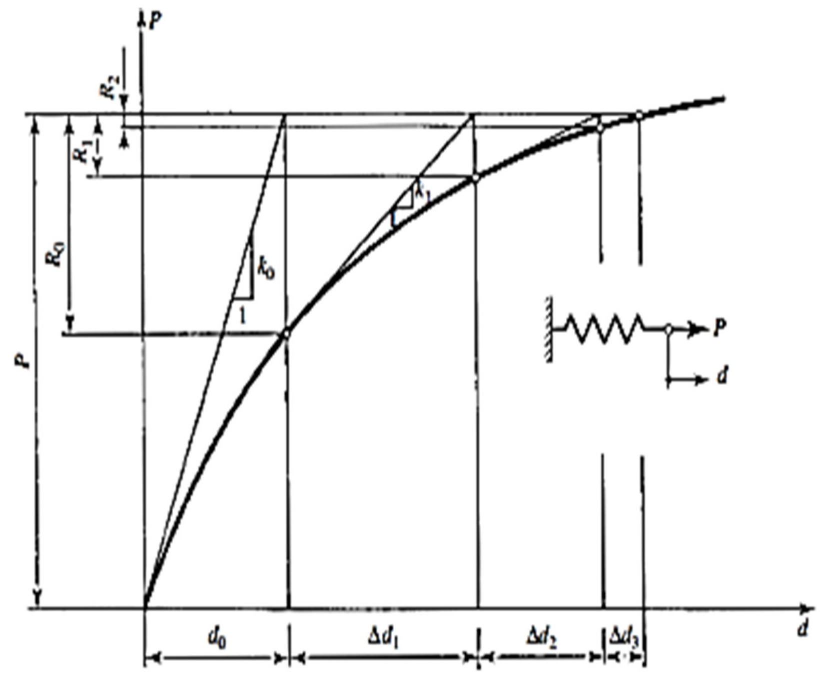

Figure 8. Iterative tangent stiffness procedure
S o u r c e: made by D.A. Mawlood.

3. Results and Discussion

This work presents a MATLAB implementation, based on the preceding theoretical framework, for nonlinear layer-wise finite element analysis specialized for triangular element formulations. To evaluate computational performance, the proposed method was applied to analyze three experimentally validated reinforced concrete slab specimens. All test cases had been previously characterized under controlled laboratory conditions, enabling direct comparison between numerical predictions and experimental results.

3.1. Analysis of One-Way Reinforced Concrete Slabs (S1)

A semi-precast one-way RC slab with dimensions 75 mm × 600 mm × 1650 mm was analyzed using the proposed layered finite element method with triangular elements. The slab incorporated mesh reinforcement consisting of 12 mm diameter steel bars spaced at 200 mm center-to-center, with a 25 mm concrete cover. Figure 9 illustrates the slab's geometric configuration, loading conditions, and boundary constraints.

The material properties were defined as follows: concrete with a modulus of elasticity of 26.420 GPa, Poisson's ratio of 0.15, and compressive strength of 31.6 MPa; steel reinforcement with an elastic modulus of 190 GPa, Poisson's ratio of 0.3, and yield stress of 535 MPa. This configuration replicates the experimental setup by Mohamed et al. [25], employing a two-point loading system with 516.7 mm spacing at mid span. The loading was applied through a hydraulic jack on a spread steel beam to create a pure bending region, with continuous load monitoring via a calibrated load cell. Strain gauges and LVDTs provided comprehensive deformation measurements through a high-frequency data acquisition system.

Taking advantage of symmetry, the finite element analysis modeled only half of the slab structure. Mesh convergence studies determined an optimal 3×4×2 grid of triangular laminated plate elements, with the thickness layered into six layers (five concrete layers and one equivalent steel layer). Figure 10 illustrates this configuration.

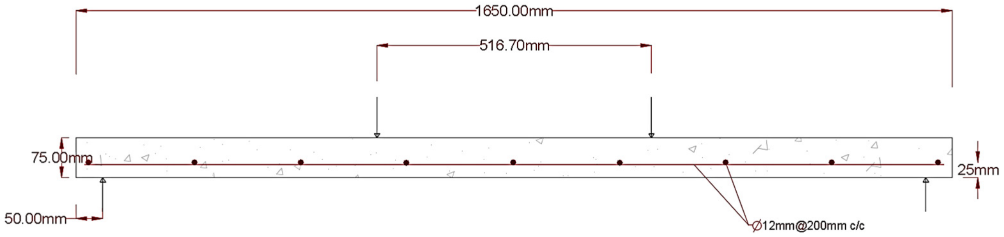

Figure 9. Schematic of the one-way RC slab: geometrical parameters, loading, and boundary conditions

S o u r c e: made by D.A. Mohamed et al. [25].

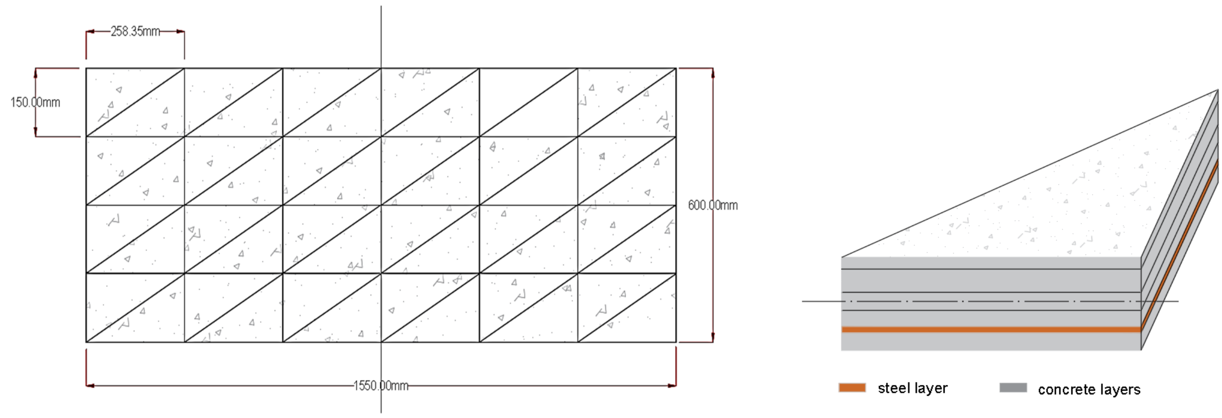

1 *2*

Figure 10. FE mesh of semi precast of reinforced concrete slab with toping concrete

1 — plan discretization; *2* — cross section discretization

S o u r c e: made by D.A. Mawlood.

Figures 11 and 12 compare the predicted load-deflection response with experimental data from Mohamed et al. and 3D ABAQUS simulations [25]. The proposed model demonstrates excellent agreement, showing a maximum deflection prediction error of 11.2% while maintaining a 99% correlation coefficient for the load-deflection relationship.

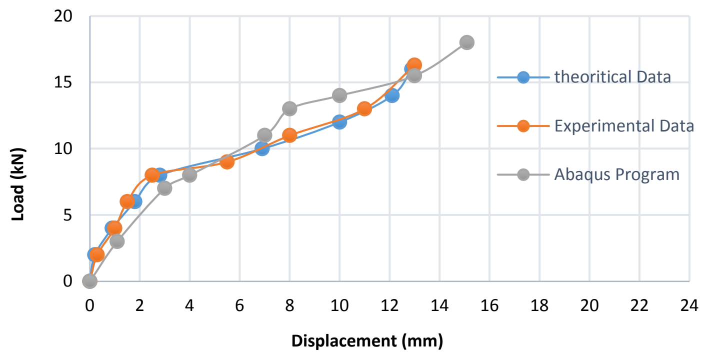

Figure 11. Load-deflection curve of the one-way RC slab at the mid-span
S o u r c e: made by D.A. Mawlood.

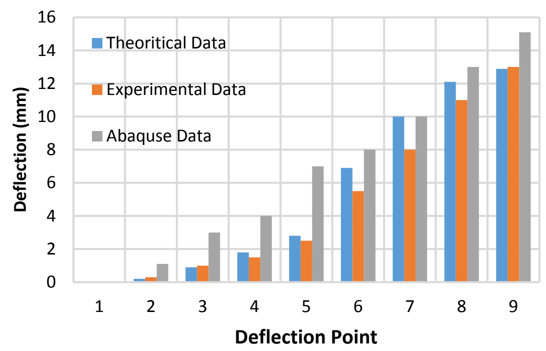

Figure 12. Deflection chat area
S o u r c e: made by D.A. Mawlood.

3.2. Two-Way Reinforced Concrete Slab with Single-Layer Reinforcement (S2)

The specimen had dimensions of 2.2 meters by 2.2 meters and a depth of 160 millimeters. All slabs had a loaded span of 2 meters in each direction, with a 0.1-meter overhang extending from the center of the supports on both sides. This study examines the two-way square reinforced concrete slab tested by Sara Nurmi et al. [26]. A point load is applied to the center of the slab, which is supported at all four corners. The tensile region of the reinforced concrete slab contains bidirectional steel reinforcement (x and y directions), with equal reinforcement ratios of $\rho_x = \rho_y = 0.23\%$. The mechanical properties of the slab are presented in Table 1, while Figure 13 depicts the geometric configuration and reinforcement arrangement. A central load was gradually applied to the slab using a hydraulic jack during testing, as conducted by Sara Nurmi et al. Deflections were measured at multiple locations, including the slab center, using LVDT sensors in Sara Nurmi's experimental setup [26].

Table 1

Material parameters of two-way slab with one layer of reinforcement

Material	Elastic modulus, MPa	Poisson's ratio	Yield stress, MPa	Compressive strength, MPa
Concrete	28,200	0.15		36
Steel	190,000	0.3	450	–

S o u r c e: made by D.A. Mawlood.

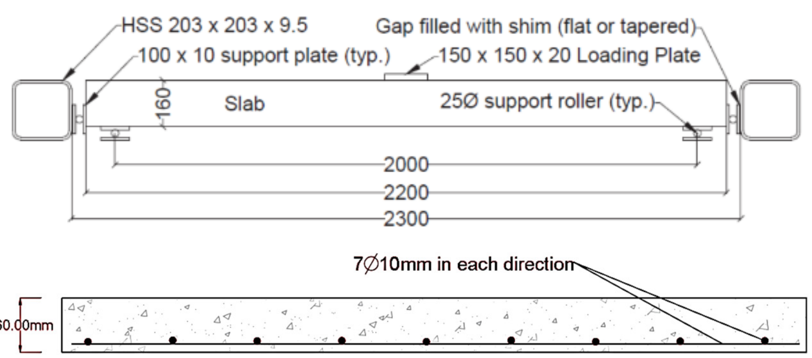

Figure 13. Geometrical parameters and reinforcement details of two way reinforced concrete slab
S o u r c e: made by Sara Nurmi's [26].

Figure 14 shows that the RC slab cross-section was discretized into five concrete layers, complemented by two equivalent steel layers representing reinforcement in orthogonal directions (*x* and *y*).

Figures 15 and 16 show the slab deflections computed using the proposed layered approach with triangular element discretization, along with the corresponding numerical results. For validation purposes, Figure 15 compares the model predictions with both experimental data from Nurmi et al. [26] and nonlinear finite element results obtained from Abaqus simulations. The comparative analysis demonstrates the effectiveness of the layered model in predicting deflection responses across the complete loading spectrum, from serviceability conditions to ultimate capacity.

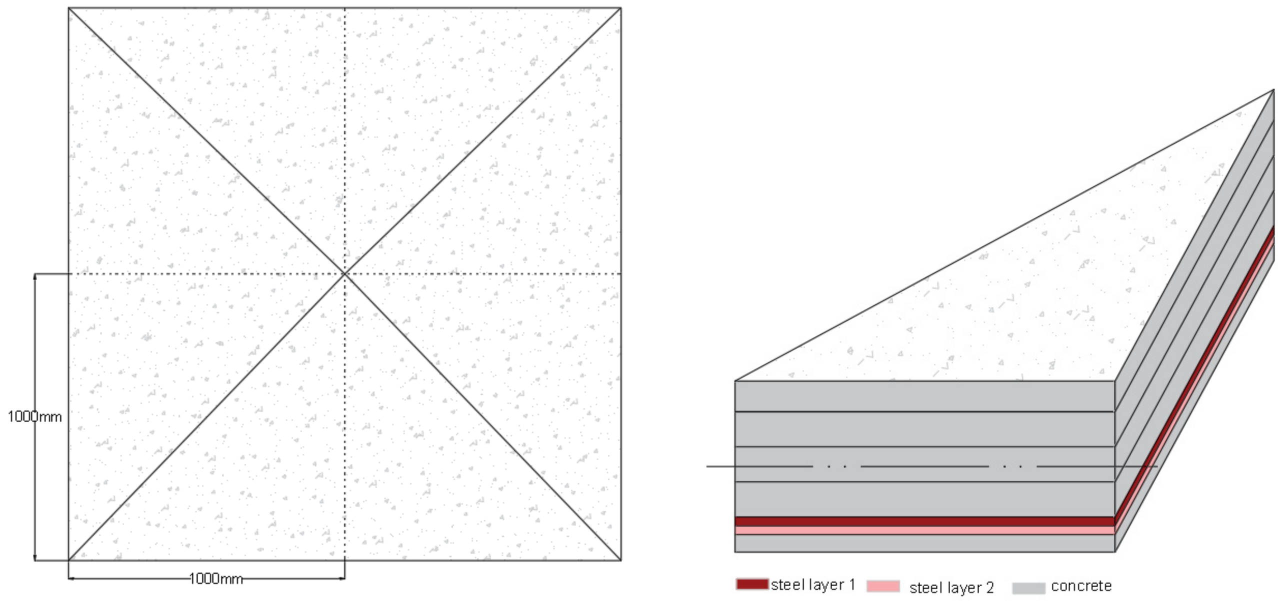

Figure 14. FE mesh of RC Slab: cross-section discretization
Source: made by D.A. Mawlood.

The benchmarking study reveals that the proposed layer method achieves superior accuracy in predicting two-way slab behavior compared to conventional Abaqus nonlinear solutions. The proposed model demonstrates excellent agreement, showing a maximum deflection prediction error of 2.59% while maintaining a 99.6% correlation coefficient for the load-deflection relationship.

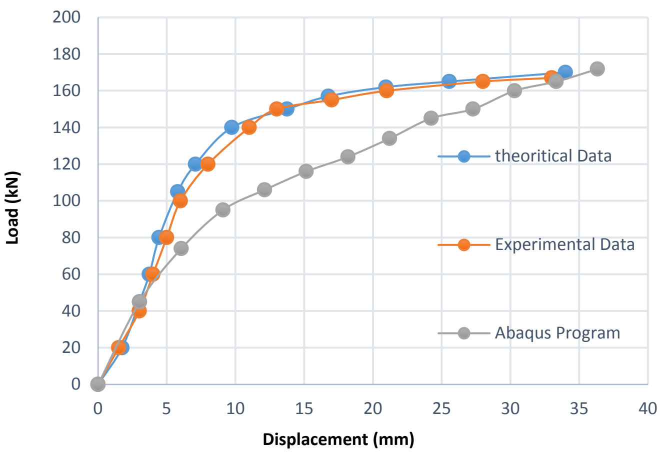

Figure 15. Load-deflection curve in the center of RC slab
Source: made by D.A. Mawlood.

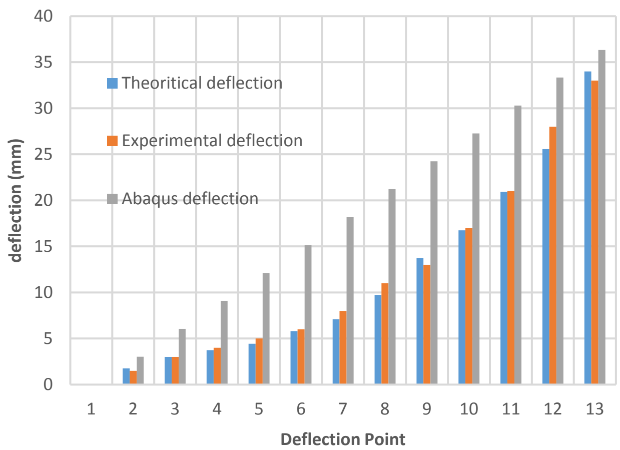

Figure 16. Deflections point
Source: made by D.A. Mawlood.

3.3. Two-Layer Reinforced Two-Way Concrete Slab (S3)

The experimental investigation conducted by Yao Xiao et al. examined a two-way RC slab system featuring dual reinforcement layers and full peripheral restraint. The test specimen comprised a 1200×1200×100 mm slab subjected to center-point loading. Key experimental parameters including material characteristics, are summarized in Table 2. The slab's reinforcement configuration consisted of orthogonal steel reinforcement distributed in both top and bottom layers, with detailed arrangement illustrated in Figure 17 [27].

Table 2

Material parameters of two-way reinforced concrete slab

Material	Elastic Modulus, MPa	Poisson's ratio	Longitude reinforcement diameter, mm	Yield stress, MPa	Compressive strength, MPa
Concrete	30,784	0.15	–	–	42.9
Steel	190,000	0.3	10	576	–

S o u r c e: made by D.A. Mawlood.

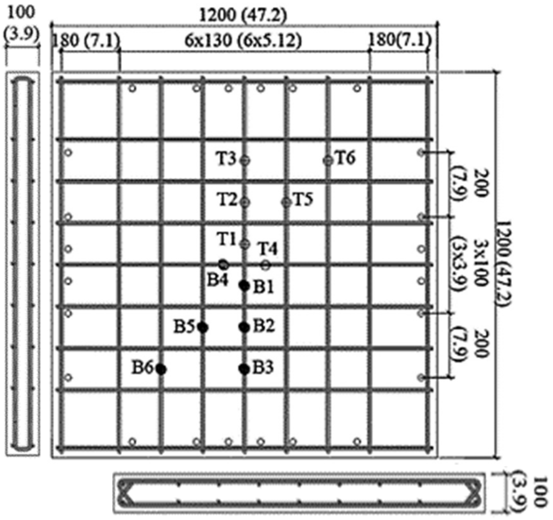

Clear cover (15 mm) and all reinforcement used diameter Φ10mm

Figure 17. Reinforced concrete slab details
S o u r c e: made by Yao Xiao et al. [27].

The two-way slab was reinforced with 10 mm diameter deformed steel bars (Grade 500) in orthogonal arrangements for both top and bottom layers, maintaining a uniform 15 mm concrete cover throughout. Figure 17 details the cross-sectional reinforcement layout and corresponding finite element discretization scheme. Figure 18 shows the load-deflection response at the slab center, capturing the complete nonlinear behavior from initial loading to ultimate capacity. This study presents the experimental results obtained by Yao Xiao et al., along with numerical results from nonlinear ABAQUS simulations and predictions from the triangular-shaped layer method. The load-deflection relationship predicted by the proposed methods shows excellent agreement with experimental observations. Compared to the nonlinear ABAQUS simulations, the triangular layer method demonstrates comparable accuracy in predicting both the ultimate load capacity and maximum deflection of the RC slab. The proposed model demonstrates a 7.32% error in maximum deflection prediction while maintaining a strong correlation coefficient of 99.6% between the predicted and experimental curves (Figures 19–20).

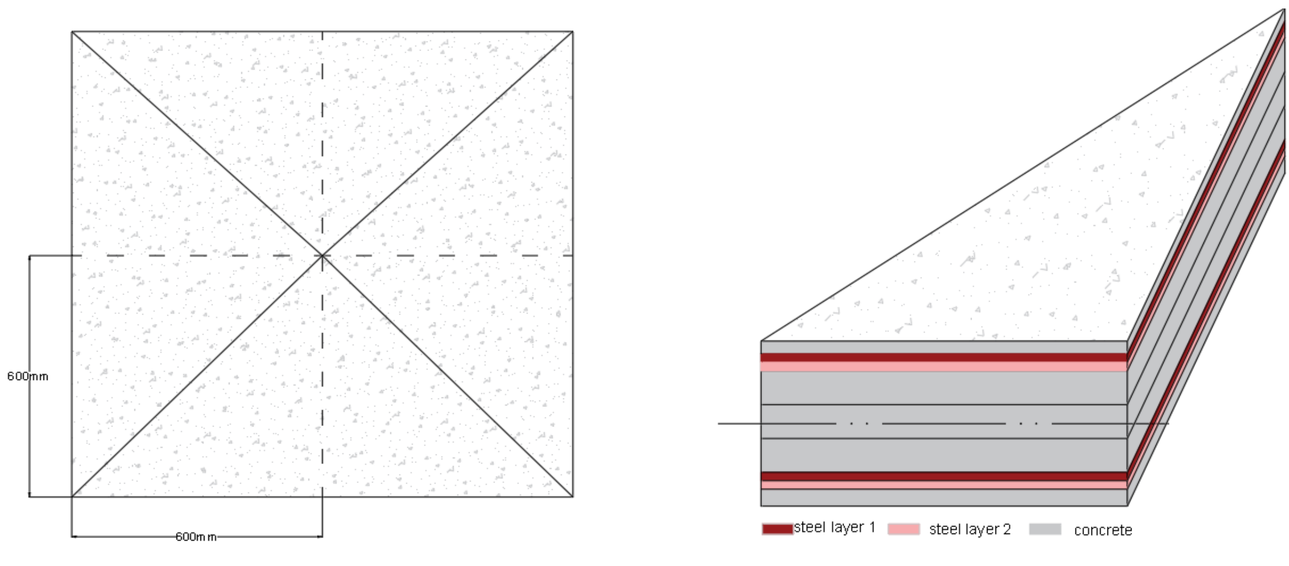

Figure 18. FE mesh of RC Slab: cross-section discretization
S o u r c e: made by D.A. Mawlood.

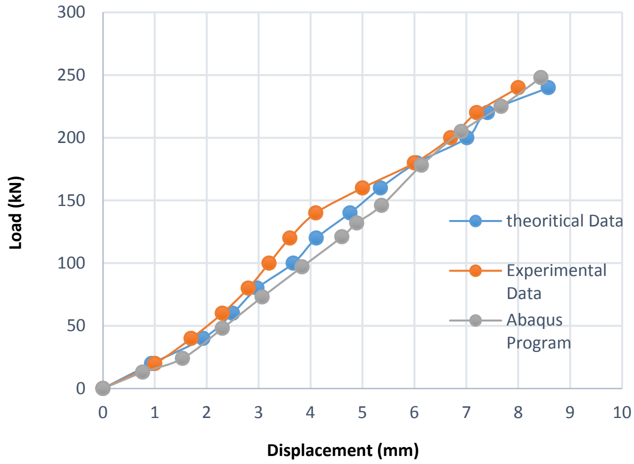

Figure 19. Load-deflection curve in the center of RC slab
S o u r c e: made by D.A. Mawlood.

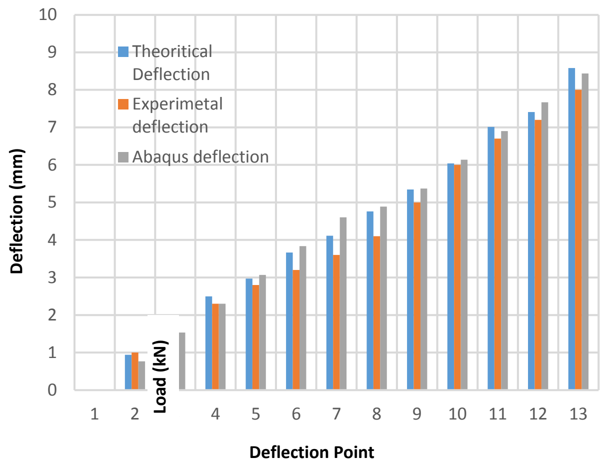

Figure 20. Deflection point
S o u r c e: made by D.A. Mawlood.

Figures 21–28 present the ABAQUS-simulated deflection patterns and stress distributions throughout the RC slab.

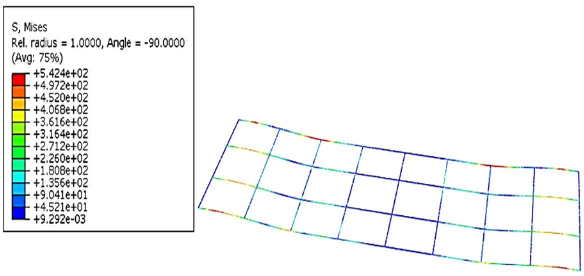

Figure 21. Stress in reinforced steel layer (S1)
S o u r c e: made by D.A. Mawlood.

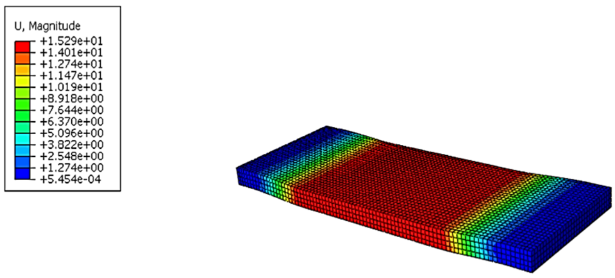

Figure 22. Deflection of concrete slab (S1)
S o u r c e: made by D.A. Mawlood.

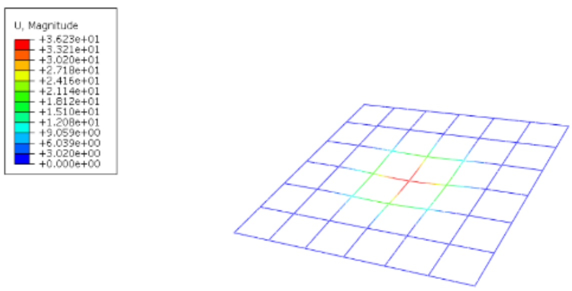

Figure 23. Effect of deflection on reinforced bars (S2)
S o u r c e: made by D.A. Mawlood.

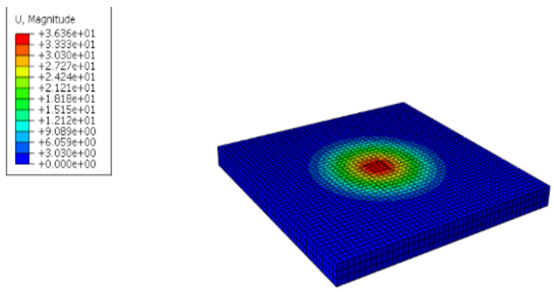

Figure 24. Effect of deflection on concrete slab (S2)
S o u r c e: made by D.A. Mawlood.

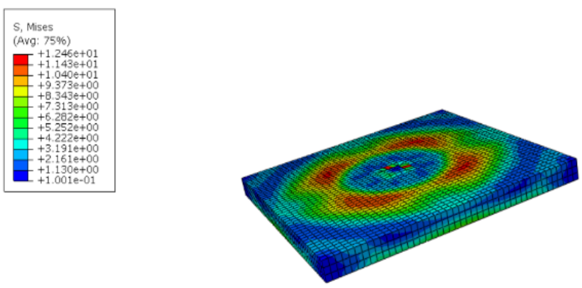

Figure 25. Effect of stress distribution on concrete slab (S2)
S o u r c e: made by D.A. Mawlood.

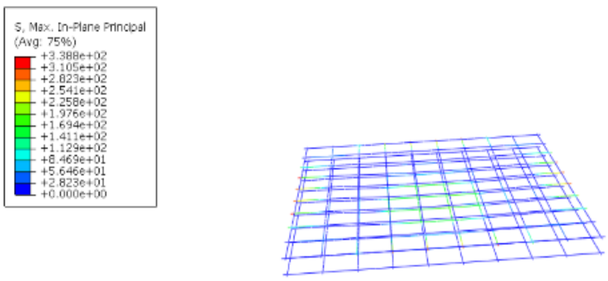

Figure 26. Stress in top and bottom reinforcement bars (S3)
S o u r c e: made by D.A. Mawlood.

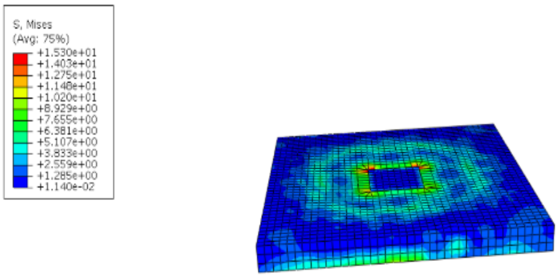

Figure 27. Stress in concrete slab (S3)
Source: made by D.A. Mawlood.

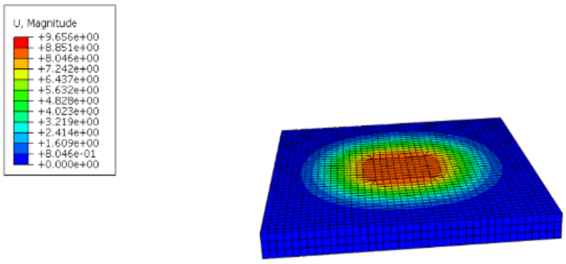

Figure 28. Deflection in concrete slab (S3)
Source: made by D.A. Mawlood.

4. Conclusion

1. The proposed triangular-layered finite element model enables direct computation of out-of-plane stress components in RC slabs, eliminating both the need for through-depth integration of equilibrium equations and the requirement for shear correction coefficients.

2. The proposed triangular-layered formulation maintains a constant number of unknown parameters for displacement and stress fields, independent of the number of layers, while preserving its layer-based framework.

3. The static nonlinear behavior of RC slabs up to failure was analyzed using a partial mixed stress-displacement variational principle combined with a three-noded triangular plate element.

4. The effectiveness of the proposed triangular-layered finite element model in predicting nonlinear structural responses was validated through comprehensive analyses of RC slabs with diverse geometries, reinforcement configurations, and boundary conditions.

5. Numerical results demonstrate that the proposed formulation accurately predicts both the ultimate load-carrying capacity and failure deflection of RC slabs.

6. Benchmark validation studies confirm the method's accuracy and computational efficiency, with ultimate deflection predictions exhibiting errors ranging from 2.59% (minimum) to 11.2% (maximum).

7. The proposed triangular-layered model accurately captures the complete load-deflection behavior of RC slabs while simultaneously predicting detailed structural responses, including deformation characteristics and stress component distributions.

8. The triangular-layered finite element model achieves an optimal balance between computational efficiency and predictive accuracy. Future work will extend this stress-displacement formulation to coupled material and geometric nonlinear analysis of reinforced concrete plate structures.

References

1. Le C.V., Ho V.Q., Ho P.L.H., Nguyen P.H. Limit state analysis of thin plates and slabs by a numerical pseudo-lower yield design approach. *Thin-Walled Structures*. 2022;172:108852. https://doi.org/10.1002/suco.202100532 EDN: BXJDTD

2. Issa M.S., Metwally I.M., Elzeiny S.M. Influence of fibers on flexural behavior and ductility of concrete beams reinforced with GFRP rebars. *Engineering Structures.* 2011;33:1754–1763. https://doi.org/10.1016/j.engstruct.2011.02.014

3. Amirkhani S., Lezgy Nazargah M. Nonlinear finite element analysis of reinforced concrete columns: Evaluation of different modeling approaches for considering stirrup confinement effects. *Structural Concrete*. 2022;23:2820–2836. https://doi.org/10.1002/suco.202100532 EDN: BXJDTD

4. Yeganeh-Salman A., Lezgy-Nazargah M. Evaluating the accuracy of mass scaling method in non-linear quasi-static finite element analysis of RC structures. *Structural Engineering and Mechanics*. 2023;85:485–500. https://doi.org/10.12989/SEM.2023.85.4.485

5. Szilard R. *Theories and applications of plate analysis: classical, numerical, and engineering methods*. Hoboken, NJ: John Wiley; 2004.

6. Werkle H. *Finite elements in structural analysis: Theoretical concepts and modeling procedures in statics and dynamics of structures*. Cham: Springer International Publ.; 2021. https://doi.org/10.1007/978-3-030-49840-5

7. Harmon T.G., Zhangyuan N. Shear strength of reinforced concrete plates and shells determined by finite element analysis using layered elements. *J Struct Eng.* 1989;115:1141–1157. https://doi.org/10.1061/(ASCE)0733-9445(1989)115:5(1141)

8. Polak M.A. Modeling punching shear of reinforced concrete slabs using layered finite elements. *SJ*. 1998;95(1): 71–80. https://doi.org/10.14359/528

9. Mahmood D., Rafiq S., Adbullah M. Nonlinear 3D Finite element model for square composite columns under various parameters. *Iraqi Journal of Civil Engineering.* 2022;16:19–28. https://doi.org/10.37650/ijce.2022.172882 EDN: NRXGDK

10. Mawlood D., Rafiq S. Nonlinear 3D Finite element model for round composite columns under various eccentricity loads. *Engineering and Technology Journal*. 2022;40:1605–1614. https://doi.org/10.30684/etj.2022.133106.1168 EDN: QTWLPF

11. Mittelstedt C. *Basics of elasticity theory. Theory of plates and shells*. Berlin, Heidelberg: Springer Berlin Heidelberg; 2023. p. 3–57. https://doi.org/10.1007/978-3-662-66805-4_1

12. Timošenko S.P., Woinowsky-Krieger S. *Theory of plates and shells*. 2nd. ed., [Nachdr.]. New York: McGraw-Hill; 1996.

13. Oñate E. *Structural analysis with the finite element method: linear statics.* Dordrecht London: Springer; 2009.

14. Jiang J., Mirza F.A. Nonlinear analysis of reinforced concrete slabs by a discrete finite element approach. *Computers & Structures.* 1997;65:585–592. https://doi.org/10.1016/S0045-7949(94)E0269-8

15. Saiah B., Bachene M., Guemana M., Chiker Y., Attaf B. On the free vibration behavior of nanocomposite laminated plates contained piece-wise functionally graded graphene-reinforced composite plies. *Engineering Structures*. 2022; 253:113784. https://doi.org/10.1016/j.engstruct.2021.113784 EDN: IKFKRC

16. Rodrigues Da Silva A., Paulo De Souza Rosa J. Nonlinear numerical analysis of prestressed concrete beams and slabs. *Engineering Structures*. 2020;223:111187. https://doi.org/10.1016/j.engstruct.2020.111187 EDN: AYEZIR

17. Van Vinh P., Avcar M., Belarbi M.-O., Tounsi A., Quang Huy L. A new higher-order mixed four-node quadrilateral finite element for static bending analysis of functionally graded plates. *Structures.* 2023;47:1595–1612. https://doi.org/10.1016/j.istruc.2022.11.113 EDN: GLXCXE

18. Cinefra M., Kumar S.K., Carrera E. MITC9 Shell elements based on RMVT and CUF for the analysis of laminated composite plates and shells. *Composite Structures*. 2019;209:383–90. https://doi.org/10.1016/j.compstruct.2018.10.039 EDN: WUDZCK

19. Moleiro F., Mota Soares C.M., Mota Soares C.A., Reddy J.N. A layerwise mixed least-squares finite element model for static analysis of multilayered composite plates. *Computers & Structures.* 2011;89:1730–1742. https://doi.org/10.1016/j.compstruc.2010.10.008

20. Liguori F.S., Corrado A., Bilotta A., Madeo A. A layer-wise plasticity-based approach for the analysis of reinforced concrete shell structures using a mixed finite element. *Engineering Structures*. 2023;285:116045. https://doi.org/10.1016/j.engstruct.2023.116045 EDN: XEVDXS

21. Wang R., Fang Z., Lezgy-Nazargah M., Khosravi H. Nonlinear analysis of reinforced concrete slabs using a quasi-3D mixed finite element formulation. *Engineering Structures.* 2023;294:116781. https://doi.org/10.1016/j.engstruct.2023.116781 EDN: HKKQXZ

22. Zhang Y.-G., Lu M.-W., Hwang K.-C. Finite element modeling of reinforced concrete structures. *Finite Elements in Analysis and Design.* 1994;18:51–8. https://doi.org/10.1016/0168-874X(94)90089-2

23. Zhang Y.X., Bradford M.A., Gilbert R.I. A new triangular layered plate element for the non-linear analysis of reinforced concrete slabs. *Commun Numer Meth Engng.* 2005;22:699–709. https://doi.org/10.1002/cnm.840

24. Willam K., Pramono E., Sture S. Fundamental issues of smeared crack models. In: Shah SP, Swartz SE, editors. *Fracture of Concrete and Rock.* New York, NY: Springer New York; 1989. p. 142–157. https://doi.org/10.1007/978-1-4612-3578-1_15

25. Mohamed M.S., Thamboo J.A., Jeyakaran T. Experimental and numerical assessment of the flexural behaviour of semi-precast-reinforced concrete slabs. *Advances in Structural Engineering.* 2020;23:1865–1879. https://doi.org/10.1177/1369433220904011 EDN: GDQHBJ

26. Nurmi S., Hoult N.A., Howell S.D. Distributed strain monitoring of two-way slabs. *Engineering Structures*. 2019;189:580–588. https://doi.org/10.1016/j.engstruct.2019.04.002

27. Xiao Y., Li B., Fujikake K. Experimental study of reinforced concrete slabs under different loading rates. *ACI Structural Journal.* 2016;113. https://doi.org/10.14359/51688067

Строительная механика инженерных конструкций и сооружений
Structural Mechanics of Engineering Constructions and Buildings

2025. 21(5). 462–473

ISSN 1815-5235 (Print), 2587-8700 (Online)

HTTP://JOURNALS.RUDN.RU/STRUCTURAL-MECHANICS

DOI: 10.22363/1815-5235-2025-21-5-462-473
EDN: DFDCNF

Научная статья / Research article

Численное моделирование формоизменения гибких стержней

П.П. Гайджуров✉, Н.Б. Даник, А.В. Климух

Донской государственный технический университет (ДГТУ), *Ростов-на-Дону, Российская Федерация*
✉ gpp-161@yandex.ru

Поступила в редакцию: 20 июня 2025 г.
Доработана: 15 сентября 2025 г.
Принята к публикации: 1 октября 2025 г.

Аннотация. Объект исследования — гибкие стержни, испытывающие в процессе нагружения большие перемещения и малые деформации. Цель исследования — численный анализ напряженно-деформированного состояния (НДС) гибких стержней с учетом геометрической нелинейности в трехмерной постановке. В качестве математического аппарата использован метод конечных элементов в форме метода перемещений. Процесс формоизменения стержня моделировался путем инкрементального нагружения в сочетании с перестроением геометрии модели с учетом полученных перемещений. Стержень моделировался набором прямолинейных балочных конечных элементов, соединенных в смежных узлах линейными и поворотными комбинированными элементами с переменной жесткостью. Для проведения вычислительных экспериментов написаны и верифицированы макросы на языке APDL, встроенного в программный комплекс ANSYS Mechanical. Выполнены вычислительные эксперименты с применением конечно-элементных моделей с упругими шарнирными вставками и без шарнирных вставок. На основании полученных результатов установлено, что предлагаемый прямой инкрементальный алгоритм решения геометрически нелинейных задач строительной механики является абсолютно сходящимся. Разработанная методика назначения жесткостей поворотных пружин может быть использована при моделировании пространственных кинематически изменяемых стержневых систем.

Ключевые слова: гибкие стержни, метод конечных элементов, геометрическая нелинейность, прямой инкрементальный метод

Заявление о конфликте интересов. Авторы заявляют об отсутствии конфликта интересов.

Вклад авторов: *Гайджуров П.П.*— научное руководство; формализация математической модели; написание исходного текста статьи; формулировка выводов; *Даник Н.Б.* — выполнение вычислительных экспериментов; обзор литературы по теме исследования; практические рекомендации по расчетам; *Климух А.В.* — обзор литературы; подготовка исходных данных; обработка результатов моделирования, оформление рисунков. Все авторы ознакомлены с окончательной версией статьи и одобрили ее.

Благодарности. Авторы выражают благодарность редакции за рекомендации, позволившие повысить качество статьи.

Для цитирования: *Гайджуров П.П., Даник Н.Б., Климух А.В.* Численное моделирование формоизменения гибких стержней // Строительная механика инженерных конструкций и сооружений. 2025. Т. 21. № 5. С. 462–473. http://doi.org/10.22363/1815-5235-2025-21-5-462-473 EDN: DFDCNF

Гайджуров Пётр Павлович, советник РААСН, доктор технических наук, профессор кафедры строительной механики и теории сооружений, Донской государственный технический университет, Российская Федерация, 344010, г. Ростов-на-Дону, пл. Гагарина, д. 1; eLIBRARY SPIN-код: 6812-9718, ORCID: 0000-0003-3913-9694; e-mail: gpp-161@yandex.ru

Даник Никита Борисович, аспирант кафедры строительной механики и теории сооружений, Донской государственный технический университет, Российская Федерация, 344010, г. Ростов-на-Дону, пл. Гагарина, д. 1; ORCID: 0009-0007-3766-6913; e-mail: danik3777@mail.ru

Климух Александр Витальевич, аспирант кафедры строительной механики и теории сооружений, Донской государственный технический университет, Российская Федерация, 344010, г. Ростов-на-Дону, пл. Гагарина, д. 1; ORCID: 0009-0001-8844-2123; e-mail: sancho.klimukh.96@mail.ru

Numerical Modeling of Change of Shape of Flexible Bars

Peter P. Gaidzhurov✉, **Nikita B. Danik**, **Alexander V. Klimukh**

Don State Technical University (DSTU), *Rostov-on-Don, Moscow, Russian Federation*
✉ gpp-161@yandex.ru

Received: June 20, 2025
Revised: September 15, 2025
Accepted: October 1, 2025

Abstract. Flexible bars experiencing large displacements and small strains during loading are investigated. The purpose of the study: numerical analysis of the stress-strain state of flexible bars, taking into account geometric nonlinearity in a three-dimensional formulation. The displacement-based finite element method is used as the mathematical framework. The process of shape changing of the bar was modeled by incremental loading in combination with the restructuring of the geometry of the model, taking into account the resulting displacements. The bar was modeled using rectilinear beam finite elements connected at adjacent nodes by linear and rotational combined elements with variable stiffness. To conduct computational experiments, macros in the APDL language, embedded in the ANSYS Mechanical software, were written and verified. Numerical experiments were performed using finite element models with elastic hinges and without hinges. Based on the results obtained, it is established that the proposed direct incremental algorithm for solving geometrically nonlinear problems of structural mechanics is absolutely convergent. The developed method of defining the stiffness of rotational springs can be used in modeling spatial unstable frames.

Keywords: flexible bars, finite element method, geometric nonlinearity, direct incremental method

Conflicts of interest. The authors declare no conflict of interest.

Authors' contribution: *Gaidzhurov P.P.* — scientific guidance; formalization of the mathematical model; writing the source text of the article; formulation of conclusions; *Danik N.B.* — performing computational experiments; literature review on the research topic; practical recommendations on calculations; *Klimukh A.V.* — literature review; preparation of initial data; processing of modeling results, design of drawings. All authors read and approved the final version of the article.

Благодарности. Авторы выражают благодарность редакции за рекомендации, позволившие повысить качество статьи.

For citation: Gaidzhurov P.P., Danik N.B., Klimukh A.V. Numerical modeling of change of shape of flexible bars. *Structural Mechanics of Engineering Constructions and Buildings.* 2025;21(5):462–473. (In Russ.) http://doi.org/10.22363/1815-5235-2025-21-5-462-473
EDN: DFDCNF

1. Введение

Упругие гибкие стержни, обладающие изгибной жесткостью, находят широкое применение в расчетных схемах газопроводов, несущих канатов большепролетных висячих мостов, трансмиссионных валов различного назначения, приводов измерительных приборов, пространственных строительных конструкций [1–3]. Конечно-элементное моделирование пространственных стержневых систем базируется на использовании матрицы жесткости балочного конечного элемента (КЭ) с шестью степенями свободы в узле[1] [4]. Как правило, при линейном анализе перемещения углы поворота балочного КЭ считаются малыми. Вместе с тем при расчете гибких стержней имеют место большие линейные и угловые перемещения при малых деформациях [5; 6]. В этом случае численное решение геометрически нелинейной задачи строится на базе итерационной процедуры Ньютона — Рафсона и метода «корректирующих дуг», суть последнего состоит в адаптивной корректировке величины шага нагружения при приближении и после прохождения точки «бифуркации» [7–10]. Следует отметить, что при расчете стрежневой системы методом конечных элементов с учетом больших переме-

[1] *Мяченков В.И., Мальцев В.П., Майборода В.П. и др.* Расчеты машиностроительных конструкций методом конечных элементов : справочник. Москва : Машиностроение, 1989. 520 с.

Peter P. Gaidzhurov, Advisor of the Russian Academy of Architecture and Construction Sciences, Doctor of Technical Sciences, Professor of the Department of Structural Mechanics and Theory of Structures, Don State Technical University, 1 Gagarin Sq., Rostov-on-Don, 344003, Russian Federation; eLIBRARY SPIN-code: 6812-9718, ORCID: 0000-0003-3913-9694; e-mail: gpp-161@yandex.ru

Nikita B. Danik, Postgraduate Student of the Department of Structural Mechanics and Theory of Structures, Don State Technical University, 1 Gagarin Sq., Rostov-on-Don, 344003, Russian Federation; ORCID: 0009-0007-3766-6913; e-mail: danik3777@mail.ru

Alexander V. Klimukh, Postgraduate Student of the Department of Structural Mechanics and Theory of Structures, Don State Technical University, 1 Gagarin Sq., Rostov-on-Don, 344003, Russian Federation; ORCID: 0009-0001-8844-2123; e-mail: sancho.klimukh.96@mail.ru

щений используется касательная матрица жесткости. Общепринятый подход к построению данной матрицы в лагранжевых координатах базируется на минимизации потенциала энергии деформации дискретной модели [11]:

$$\frac{\partial \Pi}{\partial u_m} = f_m(u_1, u_2, \dots, u_N) = 0, \ (1 \le m \le N),$$

где Π — потенциальная энергия деформации; $u_1, u_2, \dots, u_N$ — обобщенные перемещения. В результате линеаризованная (касательная) матрица жесткости конструкции получает вид

$$[K'] = \left[\sum_{n=1}^{N} \frac{\partial f_m(u_1, u_2, \dots, u_N)}{\partial u_n} \Bigg|_{\{u\}=\{u^0\}} \right].$$

При этом рекуррентная формула Ньютона — Рафсона принимает форму

$$[K']\{\Delta u\} + \{f\} = 0, \ \left\{u^{(n+1)}\right\} = \left\{u^{(n)}\right\} + \left\{\Delta u^{(n)}\right\} = \left\{u^{(n)}\right\} - \left[K'_{(n)}\right]^{-1}\left\{f^{(n)}\right\},$$

где $\{f\}$ — вектор обобщенных сил.

В [7] для минимизации потенциала энергии деформации применено следующее уравнение (использованы ранее принятые обозначения):

$$\left[\frac{\partial^2 \Pi}{\partial \{u\}^2}\right] \Delta\{u\} + \frac{\partial \Pi}{\partial \{u\}} = \{f\}^{(e)}.$$

Отмечается, что в структуре приведенного уравнения первое слагаемое является аналогом матрицы жесткости КЭ, а второе слагаемое представляет собой корректирующую составляющую для вектора узловых сил. Вычисление касательной матрицы жесткости КЭ сводится к двукратному дифференцированию энергии деформаций по обобщенным перемещениям, а вычисление корректирующей составляющей вектора упругих сил КЭ — к соответствующему однократному дифференцированию.

Следует отметить, что при численных расчетах гибких стержней в геометрически нелинейной постановке активизируется одновременно учет больших поворотов и уменьшение жесткости, обусловленное формоизменением [9; 10].

Альтернативным упрощенным методом расчета гибких упругих стержней является представление стержня набором прямолинейных балочных КЭ одинаковой длины, соединенных пружинами. Пример балочно-пружинной схемы консольного стержня показан на рис. 1[2].

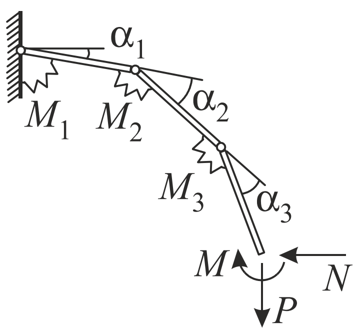

Рис. 1. Балочно-пружинная схема гибкого стержня
Источник: автор В.И. Усюкин.

Figure 1. Beam-spring diagram of a flexible bar
Source: author V.I. Usyukin.

Полагается, что между узловым моментом M_i и соответствующим углом поворота α_i существует линейная зависимость

$$M_i = k\alpha_i, \ i = 1, 2, 3,$$

где k — коэффициент пропорциональности, характеризующий в данном случае жесткость поворотной пружины. Для расчета гибких стержней в двумерной постановке[3] использован следующий функционал:

[2] *Усюкин В.И.* Строительная механика конструкций космической техники : учебник для студентов вузов. Москва : Машиностроение, 1988. 392 с. ISBN 5-217-00147-X

$$Э=\int_0^l \frac{1}{2}\frac{M^2}{EJ}dx-\sum_i\left(M_i\alpha_i\right)_{x=x_i}+\Pi .$$

При этом считается, что жесткость поворотных пружин прямо пропорциональна изгибной жесткости стержня.

В [12] на базе концепции локальности линейных перемещений и ортогональности виртуальных углов поворотов стержневого КЭ представлена методика конечно-элементного моделирования гибких составных балок, подвергающихся значительным статическим и динамическим деформациям. Отмечается, что разработанный конечный элемент позволяет с высокой точностью учесть геометрическую нелинейность в сочетании с начальной погибью составной балочной конструкции. Алгоритм построения матрицы жесткости балочного конечного элемента трубчатого сечения, основанный на гипотезе Эйлера — Бернулли, в сочетании с аппроксимациями перемещений с помощью полиномов Эрмита предложен в [13]. Для учета геометрической нелинейности введен тензор напряжений Пиолы — Кирхгофа и тензор деформаций Грина — Лагранжа.

Для решения задач механики оболочек с учетом конечных перемещений В.З. Власов[4] разработал метод последовательных нагружений. Суть метода состоит в последовательном нагружении конструкции внешними силами, подобранными таким образом, чтобы на каждом шаге перемещения и углы поворота оставались малыми. В дальнейшем этот метод В.А. Светлицкий [6] распространил на криволинейные линейно упругие гибкие стержни. В [14] приведен вариант метода последовательных нагружений для решения плоских задач механики гибких стержней. Здесь же отмечается, что данный подход может быть распространен и на пространственные стержни со сложной геометрией.

Оригинальный метод конечно-элементного моделирования стержневых систем в условиях больших перемещений и углов поворота предложен в [15]. Данный метод, названный метод материальной точки (Material Point Method), базируется на построении уравнения состояния механической системы, обладающей существенной геометрической нелинейностью, в гибридных лагранжево-эйлеровых координатах. При этом геометрия модели задается в лагранжевых (материальных) координатах, а уравнение движения решается с использованием фиксированной эйлеровой (фоновой) координатной сетки.

В [16] разработана 2D-модель ферменной конструкции, состоящей из упругих нерастяжимых стержней, связанных между собой на концах упруговязкими узловыми шарнирами, допускающими большие углы поворота. Отмечается, что формоизменение ферменной конструкции из начального положения в конечное рабочее осуществляется с помощью кинематического воздействия, имитирующего трос с изменяемой длиной.

Постановка задачи контактного взаимодействия деформируемых строительных конструкций с учетом трения при сдвиге рассмотрена в [17]. Предлагаемый подход базируется на шаговом алгоритме Лемке в виде метода перемещений.

Резюмируя, можно отметить, что рассмотренные способы численного анализа НДС гибких стержней не позволяют выполнить моделирование процесса формоизменения пространственной конструкции с регулярной решетчатой структурой при управляемом кинематическом воздействии. Для конечно-элементного моделирования таких конструкционных решений требуется разработка принципиально нового подхода, базирующегося на концепции универсальной дискретно стержневой схемы с упруго-шарнирными узловыми соединениями.

В качестве *объекта настоящего исследования* в общем случае рассмотрен пространственный гибкий стержень в условиях больших перемещений, сопровождающихся малыми деформациями. *Цель исследования* — разработка линейно упругой механико-математической модели геометрически нелинейного формоизменения исходной геометрии гибкого стержня на основе модифицированного ме-

[3] *Усюкин В.И.* Строительная механика конструкций космической техники : учебник для студентов вузов. Москва : Машиностроение, 1988. 392 с. ISBN 5-217-00147-X

[4] *Власов В.З.* Избранные труды. Общая теория оболочек. Т. 1. Москва : Изд-во Академии наук СССР, 1962. 528 с.

тода Лагранжа, суть которого состояла в пошаговом перестроении конечно-элементной сетки с учетом полученных инкрементальных перемещений. В *задачи исследования* входило построение балочно-пружинной механической модели путем введения в смежных узлах дискретной стержневой модели трехмерных блоков из комбинированных конечных элементов в виде линейных и поворотных пружин; написание и отладка макроса на языке APDL программного комплекса ANSYS Mechanical[5], позволяющего удалять и заново строить конечно-элементную сетку с сохранением исходной топологии модели; тарирование жесткостей комбинированных элементов; решение тестовых задач.

2. Метод исследования

Конечно-элементное моделирование линейно упругой деформации гибкого стержня с учетом больших перемещений при статическом нагружении выполнялось в среде программного комплекса ANSYS Mechanical. Стержень разбивался на пространственные (3D) двухузловые балочные конечные элементы. В дальнейшем были рассмотрены две конечно-элементные модели узловых соединений: обычная модель, связывающая узловые перемещения и углы поворота смежных КЭ, и модель, в которой балочные элементы соединялись в смежных узлах с помощью комбинированных (пружинных) КЭ. Процесс трансформации формы стержня из исходного состояния в конечное представлялся в виде последовательности шагов. На каждом шаге выполнялась коррекция и перестроение геометрии сетки с учетом полученных перемещений на предыдущем шаге. При перестроении исходная топологическая информация модели полностью сохранялась. В общем случае координаты в узлах i и j КЭ на k-м шаге нагружения вычислялись по формулам (рис. 2):

$$x_s^{(k)} = x_s^{(k-1)} + \Delta u_{x_s}^{(k)}\ ,\ y_s^{(k)} = y_s^{(k-1)} + \Delta u_{y_s}^{(k)}\ ,\ z_s^{(k)} = z_s^{(k-1)} + \Delta u_{z_s}^{(k)}\ ,\ s = i, j\ .$$

Для написания макросов использовался язык программирования APDL, встроенный в ANSYS. Блок-схема макроса, реализующего инкрементальное нагружение и коррекцию узловых перемещений КЭ, представлена на рис. 3.

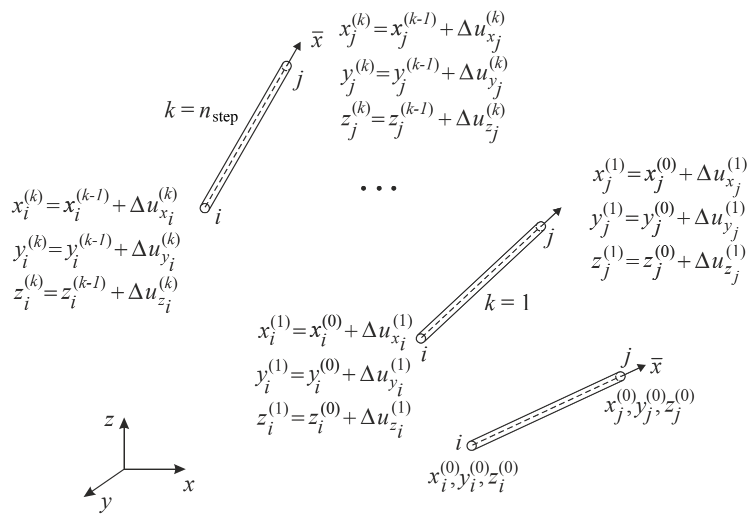

Рис. 2. Схема трансформации геометрии балочного КЭ (n_{step} — число шагов нагружения)
Источник: выполнено П.П. Гайджуровым.

Figure 2. The diagram of transformation of the geometry of the beam finite element
(n_{step} — the number of loading steps)
Source: made by P.P. Gaidzhurov.

[5] ANSYS Mechanical APDL Tutorials. URL: http://www.worldcolleges.info/sites/default/files/me1.pdf (accessed: 21.04.2025).

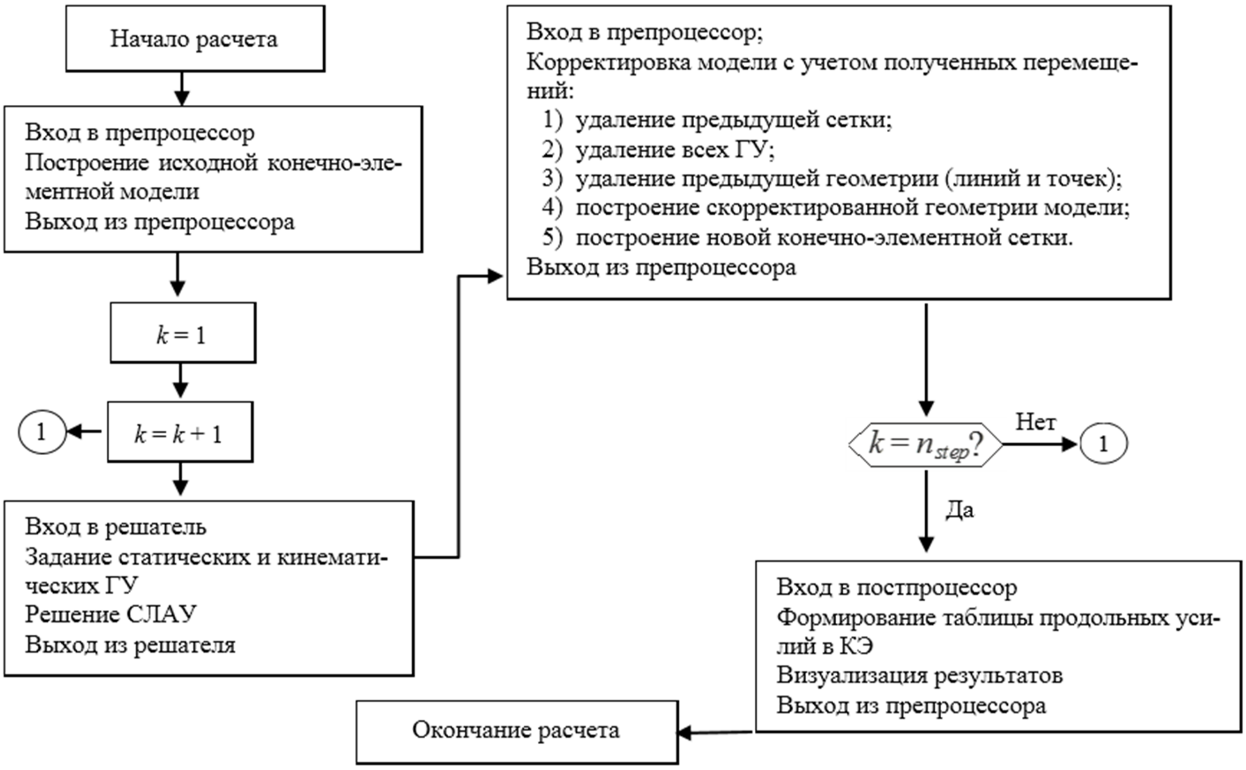

Рис. 3. Блок-схема макроса для расчета стержня с учетом корректировки геометрии:
ГУ — граничные условия; СЛАУ — система линейных алгебраических уравнений

Источник: выполнено П.П. Гайджуровым.

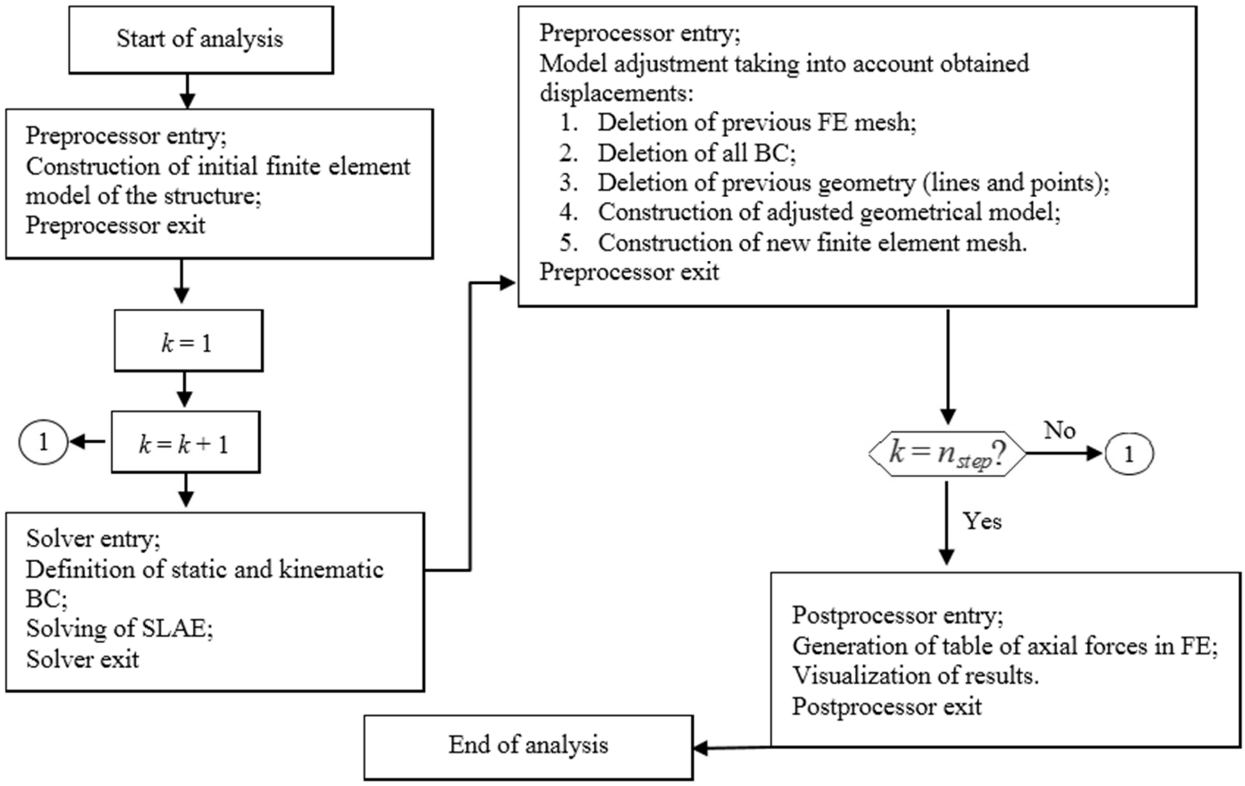

Figure 3. Flow diagram of the macro for calculating bars, taking into account geometry adjustments:
BC — boundary conditions; SLAE — system of linear algebraic equations

Source: made by P.P. Gaidzhurov.

Главным недостатком предлагаемого подхода к конечно-элементному моделированию формоизменения гибкого стержня является то, что при таком анализе НДС не учитываются осевые повороты (вращение) балочных элементов «как жесткое целое». Вместе с тем разработанный прямой инкрементальный метод расчета гибких стержней в силу своего детерминизма является, безусловно, сходящимся.

3. Результаты и обсуждение

С целью валидации разработанной математической модели формоизменения гибкого стержня, а также оценки сходимости предлагаемого вычислительного алгоритма, базирующегося на инкрементальной схеме процесса нагружения и соответствующем перестроении конечно-элементной сетки, решены тестовые примеры.

Пример 1. Расчет консольного стержня, загруженного на свободном конце сосредоточенной силой. Исходные данные: длина консоли $l = 1$ м; квадратное поперечное сечение со стороной $a = 0{,}01$ м; величина сосредоточенной силы $F = 0{,}04167$ Н. Полагалось, что в процессе деформирования консоли направление силы не изменяется. Для конечно-элементного моделирования использовался пространственный балочный КЭ с шестью степенями свободы в узле. Рассматривались две конечно-элементные модели консоли: 1 — разбивка на «стандартные» прямолинейные КЭ одинаковой длины; 2 — разбивка на недеформируемые прямолинейные КЭ одинаковой длины. Для обеих моделей смежные узлы КЭ соединялись с помощью упругих шарниров (рис. 4). Модули упругости материала балочного КЭ для первой и второй моделей: $E^{(1)} = 10^7$ Н/м² и $E^{(2)} = 10^{15}$ Н/м². Значения жесткостей упругих шарниров (рис. 4):

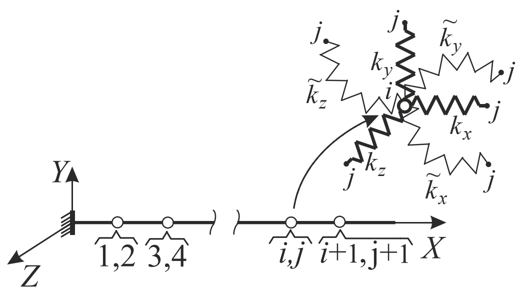

Рис. 4. Схема стержня с блоками упругих шарниров
Источник: выполнено П.П. Гайджуровым.

Figure 4. Diagram of a bar with blocks of elastic hinges
Source: made by P.P. Gaidzhurov.

$k_{x,z} = 1.0$ Н/м;

$k_y = 10^7$ Н/м;

$\tilde{k}_{x,y} = 1.0$ Н·м/рад;

для 4 КЭ $\tilde{k}_z = 0.03333$ Н·м/рад;

для 8 КЭ $\tilde{k}_z = 0.06667$ Н·м/рад.

Вычисление эквивалентной жесткости поворотной пружины выполнялось по формуле

$$\tilde{k}_z = (E^{(1)} J) / l_i,$$

где l_i — длина КЭ.

Визуализация консоли до и после деформации представлена на рис. 5. На этом рисунке x_l и y_l — результирующие координаты точки приложения сосредоточенной силы F.

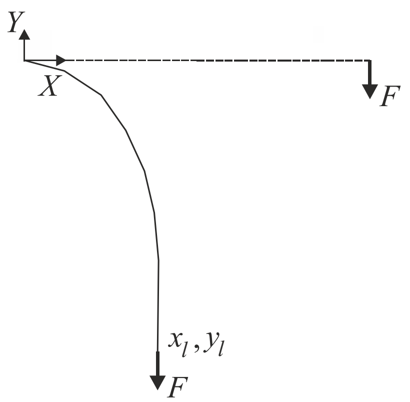

Рис. 5. Визуализация деформации гибкого консольного стержня
Источник: выполнено П.П. Гайджуровым.

Figure 5. Visualization of the deformation of a flexible cantilever bar
Source: made by P.P. Gaidzhurov.

Из графиков на рис. 6, *б* и 7, *б* видно, что уменьшение шага разбивки приводит к заметному уменьшению жесткости конечно-элементной модели консоли.

Этот эффект не наблюдается при использовании первой модели (рис. 6, *а* и 7, *а*). Из анализа представленных графиков $x_l \sim n_{\text{step}}$ и $y_l \sim n_{\text{step}}$ также следует, что процесс является монотонно сходящимся. После $n_{\text{step}} = 100$ уточнение величин x_l и y_l для обеих моделей происходит только в третьем знаке.

Для сравнения в табл. 1 приведены значения x_l и y_l, полученные для аналогичных моделей консоли с использованием нелинейного решателя комплекса ANSYS.

Таблица 1 / Table 1

Значения x_l и y_l консоли / Cantilever beam values x_l and y_l

Тип модели / Model Type	x_l, м / m		y_l, м / m	
	4 КЭ / FE	8 КЭ / FE	4 КЭ / FE	8 КЭ / FE
1	0,6121	0,6123	–0,7199	–0,7153
2	0,7362	0,5515	Процесс не сходится / The process does not converge	

Источник: выполнено Н.Б. Даником и А.В. Климух / Source: made by N.B. Danik and A.V. Klimukh.

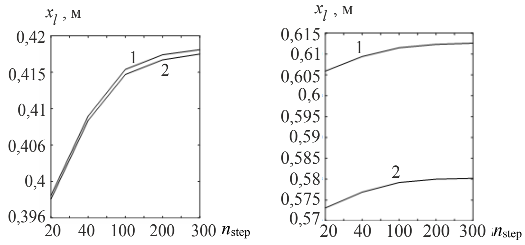

а *б*

Рис. 6. Графики $x_l \sim n_{\text{step}}$:
а — первая модель; *б* — вторая модель
Источник: выполнено Н.Б. Даником и А.В. Климух.

Figure 6. Graphs of $x_l \sim n_{\text{step}}$:
a — the first model; *б* — the second model
Source: made by N.B. Danik, A.V. Klimukh.

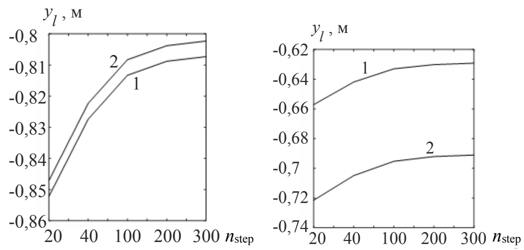

а *б*

Рис. 7. Графики $y_l \sim n_{\text{step}}$:
а — первая модель; *б* — вторая модель
Источник: выполнено Н.Б. Даником и А.В. Климух.
Figure 7. Graphs of $y_l \sim n_{\text{step}}$:
a — the first model; *б* — the second model
Source: made by N.B. Danik, A.V. Klimukh.

Сравнивая графики на рис. 7 и 8 с данными табл. 1, устанавливаем, что результаты, полученные с помощью моделей 1 и 2, качественно согласуются с величинами x_l и y_l комплекса ANSYS.

Эпюры распределения продольных сил N в элементах консоли, полученные с помощью нелинейного решателя ANSYS и по предлагаемой методике с использованием первой модели (без упругих шарниров), приведены на рис. 8 и 9. Как видно из рис. 8, максимальное значение силы $N = 0{,}03907$ Н, вычисленное при включенной опции "Large Displacement Static" (большие перемещения), по величине сопоставимо с величиной заданного усилия $F = 0{,}04167$ Н. Вместе с тем при моделировании консоли с помощью разработанной балочно-шарнирной модели продольные силы в элементах консоли с пятого по восьмой на три порядка превышают величины N, представленные на рис. 8. Отметим, что в соответствии с предлагаемой методикой продольные усилия в элементах вычислялись по «хрестоматийной» формуле

$$N_i = \frac{E A_i}{l_i} \Delta l_i^{\left(n_{\text{step}}\right)}, \quad i = 1, 2, \ldots, n_e,$$

где A — площадь поперечного сечения стержня; l_i — длина i-го КЭ; $\Delta l_i^{\left(n_{\text{step}}\right)}$ — изменение длин элементов на последнем шаге нагружения; n_e — число КЭ

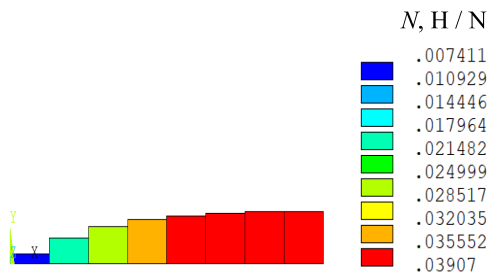

Рис. 8. Эпюра N (ANSYS нелинейный решатель)
Источник: выполнено П.П. Гайджуровым.
Figure 8. Diagram of N (ANSYS nonlinear solver)
Source: made by P.P. Gaidzhurov.

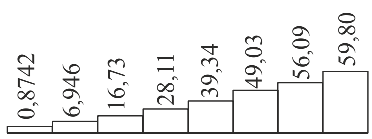

Рис. 9. Эпюра N (первая модель)
Источник: выполнено Н.Б. Даником и А.В. Климух.
Figure 9. Diagram of N (the first model)
Source: made by N.B. Danik and A.V. Klimukh.

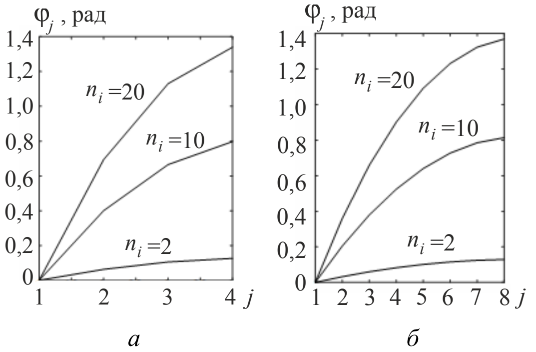

Рис. 10. График зависимости $\varphi_i \sim j$:

а — 4 КЭ; *б* — 8 КЭ

Источник: выполнено Н.Б. Даником и А.В. Климух.

Figure 10. Graph of $\varphi_i \sim j$:

а — 4 FE; *б* — 8 FE

Source: made by N.B. Danik and A.V. Klimukh.

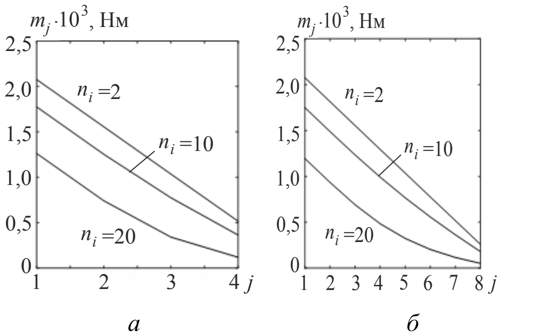

Рис. 11. График зависимости $m_i \sim j$:

а — 4 КЭ; *б* — 8 КЭ

Источник: выполнено Н.Б. Даником и А.В. Климух.

Figure 11. Graph of $m_i \sim j$:

а — 4 FE; *б* — 8 FE

Source: made by N.B. Danik and A.V. Klimukh.

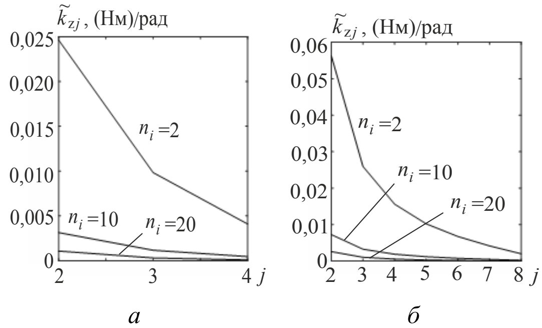

Рис. 12. График зависимости $\tilde{k}_{zi} \sim j$:

а — 4 КЭ; *б* — 8 КЭ

Источник: выполнено Н.Б. Даником и А.В. Климух.

Figure 12. Graph of $\tilde{k}_{zi} \sim j$:

а — 4 FE; *б* — 8 FE

Source: made by N.B. Danik and A.V. Klimukh.

Выявленное несоответствие в эпюрах N объясняется тем, что при использовании нелинейного решателя ANSYS активизируется режим уменьшения жесткости стержня в зависимости от степени его формоизменения. В предлагаемой методике продольная жесткость стержня в процессе деформирования не изменяется, что соответствует физической картине рассматриваемой изгибной деформации.

Графики зависимости углов поворотов (φ_j), моментов (m_j) и жесткостей ($\tilde{k}_{zj}$) от положения упругих вставок (вторая модель) для вариантов разбивки консоли на четыре и восемь КЭ показаны на рис. 10–12.

На этих рисунках значение параметра j соответствует номеру упругого шарнира (нумерация шарниров от заделки); n_i — номер ступени нагружения ($n_i = 2, 3, \ldots, 20$). Величины $\tilde{k}_{zi}$ вычислялись по формуле $\tilde{k}_{zj} = m_j / \varphi_j$.

Из приведенных на рис. 10 и 11 графиков видно, что двукратное уменьшение шага сетки практически не влияет на значения φ_j и m_j. Назначенные априори величины жесткостей поворотных пружин $\tilde{k}_{zj}$ (0,03333 Н·м/рад для 4 КЭ и 0,06667 Н·м/рад для 8 КЭ) согласуются с аналогичным максимальными значениями $\tilde{k}_{zj}$ на графиках рис. 12, *а* (0,025 Н·м/рад) и 9, *б* (0,056 Н·м/рад) при $k = 2$.

Пример 2. Гибкий криволинейный стержень прямоугольного поперечного сечения 1×1 м радиусом 100 м и углом раствора дуги 45^0, жестко закрепленный на конце ($x = 0$, $y = 0$, $z = 0$) и нагруженный на свободном конце из плоскости сосредоточенной силой $F_z = 600$ Н (рис. 13). Координаты x, y, z свободного конца стержня в исходном положении: 29,29 м; 70,71 м; 0 м. Модуль упругости материала стержня $E = 10$ МПа. Стержень разбивался на 16 пространственных КЭ балочного типа. По аналогии с предыдущим примером на стыках элементов вводились блоки из упругих шарниров (рис. 14).

Расчеты выполнялись для трех вариантов конечно-элементных моделей криволинейного стержня: *1* — используются только балочными КЭ; *2, 3* — используются балочные КЭ в сочетании с блоками из упругих шарниров. Параметры блоков шарниров:

- для модели *2*:

$$k_x = k_y = k_z = \tilde{k}_x = \tilde{k}_y = \tilde{k}_z = E;$$

- для модели *3*:

  $k_x = k_y = k_z = E = 10^{10}$ (недеформируемый стержень); $\tilde{k}_x = \tilde{k}_y = \tilde{k}_z = 0{,}295 \cdot 10^6$ Н·м/рад.

Результаты моделирования в виде координат точки приложения силы в деформированном состоянии x_ρ, y_ρ, z_ρ (рис. 13) и соответствующего радиус-вектора $\rho = \sqrt{x_\rho^2 + y_\rho^2 + z_\rho^2}$ сведены в табл. 2. Здесь построчно приведены данные для трех моделей в зависимости от числа ступеней нагружения n_{step}. Для сравнения аналогичный расчет криволинейного стержня без шарнирных блоков был выполнен в ANSYS с использованием нелинейного решателя. В итоге получены следующие значения координат:

$$x_\rho = 15{,}5639 \text{ м}; \; y_\rho = 46{,}8962 \text{ м};$$

$$z_\rho = 53{,}613 \text{ м}; \; \rho = 72{,}91 \text{ м}.$$

Данный результат достаточно хорошо согласуется с расчетом по предлагаемой методике с применением третьей модели при $n_i = 20$ (в табл. 2 подчеркнуто).

Эталонным решением рассматриваемой задачи являются координаты [7; 8]:

$$x_\rho = 15{,}56 \text{ м}; \quad y_\rho = 46{,}884 \text{ м}; \quad z_\rho = 53{,}66 \text{ м}.$$

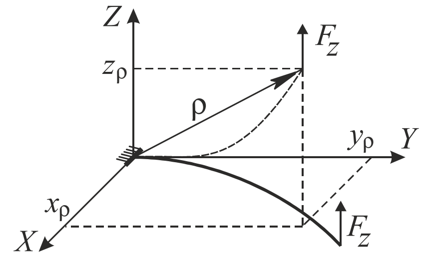

Рис. 13. Расчетная схема криволинейного стержня
Источник: выполнено П.П. Гайджуровым.

Figure 13. Model of a curved bar
Source: made by P.P. Gaidzhurov.

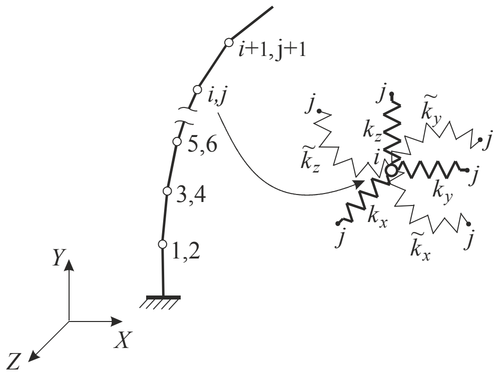

Рис. 14. Схема стержня и блока упругих шарниров
Источник: выполнено П.П. Гайджуровым.

Figure 14. Diagram of the bar and block of elastic hinges
Source: made by P.P. Gaidzhurov.

Таблица 2 / Table 2

Значения x_l и y_l для криволинейного стержня / Values of x_l and y_l for the curved bar

n_{step}	Первая модель, вторая модель, третья модель / The first model, the second model, the third model			
	x_ρ, м / m	y_ρ, м / m	z_ρ, м / m	ρ, м / m
10	14,301 7,24618 16,022	33,996 31,714 46,690	65,405 67,803 55,900	75,09 75,22 74,58
20	14,841 8,2624 **16,100**	35,122 33,037 **46,814**	61,973 63,914 **53,743**	72,76 72,42 **73,07**
60	15,171 8,7549 16,166	35,826 33,855 46,922	59,906 61,601 52,385	71,43 70,83 72,16
100	15,281 8,920 16,192	36,064 34,130 46,964	59,221 60,84 51,925	71,0 70,33 71,86

Источник: выполнено П.П. Гайджуровым / Source: made by P.P. Gaidzhurov.

Безусловно рассмотренный подход к моделированию гибких стержней является достаточно приближенным, так как не учитывает осевых поворотов балочных элементов «как жесткое целое». Однако введение дополнительный упругих шарниров позволяет качественно оценить картину деформирования стержней любой конфигурации как для консервативной, так и для «следящей» нагрузки. Это делает данную концепцию весьма привлекательной при конечно-элементном моделировании сложных трансформируемых стержневых систем.

4. Заключение

1. Преимуществом моделирования упругого гибкого стержня двухузловыми 3D балочными конечными элементами, соединенными в смежных узлах упругими шарнирными вставками, по сравнению с общепринятым подходом, базирующимся на использовании касательной матрицы жесткости, является простая алгоритмизация шаговой процедуры, которая позволяет достаточно точно для инженерной практики определить узловые перемещения и продольные усилия в исследуемом диапазоне нагрузки.

2. Предлагаемый прямой инкрементальный алгоритм решения геометрически нелинейной задачи строительной механики в отличие от нелинейного решателя комплекса ANSYS является абсолютно сходящимся при любой схеме дискретизации гибкого стержня.

3. В перспективе разработанная методика назначения жесткостей поворотных пружин может быть использована при моделировании процесса формоизменения регулярных пространственных стержневых систем при управляемом кинематическом воздействии.

Список литературы

1. *Дыховичный Ю.А.* Большепролетные конструкции сооружений Олимпиады-80 в Москве. Москва : Стройиздат, 1982. 277 с. URL: https://dwg.ru/lib/1136 (дата обращения: 21.04.2025).

2. *Перельмутер А.В., Сливкер В.И.* Расчетные модели сооружений и возможность их анализа. Москва : ДМК Пресс, 2007. 600 с. ISBN 5940743528

3. *Канчели Н.В.* Строительные пространственные конструкции. Москва : Изд-во АСВ, 2003. 112 с. ISBN 5-93093-206-9 EDN: QNKFNR

4. *Секулович М.* Метод конечных элементов. Москва : Стройиздат, 1993. 664 с. ISBN 5-274-01755-X

5. *Попов Е.П.* Теория и расчет гибких упругих стержней. Москва : Наука, 1986. 296 с. EDN: WIWUQV

6. *Светлицкий В.А.* Механика гибких стержней и нитей. Москва : Машиностроение, 1978. 222 с. URL: https://djvu.online/file/3q69M4Xs4OLyq (дата обращения: 21.04.2025).

7. *Попов В.В., Сорокин Ф.Д., Иванников В.В.* Разработка конечного элемента гибкого стержня с раздельным хранением накопленных и дополнительных поворотов для моделирования больших перемещений элементов конструкций летательных аппаратов // Труды МАИ. 2017. № 92. С. 3. EDN: YKVJZF

8. *Низаметдинов Ф.Р., Сорокин Ф.Д.* Особенности применения вектора Эйлера для описания больших поворотов при моделировании элементов конструкций летательных аппаратов на примере стержневого конечного элемента // Труды МАИ. 2018. № 102. С. 1. EDN: YQONFZ

9. *Battini J.M., Pacoste C.* Co-rotational beam elements with warping effects in instability problems. Comput // Computer Methods in Applied Mechanics and Engineering. 2002. Vol. 191. P. 1755–1789. EDN: ATXRQJ

10. *Hsiao K.-M., Horng H.-J., Chen Y. R.* A corotational procedure that handles large rotations of spatial beam structures // Computers & Structures. 1987. Vol. 27. No. 6. P. 769–781.

11. *Сахаров А.С., Кислоокий В.Н., Киричевский В.В. и др.* Метод конечных элементов в механике твердых тел / под ред. А.С. Сахарова и И. Альтенбаха. Киев : Вища школа, 1982. 480 с. URL: https://dwg.ru/dnl/6757 (дата обращения: 21.04.2025)

12. *Wu G., He X., Pai P.F.* Geometrically exact 3D beam element for arbitrary large rigid-elastic deformation analysis of aerospace structures // Finite Elements in Analysis and Design. 2011. Vol. 47. Issue 4. P. 402–412. https://doi.org/10.1016/j.finel.2010.11.008 EDN: OEKSAX

13. *Albino J.C.R., Almeida C.A., Menezes I.F.M., Paulino G.H.* Co-rotational 3D beam element for nonlinear dynamic analysis of risers manufactured with functionally graded materials (FGMs) // Engineering Structures. 2018. Vol. 173. P. 283–299. https://doi.org/10.1016/j.engstruct.2018.05.092 EDN: VHHBLD

14. *Наумов А.М.* Применение метода последовательных нагружений при решении задач механики плоских стержней // Известия высших учебных заведений. Машиностроение. 2016. № 12 (681). С. 33–42. EDN: XECQGD

15. *Kang J., Homel M.A., Herbold E.B.* Beam elements with frictional contact in the material point method // International Journal for Numerical Methods in Engineering. 2022. Vol. 123. Issue 4. P. 1013–1035. https://doi.org/10.1002/nme.6886

16. *Русских С.В.* Развертывание плоской упругой стержневой системы с тросовыми элементами, присоединенной к космическому аппарату // Известия высших учебных заведений. Машиностроение. 2018. № 4 (697). С. 80–90. https://doi.org/10.18698/0536-1044-2018-4-80-90 EDN: XOCSKT

17. *Popov A.N., Lovtsov A.D.* Frictional contact problem in building constructions analysis // Magazine of Civil Engineering. 2020. Issue 100 (8). Article no. 10001. https://doi.org/10.18720/MCE.100.1 EDN: GHIKRQ

References

1. Dykhovichny Yu.A. *Large-span structures of the 1980 Olympics in Moscow.* Moscow: Stroyizdat Publ.; 1982. (In Russ.) Available from: https://dwg.ru/lib/1136 (accessed: 21.04.2025).

2. Perelmuter A.V., Slivker V.I. *Models of structures and the possibility of their analysis*. Moscow: DMK Press; 2007. (In Russ.) ISBN 5940743528

3. Kancheli N.V. *Spatial building structures.* Moscow: DIA Publ.; 2003. (In Russ.) ISBN 5-93093-206-9 EDN: QNKFNR

4. Sekulovich M. *The finite element method*. Moscow: Stroyizdat Publ.; 1993. (In Russ.) ISBN 5-274-01755-X

5. Popov E.P. *Theory and calculation of flexible elastic bars.* Moscow: Nauka Publ.; 1986. (In Russ.) EDN: WIWUQV

6. Svetlitsky V.A. *Mechanics of flexible bars and threads.* Moscow: Mashinostroenie, 1978. (In Russ.) Available from: https://djvu.online/file/3q69M4Xs4OLyq (accessed: 21.04.2025).

7. Popov V.V., Sorokin F.D., Ivannikov V.V. A flexible rod finite element with separate storage of cumulated and extra rotations for large displacements of aircraft structural parts modeling. *Proceedings of MAI*. 2017;(92):3. (In Russ.) EDN: YKVJZF

8. Nizametdinov F.R., Sorokin F.D. Euler vector application specifics for large turns description while flying vehicles structural elements modeling on the example of a rod finite element. *Proceedings of MAI*. 2018;(102):1. (In Russ.) EDN: YQONFZ

9. Battini J.M., Pacoste C. Co-rotational beam elements with warping effects in instability problems. Comput. *Computer Methods in Applied Mechanics and Engineering*. 2002;191:1755–1789. EDN: ATXRQJ

10. Hsiao K.-M., Horng H.-J., Chen Y.-R. A corotational procedure that handles large structures of spatial beam structures. *Computers & Structures*. 1987;27(6):769–781.

11. Sakharov A.S., Kislooky V.N., Kirichevsky V.V. et al. *Finite element method in solid mechanics.* A.S. Sakharov and I. Altenbach (eds.). Kiev: Vischa School Publ.; 1982. Available from: https://dwg.ru/dnl/6757 (accessed: 21.04.2025)

12. Wu G., He X., Pai P.F. Geometrically exact 3D beam element for arbitrary large rigid-elastic deformation analysis of aerospace structures. *Finite Elements in Analysis and Design*. 2011;47(4):402–412. https://doi.org/10.1016/j.finel.2010.11.008 EDN: OEKSAX

13. Albino J.C.R., Almeida C.A., Menezes I.F.M., Paulino G.H. Co-rotational 3D beam element for nonlinear dynamic analysis of risers manufactured with functionally graded materials (FGMs). *Engineering Structures.* 2018;173:283–299. https://doi.org/10.1016/j.engstruct.2018.05.092 EDN: VHHBLD

14. Naumov A.M. The application of the method of successive loadings when solving problems of mechanics of flat rods. *BMSTU Journal of Mechanical Engineering*. 2016;12:33–42. (In Russ.) EDN: XECQGD

15. Kang J., Homel M.A., Herbold E.B. Beam elements with frictional contact in the material point method. *International Journal for Numerical Methods in Engineering*. 2021;123(4):1013–1035. https://doi.org/10.1002/nme.6886

16. Russkikh S.V. Deploying a planar elastic rod system with cable elements attached to a spacecraft. *BMSTU Journal of Mechanical Engineering*. 2018;4:80–90. (In Russ.) https://doi.org/10.18698/0536-1044-2018-4-80-90 EDN: XOCSKT

17. Popov A.N., Lovtsov A.D. Frictional contact problem in building constructions analysis. *Magazine of Civil Engineering.* 2020;100(8):10001. https://doi.org/10.18720/MCE.100.1 EDN: GHIKRQ

СТРОИТЕЛЬНАЯ МЕХАНИКА ИНЖЕНЕРНЫХ КОНСТРУКЦИЙ И СООРУЖЕНИЙ
STRUCTURAL MECHANICS OF ENGINEERING CONSTRUCTIONS AND BUILDINGS

2025. 21(5). 474–494

ISSN 1815-5235 (Print), 2587-8700 (Online)

HTTP://JOURNALS.RUDN.RU/STRUCTURAL-MECHANICS

DOI: 10.22363/1815-5235-2025-21-5-474-494
EDN: DGNKGJ

Research article / Научная статья

Thermomechanical Performance of Steel and Recycled Aluminium Plates in Tropical Savanna Climatic Conditions

Paschal Ch. Chiadighikaobi✉, **Obumneme C. Onuoha**, **Akintomiwa E. Fagbuyi**

Afe Babalola university, *Ado-Ekiti, Ekiti state, Nigeria*
✉ chiadighikaobi.paschalc@abuad.edu.ng

Received: May 13, 2025
Revised: August 7, 2025
Accepted: September 12, 2025

Abstract. This research covers and compares the thermomechanical behavior of steel and recycled aluminium plates under concentrated loading and buckling conditions in several thermal conditions simulating the tropical savanna (Aw) climate. The study aims to explore their structural behavior as a function of temperature and evaluate their applicability in heat-sensitive applications. Finite element analysis (FEA) was used to model the buckling and deformation behavior of the two materials at temperatures from 0°C to 44°C and uniaxial loading of up to 100 MPa. The analytical and numerical solutions were compared; their results would differ no more than 5%, thus validating the FEA model. The steel plates generally buckled less (greater critical buckling load) in hotter thermal conditions than the aluminium. The buckling load of steel reduced by approximately 40% in Mode 1 when it went from 33°C to 44°C, while the buckling load of aluminium reduced by just 4.71%. The same trend was observed in Mode 2. These findings validate that recycled aluminium possesses superior thermomechanical stability to tropical thermal fluctuation and can be a good alternative as a material for structures in applications of high thermal fluctuation, which will be beneficial towards maximum utilization of resources in building engineering.

Keywords: loss of stability, critical load, deformation, recycled aluminium plates, steel plate

Conflicts of interest. The authors declare no conflict of interest, financial or otherwise.

Authors' contribution: *Chiadighikaobi P.Ch.* — concept, methodology, analysis, software, supervision, project administration, validation; *Onuoha O.C.*— conceptualization, methodology, software, text writing; *Fagbuyi A.E.* — review and editing, data interpretation. All authors have read and approved the final version of the manuscript.

For citation: Chiadighikaobi P.Ch., Onuoha O.C., Fagbuyi A.E. Thermomechanical performance of steel and recycled aluminium plates in tropical savanna climatic conditions. *Structural Mechanics of Engineering Constructions and Buildings.* 2025;21(5): 474–494. http://doi.org/10.22363/1815-5235-2025-21-5-474-494 EDN: DGNKGJ

Paschal Ch. Chiadighikaobi, Ph.D., M.Sc., Senior lecturer in the Department of Civil engineering, Afe Babalola University, Ado-Ekiti, Ekiti State, Nigeria; ORCID: 0000-0002-4699-8166; e-mail: chiadighikaobi.paschalc@abuad.edu.ng

Obumneme C. Onuoha, Graduate of the Department of Civil Engineering, Afe Babalola University, Ado-Ekiti, Ekiti State, Nigeria; ORCID: 0009-0003-7191-1581; e-mail:Obumonu45@gmail.com

Akintomiwa E. Fagbuyi, Graduate of the Department of Civil Engineering, Afe Babalola University, Ado-Ekiti, Ekiti State, Nigeria ; ORCID: 0009-0002-0694-1728; e-mail:akinfagbuyi@gmail.com

Термомеханические характеристики пластин из стали и переработанного алюминия в климатических условиях тропической саванны

П.Ч. Чиадигхикаоби✉, О.С. Онуоха, А.Э. Фагбуйи

Университет Афе Бабалола, *Адо-Экити, штат Экити, Нигерия*
✉ chiadighikaobi.paschalc@abuad.edu.ng

Поступила в редакцию: 13 мая 2025 г.
Доработана: 7 августа 2025 г.
Принята к публикации: 12 сентября 2025 г

Аннотация. Рассмотрены и сравнены термомеханические характеристики пластин из стали и переработанного алюминия в условиях действия сосредоточенной нагрузки и потери устойчивости при нескольких температурных режимах, имитирующих климат тропической саванны. Цель исследования — изучение их прочностных характеристик в зависимости от температуры и оценка их применимости в термочувствительных областях. Для моделирования поведения двух материалов при потере устойчивости и деформировании при температурах от 0 °C до 44 °C и одноосной нагрузке до 100 МПа использован метод конечного элемента. Проведено сравнение аналитических и численных решений; их результаты отличались не более чем на 5 %, что подтвердило точность конечно-элементной модели. Стальные пластины, как правило, были более устойчивы (вызывающая потерю устойчивости критическая нагрузка выше) при повышенной температуре, чем алюминиевые. При повышении температуры с 33 до 44 °C критическая нагрузка стали в режиме 1 снизилась примерно на 40 %, в то время как критическая нагрузка алюминия снизилась лишь на 4,71 %. Аналогичная тенденция наблюдалась и в режиме 2. Эти результаты подтверждают, что переработанный алюминий обладает превосходной термомеханической устойчивостью к тропическим температурным колебаниям и может быть хорошей альтернативой в качестве материала для конструкций в условиях высоких температурных колебаний, что будет способствовать максимальному использованию ресурсов в строительстве.

Ключевые слова: потеря устойчивости, критическая нагрузка, деформация, переработанные алюминиевые пластины, стальные пластины

Заявление о конфликте интересов. Авторы заявляют об отсутствии конфликта интересов, финансового или иного характера.

Вклад авторов: *Чиадигхикаоби П.Ч.* — концепция, методология, расчет, программная реализация, руководство, управление проектом, валидация; *Онуоха О.С.* — концептуализация, методология, программная реализация, написание текста; *Фагбуйи А.Э.* — рецензирование и редактирование, интерпретация данных. Все авторы прочитали и одобрили окончательный вариант рукописи.

Для цитирования: *Chiadighikaobi Ph.Ch., Onuoha O.C., Fagbuyi A.E.* Thermomechanical performance of steel and recycled aluminium plates in tropical savanna climatic conditions // Строительная механика инженерных конструкций и сооружений. 2025. Т. 21. № 5. С. 474–494. http://doi.org/10.22363/1815-5235-2025-21-5-474-494 EDN: DGNKGJ

1. Introduction

The thermomechanical properties of materials are a dominant factor in defining their suitability in structural systems under varying climate conditions of tropical savanna regions. Steel is the most favoured material for load-carrying structures due to its increased strength, ductility, and proven reliability. But the highly corrosive tendencies of steel have resulted in the continuous search for alternative materials. From the integration of fibre-reinforced polymers to the use of recycled plastic bricks, several materials have been explored, with their mechanical properties analysed to obtain the potential advantages and limitations. Among these alternatives, aluminium has gained considerable attention. Aluminium is resistant to corrosion and has been used as an adequate replacement for steel in some specific conditions globally.

Beyond its mechanical advantages, the consideration of aluminium also extends to issues of material availability and life cycle utilization. Waste management has a significant environmental impact [1]. The

Чиадигхикаоби Паскал Чимеремезе, доктор философии, магистр наук, старший преподаватель кафедры гражданского строительства, Университет Афе Бабалола, Адо-Экити, штат Экити, Нигерия; ORCID: 0000-0002-4699-8166; e-mail: chiadighikaobi.paschalc@abuad.edu.ng

Онуоха Обумнем С., аспирант факультета гражданского строительства, Университет Афе Бабалола, Адо-Экити, штат Экити, Нигерия; ORCID: 0009-0003-7191-1581; e-mail: Obumonu45@gmail.com

Фагбуйи Акинтомива, аспирант факультета гражданского строительства, Университет Афе Бабалола, Адо-Экити, штат Экити, Нигерия; ORCID: 0009-0002-0694-1728; e-mail: akinfagbuyi@gmail.com

disposal of aluminium cans, commonly used for soft drinks, has become one of the prevailing issues. These cans are found littering the environment, adding to pollution and waste management challenges, as they cannot be easily decomposed. This condition presents a dual challenge: addressing environmental pollution and finding sustainable uses for these waste materials. Repurposing these aluminium cans into components for aluminium plates in construction is a sustainable solution. This approach aids in reducing environmental pollution and contributes to the development of eco-friendly construction materials.

The widespread use of aluminium cans can be traced back to advancements in food science. Today, aluminium cans are considered a conventional means of packaging food and beverages for commercial consumption. Previously, glass dominated the drink packaging market until the late 1950s.[3] The first all-aluminium beverage cans were introduced in 1958 by the Hawaii Brewing Company for their “Primo Beer”.[4] Aluminium has increasingly been used as a method of canning due to its low weight, low cost, and recyclability. “The world's beer and soda consumption uses about 180 billion aluminium cans every year. This is 6,700 cans per second, enough to go around the planet every 17 hours”.[5] Aluminium cans are made from a combination of elements to form an aluminium alloy. The chemical makeup of this alloy varies. Table 1 summarises the chemical makeup of aluminium alloys.

Table 1

Chemical makeup of aluminium alloy

Element	Symbol	Percentile make-up, %
Aluminium	Al	93.75 – 96.46
Magnesium	Mg	2.53 – 4.82
Manganese	Mn	0.27 – 0.33
Iron	Fe	0.26 – 0.32

S o u r c e: compiled by V.Y. Risonarta et al. [2].

The first step in recycling aluminium cans involves the collection and sorting of aluminium cans based on alloy type, grade, and other factors. This sorting process can be done manually or using technologies like eddy current separators, air classifiers, and density separators. After sorting, the aluminium cans are shredded and cleaned to remove any impurities or coatings. The cleaned aluminium scrap is then melted in a furnace at high temperatures, typically around 660 °C. The molten metal is poured into ingot casts to set. Alloy formulas are chosen based on the planned uses for the reprocessed aluminium. Lastly, the resulting ingots can be transported to aluminium processing or manufacturing plants to be made into new products, including structural aluminium alloy [3–6]. Although aluminium is a highly recyclable material, there are only a few recycling industries in Africa.

In Nigeria, for instance, an estimated 87% of aluminium cans are left unrecycled. Reports show that only 13 percent of recyclable goods are salvaged and recycled in Nigeria, with almost no formal waste diversion process in place.[6] The process of recycling aluminium cans into structural aluminium alloys must be given great attention; poorly recycled alloys will produce underperforming materials.

The application of aluminium in civil engineering is dependent on the physical and mechanical properties (see Table 2) of the alloy. These properties include density, elastic modulus, ultimate strength, Poisson ratio, etc.

[3] The History of Metal Packaging | A brief overview of metal packaging. 2019. Available from: https://www.shilohplastics.com.au/history-of-metal-packaging/ (accessed: 14.04.2025)

[4] Svendsen A. 60 years of the Aluminium Can — Light Metal Age Magazine. 2018. Available from: https://www.lightmetalage.com/news/industry-news/applications-design/60-years-of-the-Aluminium-can/ (accessed: 14.04.2025)

[5] The world counts. (n.d.). Available from: https://www.theworldcounts.com/challenges/consumption/foods-and-beverages/aluminium-cans-facts. (accessed: 14.04.2025)

[6] Aluminium recycling in Africa is an opportunity for big business, Op-Ed by Raymond Onovwigun | Romco Metals. 2022. Available from: https://romcometals.com/aluminium-recycling-in-africa-is-an-opportunity-for-big-business/(accessed: 03.04.2025).

Table 2

Aluminium properties

Properties	Symbol	5005-H12 Aluminium	6005-T1 Aluminium
Density, kg/m^3	Q	2,660	2,770
Elastic Modulus, MPa	E	70,300	71,000
Poisson's Ratio	v	0.30	0.33
Ultimate Strength, MPa	Ru	275	310

S o u r c e: compiled by Z. Zuo et al. [7].

The integration of aluminium alloys in civil engineering has been in existence for more than 80 years. First used in the design and construction of static transport structures like bridges, from the reconstruction of Pittsburgh's bridge roadway project in 1933 to the construction of New York's railway bridge in 1946. This work fostered the construction of other global aluminium-aided structures as well as the development of various international standard codes guiding their design [8]. The United States primarily uses the Aluminium Design Manual (ADM) as guidance in the design of aluminium structures [9]. While BS 8118-1:1991 is the "Code of Practice for the Structural Use of Aluminium" and was one of the first codes to be written in limit state format for aluminium design[7], and BS EN 1999-1-1:2007 provides the guidelines and specifications for the design of aluminium structures within the European Union[8]. Aluminium has been utilised in some major projects globally to solve various structural and environmental issues; aluminium alloy was used in the reconstruction of the Real Ferdinando bridge decking in Italy to reduce the self-weight of the bridge. Likewise, pure aluminium can be used in passive seismic protection systems due to its low yield strength and high degree of ductility. Furthermore, the integration of aluminium alloys is necessary for structures exposed to extreme temperature variations. Aluminium lacks negative implications related to brittleness at low temperatures compared to steel [8]. Aluminium is also utilized in the design of plates and shell-like structural elements. For example, the design and construction of bridges, roofs, walls, box culverts, pipe arches, silos, tanks, cooling towers, reactor vessels, culverts, storm sewers, service tunnels, recovery tunnels, stream enclosures, and underpasses[9] [10].

Despite the various advancements in international codes and multiple uses of aluminium globally, there remains a limited understanding of the effect of temperature on the deformation and buckling behaviour of aluminium plates under load. Bridging this knowledge gap is key to exploiting the full potential of the material in varying climatic conditions. As the world grapples with the challenges of urbanisation and a growing population, the demand for durable and environmentally responsible construction materials has never been more pressing. This paper reviewed several relevant articles and textbooks acquired with the aid of multiple research databases, i.e. Google Scholar, Scopus, etc. to validate the accuracy of the theories and finite element analysis (FEA) carried out in this study. FEA tool (ANSYS) was used to run a comparative analysis on aluminium and steel plates under simulated real-world scenarios.

1.1. Aluminium Plates

The recycled aluminium from aluminium cans can be forged into a variety of structural elements, like plates. A plate is a structural element that is characterised by a three-dimensional solid whose thickness is small in comparison to its other dimensions [11]. Plates serve various functions, such as providing stable surfaces for floors, roofs, and walls, as well as distributing loads efficiently throughout a structure[10] . Plates

[7] BS 8118-1. (1991). Structural use of aluminium — Code of practice for design.

[8] EN 1999-1-1 (2007) (English): Eurocode 9: Design of aluminium structures — Part 1-1: General structural rules.

[9] Aluminium structural Plate by Contech Engineered Solutions. (n.d.). — Contech Engineered Solutions. https://www.conteches.com/bridges-structures/plate/Aluminium-structural-plate/

[10] Plates. (n.d.). The structural engineer. Available from: https://www.thestructuralengineer.info/education/structural-systems/plates (accessed: 03.04.2025).

can also be defined as planar, two-dimensional components that primarily transfer forces in the direction of their plane. Plates are greatly utilised in structures in the form of floors and walls. The wall plate elements in buildings are used to transfer all vertical loads as axial forces into the foundation; they ensure the horizontal stiffening of the entire structure [12; 13].

The deformation and structural behavior of a plate under loading are dependent on the plate's material properties. Furthermore, the effects of loads on plates generate stresses predominantly normal to the element's thickness, and their mechanics are the main subject of plate theory [11]. Plate theory aims to calculate deformation and stress in a plate subjected to loads. There are two widely accepted plate theories used: the Kirchhoff-Love theory of plates (classical plate theory) and the Reissner-Mindlin theory of plates (first-order shear plate theory) [14; 15].

The Reissner-Mindlin theory is applied for thick plates, where the shear deformation and rotary inertia effects are included [14], while the Kirchhoff-Love theory is an extension of the Euler-Bernoulli beam theory to thin plates. There are three assumptions made in the Kirchhoff-Love theory. Firstly, the mid-plane is a "neutral plane," like in beam theory. Secondly, line elements remain normal to the mid-plane. Finally, vertical strain is ignored, meaning that the thickness of the plate does not change during deformation (see Figure 1) [14; 15].

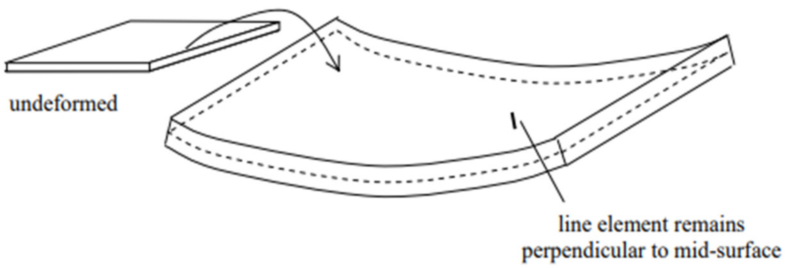

Figure 1. Deformed line elements remain perpendicular to the mid-plane
S o u r c e: compiled by Kelly. (n.d.). Plate theory[11].

Under loading, stresses are generated on and within the plate, causing bending. The bending of the plate helps to resist the applied load on the plate. In addition, the bending of the plate is greatly influenced by the Poisson ratio of the material. The smaller the Poisson ratio of the plate material, the more the loading would produce a more singly curved, deformed surface, as seen in Figure 2, *a*. However, if the plate material has a non-zero Poisson's ratio, the deflected shape will be as shown in Figure 2, *b*. Therefore, most aluminium alloy plates would have greater deformation than steel plates [17].

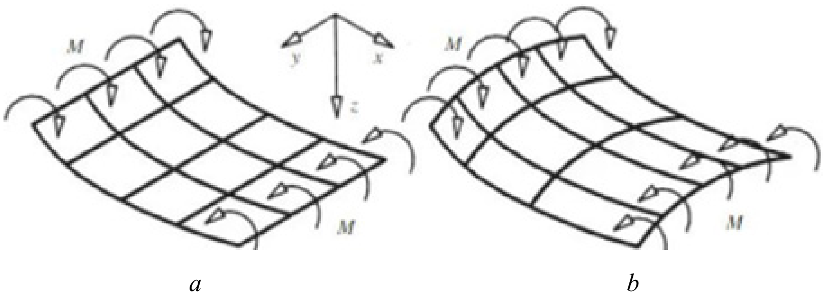

Figure 2. Deformed surface of a plate with:
a — low Poisson's ratio; *b* — high Poisson's ratio
S o u r c e: compiled by D. Johnson [17].

[11] Kelly. (n.d.). Plate theory. In Solid Mechanics Part II (pp. 120–126). Available from: https://pkel015.connect.amazon.auckland.ac.nz/SolidMechanicsBooks/Part_II/06_PlateTheory/06_PlateTheory_Complete.pdf

Other factors that influence the magnitude of deformation of a plate under loading are shapes, support conditions, and the type of loading the plate is subjected to (see Table 3) and Equations (1)–(8).

Table 3

Maximum deformation of plate formulae

Shape of plate	Support conditions & Type of load	Max deformation (at centre)
Circular	Edges are simply supported & uniformly loaded 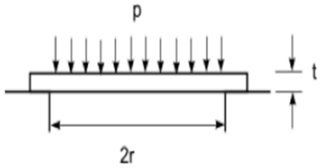	$$y_m = \frac{(5+v)pr^4}{64(1+v)D} \quad (1)$$
Circular	Edges clamped & uniform load 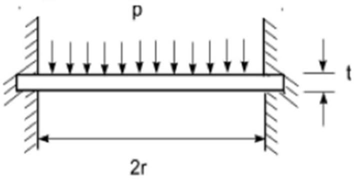	$$y_m = \frac{pr^4}{64D} \quad (2)$$
Circular	Edges simply supported & concentrated load 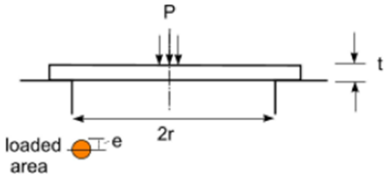	$$y_m = \frac{(3+v)Pr^2}{16\pi(1+v)D} \quad (3)$$
Circular	Edges clamped & concentrated load 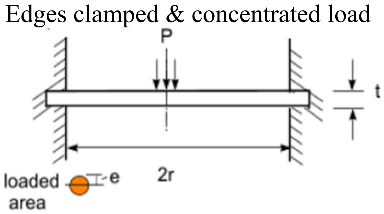	$$y_m = \frac{Pr^2}{16\pi D} \quad (4)$$
Rectangular	Edges simply supported & uniform load 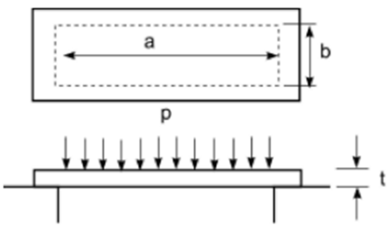	$$y_m = \frac{0.142pb^4}{Et^3\left(2.21(b/a)^3+1\right)} \quad (5)$$
Rectangular	Edges clamped & uniform load 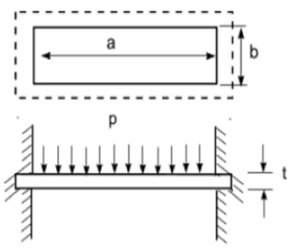	$$y_m = \frac{0.0284pb^4}{Et^3\left(1.056(b/a)^5+1\right)} \quad (6)$$

Ending of the Table 3

<table>
<tr><th>Shape of plate</th><th>Support conditions & Type of load</th><th>Max deformation (at centre)</th></tr>
<tr><td>Rectangular</td><td>Edges simply supported & concentrated load
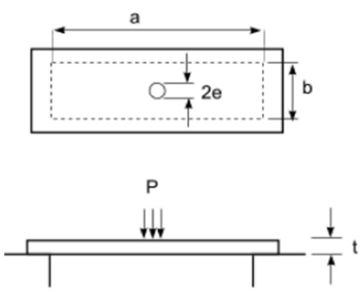</td><td>$$y_m = k_1 \frac{Pb^2}{Et^3} \quad (7)$$
<table>
<tr><td>(a/b)</td><td>k_1</td><td>(a/b)</td><td>k_1</td></tr>
<tr><td>1.0</td><td>0.127</td><td>1.6</td><td>0.17</td></tr>
<tr><td>1.1</td><td>0.138</td><td>1.8</td><td>0.177</td></tr>
<tr><td>1.2</td><td>0.148</td><td>2.0</td><td>0.180</td></tr>
<tr><td>1.4</td><td>0.162</td><td><3.0</td><td>0.185</td></tr>
</table></td></tr>
<tr><td>Rectangular</td><td>Edges clamped & concentrated load
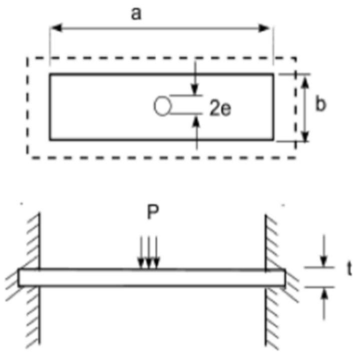</td><td>$$y_m = k_1 \frac{Pb^2}{Et^3} \quad (8)$$
<table>
<tr><td>(a/b)</td><td>k_1</td><td>(a/b)</td><td>k_1</td></tr>
<tr><td>1.0</td><td>0.061</td><td>1.8</td><td>0.0786</td></tr>
<tr><td>1.2</td><td>0.071</td><td>2.0</td><td>0.0788</td></tr>
<tr><td>1.4</td><td>0.076</td><td><3.0</td><td>0.0791</td></tr>
<tr><td>1.6</td><td>0.078</td><td></td><td></td></tr>
</table></td></tr>
</table>

S o u r c e: compiled by Loaded Flat Plates. (n.d.). Roymech
Loaded Flat Plates. (n.d.). Roymech. Available from: https://www.roymech.co.uk/Useful_Tables/Mechanics/Plates.html (accessed: 03.04.2025).

where r is the radius of the circular plate (m); a is the major length of the rectangular plate (m); b is the minor length of the rectangular plate (m); t is plate thickness (m); p is uniform surface pressure on the plate (compressive) (N/m^2); P is single concentrated force (compressive) (N); y_m is the maximum deformation (m); E = Young's modulus of elasticity (N/m^2); e is the radius of the loaded area; v is the Poisson's ratio.

Equations (1) to (8), denoted and illustrated in Table 3, are explained as follows below.

Equation (1) highlights the y_m of a simply supported circular plate of diameter 2r under pressure p. The D and v have a great influence on the deformation of the plate. Therefore, the higher the D of a plate, the less its deformation.

Equation (2) highlights the y_m of a circular plate clamped at all edges with a diameter of 2r under pressure p. The D and v have a great influence on the deformation of the plate. Therefore, the higher the D of a plate, the less its deformation.

Equation (3) highlights the y_m of a simply supported circular plate of diameter 2r under force P over an area of radius e. The D and the v have a great influence on the plate. Therefore, the higher the D of a plate, the less its deformation.

Equation (4) highlights the y_m of a circular plate clamped at all edges with a diameter of 2r under force P over an area of radius e. The D and the v have a great influence on the plate. Therefore, the higher the D of a plate, the less its deformation.

Equation (5) highlights the y_m of a simply supported rectangular plate of dimensions a and b under pressure p. The D and v have a great influence on the deformation of the plate. Therefore, the higher the D of a plate, the less its deformation.

Equation (6) highlights the y_m of a rectangular plate of dimensions *a* and *b* clamped at all edges under pressure *p*. The *D* and *v* have a great influence on the deformation of the plate. Therefore, the higher the *D* of a plate, the less its deformation.

Equation (7) highlights the y_m of a simply supported rectangular plate of dimensions a and b under force P over an area of radius e. The constant (k_1) is dependent on the aspect ratio (a/b) of the plate. Therefore, the greater the aspect ratio, the greater the deformation. Also, the *D* has a great influence on the deformation of the plate.

Equation (8) highlights the y_m of a rectangular plate of dimensions a and b clamped at all edges under force P over an area of radius e. The constant (k_1) is dependent on the aspect ratio (*a*/*b*) of the plate. Therefore, the greater the aspect ratio, the greater the deformation. Also, the *D* has a great influence on the deformation of the plate.

D is the flexural rigidity, which is determined by solving Equation:

$$D = \frac{Et^3}{12\left(1 - v^2\right)}. \tag{9}$$

Plates are susceptible to various types of failures under different loading conditions. Some of the common types of failures susceptible to plates include fatigue failure. Fatigue failure can occur in plate structures due to repeated cyclic loading, leading to the initiation and propagation of cracks in the material. This type of failure is a concern for structures subjected to varying magnitudes of loads, such as wind turbine towers or bridges. The study [17] examined the various factors affecting the fatigue strength of thin plates in large structures. Moreover, when the elastic limit of the plate material has been exceeded, this exceedance of the elastic limit can lead to ductile failure of the plate, also commonly known as yielding failure. Yielding failure results in the permanent deformation of the plate and occurs as a condition in which the compressive stress surpasses the material's yield strength.[12] The study [18] covered the prediction of yield failure points in notched aluminium plates. To study the ductile failure of the notched aluminium specimens, a brittle material with a virtual ultimate strength was used to compare with the real ductile material. Lastly, plate buckling is a phenomenon that occurs as a condition in which a thin plate moves out of the plane under a compressive load, causing it to bend in two directions [19].

1.2. Plate Buckling

Structural members in compression are susceptible to failure by buckling if the applied compressive load exceeds the critical load (buckling load). Buckling failure is not dependent on stress or strength but rather on structural stiffness. Plates are buckled in orthogonal directions (see Figure 3) [19–21].

The major parameters influencing the buckling effect of plates include the aspect ratio (*a*/*b*), plate slenderness (*b*/*t*), boundary conditions, the initial imperfections of the plane, and, lastly, the type of plane loads.

The ratio of its longer side to its shorter side has a significant impact on its buckling behavior (Figure 4). For large aspect ratios, the plate starts behaving like a column of finite width. As the aspect ratio decreases, there is a limit below which failure does not take place by elastic buckling. The ratio affects the buckling load, with the buckling load decreasing continuously as the aspect ratio increases. However, the rate decreases with an increasing ratio. Additionally, for aspect ratios less than 0.5, the plates fail by crushing and not by buckling. Beyond a certain aspect ratio, the plate behavior shifts from plate to column [21–24].

---

[12] Investigations Into Steel Structure Failures Part I: Failure Mechanisms — Built Environment, Engineering Hawkins Forensic Investigation. (2022). Hawkins Forensic Investigation. Available from: https://www.hawkins.biz/insight/investigations-into-steel-structure-failures-part-i-failure-mechanisms/ (accessed: 03.04.2025).

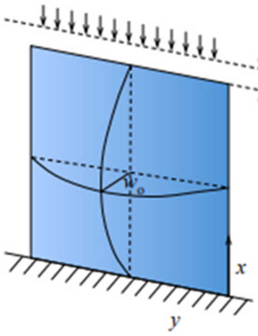

Figure 3. Two-degree-of-freedom model of the buckled plate
S o u r c e: compiled by T.Yu [22].

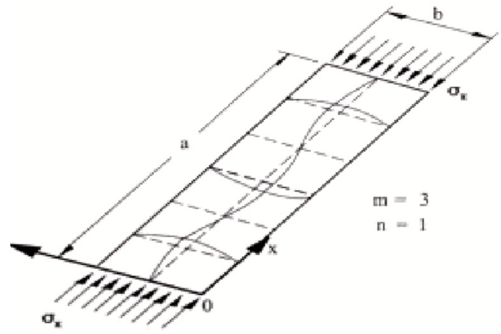

Figure 4. A plate with a high aspect ratio
S o u r c e: compiled by K.J. Rawson and E.C. Tupper [25].

In the design of plate structures, determining the thickness of the plate to be used to guard against buckling is crucial. For plate buckling, the Euler buckling limit is not final. Therefore, the Euler buckling stress is greater than the yielding stress. That is why, in plate design, an increase in the strength or grade of material must result in a decrease in the length of the plate. Higher-tensile-strength materials have an increasing risk of buckling [21; 22; 25; 27]. Equation (10) shows the critical buckling load of a supported rectangular plate:

$$N_{x_{cr}} = \frac{k_c \pi^2 D}{b^2}\ , \tag{10}$$

where $N_{x_{cr}}$ is the critical buckling load, k_c is the buckling coefficient (see Figure 4 and Table 4), b is the loaded length, and D is flexural rigidity (see Equation (9)). The type of boundary support is an important factor that influences a plate's deformation and buckling loads, along with other factors such as modulus ratio, etc. The buckling load attains its minimum value under simply supported boundary conditions and its maximum value under clamped boundary conditions. This is because the rigidity of the clamped edges provides greater restraint against lateral deformation compared to the simply supported edges, thereby increasing the buckling load capacity.

Table 4

Buckling coefficients of plates

Case	Description of support at the unloaded edges		k
1	Both edges are simply supported	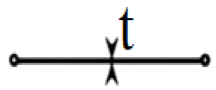	4.000
2	One edge is simply supported, the other fixed	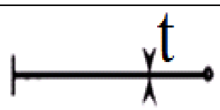	5.42
3	Both edges are fixed	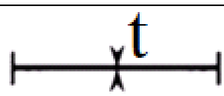	6.97
4	One edge is simply supported, the other free	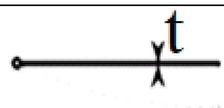	0.425
5	One edge is fixed, the other free	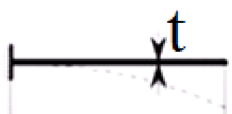	1.277

S o u r c e: compiled by U. Obinna [19].

The plate's boundary conditions and aspect ratio determine the plate's bending mode and the distance between inflection points. The closer the inflection points are, the greater the resulting axial load capacity (buckling load) of the plate. Therefore, it is essential to properly define the boundary conditions not only in the out-of-plane direction but also in the in-plane direction to accurately predict the buckling behavior of plates [19; 27]. Figure 5 shows how the aspect ratio affects the number of half-waves on the unloaded and longer axis (m). Furthermore, the aspect ratio determines how many half-waves or modes the plate will have during failure (see Figures 6–8). Figure 7 shows a plate with an aspect ratio of 3, producing 3 half-waves along the longer axis. Figure 8, on the other hand, shows a plate with 2 and a half waves along the longer axis.

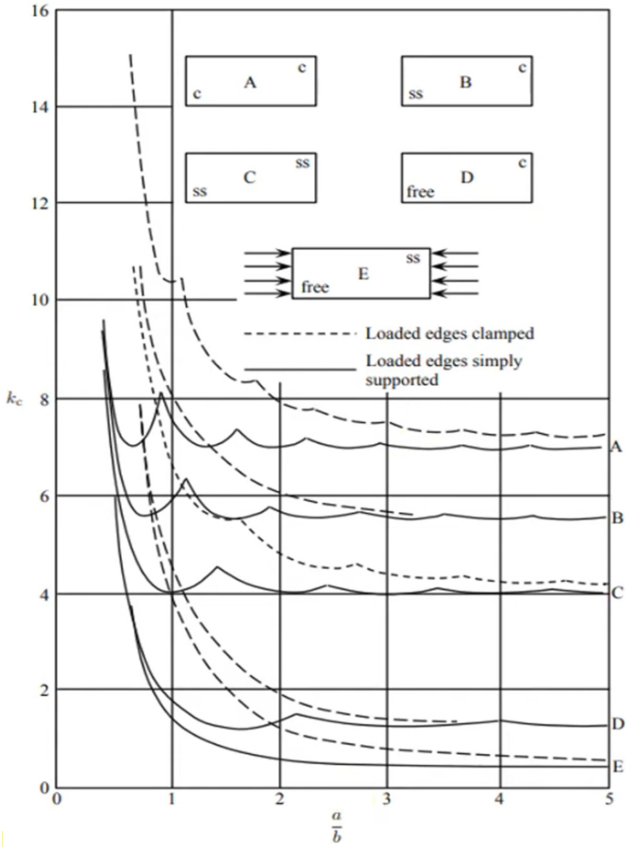

Figure 5. Buckling coefficient
for different boundary conditions:
SS — denotes simply supported; C — denotes clamped
S o u r c e: compiled by O.M.E. Suleiman et al. [31].

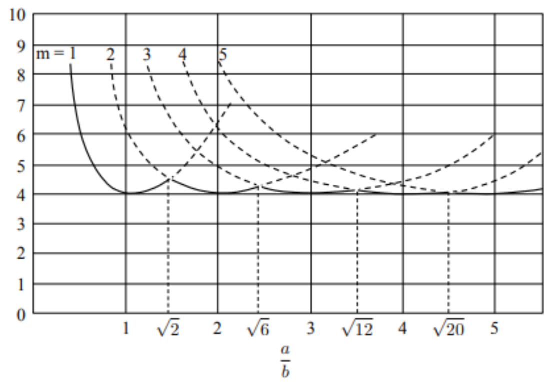

Figure 6. Buckling load as a function
of aspect ratio for a simply supported plate
S o u r c e: compiled by T.Yu. [21]

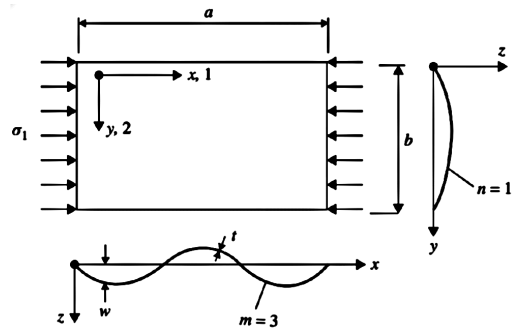

Figure 7. Simply supported plate buckling mode (3, 1)
S o u r c e: compiled by O.M.E. Suleiman et al. [31].

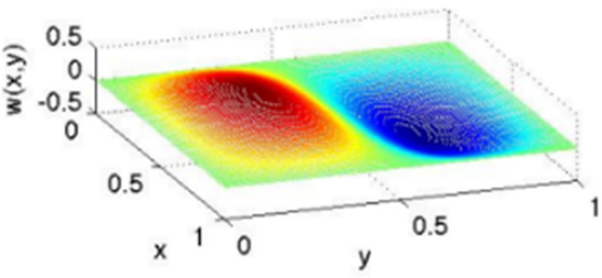

Figure 8. Buckling modes of a simply-supported thin plate — Mode (2, 1)
S o u r c e: compiled by T.Yu. [21].

1.3. Effect of Load Types and Combinations

The type and combination of loads, as well as the boundary conditions, greatly affect the deformation of plates. Restricting in-plane deformation reduces the buckling load by a factor of 3/4, but it does not change the buckling mode. The buckling coefficient is a function of the loading distribution, plate geometry, and boundary conditions. The buckling interaction curve shows the effect of applied loads and boundary conditions for different modes of buckling on plates[13] [19; 28–30]. Figures 9–12 display 4 types of load combinations applied to plates[14].

If multiple action components are present, multiple modes can occur, which may interact with one another. Therefore, in Figure 10, the existence of minimal transverse compression does not alter the mode of buckling. Nonetheless, as illustrated in Figure 12, significant transverse compression will lead to the panel warping into a single half-wave. (In certain situations, this push into a higher mode could enhance strength; for instance, in case of Figure 12, preformation/ transverse compression might boost strength in longitudinal compression.) Shear buckling, illustrated in Figure 11, fundamentally involves an interplay between the destabilising compression on one diagonal and the stabilising tension on the opposite diagonal.

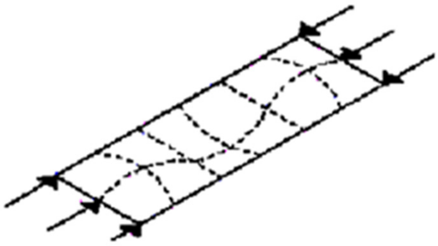

Figure 9. Uniaxial compression
S o u r c e: compiled by ESDEP WG 8 Plates and Shells.

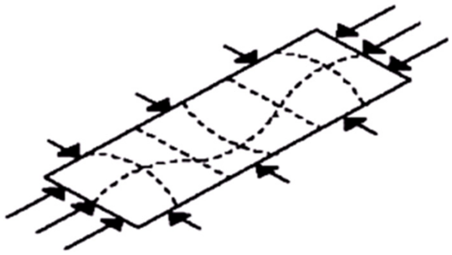

Figure 10. Biaxial compression, longitudinal compression predominating
S o u r c e: compiled by ESDEP WG 8 Plates and Shells.

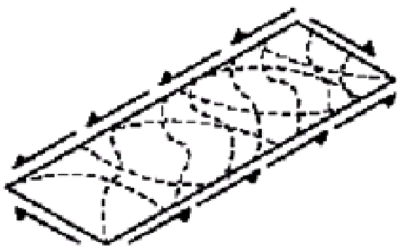

Figure 11. Shear
S o u r c e: compiled by ESDEP WG 8 Plates and Shells.

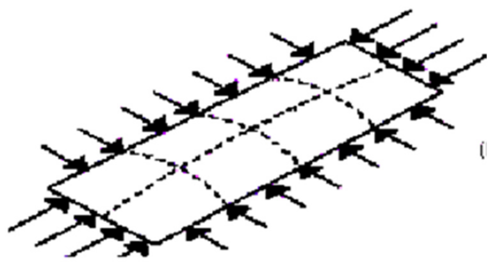

Figure 12. Biaxial compression, transverse compression predominating
S o u r c e: compiled by ESDEP WG 8 Plates and Shells.

1.4. Environmental Conditions

Environmental conditions can affect thin plates in various ways, such as through changes in temperature, humidity, and exposure to different types of loads. For example, in the previously stated context of plate structures, the buckling strength is influenced by the loading distribution, plate geometry, and boundary conditions. Additionally, the material properties of the plate, including any dependence on environmental conditions, can impact its behavior under different loads and stresses. Therefore, it is

[13] Wierzbicki T. Buckling of a simply supported plate. Structural Mechanics, Massachusetts Institute of Technology, 170-181. file:///C:/Users/user/Downloads/Full.pdf

[14] ESDEP WG 8 Plates and Shells. Lecture 8.1: Introduction to Plate, Behaviour and Design. Available from: https://fgg-web.fgg.uni-lj.si/~/pmoze/esdep/master/wg08/l0100.htm (accessed: 03.04.2025).

essential to consider the specific environmental conditions and loading scenarios when analysing the behavior of thin plates to ensure their structural integrity and performance [31; 32].

The average annual temperature in most tropical savanna regions is 26.9°C, with regional variations based on factors such as elevation and proximity to water bodies. The highest average monthly temperatures are between 30 and 32 °C, typically occurring in April, while the lowest average monthly temperatures are between 24 and 25 °C, typically occurring in December and January. Over the past 30 years, tropical savanna regions have experienced a slight increase in temperature. For example, in 2021, southern Nigeria recorded a mean average temperature of 30 to 32°C, while the northern recorded its highest temperature in 40 years. This increase in temperature is consistent with other tropical savanna regions, i.e. Ghana, Southeast Asia, Northern Australia, Brazil, etc. and global climate change trends [33; 34].

The temperature resistance of structural aluminium alloys varies depending on the specific alloy and composition. However, most aluminium alloys begin to lose strength at temperatures above 150 °C (300 °F) [35; 36]. The primary strength reduction in some alloys, such as 5083-H116 and 6082, occurs between 200 and 400 °C, leading to significant decreases in yield strength [37; 38]. Although it was revealed that aluminium alloys perform better in both strength and ductility at low temperatures. The duration of exposure plays a crucial role for cold-worked or heat-treated alloys [37; 38]. Figure 13 highlights the change in typical tensile strengths of some aluminium alloys at various temperatures.

To find out how resistant a certain structural aluminium alloy is to high temperatures, one needs to look at the mechanical and physical properties of the aluminium alloy at those temperatures, which depend on its chemical makeup and temperature [40–42]. The thermal expansivity of materials is also a key factor that influences the behavior of plates.

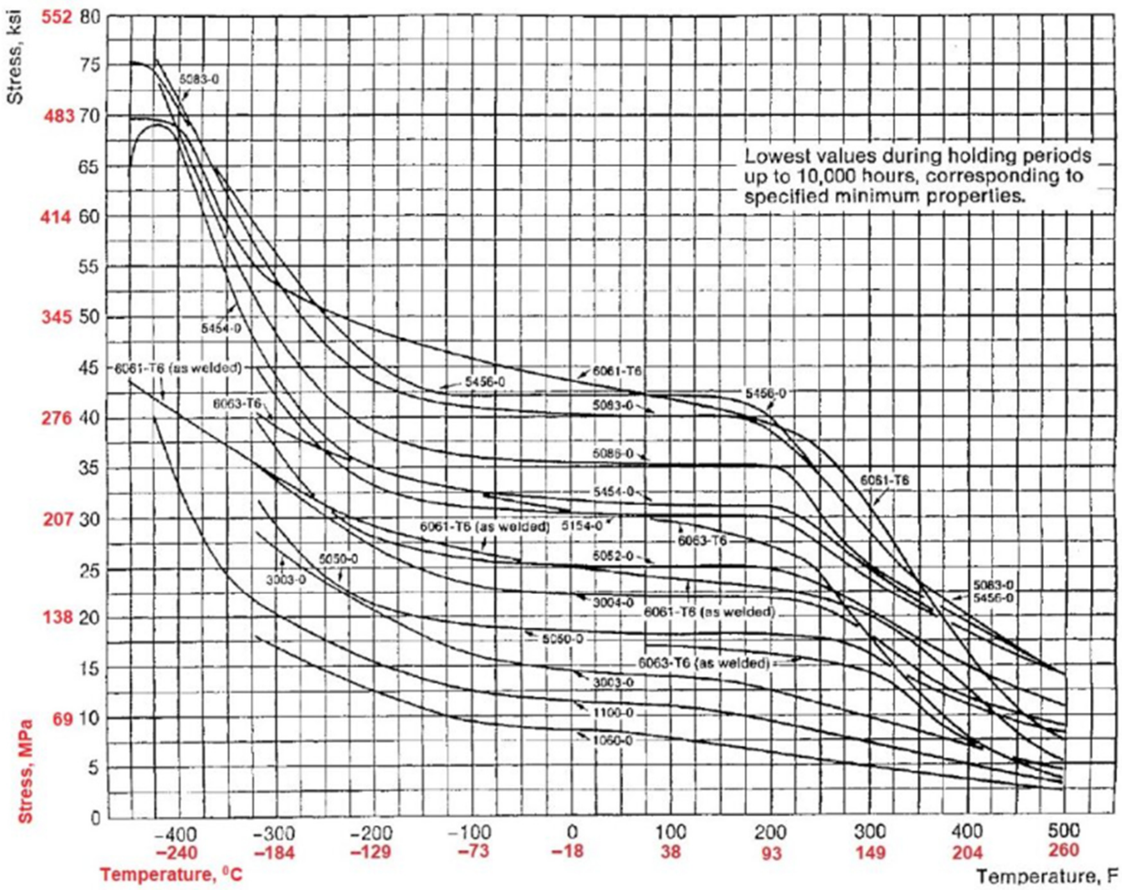

Figure 13. The strength of aluminium against temperature

S o u r c e: compiled by J.R. Kissell, R.L. Ferry [43].

1.5. Thermal Expansivity

The thermal expansivity of materials is a key factor that influences the structural behaviour of plates [44; 45]. Equation (13) shows the change in length caused by a change in temperature in materials.

$$\Delta L = \alpha L_0 \Delta T, \tag{13}$$

where ΔL is the change in length; α is the linear thermal expansion coefficient; L_0 is the original length; ΔT is the change in temperature

The thermal expansion coefficient of aluminium is relatively large compared to other metals. Linear thermal expansion coefficients for aluminium and aluminium alloys are shown in Table 5. [15]

Table 5

Coefficient of thermal expansion 10^{-6} (°C) of aluminium alloys

Metal or alloy	Temp	Coefficient of thermal expansion 10^{-6} (°C)
Aluminium (99.996%)	20–100°C	23.6
3003	20–100°C	23.2
5083	20–100°C	23.4

Source: compiled by Engineering ToolBox.

Moreover, Table 5 highlights the variety of coefficient of thermal expansion (CTE) of aluminium and its alloys. The secant CTE of aluminium and its alloys also varies. The secant CTE is a measure that accounts for the change in length or volume of a material over a specific temperature range. Unlike the linear CTE, which provides a constant value for the entire temperature range, the secant CTE calculates the average thermal expansion over a specified temperature interval. A commonly used average value for the linear CTE of aluminium is approximately 23×10^{-6} per degree Celsius (°C).

1.6. Importance of Aluminium

The transformation of discarded aluminium cans into valuable construction components aligns with the global shift towards resource efficiency and circular economy principles. The feasibility of this transformation poses several questions:

i. Can aluminium cans be effectively turned into structurally sound aluminium plates?
ii. Will these plates meet the structural requirements in terms of strength, durability, and safety?

Several studies have examined the mechanical and thermal behavior of steel and aluminium alloys; most were conducted under normal or temperate climatic conditions, with comparably few examinations of the materials' thermomechanical performance under tropical savanna climatic conditions. Additionally, previous research tended to examine deformation or buckling separately from one another, as opposed to concurrent analyses of the two in a representative range of thermal fluctuations. This study differs from existing literature by examining the coupled deformation–buckling behavior of recycled aluminium and steel plates under simulated tropical temperature variations (0°C–44°C) using finite element analysis (FEA). Thus, this paper aims to unravel the potential of aluminium plates by scrutinising their mechanical, thermal, and structural properties, to understand how the change in temperature affects the deformation and buckling of plates under loading. Hence, the objective of this is as follows:

[15] Engineering ToolBox. (2011). Thermal Expansion of Metals. Engineeringtoolbox.com. https://www.engineeringtoolbox.com/thermal-expansion-metals-d_859.html

i. Ensure the analytical theories agree with the finite element analysis (FEA) results
ii. To determine the deformation of the plate models under various loads and temperature conditions.
iii. To define how the change in temperature affects the critical buckling of the plates.

2. Materials and Models

Three analysis systems were used in this study, all done on the Ansys workbench software, i.e. Steady-state Thermal, Static Structural, and Eigenvalue Buckling. The geometrical model was created by the design modeller (see Figure 14). A circular surface was imprinted at the centre of the plate using the Boolean tool, highlighting where the load would be placed for analysis 1 (see Figure 15). A shell element model type was used with a 30 mm thickness (see Figure 15–16). Both faces were meshed using a meshing element size of 200 mm.

2.1. Material Properties

The physical and mechanical properties used for both plates (aluminium alloy and steel alloy) are summarised in Table 6.

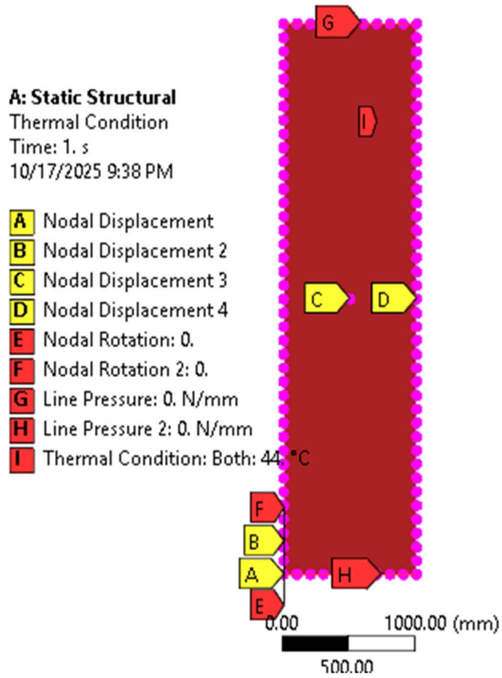

Figure 14. Analysis systems used

S o u r c e: compiled by P.C. Chiadighikaobi, O.C. Onuoha, A.E. Fagbuyi.

Table 6

Physical and mechanical properties of aluminium and steel

Properties	**Symbol**	**Aluminium alloy**	**Steel alloy**
Density, kg/m^3	Q	2,770	7,850
Elastic modulus, MPa	E	71,000	200,000
Poisson's ratio	v	0.33	0.3
Yield strength, MPa	Ru	280	250
Secant coefficient of thermal expansion	10^{-6} (°C)$^{-1}$	23	12

S o u r c e: compiled by P.C. Chiadighikaobi, O.C. Onuoha, A.E. Fagbuyi.

2.2. Supports and Loading

Both plates were simply supported. All the nodes at the edges were restrained along the z-axis, the nodes on the longer sides were free to rotate about z- and y-axis, but fixed along the x-axis, while the nodes on the shorter sides were free to rotate about z- and x-axis, but fixed along the y-axis. Lastly, the node at the centre was fixed along both the x- and y-axis. In addition, the loads placed were dependent on the analysis.

Table 7

The 5 levels of uniform loading

S/N	**Loads, MPa**
1	0
2	25
3	50
4	75
5	100

S o u r c e: compiled by P.C. Chiadighikaobi, O.C. Onuoha, A.E. Fagbuyi.

A n a l y s i s 1: Temperature-Influenced Deformation of Plates Under Concentrated Load. In this analysis, five (5) levels of uniform loading (Table 7) were applied to the circular area (diameter = 9 mm) at the centre of the plate (see Figure 15).

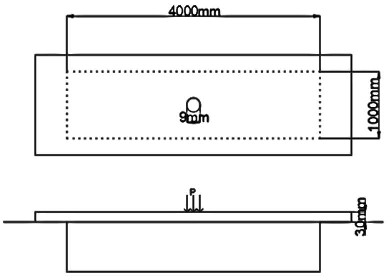

Figure 15. Analysis 1:
plate and loading area dimensions
S o u r c e: compiled by P.C. Chiadighikaobi, O.C. Onuoha, A.E. Fagbuyi.

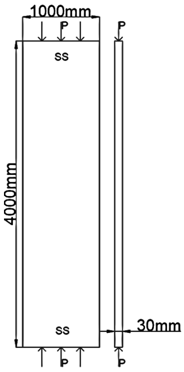

Figure 16. Analysis 2:
plate and loading area dimensions
S o u r c e: compiled by P.C. Chiadighikaobi, O.C. Onuoha, A.E. Fagbuyi.

Table 8

The 7 different temperatures

S/N	1	2	3	4	5
Temperature, °C	0	11	22	33	44

S o u r c e: compiled by P.C. Chiadighikaobi, O.C. Onuoha, A.E. Fagbuyi.

Analysis 2: Total Buckling Deformation of the Plate. In this case, the plate was subjected to a uniaxial compressive force along the y-axis (see Figure 16). The loads were applied as line pressure, and the load applied was 10000 N/m. In addition, with the aspect ratio being four, the first mode is expected to have four half-waves.

2.3. Temperature Conditions

The plates were subjected to 6 (six) different temperatures during loading in both analyses.

The reference temperature used was 22°C (Table 8).

3. Results

The FEA results for Analyses 1 and 2 are stated in this section below.

Analysis 1 result: Temperature Influenced Deformation. The derived FEA deformation results validate the formulae stated in the previous section, i.e. Equations (7) and (13). Using Equation (13), the expected total maximum deformation (TMD) for the unloaded 33 °C plate was 0.506 mm (2 × 0.253 mm) for aluminium and 0.264 mm (2 × 0.132 mm) for Steel. Tables 9 and 10 show that the TMD was 0.5216 mm and 0.27214 mm, respectively. In addition, the Equation (7) derived TMD for 25 °C plates under 100 MPa load were 0.60798 mm for aluminium and 0.21583 mm for steel. While Tables 8 and 9 show the TMD was 0.57823 mm and 0.2095 mm. These results are quite precise with less than a 5-percentile difference. Hence, proving the accuracy of the FEA results.

Table 9

Aluminium plate: total maximum deformation

	0°C	11°C	22°C	33°C	44°C
0 MPa	0.97516mm	0.50629mm	0mm	0.5216mm	1.0432mm
25 MPa	0.97516mm	0.50629mm	0.14456mm	0.5216mm	1.0432mm
50 MPa	0.97516mm	0.50629mm	0.28900mm	0.5216mm	1.0432mm
75 MPa	0.97516mm	0.50629mm	0.43368mm	0.5216mm	1.0432mm
100 MPa	0.97516mm	0.57823mm	0.57823mm	0.57823mm	1.0432mm

S o u r c e: compiled by P.C. Chiadighikaobi, O.C. Onuoha, A.E. Fagbuyi.

Table 10

Steel plate: total maximum deformation

	0°C	11°C	22°C	33°C	44°C
0 MPa	0.49892mm	0.26193mm	0mm	0.27214mm	0.54428mm
25 MPa	0.49892mm	0.26193mm	0.05240mm	0.27214mm	0.54428mm
50 MPa	0.49892mm	0.26193mm	0.10475mm	0.27214mm	0.54428mm
75 MPa	0.49892mm	0.26193mm	0.15712mm	0.27214mm	0.54428mm
100 MPa	0.49892mm	0.26193mm	0.2095mm	0.27214mm	0.54428mm

S o u r c e: compiled by P.C. Chiadighikaobi, O.C. Onuoha, A.E. Fagbuyi.

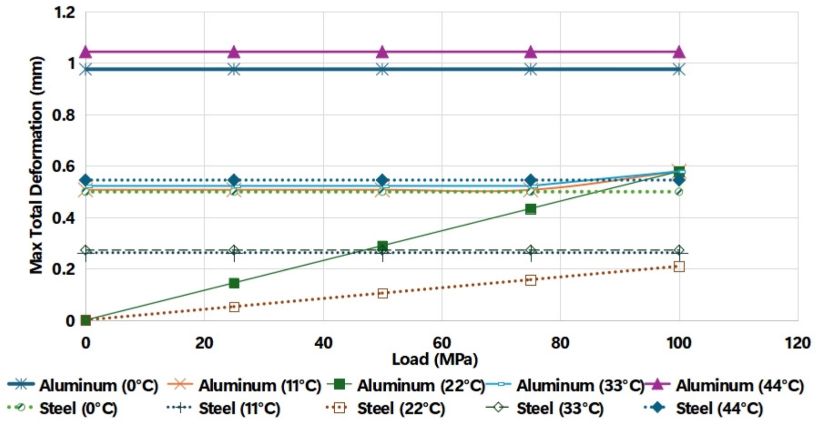

Figure 17. Total maximum deformation of aluminium and steel plates

S o u r c e: compiled by P.C. Chiadighikaobi, O.C. Onuoha, A.E. Fagbuyi.

Figure 17 shows that the TMD of plates at various temperature, except the ones at reference temperature (22 °C), are greatly dependent on the temperature of the plate and not the load acting on it. The aluminium and steel plate TMD remained constant at 0 °C, 11 °C, 33 °C, and 44 °C, particularly under the condition where the applied load was less than 100 MPa. Moreover, as seen in Figure 18, the unloaded 0 °C aluminium plate (a) and steel plate (c) TMD point is at the bottom corner of the plate, and after the 100 MPa load was applied on aluminium plate (*b*) and steel plate (*d*), the TMD point was retained. In addition, the mid node total deformation of 0 °C plates under 100 MPa loading was 0.42115 mm for aluminium and 0.20825 mm for steel, both lower than the mid node deformations at the reference temperature (22 °C), which is 0.57823 mm and 0.2095 mm, respectively (see Figure 19). Thus, proving aluminium slight gain in strength at lower temperatures. Validating the study Guo et al. [46], which stated that low temperatures improved both strength and ductility of aluminium, while higher temperatures reduced the strength due to softening. In addition, the plates (aluminium and steel) at lower temperatures (0 °C and 11 °C) deformed by contracting, while the plates at higher temperatures (33 °C and 44 °C) deformed my expanding. Thus, proving why the loaded plate mid-node total deformation was more at higher temperatures than at lower temperatures. In Figure 20, *b* and *d* total mid node deformation was 0.57823 mm and 0.22573 mm, respectively, which is higher than the other temperature cases.

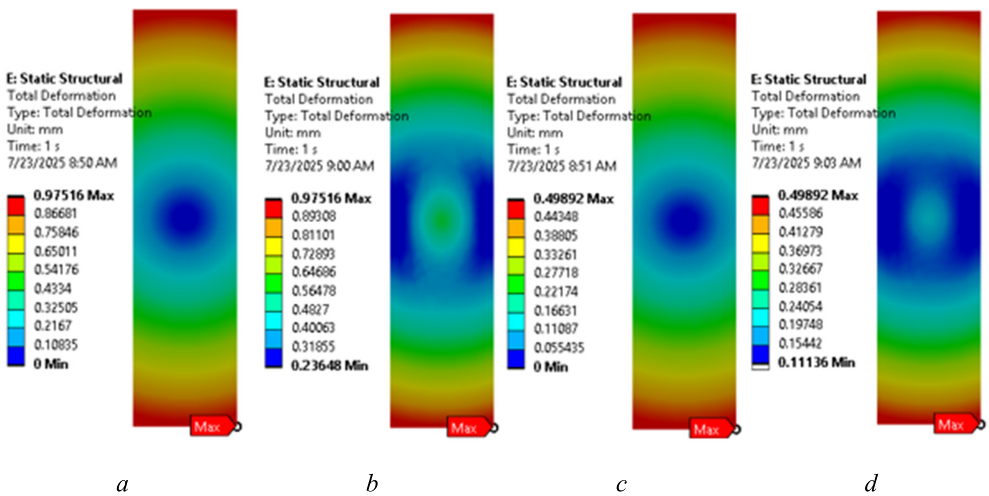

Figure 18. Total maximum deformation for unloaded and loaded 0 °C plates:
a — Aluminium; *b* — Aluminium; *c* — Steel; *d* —Steel

S o u r c e: compiled by P.C. Chiadighikaobi, O.C. Onuoha, A.E. Fagbuyi.

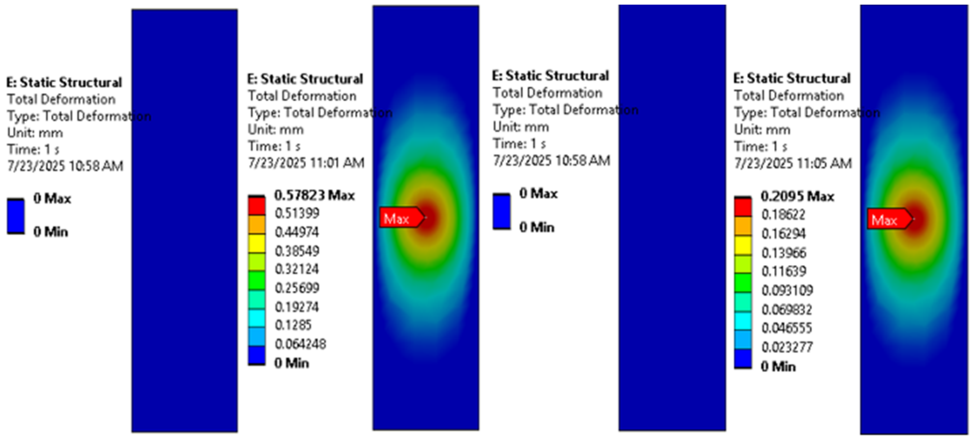

a *b* *c* *d*

Figure 19. Total maximum deformation for unloaded and loaded 22 °C plates:
a — Aluminium; *b* — Aluminium; *c* — Steel; *d* — Steel

S o u r c e: compiled by P.C. Chiadighikaobi, O.C. Onuoha, A.E. Fagbuyi.

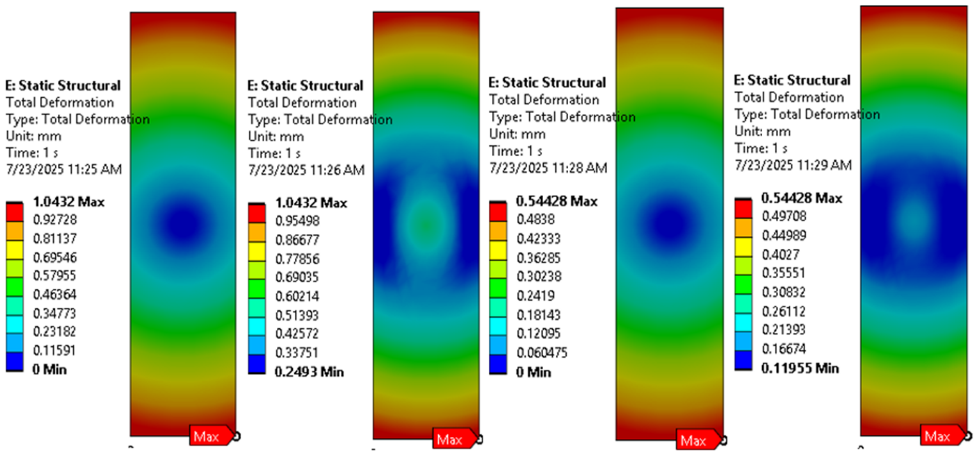

a *b* *c* *d*

Figure 20. Total maximum deformation for unloaded and loaded 44 °C plates:
a — Aluminium; *b* — Aluminium; *c* — Steel; *d* — Steel

S o u r c e: compiled by P.C. Chiadighikaobi, O.C. Onuoha, A.E. Fagbuyi.

Analysis 2 Result: Temperature Influenced Buckling. The FEA buckling results accuracy was validated by equation (10). Equation (10) derived buckling load for plates at reference temperature was 7,070,232 N/m for aluminium and 19,502,505 N/m for steel, while the FEA load was 7,330,000 N/m and 20,237,000 N/m (see Table 10). The results are quite precise with less than a four-percentile difference. Thus, proving accuracy of the FEA method used.

Table 10

Critical buckling load results

	Aluminium		**Steel**	
	Mode 1	**Mode 2**	**Mode 1**	**Mode 2**
Uniaxial Compression Load, 10,000 N/m				
0 °C	–761.76	733.5	–1576	2024.1
11 °C	733.47	781.16	2024.1	2155.6
22 °C	733.33	781.29	2023.7	2156.1
33 °C	732.89	781.43	2020.3	2156.7
44 °C	699.88	739.80	1435.6	1856.3

S o u r c e: compiled by P.C. Chiadighikaobi, O.C. Onuoha, A.E. Fagbuyi.

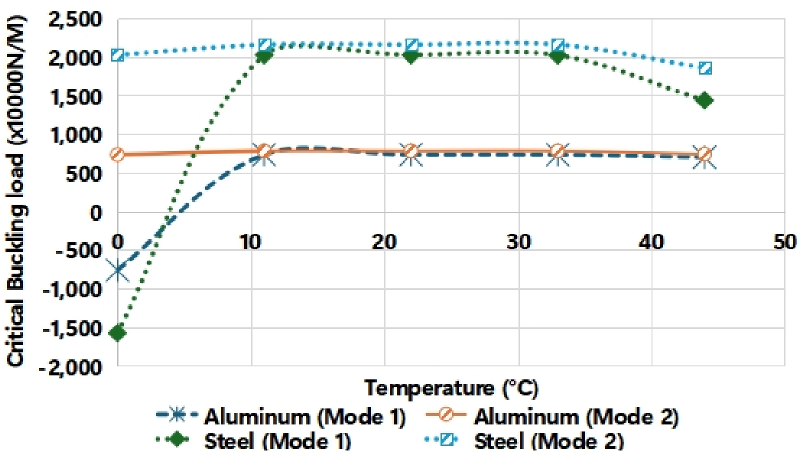

Figure 21. Critical buckling of uniaxially compressed plates
S o u r c e: compiled by P.C. Chiadighikaobi, O.C. Onuoha, A.E. Fagbuyi.

Figure 21 shows that both plates mode 1 critical buckling load is quite temperature sensitive, with the higher buckling loads observed near the reference temperature. At mode 1, the steel critical bulking load significantly dropped by 40.7% due to the temperature change from 33 °C to 44 °C (see Figure 24), while aluminium dropped only by 4.71%. A similar phenomenon was observed in mode 2, where the critical buckling load for the steel plate dropped by 16.18% when the temperature changed from 33 °C to 44 °C (see Figure 24), while aluminium dropped 5.63%. Validating that, despite the buckling mode, the steel critical buckling load is much more sensitive to temperature than aluminium. In addition, it was observed that despite the mode, the plates at 0 °C and 44 °C had no more than 4 half-wavelengths. While for mode 2 plates closer to the reference temperature (22°C), an additional wavelength was formed (see Figure 23). Hence proving that the environmental temperature plays a crucial role in plate buckling modes (see Figure 24).

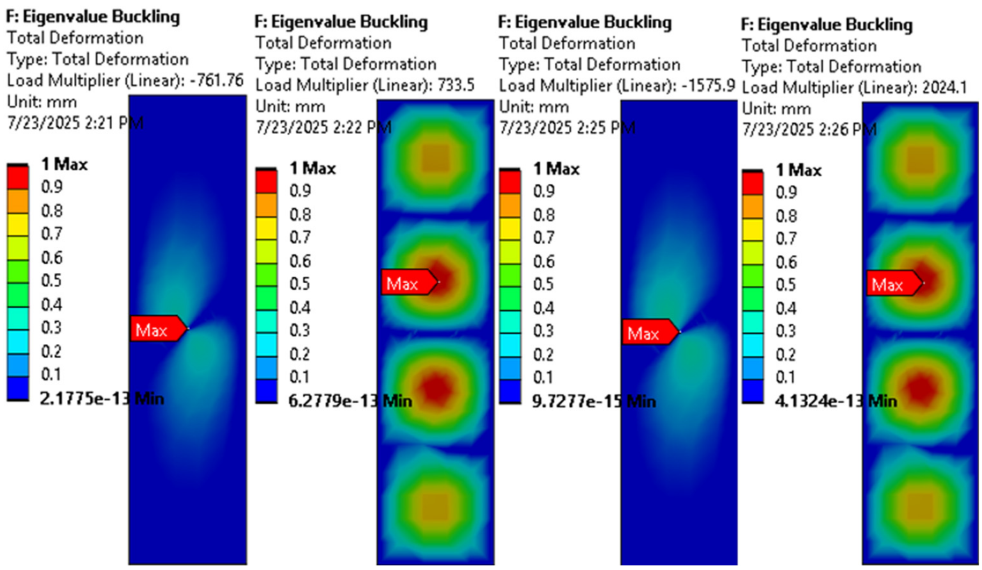

a *b* *c* *d*

Figure 22. Buckling deformation of plates at 0 °C:
a — Aluminium (mode 1); *b* — Aluminium (mode 2); *c* — Steel (mode 1); *d* — Steel (mode 2)
S o u r c e: compiled by P.C. Chiadighikaobi, O.C. Onuoha, A.E. Fagbuyi.

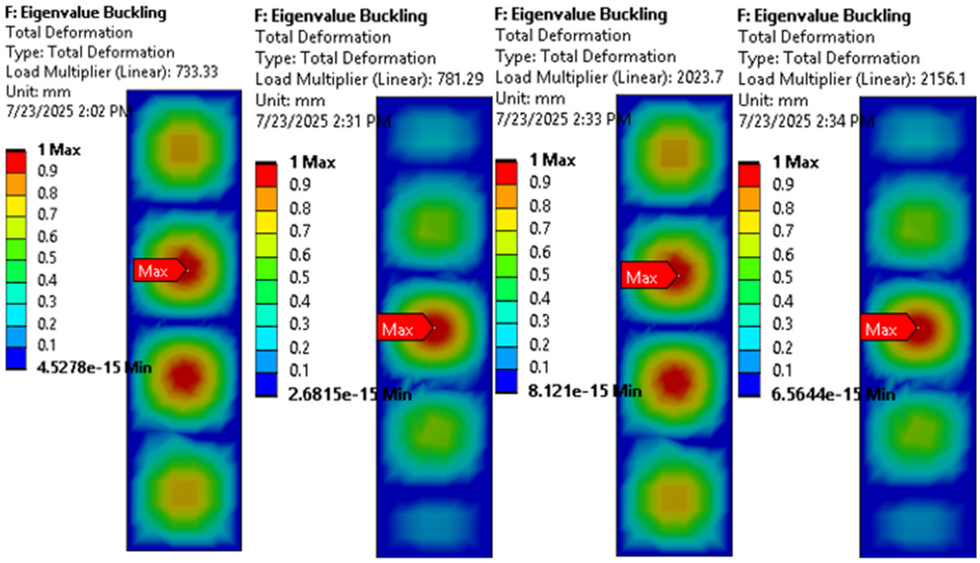

a *b* *c* *d*

Figure 23. Buckling deformation of plates at 22 °C:
a — Aluminium (mode 1); *b* — Aluminium (mode 2); *c* — Steel (mode 1); *d* — Steel (mode 2)
S o u r c e: compiled by P.C. Chiadighikaobi, O.C. Onuoha, A.E. Fagbuyi.

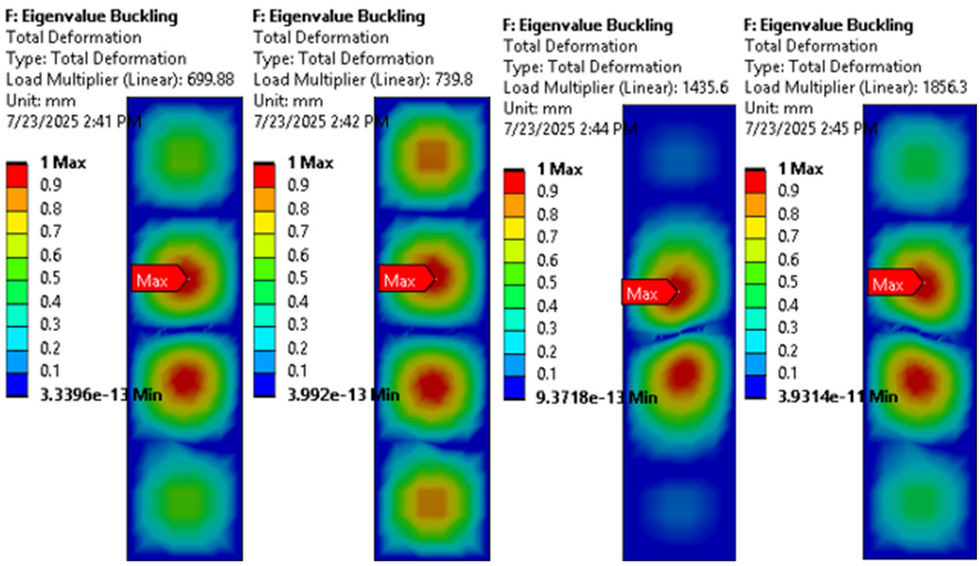

a *b* *c* *d*

Figure 24. Buckling deformation of plates at 44 °C:
a — Aluminium (mode 1); *b* — Aluminium (mode 2); *c* — Steel (mode 1); *d* — Steel (mode 2)
S o u r c e: compiled by P.C. Chiadighikaobi, O.C. Onuoha, A.E. Fagbuyi.

4. Conclusion

In conclusion, this study illuminates the potential for aluminium as a suitable construction material. The finite element analysis (FEA) results agreed with their analytical formulations with less than 5 percentile difference, thus proving the efficiency of FEA. The conclusive findings of this study are as follows.

1. The results showed that aluminium plates experienced slightly greater overall maximum deformation than steel under every temperature and loading condition. However, aluminium was discovered to be more thermally stable. At low temperatures (0° C and 11 °C), aluminium experienced lesser deformation, with mid-node deformation going down to 0.42115 mm under 100 MPa, whereas 0.57823 mm at the reference

temperature (22°C). Steel also performed well at low temperatures, but with minimal change in mid-node deformation.

2. Under buckling analysis, aluminium experienced stable performance with a reduction of just 4.71% in critical buckling load between 33 °C and 44 °C. Steel's critical buckling load in Mode 1, on the other hand, dropped precipitously by 40.7% over the same temperature range, illustrating its vulnerability to temperature change. Mode 2's results also indicated a lower but noticeable drop in steel performance, whereas aluminium again remained relatively stable.

These findings show that while steel offers higher stiffness and lower deformation at moderate conditions, recycled aluminium offers a better performance under large temperature fluctuations, thus highlighting its potential as a viable material for enhancing thermal and structural efficiency in a hot climate.

References

1. Eze F.O., Nnamani E. Effective supply chain network: A sustainable approach to waste management in South-Eastern Nigeria. *International Digital Organization for Scientific Research Journal of Applied Sciences*. 2019;4(1):74–85. Available from: https://www.idosr.org/wp-content/uploads/2019/04/IDOSR-JAS-41-74-85-2019.pdf (accessed: 03.04.2025).

2. Risonarta V.Y., Anggono J., Suhendra Y.M., Nugrowibowo S., Jani Y. Strategy to improve recycling yield of aluminium cans. *E3S Web of Conferences*. 2019;130:01033. https://doi.org/10.1051/e3sconf/201913001033

3. Wallace G. Production of secondary aluminium. In: *Elsevier eBooks*. 2011. p. 70–82. https://doi.org/10.1533/9780857090256.1.70

4. Falde N., Falde N. How is Aluminium Recycled? Step by Step | Greentumble. Greentumble. 2020. Available from: https://greentumble.com/how-is-Aluminium-recycled (accessed: 03.04.2025).

5. Nunes H., Emadinia O., Soares R., Vieira M.F., Reis A. Adding Value to Secondary Aluminium Casting Alloys: A review on Trends and Achievements. *Materials*. 2023;16(3):895. https://doi.org/10.3390/ma16030895 EDN: WAVSVT

6. Brough D., Jouhara H. The aluminium industry: A review on state-of-the-art technologies, environmental impacts and possibilities for waste heat recovery. *International Journal of Thermofluids*. 2020;1–2:100007. https://doi.org/10.1016/j.ijft.2019.100007 EDN: IRGUBX

7. Zuo Z., Liu Y., Kang J., Yu G., Liu F., Zhao H. Basic physical properties of Aluminium alloys and their electrolyte systems prepared by Molten Salt electrolysis using black Aluminium dross as raw material. *JOM.* 2022;74(5):2037–2046. https://doi.org/10.1007/s11837-021-05149-0

8. Mazzolani F.M. *Structural applications of aluminium in civil engineering. Structural Engineering International.* 2006;16(4):280–285. https://doi.org/10.2749/101686606778995128

9. Kissell J.R., Ziemian R.D. *The 2020 Aluminium Design Manual*. Trinity Consultants, Bucknell University. 2019; 77(4):2.

10. Mittelstedt C. Introduction to shell structures. In: *Springer eBooks*. 2023. p. 477–490. https://doi.org/10.1007/978-3-662-66805-4_14

11. Steele C.R., Balch C.D. *Introduction to the Theory of Plates.* Stanford University. Retrieved 2020-12-14. 2009.

12. Ali M.M., Al-Kodmany K. Structural systems for tall buildings. *Encyclopedia.* 2022;2(3):1260–1286. https://doi.org/10.3390/encyclopedia2030085

13. Arslan E., Kayaturk D., Durmus M.R., Bagca I., Imamoglu T., Sert S. The role of utilizing load in different cases while numerical modeling of multi-story buildings on alluvial stratum: a comparison study. *Arabian Journal for Science and Engineering*. 2024;49(10):13845–13860. https://doi.org/10.1007/s13369-024-08800-5

14. Van A.L. Reissner-Mindlin Plate Theory. In: *Elsevier eBooks*. 2017. p. 67–82. https://doi.org/10.1016/b978-1-78548-227-4.50004-6

15. Abrate S. Impact on composite plates in contact with water. *Dynamic Response and Failure of Composite Materials and Structures.* In: *Elsevier eBooks*. 2017. p. 183–216. https://doi.org/10.1016/b978-0-08-100887-4.00006-8

16. Wang C., Reddy J., Lee K. Chapter 1 — Introduction. Shear Deformable Beams and Plates Relationships with Classical Solutions 2000. p. 1–7. https://doi.org/10.1016/b978-008043784-2/50001-0

17. Johnson D. *Advanced structural mechanics: an introduction to continuum mechanics and structural mechanics.* Nottingham Trent University. Thomas Telford; 2010. ISBN 0 7277 2860 1

18. Remes H., Romanoff J., Lillemäe I., Frank D., Liinalampi S., Lehto P., & Varsta P. Factors affecting the fatigue strength of thin-plates in large structures. *International Journal of Fatigue*. 2026;101:397–407. https://doi.org/10.1016/j.ijfatigue.2016.11.019

19. Torabi A.R., Campagnolo A., Berto F. Large-Scale yielding failure prediction of notched ductile plates by means of the linear elastic notch fracture mechanics. *Strength of Materials.* 2017;49(2):224–233. https://doi.org/10.1007/s11223-017-9861-9 EDN: RREBNY

20. Obinna U. Buckling of Thin Plates — Structville. 2022. Available from: https://structville.com/2022/05/buckling-of-thin-plates.html (accessed: 03.04.2025).

21. Audoly B. Buckling and Post-buckling of Plates. *Encyclopedia of Continuum Mechanics*. 2020. p. 222–237. https://doi.org/10.1007/978-3-662-55771-6_134

22. Yu T. Buckling of Thin Plate. University of Massachusetts Lowell, Lowell, Massachusetts. 2017.

23. Quiel S.E., Moreyra E. Calculating the buckling strength of steel plates exposed to fire. *Thin-Walled Structures*. 2010;48(9):684–695. https://doi.org/10.1016/j.tws.2010.04.001 EDN: OEJYKD

24. Traub L.W. Examination and Prediction of the Lift Components of Low Aspect Ratio Rectangular Flat Plate Wings. *Aerospace*. 2023;10(7):597. https://doi.org/10.3390/aerospace10070597 EDN: ZSODWT

25. Rawson K.J., Tupper E.C. 7 — Structural design and analysis. *Basic Ship Theory (Fifth Edition)*. 2001. p. 237–285. https://doi.org/10.1016/B978-075065398-5/50010-8

26. Shrivastava A., Singh R. Effect of aspect ratio on buckling of composite plates. *Composites Science and Technology*. 1999;59(3):439–445. https://doi.org/10.1016/s0266-3538(98)00087-6

27. El-Sawy K.M., Nazmy A.S. Effect of aspect ratio on the elastic buckling of uniaxially loaded plates with eccentric holes. *Thin-Walled Structures*. 2001;39(12):983–998. https://doi.org/10.1016/s0263-8231(01)00040-4

28. Panda S.K., Ramachandra L. Buckling of rectangular plates with various boundary conditions loaded by non-uniform inplane loads. *International Journal of Mechanical Sciences*. 2010;52(6):819–828. https://doi.org/10.1016/j.ijmecsci.2010.01.009

29. Wang C., Liu Q. Buckling behaviour of rectangular and skew plates with elastically restrained edges under non-uniform mechanical edge loading. *PLoS ONE*. 2024;19(9):e0308245–e0308245. https://doi.org/10.1371/journal.pone.0308245 EDN: VXQKWY

30. Prabowo A.R., Ridwan R., Muttaqie T. On the Resistance to Buckling Loads of Idealized Hull Structures: FE Analysis on Designed-Stiffened Plates. *Designs*. 2022;6(3):46. https://doi.org/10.3390/designs6030046 EDN: PCPUXW

31. Suleiman O.M.E., Osman M.Y., & Hassan T. Effect of Boundary Conditions on Buckling Load for Laminated Composite Plates. *Global Journal of Engineering Sciences*. 2019;2(1). https://doi.org/10.33552/gjes.2019.02.000527

32. Shi P., Viet N., Yang J., Shou H., Li Q., Turan F. Free vibration and nonlinear transient analysis of blast-loaded FGM sandwich plates with stepped face sheets: Analytical and artificial neural network approaches. *Thin-Walled Structures*. 2024;206:112667–112667. https://doi.org/10.1016/j.tws.2024.112667 EDN: FZZWTS

33. Ren G., Pan R., Sun F., Dong Z., Lan T. Advanced Analysis of Structural Performance in Novel Steel-Plate Concrete Containment Structures. *Buildings*. 2024;14(9):2771–2771. https://doi.org/10.3390/buildings14092771 EDN: BCHYZI

34. Atuma I.M., Efe S.I., Ndakara O.E. Temperature trend in Niger Delta Region, Nigeria. *Journal of Management and Social Science Research*. 2023;4(1):29–39. https://doi.org/10.47524/jmssr.v4i1.30 EDN: JNEOPB

35. Stresman G.H. Beyond temperature and precipitation: Ecological risk factors that modify malaria transmission. *Acta Tropica*. 2010;116(3):167–172. https://doi.org/10.1016/j.actatropica.2010.08.005

36. Czerwinski F. Thermal stability of Aluminium alloys. *Materials*. 2020;13(15):3441. https://doi.org/10.3390/ma13153441 EDN: ZVPFGE

37. Rajaram G., Kumaran S., Rao T.S. High temperature tensile and wear behaviour of Aluminium silicon alloy. *Materials Science and Engineering A*. 2010;528(1):247–253. https://doi.org/10.1016/j.msea.2010.09.020

38. Summers P.T., Chen Y., Rippe C.M., Allen B., Mouritz A.P., Case S.W., Lattimer B.Y. Overview of Aluminium alloy mechanical properties during and after fires. *Fire Science Reviews*. 2015;4(1). https://doi.org/10.1186/s40038-015-0007-5

39. Lemmon A., Weritz J. *Fire Safety of Aluminium & Its Alloys*. The Aluminium Association. 2021. Available from: https://www.Aluminium.org/sites/default/files/2021-11/FireSafetyAluminiumAlloys_9.8.20.pdf (accessed: 03.04.2025).

40. Guo X., Tao L., Zhu S., Zong S. Experimental investigation of mechanical properties of Aluminium alloy at high and low temperatures. *Journal of Materials in Civil Engineering*. 2019;32(2). https://doi.org/10.1061/(asce)mt.1943-5533.0003002 EDN: HOHMZH

41. Su M., Young B. 10.37: Mechanical properties of high strength aluminium alloy at elevated temperatures. *Special Issue:Proceedings of Eurosteel 2017. Ce/Papers*. 2017;1(2–3):2831–2839. https://doi.org/10.1002/cepa.334

42. Sharma R., Sharma K., Saraswat B.K. A review of the mechanical and chemical properties of aluminium alloys AA6262 T6 and its composites for turning process in the CNC. *Materials Today: Proceedings*. 2023. https://doi.org/10.1016/j.matpr.2023.01.421 EDN: MHBYWF

43. Kissell J.R., Ferry R.L. *Aluminium Structures: A Guide to Their Specifications and Design*. John Wiley & Sons. 2002. ISBN 978-0-471-01965-7

44. Baytak T., Tosun M., Ipek C., Mollamahmutoglu C., Bulut O. Thermal Stress Analysis for Functionally Graded Plates with Modulus Gradation, Part II. *Experimental Mechanics*. 2024;64(8):1229–1247. https://doi.org/10.1007/s11340-024-01091-9 EDN: TECQLZ

45. Zhang H. *Building Materials in Civil Engineering*. Woodhead Publishing Series in Civil and Structural Engineering, 2011;423:7–28. ISBN 161344351X, 9781613443514

46. Guo X., Tao L., Zhu S., Zong S. Experimental investigation of mechanical properties of Aluminium alloy at high and low temperatures. *Journal of Materials in Civil Engineering*. 2020;32(2):06019016. https://doi.org/10.1061/(asce)mt.1943-5533.0003002 EDN: HOHMZH